



# University of HUDDERSFIELD

## University of Huddersfield Repository

Grossoni, Ilaria

Design methodology for track systems considering the long-term ballast behaviour: application to crossings

### Original Citation

Grossoni, Ilaria (2019) Design methodology for track systems considering the long-term ballast behaviour: application to crossings. Doctoral thesis, University of Huddersfield.

This version is available at <http://eprints.hud.ac.uk/id/eprint/35411/>

The University Repository is a digital collection of the research output of the University, available on Open Access. Copyright and Moral Rights for the items on this site are retained by the individual author and/or other copyright owners. Users may access full items free of charge; copies of full text items generally can be reproduced, displayed or performed and given to third parties in any format or medium for personal research or study, educational or not-for-profit purposes without prior permission or charge, provided:

- The authors, title and full bibliographic details is credited in any copy;
- A hyperlink and/or URL is included for the original metadata page; and
- The content is not changed in any way.

For more information, including our policy and submission procedure, please contact the Repository Team at: [E.mailbox@hud.ac.uk](mailto:E.mailbox@hud.ac.uk).

<http://eprints.hud.ac.uk/>

# **Design methodology for track systems considering the long-term ballast behaviour: application to crossings**

Ilaria Grossoni

A thesis submitted to the University of Huddersfield in partial fulfilment of the requirements of the degree of Doctor of Philosophy

Institute of Railway Research  
School of Computing and Engineering  
University of Huddersfield

*December 2019*



*To*

*Nonna Francesca*

“Let’s not pretend that things will change if we keep doing the same things. A crisis can be a real blessing to any person, to any nation. For all crises bring progress.

Creativity is born from anguish, just like the day is born from the dark night. It’s in crisis that inventiveness is born, as well as discoveries made and big strategies. He who overcomes crisis, overcomes himself, without getting overcome. He who blames his failure to a crisis neglects his own talent and is more interested in problems than in solutions. Incompetence is the true crisis. The greatest inconvenience of people and nations is the laziness with which they attempt to find the solutions to their problems.

There’s no challenge without a crisis. Without challenges, life becomes a routine, a slow agony.

There’s no merit without crisis. It’s in the crisis where we can show the very best in us. Without a crisis, any wind becomes a tender touch. To speak about a crisis is to promote it. Not to speak about it is to exalt conformism. Let us work hard instead. Let us stop, once and for all, the menacing crisis that represents the tragedy of not being willing to overcome it.”

*Albert Einstein*

## **Executive Summary**

Switches and Crossings (S&Cs), also called turnouts, refer to the components of the railway that provide flexibility to the system in terms of possible routes of a rail vehicle. Nevertheless, they are the asset which experiences the highest number of failures due to a number of reasons, including discontinuities in the rail geometry and track properties. Impact forces along the S&C panels cause faster degradation than in plain line track and, hence, the turnouts incur very high maintenance and renewal costs, in addition to significant investment costs. From a modelling perspective, S&C are also a considerably complex part of the railway system due to physical non-linearities, including rapidly changing rail geometry and trackbed characteristics, sharp radius with little or no transitions in the diverging route and rail profiles subject to heavy wear.

This research proposes a scientific based design methodology that is able to assess different assets and support the infrastructure manager's decision, based on knowledge of the long-term trackbed evolution, which is considered one of the most significant causes of whole track degradation. Special attention is given to the crossing panel, but the methodology can be applied to the switch panel as well as plain line and other discrete features.

To support the methodology, a three-dimensional vehicle-track interaction model has been developed using Matlab. This model includes a comprehensive Finite Element (FE) model of a ballasted track section, various vehicle configurations and a contact model solved in the normal direction using the non-linear Hertzian theory with a single point of contact and in the tangential direction using the linear Kalker theory modified according to the Shen & Hendrick correction. The modelled track response is validated against experimental data from a UK site equipped with Under Sleeper Pads (USPs) achieving a very good agreement in terms of bearer vertical displacement. The long-term ballast behaviour in plain line is firstly assessed using a vertical two-dimensional track model under a point load with various settlement models available in literature for different load characteristics (i.e. amplitude and loading frequency) and trackbed stiffness values. A new settlement equation is then proposed in order to overcome the limitations of the current approaches. The results from the simplified model are applied at the crossing panel. The iterative process is validated against the calculated rate of longitudinal level defect growth using two consecutive Track

Recording Coach (TRC) data signals.

The results from the simplified plain line track model show that the settlement rate, according to the equations available in literature, not only varies in magnitude but also in trend. For instance, the Guérin's and the Fröhling's predictions decrease non-linearly with increasing trackbed stiffness (i.e. stiffer supports will settle less than softer ones), while the Sato's prediction shows the opposite tendency (i.e. stiffer supports will settle more than softer ones). This can be explained with the opposite behaviours revealed by the physical quantities involved, i.e. displacement for the Guérin's equation, the ballast force for the Sato's equation and variation in load and stiffness for the Fröhling's equation. It is felt that none of these results are entirely satisfactory and there is a need for a more comprehensive equation that can capture the trends seen on track as well as physical quantities that can be easily recorded *in situ*. A new settlement equation is therefore proposed based on the maximum energy transmitted to the ballast layer, which has been demonstrated to be the only physical quantity that reflects all the main track modes as well as the vehicle characteristics. Through this research, it has been proven that it is necessary to include the longitudinal variation of trackbed stiffness in the numerical model in order to correctly capture the long-term ballast behaviour. The tool developed can also be (but not limited to) used to assess (1) the modification of the resilient track layers, such as rail-pads and potential USPs; (2) the change of the crossing geometry design on the long-term system degradation; (3) the variation of the crossing layout due to a change in bearer spacing; (4) the modification of sleeper design and sleeper material design.

As further work, additional validation of the VTI model can be achieved using available on-track acceleration data not only at the bearer level but also at the rail level. Further verification of the proposed settlement equation should also be carried out against laboratory tests in order to capture the overall behaviour under controlled conditions and for low loading frequencies. Finally, measurement sites should be also considered in order to assess the influence of higher loading frequency.

## **Acknowledgements**

I would like to extend thanks to the many people who contributed to both my professional and personal growth.

First, I would like to thank my main Supervisor Dr Yann Bezin for his dedicated support and guidance. He was always enthusiastic to assist and support me throughout this long journey. I learnt a lot every day during the past six years and I am very grateful for that.

Many thanks also go to Prof Simon Iwnicki for providing always well thought advices.

All the IRR staff is also gratefully acknowledged, especially those whom I met when I first came to UK for my internship and who made me feel very welcome from the very beginning. A very special mention goes to Dr Philip Shackleton, David Crosbee, Dr Cencen Gong, Dr Yunshi Zhao, Thomas Colantuono, Dr Antonio Andrade, Dr Dimitrios Kostovasilis.

In addition to that, I would like to acknowledge the research projects Track to the Future (EPSRC project, grant agreement no. EP/M025276/1), Capacity4Rail (European Union's Seventh Framework Programme, grant agreement no. 605650) and In2Rail (European Union's Horizon 2020 Research and Innovation Programme, grant agreement no. 635900) for the partial support to this project.

Lastly, but absolutely not least, thanks to Nonna Francesca, who has been next to me in every step of my life, my beloved parents and my husband Christopher for their daily protection and encouragement. My daughter Carlotta Francesca, who was born in January 2020 at the beginning of the pandemic, gave me the ultimate motivation to finish this thesis.

# Table of Contents

<b>EXECUTIVE SUMMARY .....</b>	<b>II</b>
<b>ACKNOWLEDGEMENTS .....</b>	<b>IV</b>
<b>TABLE OF CONTENTS.....</b>	<b>V</b>
<b>LIST OF FIGURES.....</b>	<b>IX</b>
<b>LIST OF TABLES .....</b>	<b>XVI</b>
<b>GLOSSARY OF TERMS.....</b>	<b>XVIII</b>
<b>DEFINITION OF SYMBOLS USED .....</b>	<b>XIX</b>
<b>1 INTRODUCTION .....</b>	<b>1</b>
1.1 AIM OF THE RESEARCH .....	2
1.2 OBJECTIVES .....	2
1.3 NOVELTY OF THE RESEARCH .....	3
1.4 METHODOLOGY .....	3
1.5 OVERVIEW OF THE THESIS.....	5
1.6 PUBLICATIONS RELATED TO THE RESEARCH .....	6
<b>2 BACKGROUND .....</b>	<b>9</b>
2.1 SWITCHES & CROSSINGS.....	9
2.1.1 <i>Classification of S&amp;Cs</i> .....	10
2.1.2 <i>The crossing panel</i> .....	12
2.1.3 <i>Design parameters for the crossing panel</i> .....	14
2.2 BALLAST SETTLEMENT.....	15
<b>3 LITERATURE REVIEW.....</b>	<b>18</b>
3.1 MODELLING THE DYNAMIC BEHAVIOUR OF THE RAILWAY SYSTEM .....	18
3.1.1 <i>Track system models</i> .....	18
BOEF.....	20
Continuously supported track models .....	21
Discretely supported track models .....	21
3.1.2 <i>Track fixing systems</i> .....	22
3.1.3 <i>Wheel-rail contact model</i> .....	25
Normal contact model .....	26
Tangential contact model .....	30
MBS packages .....	32



*Design methodology for track systems considering the long-term ballast behaviour:  
application to crossings*

3.1.4	Vehicle system model .....	33
	Unsprung mass.....	33
	Suspensions [23, 65] .....	33
3.2	MODELLING THE TURNOUT SYSTEM: STATE OF THE ART .....	34
3.2.1	Vehicle-track interaction modelling.....	34
3.2.2	Trackbed degradation .....	35
3.3	MODELLING THE LONG-TERM BALLAST BEHAVIOUR .....	35
3.3.1	Laboratory testing .....	36
3.3.2	In situ testing .....	42
3.4	COUPLING THE LONG-TERM BALLAST BEHAVIOUR WITH VEHICLE-TRACK INTERACTION MODELS .....	46
<b>4</b>	<b>STATISTICAL ANALYSIS OF CROSSING FAILURES .....</b>	<b>51</b>
4.1	DATA ANALYSED.....	51
4.2	CLASSIFICATION OF THE FAILURE TYPES .....	52
4.3	DAMAGES OCCURRING ONLY AT CROSSING PANEL .....	54
4.4	RECOMMENDATION.....	55
4.4.1	Impact of the results on the present research .....	56
<b>5</b>	<b>VEHICLE-TRACK INTERACTION MODEL .....</b>	<b>57</b>
5.1	MODELLING THE TRACK SYSTEM .....	57
5.1.1	Fundamental assumptions .....	57
5.1.2	Track model .....	59
	FE model of rail with discrete support .....	59
	Crossing geometry .....	63
	Bearer model.....	64
	Track model.....	65
5.1.3	Validation of the track model.....	66
	Description of the present track model applied to a crossing panel.....	67
	Description of the Chalmers track model.....	67
	Receptance at the crossing nose.....	69
	Static stiffness along the crossing panel .....	70
5.2	MODELLING THE VEHICLE .....	71
5.2.1	Fundamental assumptions .....	72
5.2.2	Modelling the vehicle system .....	72
5.3	MODELLING THE VEHICLE-TRACK INTERACTION.....	74
5.3.1	Fundamental assumptions .....	74
5.3.2	Contact model .....	75
	On-line approach.....	75

*Design methodology for track systems considering the long-term ballast behaviour:  
application to crossings*

Normal problem.....	76
Tangential problem.....	76
5.3.3 <i>Numerical solution of the wheel/track interaction model</i> .....	78
5.4 SIMULATION RESULTS .....	81
5.4.1 <i>Wheelset motions and contact geometry outputs</i> .....	82
5.4.2 <i>Wheel-rail contact forces</i> .....	84
5.5 INITIAL VALIDATION OF THE CONTACT ALGORITHM.....	90
5.5.1 <i>Contact geometry</i> .....	91
5.5.2 <i>Contact indices</i> .....	93
<b>6 VALIDATION OF THE DYNAMIC MODEL WITH EXPERIMENTAL DATA.....</b>	<b>95</b>
6.1 SITE DATA .....	95
6.1.1 <i>Site description</i> .....	95
6.1.2 <i>Field data: measurements with geophones</i> .....	96
6.1.3 <i>Field data: TRC data</i> .....	97
Top level.....	98
Gauge.....	100
Alignment.....	101
6.2 CONSIDERATIONS FOR LONG BEARER MODELLING IN THE CROSSING PANEL .....	102
6.2.1 <i>Long bearer FE model</i> .....	103
6.2.2 <i>Influence of trackbed stiffness transversal distribution on the vehicle-track dynamics</i> 106	106
6.2.3 <i>Frequency analysis of the long bearer behaviour and modelling selection</i> .....	108
6.3 TUNING THE TRACKBED STIFFNESS ALONG THE CROSSING PANEL .....	112
6.3.1 <i>Methodology</i> .....	113
6.3.2 <i>Initial estimation of support stiffness distribution</i> .....	113
6.3.3 <i>Tuned trackbed stiffness distribution along the crossing panel</i> .....	114
6.4 BEARER DISPLACEMENT VALIDATION ALONG THE CROSSING PANEL.....	116
6.5 THE INFLUENCE OF BEARER FLEXIBILITY .....	119
6.6 SUMMARY.....	122
<b>7 MODELLING THE BALLAST LONG-TERM BEHAVIOUR .....</b>	<b>124</b>
7.1 APPLICATION OF AN EXTERNAL QUASI-STATIC LOAD .....	124
7.2 APPLICATION OF AN EXTERNAL MOVING LOAD .....	132
7.3 VARIATION OF BALLAST SETTLEMENT PREDICTIONS .....	138
7.4 SUMMARY.....	142
<b>8 PREDICTING THE RATE OF DEGRADATION AT THE STUDY SITE.....</b>	<b>144</b>

*Design methodology for track systems considering the long-term ballast behaviour:  
application to crossings*

8.1	INTERPRETATION OF TRACK RECORDED GEOMETRY DATA .....	144
8.2	COMPARISON BETWEEN NUMERICAL MODEL AND TRC DATA .....	146
8.3	THE INFLUENCE OF SLEEPER FLEXIBILITY .....	148
8.4	THE INFLUENCE OF TRACKBED CONDITIONS.....	149
8.4.1	<i>Dynamic results of two wheelset passages .....</i>	<i>149</i>
8.4.2	<i>Settlement rate analysis .....</i>	<i>151</i>
8.5	SUMMARY .....	152
<b>9</b>	<b>CONCLUSIONS, DISCUSSION AND FURTHER WORK .....</b>	<b>153</b>
9.1	SUMMARY OF ACHIEVEMENTS AND CONCLUSIONS.....	153
9.2	FURTHER WORK .....	156
<b>10</b>	<b>REFERENCES .....</b>	<b>158</b>
	Appendix A Degradation modes at the rail level .....	169
	Appendix B Hertz contact theory.....	176
	Appendix C Coefficients for the tangential contact problem .....	179
	Appendix D Newmark Beta integration method .....	180

## **List of Figures**

<i>Figure 1.1: Methodology overview.....</i>	<i>5</i>
<i>Figure 2.1: (a) Components of a single right hand turnout [3] and (b) example of symmetrical turnout [10]......</i>	<i>10</i>
<i>Figure 2.2: An example of crossing panel.....</i>	<i>12</i>
<i>Figure 2.3: Central Line Method [13].....</i>	<i>13</i>
<i>Figure 2.4: (a) Acute crossing [15]; (b) Diamond crossing [16]; (c) Square crossing [17]. .....</i>	<i>14</i>
<i>Figure 2.5: General ballast settlement trend.....</i>	<i>16</i>
<i>Figure 2.6: Evolution in time of the ballast settlement for several tamping cycles. ....</i>	<i>17</i>
<i>Figure 3.1: Summary of track models [25]. ....</i>	<i>19</i>
<i>Figure 3.2: Beam on elastic foundation (BOEF). ....</i>	<i>20</i>
<i>Figure 3.3: Two-layer continuously supported track model [31]. ....</i>	<i>21</i>
<i>Figure 3.4: Three-layer discretely supported model [35].....</i>	<i>22</i>
<i>Figure 3.5: Test arrangement for static pad test [41].....</i>	<i>23</i>
<i>Figure 3.6: Test arrangement for high frequency pad and assembly tests: (a) direct method, (b) indirect method [41]. ....</i>	<i>25</i>
<i>Figure 3.7: Wheel-rail contact problem and sets of coordinate systems [46]. ....</i>	<i>26</i>
<i>Figure 3.8: Comparison, with respect to maximum contact pressure and the contact area, between three different contact mechanics analysis methods [52]. ....</i>	<i>29</i>
<i>Figure 3.9: Main methods to solve non-Hertzian contact problems: (a) approximation with set of ellipsis and (b) virtual penetration of contact bodies [53]. ....</i>	<i>29</i>
<i>Figure 3.10: Ratio of lateral creep force to available maximum vertical friction force in Hertzian rolling contact with pure spin: comparison between results from CONTACT and linear theory [60].....</i>	<i>32</i>
<i>Figure 3.11: Comparison of settlement equations obtained with laboratory tests. ....</i>	<i>38</i>
<i>Figure 3.12: The effect of axle load according to (a) Shenton [100] and (b) Jeff [93]. ....</i>	<i>40</i>
<i>Figure 3.13: The influence of axle load on vertical settlement considering all the equations analysed in Figure 3.11. ....</i>	<i>40</i>
<i>Figure 3.14: The effect of loading frequency according to (a) Shenton [100] and (b) Indraratna [107].....</i>	<i>41</i>

*Design methodology for track systems considering the long-term ballast behaviour:  
application to crossings*

<i>Figure 3.15: The influence of loading frequency on vertical settlement considering all the equations analysed in Figure 3.11. ....</i>	<i>42</i>
<i>Figure 3.16: Variation of settlement predictions with trackbed stiffness using the Fröhling equation as defined (<math>\ln N = 1</math>; <math>P_{dyn}/P_{stat} = 1</math>) ([9]) .....</i>	<i>43</i>
<i>Figure 3.17: Comparison of settlement equations obtained with in situ tests. ....</i>	<i>44</i>
<i>Figure 3.18: Comparison of settlement equations obtained with in situ tests and laboratory tests. ....</i>	<i>44</i>
<i>Figure 3.19: Comparison of settlement equations obtained at 100,000 cycles using the input values in Table 3.4 ([9]). ....</i>	<i>45</i>
<i>Figure 3.20: Coupling the vehicle-track interaction model with the long-term ballast behaviour ([9]). ....</i>	<i>47</i>
<i>Figure 3.21: Settlement rate according to (a) Eq. 3.4 and (b) Eq. 3.5 [114]. ....</i>	<i>48</i>
<i>Figure 4.1: Degradation mechanisms at the crossing panel in the GB network from 2011 to 2017. ....</i>	<i>54</i>
<i>Figure 5.1: Track model in the (a) x-z plane and in the (b) y-z plane. ....</i>	<i>57</i>
<i>Figure 5.2: Positive axis system. ....</i>	<i>59</i>
<i>Figure 5.3: Generic beam element .....</i>	<i>59</i>
<i>Figure 5.4: Hermitian interpolation. ....</i>	<i>61</i>
<i>Figure 5.5: Present model (not in proportion). ....</i>	<i>67</i>
<i>Figure 5.6: Chalmers FE model [12]. ....</i>	<i>68</i>
<i>Figure 5.7: Receptance magnitude at the crossing nose for the Chalmers model and present model (<math> H_{22} </math>: direct receptance at the inner rail; <math> H_{33} </math>: direct receptance at the outer rail). ....</i>	<i>70</i>
<i>Figure 5.8: Normalised static track stiffness along through route of turnout for the (a) Chalmers model and (b) present model. ....</i>	<i>71</i>
<i>Figure 5.9: Vehicle-track interaction model considered ((a) y-z plane and (b) x-z plane). ....</i>	<i>72</i>
<i>Figure 5.10: Vehicle-track interaction model considered (y-z plane). ....</i>	<i>75</i>
<i>Figure 5.11: Flow chart of the resolution algorithm. ....</i>	<i>81</i>
<i>Figure 5.12: Wheelset outputs: vertical displacement (black line), lateral displacement (black dashed line) and yaw rotation (grey line). ....</i>	<i>82</i>
<i>Figure 5.13: Rolling radius difference along the crossing panel. ....</i>	<i>83</i>
<i>Figure 5.14: Comparison between nominal rail (black line) and initial crossing profile (grey</i>	

*Design methodology for track systems considering the long-term ballast behaviour:  
application to crossings*

<i>line).</i> .....	83
<i>Figure 5.15: Three-dimensional wheel trajectory on the crossing surface.</i> .....	84
<i>Figure 5.16: Dynamic contact forces at left (grey line) and right (black line) wheel compared with vertical irregularity seen by the right wheel.</i> .....	85
<i>Figure 5.17: Unfiltered (black) and filtered (grey) dynamic contact force at right wheel.</i>	86
<i>Figure 5.18: Typical wheel-rail vibration modes.</i> .....	86
<i>Figure 5.19: FFT of the vertical dynamic force at the right wheel.</i> .....	87
<i>Figure 5.20: Lateral wheel-rail contact forces at the left (grey line) and right wheel (black line).</i> .....	88
<i>Figure 5.21: Vehicle-track interaction model including sprung masses.</i> .....	88
<i>Figure 5.22: Dynamic vertical contact force at the right wheel considering only the unsprung mass (grey line) and considering unsprung and sprung masses (black line).</i> .....	89
<i>Figure 5.23: FFT of the vertical dynamic force at the right wheel considering only the unsprung mass (grey line) and considering unsprung and sprung masses (black line).</i> .....	89
<i>Figure 5.24: Lateral contact force at the right wheel considering only the unsprung mass (grey line) and considering unsprung and sprung masses (black line).</i> .....	90
<i>Figure 5.25: Track model in VI-Rail.</i> .....	91
<i>Figure 5.26: Comparison between the present model and VI-Rail in terms of rolling radius difference along the crossing panel.</i> .....	92
<i>Figure 5.27: Comparison between the present model and VI-Rail in terms of wheel-rail lateral contact position along the crossing panel.</i> .....	92
<i>Figure 5.28: Comparison between the present model and VI-Rail in terms of wheel vertical trajectory along the crossing panel.</i> .....	93
<i>Figure 5.29: Comparison between the present model and VI-Rail in terms of vertical wheel-rail contact force along the crossing panel.</i> .....	93
<i>Figure 5.30: Comparison between the present model and VI-Rail in terms of lateral wheel-rail contact force along the crossing panel.</i> .....	94
<i>Figure 6.1: Site plan. The bearers monitored are marked with “v” (Le Pen [123]).</i> .....	96
<i>Figure 6.2: Geophones measurements up to 250 Hz at bearer (a) 3, (b) 4 and (c) 6 for cess and 6ft side.</i> .....	97
<i>Figure 6.3: Main dimensions of the analysed site.</i> .....	98
<i>Figure 6.4: (a, b) Top level measurements and (c, d) top level rate of growth in mm/100 days</i>	

*Design methodology for track systems considering the long-term ballast behaviour:  
application to crossings*

*for cess and 6ft sides, respectively (--- Welded joint; — Underbridge; - - - Switch toe/crossing nose). ..... 100*

*Figure 6.5: (a) Gauge measurement and (b) gauge rate of growth in mm/100 days (--- Welded joint; --- Insulated joint; — Underbridge; - - - Switch toe/crossing nose; - · - · First/last long bearer)..... 101*

*Figure 6.6: Alignment measurements filtered at 35 m for (a) cess and (b) 6ft side (--- Welded joint; --- Insulated joint; — Underbridge; - - - Switch toe/crossing nose; - · - · First/last long bearer)..... 102*

*Figure 6.7: Bearer loading point configuration..... 103*

*Figure 6.8: Stiffness distribution arrangements along the bearer. .... 104*

*Figure 6.9: Bearer displacement for different type of loading and different type of trackbed ((a): constant; (b): variable 1; (c): variable 2). ..... 106*

*Figure 6.10: Bearer displacement at the middle of the track for various trackbed distributions and different impact types. Continuous lines refer to perfect track, dashed lines to dip joint case and dotted lines to top level irregularities. Yellow lines refer to constant distribution, blue to “variable 1” type and green to “variable 2” type. The vertical dashed lines refer to both loads transversal position. .... 107*

*Figure 6.11: Modal analysis for the bearer under the crossing nose. .... 109*

*Figure 6.12: Influence of the bearer length and the material Young’s modulus on the bending modes considered. .... 110*

*Figure 6.13: Equivalent vertical and roll stiffness to account for the adjacent track. .... 111*

*Figure 6.14: Comparison between fully flexible (black), semi-flexible (blue) and rigid (red) bearer models in terms of displacement. The continuous lines refers to case of no additional stiffness, the dashed lines to case of vertical stiffness addition, the dotted lines to case of roll stiffness addition and the dashed-dotted lines to case of vertical and roll stiffness addition. .... 111*

*Figure 6.15: Methodology flow chart. .... 113*

*Figure 6.16: Variation of total trackbed stiffness after the tuning..... 115*

*Figure 6.17: Objective function evolution with number of iterations (○: cess end; □: 6ft end). ..... 115*

*Figure 6.18: Bearer displacement of the 6ft end at location (a) 3, (b) 4 and (c) 6 (red line: experimental data; black line: numerical results with un-linked unsprung masses; blue line:*

*Design methodology for track systems considering the long-term ballast behaviour:  
application to crossings*

*numerical results with complete vehicle). The displacement data has been collected by the Infrastructure Group team at University of Southampton, which is greatly acknowledged.*  
..... 117

*Figure 6.19: Comparison between numerical and experimental results in terms of bearer vertical displacement at (a) cress side and (b) 6ft side at first axle.*..... 118

*Figure 6.20: Semi-rigid bearer model.*..... 119

*Figure 6.21: Comparison of rigid and flexible bearer model in terms of trackbed stiffness distribution at the (a) cress and (b) 6ft side.* ..... 120

*Figure 6.22: Comparison between numerical results with rigid bearer model and flexible bearer model and experimental results in terms of bearer vertical displacement at (a) cress side and (b) 6ft side at first axle.* ..... 120

*Figure 6.23: 3D map of bearer displacement along the crossing panel considering the flexible model. The rail positions are marked in red. The cress side is at node 2 and 6ft side at node 4.*..... 121

*Figure 6.24: 3D map of maximum ballast force along the crossing panel considering the flexible model. The rail positions are marked in red. The cress side is at node 2 and 6ft side at node 4.*..... 121

*Figure 7.1: Vertical two-dimensional ballasted track model with sinusoidal force input.* 125

*Figure 7.2: Variation of (a) bearer displacement, (b) velocity and (c) accelerations for different load and frequency considered.* ..... 126

*Figure 7.3: Variation of (a) ballast forces, (b) ballast energy and (c) ballast power for different load and frequency considered.* ..... 127

*Figure 7.4: Variation of (a) bearer displacement, (b) velocity and (c) accelerations for different trackbed stiffness values and three loads considered.* ..... 128

*Figure 7.5: Variation of (a) ballast forces, (b) ballast energy and (c) ballast power for different trackbed stiffness values and three loads considered.* ..... 129

*Figure 7.6: Three-dimensional variation of (a) bearer displacement, (b) bearer velocity and (c) bearer acceleration considering load characteristics and trackbed stiffness.*..... 130

*Figure 7.7: Three-dimensional variation of (a) ballast forces, (b) ballast energy and (c) ballast power considering load characteristics and trackbed stiffness.*..... 131

*Figure 7.8: Vertical two-dimensional ballasted track model with travelling sinusoidal force input.* ..... 132



*Design methodology for track systems considering the long-term ballast behaviour:  
application to crossings*

<i>Figure 7.9: Three-dimensional variation of sleeper (a) displacement, (b) velocity and (c) acceleration considering load characteristics and trackbed stiffness at 100 km/h.....</i>	<i>133</i>
<i>Figure 7.10: Three-dimensional variation of ballast (a) force, (b) energy and (c) power considering load characteristics and trackbed stiffness at 100 km/h.....</i>	<i>134</i>
<i>Figure 7.11: The influence of loading frequency on sleeper (a) displacement, (b) velocity and (c) acceleration for three different trackbed stiffness. The static load considered is 100 kN and the travelling speed is 100 km/h.....</i>	<i>135</i>
<i>Figure 7.12: Mobility curve for three selected trackbed stiffness values.....</i>	<i>136</i>
<i>Figure 7.13: The influence of loading frequency on ballast force, energy and power for three different trackbed stiffness. The static load considered is 100 kN and the travelling speed is 100 km/h. ....</i>	<i>136</i>
<i>Figure 7.14: Variation of settlement rate predictions according to the Guérin's, Sato's and Fröhling's equation varying (a) the load amplitude and (b) trackbed stiffness.....</i>	<i>139</i>
<i>Figure 7.15: Variation of settlement rate predictions according to the Guérin's and Sato's equations for increasing loading frequency and three different trackbed stiffness (20, 70, 150 kN/mm for increasing line thickness). The static load considered is 100 kN and the travelling speed is 100 km/h. ....</i>	<i>140</i>
<i>Figure 7.16: Variation of settlement rate predictions according to the Guérin's, Sato's and proposed equations for increasing (a) load, (b) trackbed stiffness and (c) loading frequency (scenarios considered: three trackbed stiffness values, i.e.20, 70, 150 kN/mm represented by increasing line thickness, static load equal to 100 kN and travelling speed 100 km/h)....</i>	<i>141</i>
<i>Figure 8.1: (a) Rate of growth of the track top level; (b) back-calculated trackbed stiffness and stiffness absolute gradient; (c) predicted wheel-rail contact forces at the 6ft side. The crossing nose is marked with a vertical dashed line and the locations of leg ends with a green line. ....</i>	<i>145</i>
<i>Figure 8.2: Comparison between TRC data (continuous line) and numerical predictions using the Sato's equation (dashed line) and Guérin's equation (dashed-dotted line) in terms of settlement rate. The crossing nose position is marked with the dashed red line. ....</i>	<i>147</i>
<i>Figure 8.3: Comparison between TRC data (continuous line) and numerical predictions using the Sato's equation (dashed line), Guérin's equation (dashed-dotted line) and the proposed equation (dotted red line) in terms of settlement rate. The crossing nose is marked with the dashed red line.....</i>	<i>148</i>

*Design methodology for track systems considering the long-term ballast behaviour:  
application to crossings*

*Figure 8.4: Comparison between TRC data (continuous line) and numerical predictions using the rigid bearer model (dashed-dotted line) and the flexible bearer model (dotted line) in terms of settlement growth. The crossing nose is marked with the dashed red line. .... 149*

*Figure 8.5: Comparison between the case with and without considering variable trackbed stiffness in terms of bearer displacement at the 6ft side. .... 150*

*Figure 8.6: Comparison between the case with and without considering variable trackbed stiffness in terms of contact forces at 6ft side. .... 150*

*Figure 8.7: Comparison between the case with and without considering variable trackbed stiffness in terms of ballast forces at 6ft side of bearer 4. .... 150*

*Figure 8.8: Comparison of the case considering (continuous line) and not considering (dashed line) the longitudinal variation of trackbed stiffness in terms of settlement growth rate along the crossing panel. The crossing nose is marked with the vertical line. .... 151*

*Figure 10.1: WLRM Damage Index algorithm, showing separate RCF and Wear functions as well as the..... 170*

*Figure 10.2: Shakedown map showing the  $FI_{surf}$  index [149]. .... 172*

*Figure A.10.3 – The normal deformation of elastic bodies in contact. .... 176*

*Figure A.10.4 – Angles between the principal directions of contacting bodies. .... 177*

## **List Of Tables**

<i>Table 1.1: Overview of the main topics in the selected papers. ....</i>	<i>8</i>
<i>Table 2.1: Type of turnout layouts [11]. ....</i>	<i>11</i>
<i>Table 2.2: Typical turnouts on European railways [1].....</i>	<i>12</i>
<i>Table 2.3: Critical dimension for common fixed crossing [13]. ....</i>	<i>15</i>
<i>Table 3.1: Static and dynamic stiffness of rail-pads and baseplate pads (pad reference dimensions: 140 x 140 mm). ....</i>	<i>23</i>
<i>Table 3.2: Settlement equations obtained with laboratory tests (<math>S_N</math> is the vertical settlement at the cycle number <math>N</math>). ....</i>	<i>39</i>
<i>Table 3.3: Settlement equations obtained with in situ tests (<math>S_N</math> is the vertical settlement at the cycle number <math>N</math>). ....</i>	<i>44</i>
<i>Table 3.4: Overview of the experiments considered ([9]). ....</i>	<i>45</i>
<i>Table 3.5: Parameters used in Sato's equation [114]. ....</i>	<i>48</i>
<i>Table 3.6: Summary of the different settlement equation considered for use in VTI. ....</i>	<i>50</i>
<i>Table 4.1: The 22 most common degradation mechanisms registered at S&amp;Cs in the GB network from 2011 to 2017. ....</i>	<i>52</i>
<i>Table 4.2: Division between switch and crossing panel based on rail profile type. ....</i>	<i>53</i>
<i>Table 4.3: Percentage S&amp;C failure occurrence at each panel using only the database or using database and word analysis. ....</i>	<i>54</i>
<i>Table 5.1: Main input parameters for the vehicle-track interaction model ....</i>	<i>69</i>
<i>Table 5.2: Main differences between the present model and Chalmers model. ....</i>	<i>70</i>
<i>Table 5.3: Main parameters of the track and vehicle system. ....</i>	<i>81</i>
<i>Table 5.4: Main parameters of the co-running track model. ....</i>	<i>91</i>
<i>Table 5.5: Main differences between the contact algorithms considered. ....</i>	<i>91</i>
<i>Table 6.1: Bearer input values. ....</i>	<i>103</i>
<i>Table 6.2: Cases analysed in terms of loading configuration and trackbed stiffness type. ....</i>	<i>105</i>
<i>Table 6.3: Main input values for the plain line model. ....</i>	<i>107</i>
<i>Table 6.4: Summary of displacements and percentage differences at key locations for the irregularity types and trackbed distributions considered. All displacement values are in mm. ....</i>	<i>108</i>

*Design methodology for track systems considering the long-term ballast behaviour:  
application to crossings*

<i>Table 6.5: Natural frequency for the first bending mode considering different lengths and material Young's moduli.....</i>	<i>110</i>
<i>Table 6.6: Summary of displacements from the bearer models considered and differences w.r.t. fully flexible model. All displacement values are in mm. ....</i>	<i>112</i>
<i>Table 6.7: Initial estimation for the variation of total trackbed stiffness (all stiffness per bearer end).....</i>	<i>114</i>
<i>Table 6.8: Variation of total trackbed stiffness after the tuning (all stiffness per bearer end). .....</i>	<i>115</i>
<i>Table 6.9: Main parameters of the track and vehicle system. ....</i>	<i>116</i>
<i>Table 7.1: Main inputs for the track model. ....</i>	<i>125</i>
<i>Table 7.2: Parametric study on the track model. ....</i>	<i>125</i>
<i>Table 7.3: Summary of the findings from the parametric study. ↑: increase with the parameter consider; ↓: decrease with the parameter consider; -: no influence. The intensity is marked with the number of arrows from 1 (low influence) to 3 (high influence). ....</i>	<i>131</i>
<i>Table 7.4: Parametric study on the track model with travelling load.....</i>	<i>132</i>
<i>Table 7.5: Summary of the main dominating frequencies for the sleeper and ballast quantities.....</i>	<i>138</i>
<i>Table 8.1: Summary of contact forces and bearer displacements for the cases analysed.</i>	<i>151</i>
<i>Table 10.1: Yield stress in pure shear for manganese crossing during the service life. ...</i>	<i>172</i>

## **Glossary of Terms**

<b>Term</b>	<b>Meaning / Definition</b>
BOEF	Beam On Elastic Foundation
CCB	Cast Centre Block
DOF	Degree Of Freedom
EVA	Ethylene Vinyl Acetate
FDM	Finite Difference Method
FE	Finite Element
FFT	Fast Fourier Transform
IM	Infrastructure Manager
I.P.	Intersection Point
LCC	Life Cycle Cost
MBS	Multi-Body Systems
MGT	Million Gross Tonnes
NR	Network Rail
ORE	Office of Research and Experiments of the UIC
PDE	Partial Differential Equation
RBC	Rubber Bounded Cork
RCF	Rolling Contact Fatigue
RDMS	Rail Defect Management System
RMS	Root Mean Square
S&Cs	Switches and Crossings
$T_\gamma$	T-gamma
T.I.P.	Theoretical Intersection Point
TRC	Track Recording Coach
UIC	International Union of Railways
UoH	University of Huddersfield
UoS	University of Southampton
USPs	Under Sleeper Pads
w.r.t.	With Respect To

## Definition of Symbols Used

Latin term	Meaning / Units
$A_{1s}, A_{2s}, A_{3s}$	Coefficients for the proposed settlement equation
$A_c$	Contact area [m <sup>2</sup> ]
a,b,c,d,e	Sato equation constants
a,b	Semi-axes of the Hertzian contact patch [m]
$a_{l,max}$	Maximum lateral acceleration [m/s <sup>2</sup> ]
$a_{w,1}, a_{w,2}$	Distance of the left, right contact patch from the wheelset centre [m]
$C$	System damping matrix [Ns/m]
$C_{11}, C_{22}, C_{23}, C_{33}$	Kalker creepage coefficients
$C_{s1,x}, C_{s1,y}, C_{s1,z}$	Damping constant of the primary suspension along the longitudinal, lateral, vertical direction [Ns/m]
$[C]_{rail}$	Total rail damping matrix
$[C_{rail,l}], [C_{rail,r}]$	Left and right rail damping matrix
$[C_{rp,l}], [C_{rp,r}]$	Left and right rail damping matrix due to rail-pad layer
$[C]_{bearer}$	Bearer damping matrix
$[C]_{s-r}$	Bearer-rail damping matrix
$[C]_T$	Track damping matrix
$C_v$	Vehicle damping matrix [Ns/m]
$c_{b,v}, c_{b,l}$	Vertical and lateral ballast damping [Ns/m]
$c_r$	Rail-pad damping [Ns/m]
$c_{r,v}, c_{r,l}$	Vertical and lateral rail-pad damping [Ns/m]
$d$	Lateral span of the primary suspension system [m]
$d_r$	Transversal distance between rail-pads [m]
$E_{b,max}$	Maximum ballast energy [Nm]
$EI$	Beam bending stiffness [Nm <sup>2</sup> ]
$e_N$	Settlement after N cycles [mm]
$e_T$	Settlement after T tonnage [mm]
$e_1$	Settlement after the first cycle [mm]
$\hat{F}(\omega)$	Amplitude of the complex-valued input force [N]
$F_{b,max}$	Maximum ballast force [N]
$F_{b,stat}$	Static ballast force [N]
$F_{s/b}$	Bearer-ballast contact force [N]
$F_{ext}$	External force vector [N]
$F_{i,x}, F_{i,y}, F_{i,z}$	Component of the creep force along the x,y,z direction for the i <sup>th</sup> wheel (i=1,2) [N]
$F_R$	Linear resultant creep force [N]
$F_\xi$	Longitudinal creep force [N]
$F_\eta$	Lateral creep force [N]
$f_{11}, f_{22}, f_{23}, f_{33}$	Kalker linear creepages coefficient

*Design methodology for track systems considering the long-term ballast behaviour:  
application to crossings*

<b>Latin term</b>	<b>Meaning / Units</b>
H	Receptance [m/N]
$I_s$	Bearer roll inertia [kgm]
irr <sub>1</sub> , irr <sub>2</sub>	Vertical irregularity at the left, right wheel [m]
$J_{s,x}$	Bearer inertia around x axis [kgm]
$J_{w,x}, J_{w,z}$	Wheelset inertia around x and z axis [kgm]
K	System stiffness matrix [N/m]
$K_H$	Hertzian contact constant [(m/N) <sup>-3/2</sup> ]
$K_{r,x}, K_{r,y}, K_{r,z}$	Rail-pad stiffness along the lateral, vertical direction [N/m]
$K_{s1,x}, K_{s1,y}, K_{s1,z}$	Primary suspension stiffness along the longitudinal, lateral, vertical direction [N/m]
$[K]_{\text{rail}}$	Total rail stiffness matrix
$[K_{\text{rail,l}}], [K_{\text{rail,r}}]$	Left and right rail stiffness matrix
$[K_{\text{rp,l}}], [K_{\text{rp,r}}]$	Left and right rail stiffness matrix due to rail-pad layer
$[K]_{\text{bearer}}$	Bearer stiffness matrix
$[K]_{\text{s-r}}$	Bearer-rail stiffness matrix
$[K]_T$	Track stiffness matrix
$K_v$	Vehicle stiffness matrix [N/m]
k	Foundation stiffness [N/m <sup>2</sup> ]
$k_{b,v}, k_{b,l}$	Vertical and lateral ballast stiffness [N/m]
$k_r$	Rail-pad stiffness [N/m]
$k_{r,v}, k_{r,l}$	Vertical and lateral rail-pad stiffness [N/m]
L	Rail influence factor in Sato's model
$L_e$	Element length [m]
l	Typical body length [m]
$l_g$	Gauge [m]
M	System mass matrix [kg]
$M_s$	Structure factor in Sato's model
$M_w$	Wheelset mass [kg]
$M_\phi$	Spin creep moment [Nm]
$[M]_{\text{rail}}, [M_{\text{rail,l}}], [M_{\text{rail,r}}]$	Total rail, left rail and right rail mass matrix
$[M]_{\text{bearer}}$	Bearer mass matrix
$[M]_T$	Track mass matrix
m	Intermediate mass taking in account bearers, ballast and sub-ballast layers [ton]
m, n	Coefficients for the calculation of the contact ellipse semi-axes
$M_{i,x}, M_{i,y}, M_{i,z}$	Component of the creep moment along the x,y,z direction for the i <sup>th</sup> wheel (i=1,2) [Nm]
$m_{r1}, m_{r2}$	Equivalent mass of the left, right rail [kg]
$m_s$	Equivalent mass of the bearer [kg]
$M_w$	Wheelset mass [kg]
N	Number of passes [cycles] or [tons]
$N_1, N_2, N_3, N_4$	Terms of the shape function

*Design methodology for track systems considering the long-term ballast behaviour:  
application to crossings*

<b>Latin term</b>	<b>Meaning / Units</b>
$N_{i,x}, N_{i,y}, N_{i,z}$	Component of the normal force along the x,y,z direction for the $i^{\text{th}}$ wheel ( $i=1,2$ ) [N]
$n$	Crossing nose rate of inclination
$n_r$	Number of rail nodes
$P$	Sub-grade influence factor in Sato's model
$P_b$	Maximum bearer-ballast pressure due to a wheel load [Pa]
$P_{\text{th}}$	Bearer-ballast pressure threshold [Pa]
$P_z$	Normal force [N]
$q(x)$	Distributed load on the rail depending on the position $x$ [N/m]
$R$	Curve radius [m]
$R_w$	Wheel radius [m]
$R_{r,1}, R_{r,2}$	Rail radius along the longitudinal and transversal direction [m]
$R_{w,1}, R_{w,2}$	Wheel radius along the longitudinal and transversal direction [m]
$R_{1,x}, R_{1,y}, R_{2,x}, R_{2,y}$	Principal radii of curvature of two bodies in contact [m]
$r_0$	Nominal rolling radius [m]
$r_1, r_2$	Rolling radius of the left, right wheel [m]
$S$	Average growth of irregularities [mm/100 days]
$S_N$	Settlement at N-th cycle [mm]
$s$	Sliding distance [m]
$T$	Passed tonnage in Sato's settlement model [MGT/year]
$T_1, T_2, T_3$	Longitudinal, lateral and spin component of creep force [N]
$v$	Running speed [m/s]
$V$	Running speed [km/h]
$V_{\text{max}}$	Maximum allowable speed in the diverging route [m/s]
$v_1, v_2, \Omega_3$	Longitudinal, lateral and spin component of actual wheel velocity [m/s], [m/s], [rad/s]
$v'_1, v'_2, \Omega'_3$	Longitudinal, lateral and spin component of pure rolling velocity [m/s], [m/s], [rad/s]
$x, \dot{x}, \ddot{x}$	System displacement, velocity, acceleration vector [m]
$x_c, y_c$	Contact point location [m]
$x_1, y_1, x_2, y_2$	Principal directions of two bodies in contact
$x/L_e$	Relative longitudinal position of the generic point $x$
$[y_i]^e$	Element vector of the nodal displacements
$\{y\}^s$	Bearer vector



*Design methodology for track systems considering the long-term ballast behaviour:  
application to crossings*

<b>Latin term</b>	<b>Meaning / Units</b>
$y_j, z_j, y_{j+1}, z_{j+1}$	Lateral and vertical displacement of the node (j) and (j+1) [m]
$\dot{y}_j^l, y_j^l, \dot{y}_j^r, y_j^r$	Nodal lateral velocity and displacement for the left and right rail [m/s], [m], [m/s], [m]
$y_{ri}(x)$	Rail displacement at the generic position x [m]
$\ddot{y}_s, \dot{y}_s, y_s$	Bearer lateral acceleration, velocity and displacement [m/s <sup>2</sup> ], [m/s], [m]
$y_{1,min}, y_{2,min}$	Lateral position of the left, right point at which the vertical wheel-rail difference is minimum [m]
$w(x)$	Rail deflection at position x [m]
$\hat{z}(\omega)$	Amplitude of the complex-valued displacement [m]
$\dot{z}_j^l, z_j^l, \dot{z}_j^r, z_j^r$	Nodal vertical velocity and displacement for the left and right rail [m/s], [m], [m/s], [m]
$\ddot{z}_s, \dot{z}_s, z_s$	Bearer vertical acceleration, velocity and displacement [m/s <sup>2</sup> ], [m/s], [m]

<b>Greek term</b>	<b>Meaning / Definition</b>
$\alpha, \beta, \gamma$	Coefficient in Sato's settlement model
$\alpha_c$	Correction factor of the creep forces
$\alpha_{rd}, \beta_{rd}$	Coefficient of the Rayleigh damping theory
$\gamma_1, \gamma_2$	Creepage (longitudinal and lateral component)
$\Delta N$	Number of axial passes in the initial phase of settlement
$\Delta R_{w,1}, \Delta R_{w,2}$	Left, right incremental wheel rolling radius [m]
$\Delta Z_1, \Delta Z_2$	Left, right distance between wheel and rail [m]
$\Delta Z_{1,min}, \Delta Z_{2,min}$	Left, right minimum distance between wheel and rail [m]
$\Delta z_1, \Delta z_2$	Left, right incremental wheel vertical position [m]
$\Delta z_{wr,1}, \Delta z_{wr,2}$	Left, right incremental wheel-rail vertical relative position [m]
$\delta_1, \delta_2$	Left, right contact angle [rad]
$\delta_{wr}$	Normal penetration between wheel and rail [m]
$\zeta_i, \zeta_j$	Damping ratio for the <i>i</i> -th and <i>j</i> -th mode
$\kappa_{r,1}, \kappa_{r,2}$	Rail curvature along the longitudinal and transversal direction [1/m]
$\kappa_{w,1}, \kappa_{w,2}$	Wheel curvature along the longitudinal and transversal direction [1/m]
$\mu$	Utilized friction coefficient
$\mu_a$	Available friction coefficient

*Design methodology for track systems considering the long-term ballast behaviour:  
application to crossings*

$v$	Normalized vertical load
$\nu_c$	Poisson's ratio of the contacting bodies
$\sigma_{h,res}$	Residual hydrostatic stress [N/m <sup>2</sup> ]
$\tau$	Settlement rate [mm]
$\tau_{xc}, \tau_{yc}$	Longitudinal, lateral tangential stress at the contact point [N/m <sup>2</sup> ]
$d\varphi_w$	Incremental wheelset roll angle
$\ddot{\varphi}_s, \dot{\varphi}_s, \varphi_s$	Bearer roll acceleration, velocity and rotation [rad/s <sup>2</sup> ], [rad/s], [rad]
$\varphi_w$	Wheelset roll angle [rad]
$\varphi_{w,0}$	Initial estimation of the wheelset roll angle [rad]
$\varphi_j, \theta_j, \varphi_{j+1}, \theta_{j+1}$	Rotation around the y and z axis of the node (j) and (j+1) [rad]
$\psi$	Angle between the principal directions of the bodies considered [rad]
$\psi_w, \dot{\psi}_w$	Wheelset yaw angle, velocity [rad], [rad/s]
$\omega_3$	Creepage (spin component) [1/m]
$\omega$	Frequency of excitation [Hz]



# 1 Introduction

Switches and Crossings (S&Cs), also called turnouts, refer to the components of the railway that provide flexibility to the system in terms of possible routes of a rail vehicle. They are the only locations at which routes cross, converge or diverge and thus trains can change path. Therefore, the productivity of the entire network is deeply influenced by the number and the types of its turnouts [1].

They are divided in three main parts:

- the switch panel: this includes the movable components which allow the train to change path;
- the closure panel: this connects the switch and the crossing panels;
- the crossing panel: the part which allows the wheel passage in either the through or the diverging route.

Undoubtedly, they are essential for the system flexibility. Nevertheless, they are the asset which experiences the highest number of failures [2, 3] due to a number of reasons, including discontinuities in the rail geometry and track properties, which leads to high dynamic forces. Impact mechanisms along the panels cause faster degradation than the plain line. Hence, turnouts incur very high maintenance and renewal costs, in addition to significant investment costs. For example, one metre of S&C can cost up to four times more than one metre of plain line [1]. Derailment risk is also higher according to [4], in the UK about 30% of the track related derailments between 2008/9 and 2012/3 are related to turnouts.

From a modelling perspective, S&Cs are also a considerably complex part of the railway system due to physical non-linearities, including rapidly changing rail geometry and trackbed characteristics, sharp radius with little or no transitions in the diverging route and rail profiles subject to heavy wear. This research proposes a design methodology that is able to assess different assets supporting the Infrastructure Manager (IM) decision based on the long-term trackbed evolution, which is considered one of the most significant causes of whole track degradation (see Chapter 4). Special attention is given to the crossing panel, but the methodology can be applied to the switch panel as well as plain line and its features.

## **1.1 Aim of the research**

Specific technical requirements, including safety, stability, reliability, accuracy, ride quality, maintainability, should be met when S&Cs are designed in order to ensure their sustained performance during their service life. Historically, due to the lack of a reference standard, the design of turnouts has often been based on the knowledge of a limited group of experts as well as elementary rules reflecting empirical practices on track. Often, those turnouts show degraded riding quality and safety within a short period of time, leading to speed restrictions or, in the most severe cases, early replacements and therefore a substantial increase in life cycle costs (LCCs).

The main aim of the research is to develop a design methodology to support the design of innovative railway crossings which takes into consideration the effect of ballast long-term behaviour. This will be based on developing a three-dimensional vehicle-track interaction model that is then coupled with selected settlement equations, both available in literature and proposed by the Author, in order to predict the settlement rate at the studied site. The methodology can be used also for other track forms, such as plain line and switch panel.

## **1.2 Objectives**

The main objectives of this research are defined as follows:

- Examine the crossing design parameters and the main crossing degradation modes from Infrastructure Manager (IM) failure database, linking back to those resulting from the trackbed degradation;
- Review the existing dynamic models of the vehicle-track coupling system and the existing degradation prediction models, focussing on the trackbed layer long-term behaviour;
- Develop a vehicle-track interaction model which can consider the varying crossing properties, including section area and inertia and varying trackbed conditions, and able to predict the dynamic behaviour of the whole system;
- Include the long-term ballast behaviour in the prediction model. Equations available in literature will be compared and a new one will be proposed in order to bridge the current approaches' flaws;
- Validate and calibrate the model constituents against available measured data;
- Show how the methodology can successfully be employed to optimise the crossing design with particular attention to the trackbed stiffness variation along the panel, demonstrating the validity and usefulness of the tool developed.

### 1.3 Novelty of the research

The novelty of this research consists of developing a tool which brings together cross-disciplinary modelling techniques and applying them in order to establish a new and fast design methodology based on accumulated long-term ballast behaviour. The methodology is divided in two main parts, i.e. the vehicle-track interaction model and the long-term ballast prediction.

Regarding the vehicle-track interaction model, (1) the contact model is simplified but yet accurate enough to capture the impact loads at the crossing panel, (2) the track model takes in account a detailed description of the variability of the superstructure characteristics of each component (i.e. rail profile, sleeper length) as well as (3) the longitudinal variability in trackbed conditions, which is usually not considered while modelling the crossing panel [2, 3]. Focussing on the latter point, it is demonstrated that not including this modelling aspect can lead to significant under-/over-predictions not only in the dynamic context but also in the long-term behaviour.

Regarding the long-term ballast behaviour, a detailed analysis of the models available in literature has been carried out in terms of dynamic behaviour of sleeper and ballast highlighting the main limitations of each in the vehicle-track interaction context. On this basis, a new settlement approach is proposed with the purpose of correctly capturing the main space-variant vehicle and track parameters, including travelling speed, axle load and trackbed stiffness. It is then calibrated against track measurements achieving a good match and compared with the other models.

### 1.4 Methodology

The main steps adopted in the research are listed as follows (Figure 1.1):

- The three-dimensional vehicle-track interaction model includes:
  - *Track model*: a comprehensive two-layer Finite Element (FE) model of a ballasted track section is developed using the Matlab software, including the variability in rail section properties, sleeper characteristics and rail-pad and trackbed resilient properties;
  - *Vehicle model*: one wheelset is considered with longitudinal, lateral and

*Design methodology for track systems considering the long-term ballast behaviour:  
application to crossings*

vertical primary suspensions linking to the sprung mass. For the validation purposes, two independent wheelsets are modelled;

- *Contact model:* actual crossing and wheel profiles are included. The normal problem is solved using non-linear Hertzian theory with a single point of contact and the tangential problem using linear Kalker theory modified according to Shen & Hendrick correction. Both contact theories (i.e. Hertzian and Kalker theory) have been chosen as they are a good trade-off between ease of implementation, computational costs and reliability of the results.
- The model is validated against experimental data from a UK site equipped with Under Sleeper Pads (USPs) in terms of bearer displacement. The comparison between modelling rigid and flexible sleepers is presented.
- The long-term ballast behaviour in the plain line is assessed using a vertical two-dimensional track model under a point load with various settlement models available in literature for different load characteristics, including amplitude and frequency, and trackbed stiffness values.
- A new settlement equation based on the energy transmitted to the ballast layer is proposed. The main purpose is to overcome the discussed limitations of the current modelling approaches available in literature in the context of vehicle-track interaction.
- The results from the simplified model are then applied at the crossing panel. The iterative process is validated against the calculated rate of longitudinal level defect growth using two consecutive Track Recording Coach (TRC) data signals.
- The longitudinal variation of trackbed stiffness is assessed as it plays a fundamental role in the wheel-rail and vehicle-track dynamics as well as in the long-term performances.

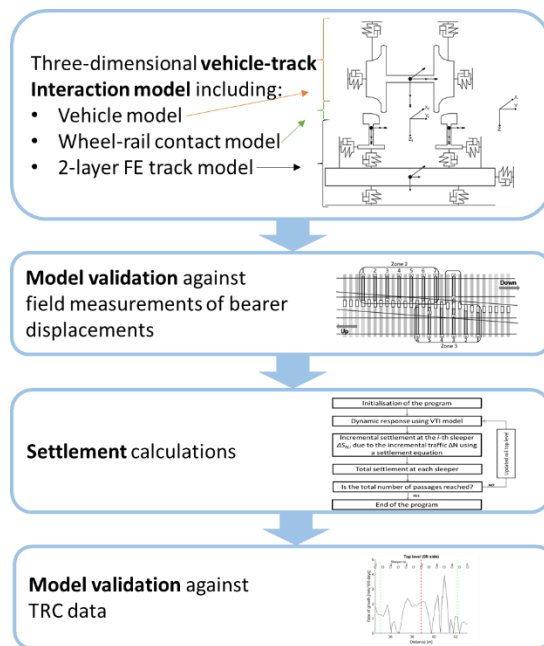


Figure 1.1: Methodology overview.

## 1.5 Overview of the thesis

This thesis is organised as follows:

Chapter 2 gives background about the main characteristics of the switch panel and crossing panel, focussing on their classification and design parameters, as well as the feature of ballast long-term behaviour, or settlement.

A detailed literature review is presented in Chapter 3 about generic vehicle-track interaction modelling and more specific models applied at the switch and crossing panel. A wide range of settlement equations are classified on the basis of the way they have been derived and assessed from a vehicle-track interaction point of view.

A summary of the statistical analysis of a seven-year failure database using advanced techniques of text reading is presented in Chapter 4 with particular focus on the crossing panel and some proposed research directions.

The three-dimensional vehicle-track interaction model that is able to predict the dynamic system behaviour is developed in Chapter 5. An early validation against the Multi Body System (MBS) commercial software VI-Rail is also presented.

The validation of the model against field data in terms of dynamic bearer displacements is discussed in detail in Chapter 6, including a discussion on the long bearer



modelling and the methodology proposed to tune the trackbed stiffness.

Chapter 7 poses the bases for the modelling of the ballast long-term evolution looking at the influence of the loading and trackbed characteristics on the main physical quantities at the sleeper and ballast level. A simplified track FE model for plain line under a quasi-static excitation and a moving sinusoidal excitation is used to capture mainly the loading frequencies typically used during laboratory tests and higher loading frequencies that are typical of VTI, respectively. The new settlement approach is then proposed to overcome the main issues raised.

In Chapter 8 the outcomes of the long-term ballast degradation modelling discussed previously are integrated in the dynamic model at the crossing panel for the study site. The influence of the longitudinal variation of trackbed stiffness is then presented in relation to both the dynamic and the long-term ballast behaviour.

Finally, the main conclusions and further work are summarised in Chapter 9.

## **1.6 Publications related to the research**

Five journal papers have been published during the course of the research:

- **Paper A (“Observed failures at railway turnouts: failure analysis, possible causes and links to current and future research”** – published in Engineering Failure Analysis) [5]:

A large UK database of rail defects occurring at S&Cs was analysed using both numerical and text-based techniques in order to determine the most common failure mechanisms appearing at each panel. Selected defects were analysed in more detail, linking them to the main track characteristics, including line type and type of rail, and to other defects. Recommendations to guide future research as well as to enhance the data collection methodology were made.

Contribution of the Author: contribution to methodology, failure analysis using the database (not the free-text analysis), writing up and editing.

- **Paper B (“Optimisation of support stiffness at railway crossings”** – published in Vehicle Systems Dynamics) [6]:

A three-dimensional vehicle-track interaction model was developed to analyse the dynamic

interaction at the crossing panel. The failure mechanisms occurring in this part of the track are captured through indicators directly derived from the dynamic model. An optimisation routine is proposed in order to minimise the most common modes tuning the resilient layer between rail and sleeper. The cases of direct and indirect fixings and the influence of travelling direction and speed are discussed and compared in detail.

Contribution of the Author: main developer of the three-dimensional vehicle-track interaction model, optimisation methodology, study on direct and direct fixing, writing up and editing.

- **Paper C (“The role of support stiffness in switches and crossings: comparison of vehicle-track interaction models against field measurements”** – published in Part F: Journal of Rail and Rapid Transit) [7]:

A UK site with a double cross-over equipped with Under Sleeper Pads (USPs) has been selected to carry out field measurements of bearer vertical displacements using geophones. The numerical model presented in Paper B and the model developed using the commercial Multi-Body System (MBS) software VI-Rail have been used to develop some insights on the dynamic behaviour of the system at both switch and crossing panel. Special attention has been given to the importance of correctly model the longitudinal and transversal variability of trackbed stiffness and to the beneficial role of USPs helping in the prevention of differential settlement.

Contribution of the Author: main developer of three-dimensional vehicle-track interaction model for switch panel and crossing panel, comparison with field data, methodology to tune the trackbed stiffness variation, writing up and editing.

- **Paper D (“The role of track stiffness and its spatial variability on long-term track quality deterioration”** – published in Part F: Journal of Rail and Rapid Transit) [8]:

The longitudinal variability of trackbed stiffness occurring at two UK sites has been studied from a statistical point of view. An advance methodology based on the ARIMA theory has been proposed in order to capture and correctly reproduce the systematic and the random naturally occurring variability. A vertical vehicle-track interaction model in conjunction with the Guérin’s settlement model is then used to simulate a large number of scenarios in terms

*Design methodology for track systems considering the long-term ballast behaviour:  
application to crossings*

of vertical top level irregularities and trackbed stiffness distributions. The results in terms of settlement rates are linked back to the site characteristics, showing the importance of considering the mean and the standard deviation values.

Contribution of the Author: developer of vertical vehicle-track interaction model and coupling with settlement modelling, writing up and editing.

- **Paper E (“Modelling railway ballasted track settlement in vehicle-track interaction analysis”** – published in Transportation Geotechnics) [9]

An exhaustive review of the main settlement equations available in literature is carried out from the vehicle-track interaction point of view. A new semi-empirical settlement equation is proposed and coupled with a vertical vehicle-track interaction model. The results in terms of track longitudinal level evolution and settlement predictions are compared with the available equations that are usually used in this context (i.e. Sato’s, Guérin’s, Fröhling’s equation) using two sets of measured trackbed stiffness distributions.

Contribution of the Author: developer of vertical vehicle-track interaction model and coupling with settlement modelling, writing up and editing.

An overview of the main topics addressed in the selected papers is presented in Table 1.1.

*Table 1.1: Overview of the main topics in the selected papers.*

	<b>Paper A</b>	<b>Paper B</b>	<b>Paper C</b>	<b>Paper D</b>	<b>Paper E</b>
S&Cs	X	X	X		
Failure analysis	X	X			
Dynamic modelling		X	X	X	X
Ballast settlement				X	X
Field data	X		X	X	X

## 2 Background

Switches and Crossings (S&Cs), also called turnouts, are the part of the railway that actually provides flexibility to the system. They are the only locations at which routes can cross, converge or diverge and thus trains can change trajectory. Therefore, the productivity of the entire network is deeply influenced by the number and the types of its turnouts [1].

On the other hand, they are the asset which experiences the highest number of failures [2, 3] due to a discontinuity in the track geometry which leads to high dynamic impact forces. From a dynamic point of view, the load is quickly transferred from the wing rail to the crossing nose and the wheel is accelerated upwards after the downward motion by the geometry. This impact load mechanism causes faster degradation than for plain line. Hence, turnouts require very high investment, maintenance and renewal costs: as a rough idea, one metre can cost up to four times more than one metre of plain line [1].

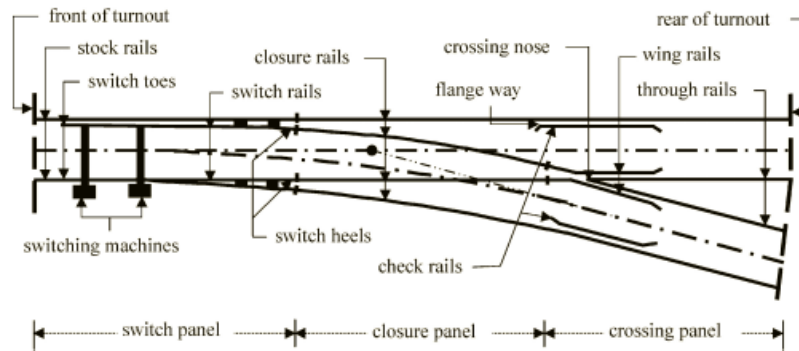
Also from a modelling perspective, S&Cs are a considerably complex part of the railway system due to the non-homogeneities, including rapidly changing geometry, sharp radius in the diverging route and heavily worn profiles.

In this Chapter, a brief background of the problem will be presented. In particular, Section 2.1 will describe S&C geometry and Section 2.2 the main characteristics of ballast settlement.

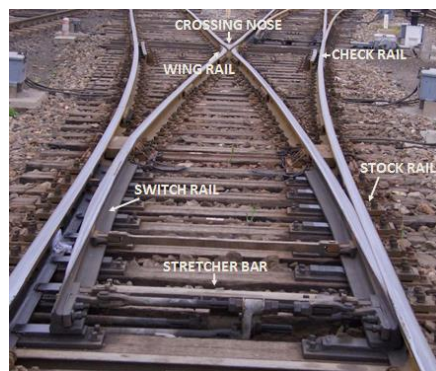
### 2.1 Switches & Crossings

A sketch of a right hand turnout and an example of a symmetrical S&C is shown in Figure 2.1.

*Design methodology for track systems considering the long-term ballast behaviour:  
application to crossings*



(a)



(b)

Figure 2.1: (a) Components of a single right hand turnout [3] and (b) example of symmetrical turnout [10].


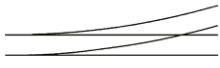
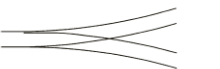


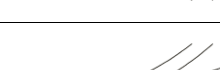
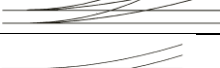
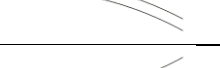
In the case shown in Figure 2.1(a), there are four possible way to negotiate the turnout depending on:

- Direction:
  - *Through route*: when the vehicle is running on the main line;
  - *Diverging route*: when the vehicle is running on the diverging line.
- Versus:
  - *Trailing*: when the vehicle is running from the crossing nose to the switch toe;
  - *Facing*: when the vehicle is running from the switch toe toward the crossing nose.

### 2.1.1 Classification of S&Cs

There are several types of S&C layouts as reported in Table 2.1.

Table 2.1: Type of turnout layouts [11].

Type of turnout		Example
<i>Diverging turnout</i>	<i>Right hand turnout (RH)</i>	
	<i>Left hand turnout (LH)</i>	
<i>Symmetrical turnout (S)</i>		
<i>Tandem turnout</i>	<i>Symmetrical or Three throw (S3)</i>	
	<i>Asymmetrical same side to right (RR)</i>	
	<i>Asymmetrical same side to left (LL)</i>	
	<i>Asymmetrical to the right and to the left (RL)</i>	
	<i>Asymmetrical to the left and to the right (LR)</i>	

The abbreviations in brackets in Table 2.1 are used to classify an S&C, in addition to the rail type (e.g. 56E1, 60E1), the radius of the diverging route and the crossing angle. An example is “60E1-760-1:15” [12], where “60E1” denotes the rail type and weight, “760” the diverging route radius and “1:15” the crossing angle.

Some examples of typical turnout layouts on European lines are reported in Table 2.2. In particular, the maximum speed  $V_{max}$  is usually calculated depending on the allowable lateral acceleration in the diverging route as following:

$$V_{max} = 3.6 \cdot \sqrt{R \cdot a_{l,max}} \quad 2.1$$

Where:

R = radius of the diverging route [m];

$a_{l,max}$  = maximum lateral acceleration [m/s<sup>2</sup>].

Table 2.2: Typical turnouts on European railways [1].

Angle n [1:n]	Radius [m]	Maximum speed [km/h]
7	190	40
7.5	190	40
9	190	40
9	300	50
12	500	60
14	300	50
14	500	60
14	760	80
18.5	760	80
18.5	1200	100
26.5	2500	130
33.5	4000	160
42	6000/7000	200

## 2.1.2 The crossing panel

Figure 2.2 shows an example of crossing panel.

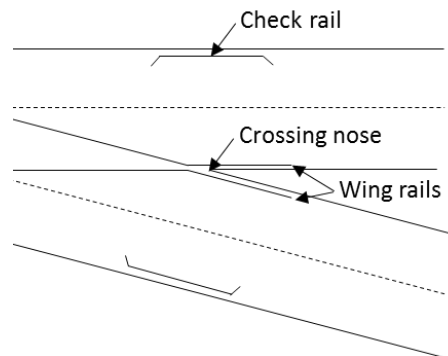


Figure 2.2: An example of crossing panel.

The crossing panel includes the following main parts:

- Check rails: the two side rails whose main function is to ensure that at least one wheel in the wheelset does not lose the contact at the moment of wing rail-crossing nose transfer area;
- Crossing nose: physical point where the two (or more) trajectories converge. In the horizontal plane, it is characterised by the angle between the rails gauge faces. This is the most important parameter that usually describes the crossing geometrical configuration. There are two accepted crossing angle measurement methods, which are:
  - *Tangent measure*: the crossing rate of inclination  $n$  is defined as the tangent of the angle [13]:

$$n = \operatorname{arctg}\left(\frac{1}{\text{angle}}\right) \quad 2.2$$

- *Central Line Method (C.L.M.)*: the crossing rate of inclination  $n$  is defined as half the cotangent of half the angle [13]:

$$n = \frac{1}{2} \operatorname{arctg}\left(\frac{\text{angle}}{2}\right) \quad 2.3$$

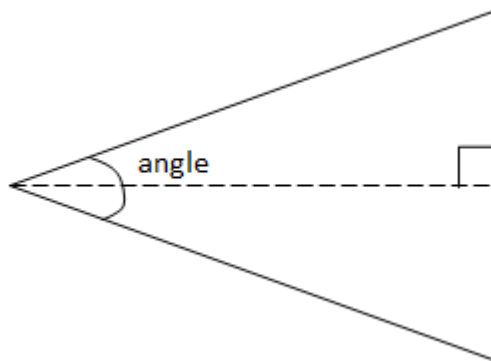


Figure 2.3: Central Line Method [13].

The British Railways use the latter method [14]. Note that there are two main intersection point definitions:

- *Intersection point (I.P.)*: the intersection point of the gauge faces of the rails;
- *Theoretical Intersection point (T.I.P.)*: the ends of the projected rail continuation. It is slightly away from the I.P.

Crossings can be classified as follows:

- *Acute crossing* (Figure 2.4(a)): when the arrangement of the layout ensures the possibility of changing route;
- *Obtuse crossing (or diamond crossing)* (Figure 2.4(b)): when the arrangement of the layout ensures the continuity of two routes;
- *Square crossing* (Figure 2.4(c)): when two tracks of different gauges cross each other at square angles.



*Design methodology for track systems considering the long-term ballast behaviour:  
application to crossings*



(a)

(b)

(c)

*Figure 2.4: (a) Acute crossing [15]; (b) Diamond crossing [16]; (c) Square crossing [17].*

Another type of classification is the one based on the crossing assembly, i.e. crossing with or without movable parts. Usually, the crossing with movable parts is used in the high speed lines.

Depending on the way of construction, the crossings can be defined as [18]:

- *Cast centre block*: the nose and the throat are made as one block, the leg ends are welded and the wing rails are attached with tension controlled bolts (or similar);
- *Monobloc*: all the components up to the joints to plain line are moulded as one piece;
- *Semi-fabricated*: the cast-nose piece is welded to manganese steel rail legs and the wing rails are attached with tension controlled bolts (or similar).

Depending on the way they are attached to the adjacent track, the crossings are classified as [18]:

- *Welded*: the leg ends terminates with pearlitic rails so that they can be welded to track with standard techniques;
- *Bolted*: the leg ends are attached to track through fish-plated connections.

### **2.1.3 Design parameters for the crossing panel**

Designing a crossing which can satisfy the performance requirements set by the costumer is a very challenging task. Also, the design is strictly dependant on the line characteristics, including the type of traffic and the line speed. Nevertheless, the IMs and the manufacturers are aiming to standardise the whole process as far as possible.

There are several critical dimensions listed in Table 2.3, which are subject to tolerances presented in [13].

Table 2.3: Critical dimension for common fixed crossing [13].

Crossing part	Critical dimensions
<i>Top surface</i>	Running table flatness Running table flatness over 1000 m
<i>Bottom surface</i>	Underside flatness
<i>Openings and lengths</i>	Straightness of wing rail Wing front opening Flangeway Throat opening Vee opening Length – nose to wing end opening Length – nose to heel Overall crossing length
<i>Cross section</i>	Width at baseplate Transverse shape of nose Underside flatness Position of running edge relative to foot
<i>Hole position</i>	Diameter of fishbolt holes Chamfering of holes Hole position to the end of crossing Position of running edge relative to foot
<i>Opening and topping</i>	Radius of wing rail head Throat opening Difference between actual and theoretical topping
<i>Running edge alignment</i>	Deviation along full length Deviation at intermediate offset

In addition to that, there are two more aspects that should be considered in the design process [18]:

- *wheel transfer trajectory*: the maximum equivalent dip angle allowed the wheel negotiates in the load transfer area is limited in order to limit the consequent P1 and P2 impact forces [19];
- *fatigue life*: the fatigue life of three areas (i.e. leg end, base of crossing in load transfer area, base of crossing in the remaining length) should be calculated using the provided S-N curve at the stress level calculated. The estimation of bending stresses should be carried out using a FE model of crossing under a given P2 force level (or under a calculated force level using an established MBS package) and with prescribed support stiffness.

## 2.2 Ballast settlement

The main degradation modes occurring at the crossing panel are described in detail in

*Design methodology for track systems considering the long-term ballast behaviour:  
application to crossings*

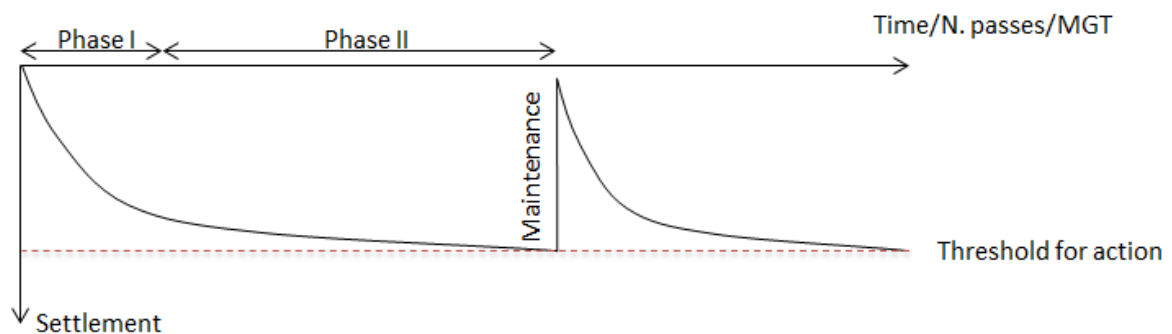
Grossoni [5] and Appendix A. The focus of this section is the ballast settlement.

Track settlement is the progressive phenomenon during which ballast and subgrade lose their initial geometrical configuration due to the accumulation of plastic deformations, leading to a progressive deterioration of the track geometry (absolute position) and quality (spatial shape and rate of variation). The rate of settlement depends on a large variety of factors, mainly:

- the type of traffic: axle load, speed, unevenness of loads;
- the superstructure characteristics: rail type, bearer type, bearer spacing, pad characteristics, eventual additional resilient layers (such as under-bearer pads);
- the conditions of ballast, sub-ballast and sub-grade layers: layer depth, layer density, layer size distribution curve, layer material (abrasion, coefficient of fracture, sharpness, ...), presence of contamination, drainage.

In particular, space-variant (hereafter, called “differential”) settlement is one of the principal problems in ballasted railways and occurs when the distribution of those deformations is not constant. The differential settlement therefore may be critical in the crossing panel, where the track and the vehicle experience high transient forces due to the load transfer from wing rail to crossing nose [20] leading to an amplification of vibrations and localised damages.

Usually the settlement evolution is represented as a function of time, number of passes or weight (Million Gross Tonnes (MGT)), as in Figure 2.5. When the defect reaches a threshold, tamping is carried out in order to bring the settlement curve back near to the initial values.



*Figure 2.5: General ballast settlement trend.*

Two distinctive phases describe the settlement evolution:

- First phase (ca. 0.5-2 MGT): after tamping, there is a relatively fast rearrangement of ballast stones when the intra-granular material gaps are reduced and the overall structure is consolidated. This phase is characterised by a rapid logarithmic development.
- Second phase (from ca. 2 MGT): this phase is slower than the first one and the trend is reasonably linear with time. Several mechanisms are involved caused by repeated train loading, including *volume reduction* due to particle rearrangement, particle breakage and abrasive wear at the contact points, inelastic recovery on unloading, due to micro-slip between ballast particles and sub-ballast and/or subgrade penetration into ballast voids [21]. All those phenomenon can be divided into two main mechanisms, which are friction sliding and volumetric compaction, as shown in Suiker [22].

Certainly, the geometry is not fully recovered (Figure 2.6) due to the ballast plastic characteristic of remembering the previous history (i.e. the so called “ballast memory”). Also, after several maintenance activities the benefits decrease and the period between two tamping cycles becomes shorter and shorter. Therefore, it is eventually necessary to renew the ballast bed [1].

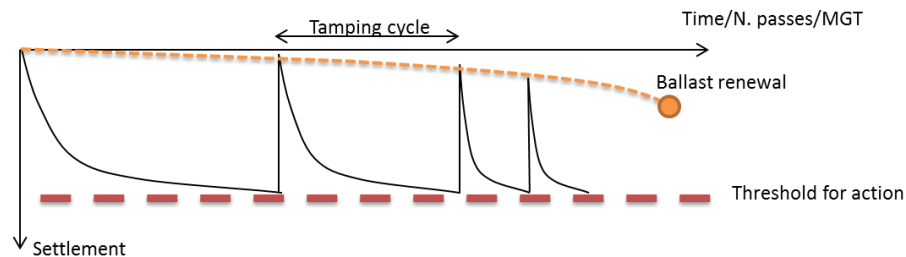


Figure 2.6: Evolution in time of the ballast settlement for several tamping cycles.

## **3 Literature review**

As explained in the previous Chapter, turnouts are the railway elements which experience the highest number of failures [2, 3] causing a significant proportion of delays: for instance, in the UK those failures account for circa 10% of the total delays. Hence, it is evident that future design process of S&C components should correctly address the long-term degradation mechanisms, designing them out in order to increase the Life Cycle Costs (LCCs) and ensure the flexibility of the whole network.

This Chapter is divided in four main parts. Firstly, the dynamic vehicle-track system models are presented in Section 3.1. Secondly, the modelling techniques for S&Cs are reviewed in Section 3.2. Thirdly, a detailed comparison of the settlement equations available in literature is shown in Section 3.3. Finally, a survey of the engineering techniques to predict ballast long-term behaviour using vehicle-track interaction models is discussed in Section 3.4.

### **3.1 Modelling the dynamic behaviour of the railway system**

In this Section, a survey of track system models (Section 3.1.1), track fixing systems (Section 3.1.2), wheel-rail contact models (Section 3.1.3) and vehicle models (Section 3.1.4) is provided.

#### **3.1.1 Track system models**

In the literature, a wide range of track system models are found which were developed for design and maintenance purposes. They are generally developed to look at plain line track and include the rails, bearers and in some cases the ballast, as well as the connections between layers, i.e. the fastening system, the bearer-ballast interface and the foundation.

Typically, the rails are modelled using the Euler-Bernoulli beam theory or as a Timoshenko beam theory. The first model only takes into account the bending motion of the beam whereas the latter does consider the shear deformations and hence, it is strongly recommended to be used when the frequency range of interest is greater than 500 Hz [23-25].

Regarding the trackbed model, that is modelling all the structures under the rail level,

there are various levels of detail and different solving techniques, as shown in Figure 3.1. In this figure, the level of details is presented in the rows and the solving techniques in the columns.

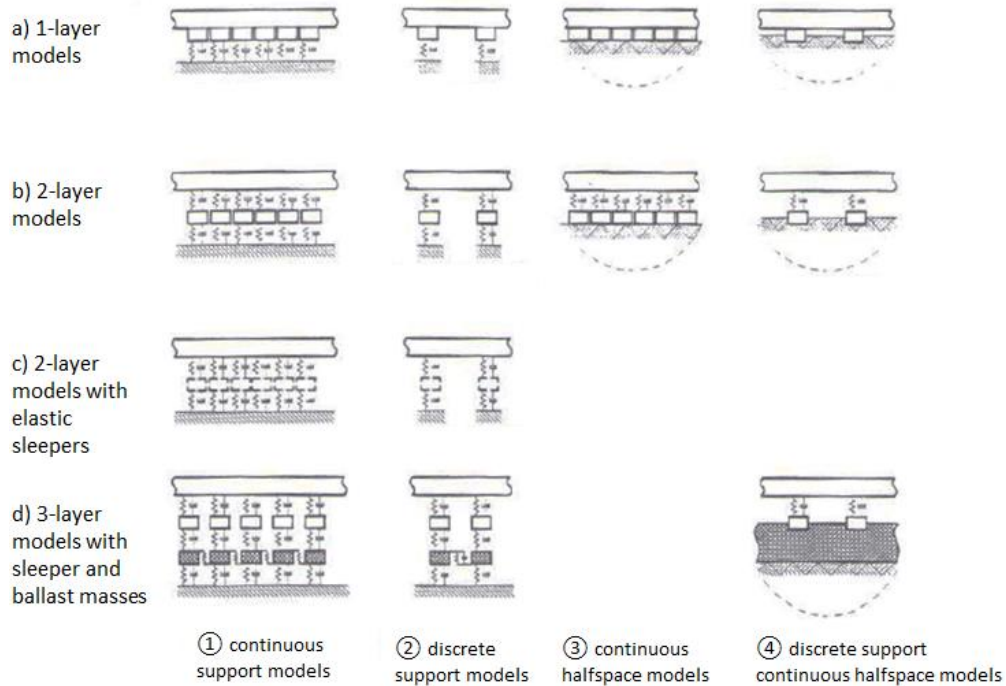


Figure 3.1: Summary of track models [25].

All those models can be solved in frequency and time domain. In the first case, the track and the wheel receptance curves are connected to form the appropriate transfer function considering also the wheel-contact stiffness and the system response is obtained through the Fourier transform. Even if this solution technique allows very low computational costs, it is required that all the system characteristics are linear. Thus, it is not applicable in the case of localised events, including rail joints and turnouts. In the time domain, on the contrary, the non-linearity of the systems can be considered. The deflections, velocities and accelerations can be calculated through the integration of the whole system equation:

$$M \cdot \ddot{x} + C \cdot \dot{x} + K \cdot x = F_{ext} \quad 3.1$$

Where:

$M$  = system mass matrix [kg];

$C$  = system damping matrix [Ns/m];

$K$  = system stiffness matrix [N/m];

*Design methodology for track systems considering the long-term ballast behaviour:  
application to crossings*

$\ddot{x}$ ,  $\dot{x}$ ,  $x$  = system acceleration, velocity and displacement vectors [m/s<sup>2</sup>,m/s,m];

$F_{ext}$  = external force vector [N].

In the followings, the theory of Beam on Elastic Foundation (BOEF), the continuously and the discretely supported track models will be described in more detail.

**BOEF**

An infinite beam rested on a continuous elastic foundation, known as the Winkler foundation, is considered (Figure 3.2).

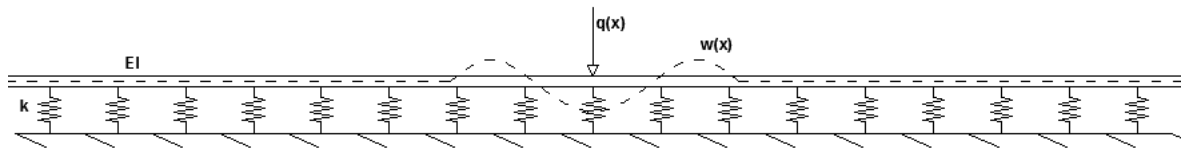


Figure 3.2: Beam on elastic foundation (BOEF).

Considering an infinitesimal beam subjected to the external load  $q(x)$  and neglecting the shear characteristics, the vertical equilibrium is applied and the fourth order Partial Differential Equation (PDE) is developed as follows:

$$EI \cdot \frac{d^4 w(x)}{dx^4} + kw(x) = q(x) \quad 3.2$$

Where:

$EI$  = beam bending stiffness [Nm<sup>2</sup>];

$w(x)$  = rail deflection at position  $x$  [m];

$k$  = foundation stiffness [N/m<sup>2</sup>];

$q(x)$  = distributed load on the rail depending on the position  $x$  [N/m].

It is possible to describe the deformed beam shape solving analytically Equation 3.2.

This model is extremely simplified as all the masses under the rail level, including the bearer and the ballast masses, are neglected. Thus, it cannot be used for dynamic simulations, but only to understand the static (or at very low frequencies) system answer.

Several authors, for example [26-28], have used that formulation, especially in the last century. In Jenkins [29] the Authors applied it to the case of a rail joint in order to describe semi-analytically the magnitude of the impact forces, which are commonly called P1 and P2

forces [30]. These formulae are still widely used in all the cases of impact situations, including those at crossing panel, due to the simple application. Nevertheless, they are not able to capture the variability of the superstructure characteristics and the dynamic effects of travelling variable loads.

### *Continuously supported track models*

This category includes the models which consider the bearers as a continuous support. An example is shown in Figure 3.3.

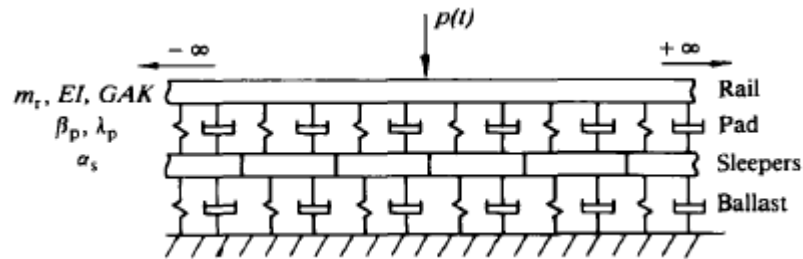


Figure 3.3: Two-layer continuously supported track model [31].

In Grassie [24] the dynamic response of a track system is studied through a two-layer continuously supported track model and the input load is modelled with a wheel rolling over rails with sinusoidal profile, i.e. corrugated rails. In Grassie [31] a similar study has been conducted considering the flexibility of the bearers. Moreover, it is claimed that a continuous model is adequate in the frequency range 50-1500 Hz, as demonstrated by the good agreement between the simulated results and the experimental data.

In Wu [32] a theoretical study into the wheel-rail interaction excited by the roughness is presented. The comparison between the frequency response function of the continuously supported model and the discretely supported model shows how the second type can describe the so-called pinned-pinned resonance, which occurs when bearer spacing is equal to half the wavelength of the flexural waves [33, 34].

This type of model represents a positive step forward in modelling the correct response of track dynamics w.r.t. the BOEF theory, even if it still missing the effect of the discrete support given by the sleeper as well as the effect of the wheel-rail contact.

### *Discretely supported track models*

More recently, several discretely supported track models, for example in [35-38], have been proposed as in reality the rails are supported at discrete locations. The layers include a



*Design methodology for track systems considering the long-term ballast behaviour:  
application to crossings*

detailed description of bearers, ballast and sometimes sub-ballast masses which are attached by flexible connections including springs and dampers. An example is shown in Figure 3.4.

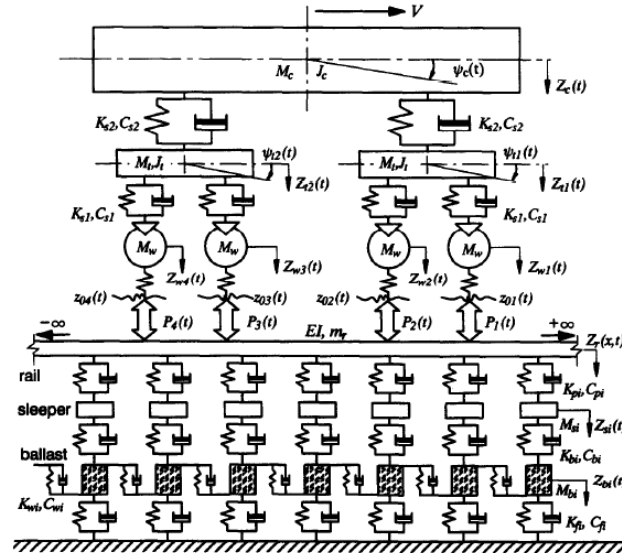


Figure 3.4: Three-layer discretely supported model [35].

This type of modelling has been chosen for the present research. It allows a reasonably accurate evaluation of the dynamic behaviour of the vehicle and track system components with a relatively low computational costs, capturing the potential variability of the superstructure characteristics. In addition to that, it is flexible to be used in a more generic degradation process algorithm, such as the long-term ballast prediction.

### 3.1.2 Track fixing systems

Pads are required to maintain the track geometry, provide impact protection of component, comfortable interface between rail and bearer to prevent component wear, electrical insulation, resistance to rail creep and contribute to minimise noise and vibration emissions [39].

In S&Cs, there are two main ways to link the rail to the bearer:

- *Direct fastening*: the rail and the bearer are directly connected through rail-pads;
- *Indirect fastening*: between the rail and the bearer there is an intermediary baseplate system, that includes a rail-pad and a baseplate pad.

In both cases, the fastening provides the desired preload force through the pads. In the UK, the direct fastening is usually used in the case of crossings with 56E1 profile as

reference rail profile and the indirect fastening in the case of crossings with 60E1 or 60E2 profile as reference rail profile.

Typical values of static and dynamic rail-pad vertical stiffness are reported in Table 3.1. Focusing on the crossing panel, it is common to use soft pads (micromax pads) in the case of direct fixing and use hard pads (Ethylene Vinyl Acetate (EVA) pads) in series with very soft baseplate pads (such as rubber bonded cork (RBC) pads) in the case of indirect fixing [40]. In particular, EVA pads are classified as type C (i.e. pad for specific circumstances where softer pads may give unacceptable dynamic gauge widening or acoustic performance) and RBC as type A (i.e. pad with high impact attenuation properties) [39].

Table 3.1: Static and dynamic stiffness of rail-pads and baseplate pads (pad reference dimensions: 140 x 140 mm).

Description	Thickness [mm]	Static stiffness [kN/mm]	Dynamic stiffness [kN/mm]	Dynamic/static ratio	Visual identification
Rail pad	5.5-10.5	50-120	80-200	1.2-2.4	Soft pad
Rail pad	5-10	150-520	600-1300	2-3	Medium pad
Rail pad	5	550	-	-	Hard pad
Baseplate pad	5-10	15-30	20-40	1.3	
Baseplate pad	3-5	50-80	90-140	1.8	

The pad static stiffness and the pad dynamic stiffness should be measured in accordance with the Euro Norms [41]:

- Static test: a force is applied normally to the pad through a spherical seating in the actuator and the displacement is measured in a controlled temperature area (Figure 3.5). The testing plate dimensions are given in relation with the rail dimensions. The procedure consists, firstly, on two loading cycles between the nominal load and the notional fastening assembly clip force and, secondly, measuring the average displacement when the force is increased to 80% of the nominal load.

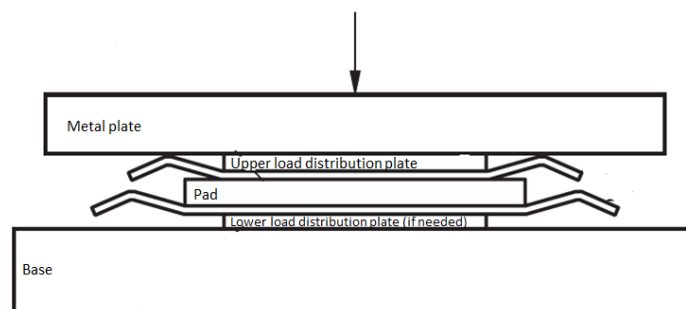


Figure 3.5: Test arrangement for static pad test [41].

*Design methodology for track systems considering the long-term ballast behaviour:  
application to crossings*

- Dynamic test (in the range between 3 Hz and 30 Hz): a cyclic force is applied normally to the pad through an actuator at a single specified frequency and the resulting maximum and minimum displacements of the surface of the pad are measured at the maximum and minimum forces in a controlled temperature area. The procedure consists, firstly, on loading cycles between 80% the nominal load and the notional fastening assembly clip force at the required frequency for 10 s and, secondly, measuring the average displacement for at least 10 cycles and with a minimum of 20 samples per cycle. The sampling frequency should be quoted. If not specified, the sampling frequency is  $(5\pm 1)/(10\pm 1)/(20\pm 1)$  Hz.
- Dynamic test (high frequency): there are two main alternative methods, which are the direct method and the indirect method. Here the corrected driving point method is not discussed as valid up to 120 Hz.
  - Direct method (Figure 3.6(a)): the equivalent transfer stiffness is calculated over each one-third octave band measuring the input acceleration, the acceleration at the measuring platform and the output force and correcting it with the transfer function. The measurements results are valid in the frequency range considered if the acceleration level is higher than 20 dB;
  - Indirect method (Figure 3.6(b)): the average transfer stiffness is calculated over each one-third octave band measuring the input acceleration and the output acceleration.

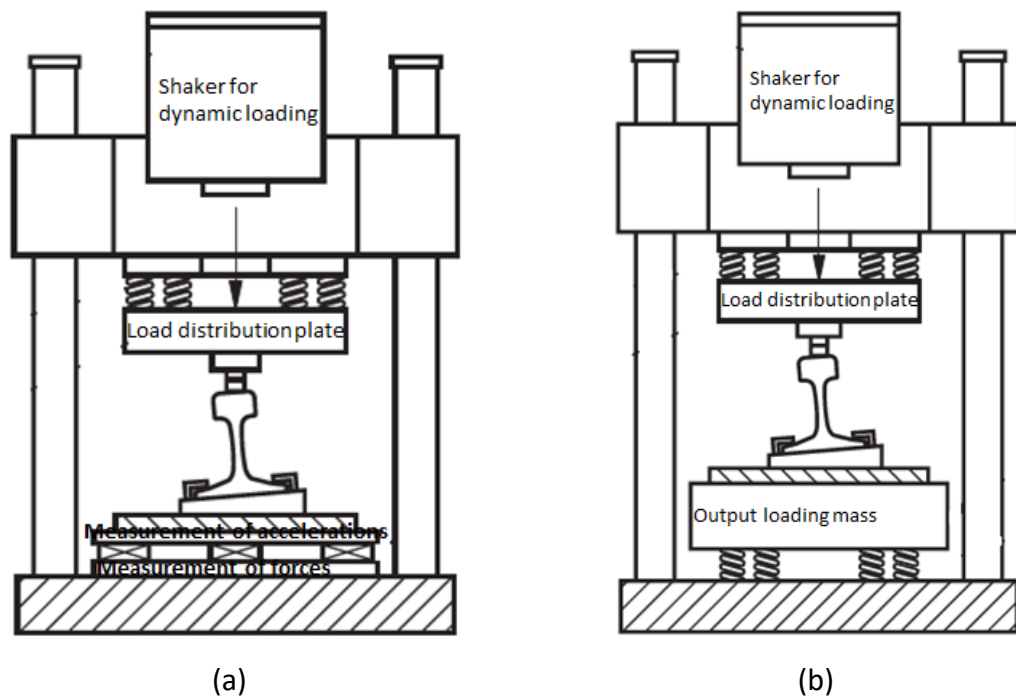


Figure 3.6: Test arrangement for high frequency pad and assembly tests: (a) direct method, (b) indirect method [41].

Similar procedures are applied in the case of assembly, considering the rail, the fastening system and the bearer.

The load cases and the testing frequencies are given according to the relevant standard ([42-45]).

### 3.1.3 Wheel-rail contact model

The wheel-rail interaction has been studied intensively in the last 40 years and several theories and commercial packages are now available to calculate the contact forces that are transmitted between the track and the vehicle.

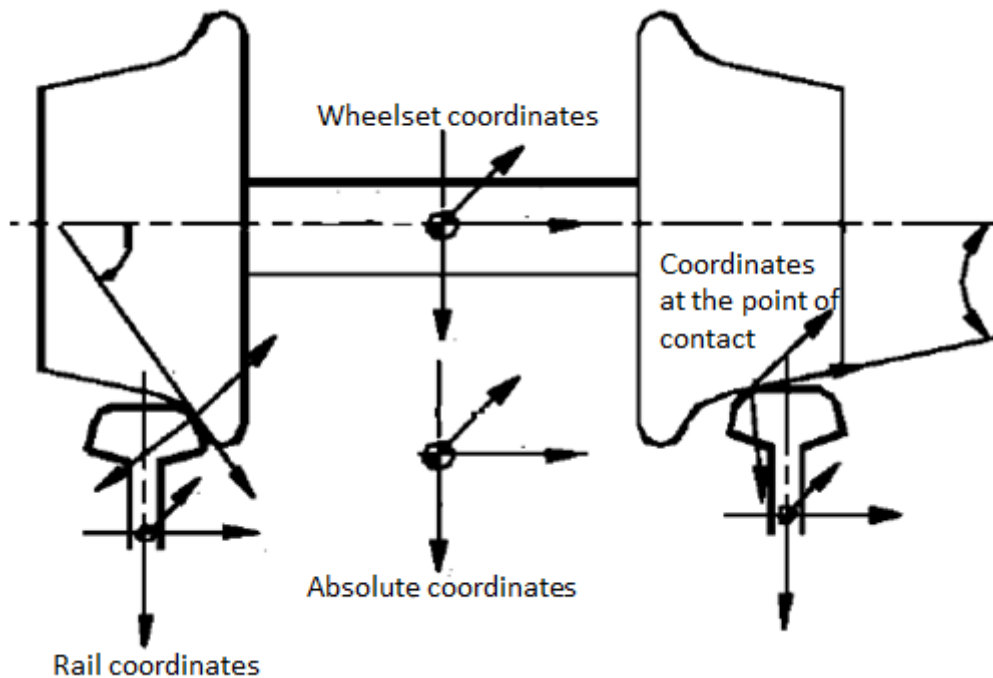
Firstly, it is necessary to define different coordinate systems, as follows (Figure 3.7):

- *Absolute coordinate system*: fixed to the track centre line, it is independent from the wheel movements;
- *Wheelset coordinate system*: fixed to the wheelset centre of mass and on its axis of rotation, it moves according to the wheels movements, taking into account lateral displacement as well as yaw and rolling angles;
- *Rail coordinate system*: fixed at the centre of rail mass, it moves according to

*Design methodology for track systems considering the long-term ballast behaviour:  
application to crossings*

the rail movement;

- *Coordinate system at the point of contact*: fixed at the wheel-rail contact point, it moves according to the contact movements.



*Figure 3.7: Wheel-rail contact problem and sets of coordinate systems [46].*

Usually, the total forces acting at the contact are separated into two main problems: the normal problem, including the pressure distribution across the contact area in a direction normal to the contact plane, and the tangential problem, including the creep forces and induced shear stresses, which are affected by steering and the transfer of tractive and breaking forces between wheel and rail. Also, a general overview of the main Multi Body Systems (MBS) commercial packages employing wheel-rail contact calculation algorithms is given.

***Normal contact model***

When two bodies are compressed one against the other, they will deform near the point of first contact.

The normal contact depends on the geometrical characteristics of the contact patch, including its shape and location. For the off-line methodology, the contact algorithms start with a pre-processor that, for a given set of wheel and rail profiles, calculates all the

geometrical properties in the two-dimensional vertical plane for a wide range of wheelset lateral positions. At each wheel this includes the position of the contact point, the contact angle, the roll and the yaw angle, thus producing a contact table through an iterative process [47]. In reality, the yaw angle, especially in the case of high values, influences the contact point location shifting it out of the vertical plane and therefore, its determination should be performed in the three-dimensional space. This may complicate the calculations and for low values of yaw, this can be neglected.

If the hypothesis of rigid bodies is removed in the routine explained above, it is possible to find more than one contact point, for example at the crossing nose [2, 3].

Usually, the approaches to solve the normal problem are divided into two main categories, considering Hertzian and non-Hertzian wheel-rail contact.

- Hertzian wheel-rail contact

The main assumptions are summarised as follows:

- The bodies are homogeneous, isotropic, follow Hooke's law and are characterised by small strains and rotations;
- The effect of elastic deformation in the vicinity of contact area are neglected because the dimensions remain small compared to the principal radii of the un-deformed surfaces;
- The curvature of wheel and the rail are constant in the contact area and that contact area is small compared with the radii of curvature. Therefore, the contact bodies are described by continuous and quadratic surfaces;
- The material is considered frictionless because the material properties of wheel and rail are assumed the same. In that case, it can be demonstrated that the tangential tractions do not affect the normal pressures between the two bodies.

Under those hypotheses, two infinite cylinders when pressed together deform and the resulting contact patch is a two-dimensional ellipsis with an elliptical normal pressure distribution.

A detailed description can be found in Johnson [48] and in Appendix B.

*Design methodology for track systems considering the long-term ballast behaviour:  
application to crossings*

Undoubtedly, these assumptions are can be restrictive while applying this theory to the realistic cases where the assumptions are not correct. Nevertheless, it has been demonstrated how the results are sufficiently accurate in cases where the curvatures do not change inside the contact area [49].

- *Non-Hertzian wheel-rail contact*

In the past two decades, researchers have been trying to move forward considering more than one contact point and more realistic contact patch shapes in order to overcome the discrepancies in the case of non-ideal conditions (e.g. in presence of plastic deformation [49] or wear [50] and where the rail geometry rapidly changes such as in switches and crossings [51]).

In Telliskivi [52] a tool based on the commercial FEA software ANSYS has been developed and applied in the case of a sharp curve negotiated by two types of passenger train. The wheel and the rail profiles have been measured with the MiniProf device. Two cases of contact have been found, that is on the top of the rail and on the gauge corner. The results from the current FE model have been compared with the Hertzian theory and Kalker software CONTACT (Figure 3.8). As concluded previously, the maximum contact pressures calculated with the three methods considered are comparable when the contact occurs on the top of the rail head, when the conditions are reasonably ideal. On the contrary, in the case of gauge contact, the curvatures of both wheel and rail are high and therefore the Hertz theory largely overestimates the contact pressure.

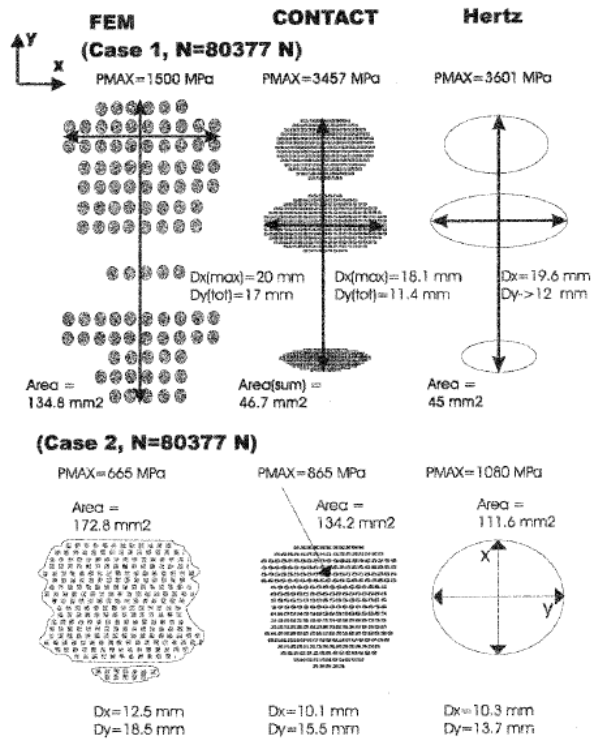


Figure 3.8: Comparison, with respect to maximum contact pressure and the contact area, between three different contact mechanics analysis methods [52].

As presented in Piotrowski [53], there are two main types of method to solve the non-Hertzian wheel-contact problems: (1) approximation of the contact patch with a set of ellipsis and (2) approximation based on virtual penetration of contact bodies. The common assumption for the latter method is that the normal stress distribution in the direction of rolling is semi-elliptical. Examples of the two methods are shown in Figure 3.9.

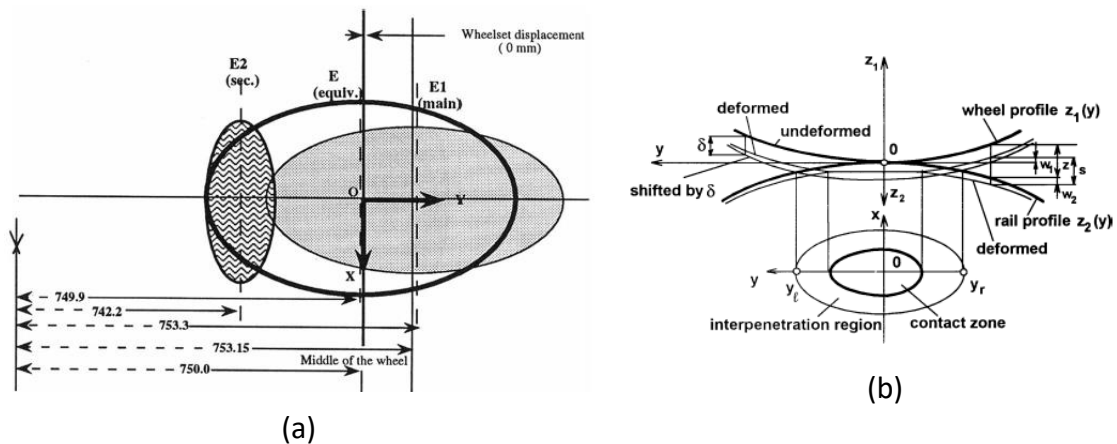


Figure 3.9: Main methods to solve non-Hertzian contact problems: (a) approximation with set of ellipsis and (b) virtual penetration of contact bodies [53].

Within the first category Pascal [54] propose to use a fictitious single contact patch when several contact patches are simultaneously occurring. Its characteristics are determined in



the way that the normal and the tangential forces are the same of the multi-contact code, or, at least, for one case.

Within the second category, Piotrowski [55] have assumed a quasi-Hertzian contact, i.e. the normal pressure distribution is semi-elliptical in the direction of rolling. A good agreement with results from the CONTACT software has been obtained for a wide range of conditions, including multiple points of contact.

### ***Tangential contact model***

The tangential forces guide the vehicle on the track. They depend on several factors, including the shape and the size of contact region, the distribution of normal pressure and the wheel-rail friction.

An exhaustive history of the tangential contact models is given in Kalker [56], starting from Carter's theory. The main assumptions are a circular contact patch with a localised Coulomb's law and a linear relationship between creep forces and creepages.

In particular, creepages are defines as the relative motion between wheel and rail in the longitudinal, lateral and spin directions:

$$\begin{aligned}\gamma_1 &= \frac{v'_1 - v_1}{v} \\ \gamma_2 &= \frac{v'_2 - v_2}{v} \\ \omega_3 &= \frac{\Omega'_3 - \Omega_3}{v}\end{aligned}\tag{3.3}$$

Where:

$\gamma_1, \gamma_2, \omega_3$  = longitudinal, lateral and spin component of creepages [-], [-], [rad/m];

$v_1, v_2, \Omega_3$  = longitudinal, lateral and spin component of actual wheel velocity [m/s], [m/s], [rad/s];

$v'_1, v'_2, \Omega'_3$  = longitudinal, lateral and spin component of pure rolling velocity [m/s], [m/s], [rad/s];

$V$  = travelling speed [km/h].

The principal result was that a 2-axle rigid vehicle always runs unstably, but stability may be found with a suitable secondary suspension.

The most complete study was carried out by Kalker, whose merit was to develop numerical methods for wheel-rail rolling contact and implement them in commercial software.

Firstly, the linear theory assumes a linear creep-force law. It is approximate as the condition about maximum transmissible tangential force is not satisfied in the borders of the contact patch. The creepage coefficients  $C_{ij}$  have been calculated analytically for the contact patch dimension ratio  $(a/b)$  and  $(b/a)$  tending to zero and presented as a table (Appendix C). This theory is still currently used, as it allows the achievement of reasonably accurate results with low computational costs. Usually, the limitation in the creep force due to saturation proposed in Shen [57] is applied. In particular, this formulation uses a cubic saturation law presented in Vermeulen [58], including also the spin term. Several comparisons have been carried with results from DUVOROL and FASTSIM and the differences increase for increasing spin level.

Secondly, the complete theory has been developed including a non-linear creepage law and included in the programme CONTACT [59]. As expected, it requires higher computational costs.

Figure 3.10 shows the comparison between the linear theory and the complete theory (CONTACT) in terms of total lateral force with pure spin. It is noticeable that for low yaw angles there is a good agreement, while the differences are increasingly remarkable (up to 80%) for increasing yaw angles.

*Design methodology for track systems considering the long-term ballast behaviour: application to crossings*

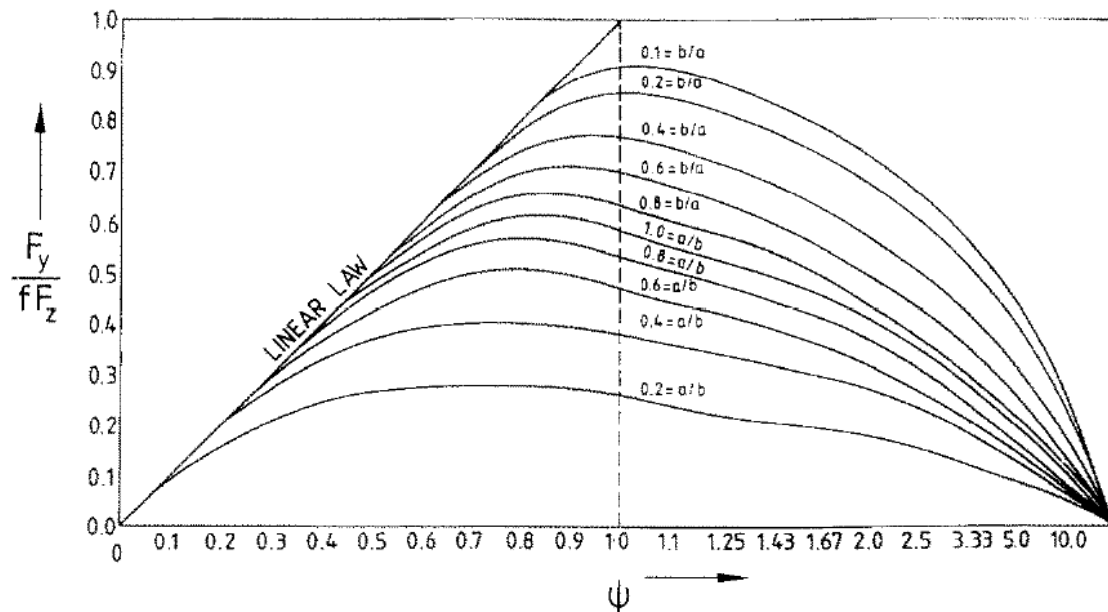


Figure 3.10: Ratio of lateral creep force to available maximum vertical friction force in Hertzian rolling contact with pure spin: comparison between results from CONTACT and linear theory [60].

**MBS packages**

Currently, a large number of MBS packages are commercially available and widely used to simulate the dynamic behaviour of the railway vehicles. A comprehensive and critical comparison of the wheel-rail contact solutions for the case of single wheelset and full vehicle has been presented in the Manchester benchmark ([61]). Ten major codes participated, including Vampire, GENSYS and VOCOLIN. The main differences in terms of normal and tangential contact models are presented in Table 1 of the paper. The initial main results show how all the codes predict similar contact position both in the wheel and in the rail, whereas the contact patch size and the creepages present slight differences. Therefore, it is fundamental that the choice of the software is made according to the intended use.

As pointed in Bezin [34], all the contact routines present certain limitations to the case of S&Cs due to the assumptions made (rigid wheel, rigid rail and constant linear-elastic material properties) as well as the inaccuracies of using contact tables at fixed locations with linear interpolation in between them, leading to potential errors in areas of rapid geometry change such as crossing nose and switch blades.

### 3.1.4 Vehicle system model

The railway vehicle is usually modelled using the rigid body approach with a set of interconnected masses which are propelled along the track at a given speed.

The most important parameters in the vehicle model are:

#### *Unsprung mass*

The unsprung mass is defined as “the mass of a wheel, or wheelset, and other associated components which are not dynamically isolated from the track by vehicle suspension arrangements” [62]. In practice, it includes the wheelset, all the arrangements for the primary suspensions and, in the case of power wheelsets, the motor.

It has been demonstrated that the medium-frequency P2 force is directly linked with the unsprung mass [29]. Due to the fact that this frequency matches with the typical track modes [24], it is transmitted to the infrastructure, producing an acceleration of deterioration of the whole track system, in particular ballast settlement. Therefore, some authors (e.g. Grassie [24] and Kabo [63]) limit their vehicle model only to the unsprung mass.

Also, the UK Infrastructure Manager Network Rail (NR) defines track access prices depending on the concept of the vehicles “track friendliness”, which is directly linked to the unsprung mass.

Looking in particular to the wheelset, it is the assembly of two conical wheels connected through a rigid axle. The parameter which is usually used to describe the conical shape is the equivalent conicity, which is defined as “the tangent of the cone angle  $\tan\gamma_e$  of a wheelset with coned wheels whose lateral movement has the same kinematic wavelength as the given wheelset” [64]. It is worth noticing that the quoted kinematic wavelength is calculated with the Klingel’s formula.

Nevertheless, an essential aspect to correctly model the wheel-rail contact mechanic is the actual profile shape, which is typically measured using a MiniProf device or else taken from engineering drawings.

#### *Suspensions [23, 65]*

There are two main types of suspensions in a rail vehicle: primary and secondary suspensions. The former ones connect the wheelsets and the bogie frame, the latter ones the

bogie frame and the bolster or the car body. Passenger coaches have both of them, while the freight wagon usually only have a primary suspension. Nevertheless, the trend is to include more resilience in freight bogie design. An example is the innovative bogie design carried out during the European Project SPECTRUM [66]. Suspensions usually include elastic elements (i.e. linear/non-linear springs) and dampers.

An extensive state-of-art of suspension component modelling is presented in Eickhoff [67], where it is stated how important understanding the physical processes is. More recently, in Bruni [68] mathematical models of railway vehicle suspension components are discussed in detail as well as the effect of model uncertainties on simulation results. This is relevant in the case of virtual homologation, which is used more and more nowadays.

## **3.2 Modelling the turnout system: state of the art**

### **3.2.1 Vehicle-track interaction modelling**

In the past decade, various numerical models have been developed to describe the vehicle-turnout interaction behaviour. Several aspects have been addressed, including the type of modelling used (i.e. MBS approach, FE approach) and the necessity of a refined wheel-rail contact model.

The MBS approach has been used by few researchers, for example Lagos [69], Sun [70] and Pau [71], while several FE models have been built in-house, including in Alfi [72] and Bruni [73], or using commercial packages, such as in Coleman [74]. Kassa [75] presented a comprehensive comparison between the two approaches and against field measurements of vertical and lateral contact forces. It has been pointed out that while the MBS approach is more suitable for lateral dynamics at the switch panel due to the consideration of the whole vehicle and the shorter computational times, the FE approach produces more accurate results and is suitable to assess the influence of component properties, such as trackbed stiffness.

Solving the wheel-rail contact problem at the switch and crossing panel has been the focus of some studies. For example, in Ren [76] a practical methodology to determine the location and the entity of two contact patches in a turnout is presented and applied to optimise the top height of the nose. Burgelman [77] describes a new computer program called WEAR, which is an extension of the CONTACT algorithm of Kalker and which is able to take into

account conformal contact situations by using influence numbers for a quasi-quarter space as well as the local and varying spin creepage in each element in the contact patch. Similarly, Sebes [78] presents a semi-Hertzian method to solve the wheel-rail contact problem for high-speed switches with moveable frog. This consists on dividing the rail in narrow strips and assigning a stiffness, which depends on the local curvatures and elastic properties of the material, to each of them. Even if non-Hertzian theory seems to be necessary in the particular case of wheel-crossing contact, it has been shown in Wiest [51] that similar trends of calculated contact pressure, contact patch size and penetration depth can be found when the Hertzian contact theory, the non-Hertzian contact theory implemented in CONTACT and the elastic FE contact model are considered.

### **3.2.2 Trackbed degradation**

The topic of trackbed degradation at turnout has not been fully addressed in the literature. It is possible to divide the few relevant studies found on the basis of two main approaches, i.e. the statistical approach, when measured data is available, and the numerical modelling approach.

Using the time series of measured longitudinal level of turnouts on a Swedish heavy haul line, Khouy [79] demonstrated that there is a limit to the settlement at the location of the crossing. Before reaching that limit, the highest degradation rate occurs at the crossing position, while afterwards it propagates in the vicinity. Kennedy [80] presented a practical application of polyurethane ballast reinforcement to reduce track settlement at the crossing panel. It has been demonstrated how it helps greatly to save up to 30 maintenance cycles, as the site has never required any intervention for 10 years.

Some papers adopt an iterative procedure to numerically calculate the track settlement in a turnout using either established settlement equations (e.g. Li [12], Nielsen [81]) either proposing new approaches (e.g. Li [82]). The results obtained can be used both in a design and maintenance phase.

## **3.3 Modelling the long-term ballast behaviour**

A detailed critical literature review about settlement equations has been presented in Dahlberg [21], considering Japanese models (Sato models), US models (Alva-Hurtado model, Ford model), European models (ORE model), German models (Dietrich model,

Hettler model, Holzlohner model), British models (Shenton model), French models (Guérin model), South African model (Fröhling model), Australian models. Also Indraratna [83] and Abadi [84] presented a comparison between settlement curves based on the form of the proposed equation form (i.e. exponential type in the form of  $A \cdot N^B$  or logarithmic type in the form of  $C \cdot \log N^D$ ). Recently, Grossoni [9] published a literature review from the vehicle-track interaction point of view.

Various authors have used these models in an iterative process to calculate the evolution of the track geometry over time. For example, Mauer [85] presents a dynamic settlement model to calculate the track growth evolution of some theoretical rail geometry deviations using the exponential Hettler settlement equation. Fröhling [86] applied a similar approach using a settlement equation which takes into account measurable track parameters and validated it against *in situ* tests. Iwnicki [87] compared Sato [88] and TU Munich [89] settlement equations using VI-Rail commercial package and showed that the predicted settlement rate is significantly dependent on the model used. Finally, Nguyen Gia [90] and Ferreira [91] applied the Guérin [92] equation to analyse the degradation behaviour in high speed lines. Further details about the link between dynamic vehicle-track modelling and long-term predictions will be given in Section 3.4.

In this Section, a number of these settlement equations will be examined and compared, highlighting how they have been derived (in laboratory or *in situ*). Although geotechnical characteristics of the granular materials are fundamental in the settlement process, only the directly available following parameters will be used for the comparison (see Grossoni [9] as main reference):

- the type of traffic: equivalent axle load, speed;
- the superstructure characteristics: bearer type, bearer spacing;
- the conditions of ballast, sub-ballast and sub-grade layers: ballast depth.

### **3.3.1 Laboratory testing**

In the tri-axial tests, the axial stress (axial load) is varied between pre-determined limits, as well in Jeffs [93], Guérin [92], Indraratna [83, 94, 95], Thom [96] and Abadi [84]. Cedex [97, 98] takes into account a full bogie and the partial unloading between the first and second wheelset. Finally, Steward [99] does not provide any information about the loading

methodology.

- Tri-axial tests

Shenton [100] presents standard tri-axial tests of dry ballast. A servo-hydraulic compressive/tension loading system has been used in order to be able to simulate high speed cases as well as large number of loading cycles in a realistic time scale. The testing frequencies go from 0.1 Hz (loading of the first 8 cycles in all the tests to keep consistent test conditions) to 30 Hz. Three axle loads (10, 20.5 and 30 t) has been considered in the experiment.

Laboratory tri-axial tests on ballast as well as ballast box tests using wood bearer segment have been presented in Selig [101]. The vertical loading varies between 0.22 kN (unloaded condition corresponding to the minimum siting loading) and 21.8 kN (loaded condition representing a 35 t axle).

- Reduced scale ballast box tests

Steward [99] carried out laboratory box tests using the apparatus including half timber bearer. The load applied corresponds to an equivalent 30 t axle load.

In Jeffs [93] the ballast elastic and plastic response to a variety of accurately controlled vertical load conditions have been studied in laboratory using a box apparatus. Two loading frequencies (6 and 10 Hz), three axle load values (32.5, 40 and 50 t) and three bearer materials (steel, concrete and timber) have been considered.

Guérin [92] carried out an extensive series of one-third scaled tests to simulate the passage of 20 t axle load at 250 km/h. The loading frequency is 30 Hz.

In Indraratna [83, 94, 95] a large-scale test rig has been used to predict a settlement equation in the case of new and recycled ballast in combination with geosynthetics. A single rail is accommodated on timber bearer on top of ballast, sub-ballast and subgrade layers. A harmonic sinusoidal cyclic stress load corresponding to a 25 t axle load is applied at a frequency of 15 Hz in order to simulate a speed of 109 km/h and a wheelbase of 2.02 m.

- Full-scale ballast box tests

The Nottingham railway test facility [102] is a full-scale test box facility consisting on three concrete bearers loaded with servo-controlled hydraulic actuators through loading rollers and spreader beams. The vertical loading varies between 4 kN and 94 kN at 3 Hz,



*Design methodology for track systems considering the long-term ballast behaviour: application to crossings*

corresponding to ca. 27 km/h [103].

The CEDEX Track Box, which includes a 21 m long track (32 bearers also with three bituminous mix sub-ballast sections), has been used to evaluate the long-term ballast behaviour [97, 98]. The load is applied through six actuators commanded by a servo-hydraulic system. Three loading frequencies (7, 27 and 40 Hz) have been used to simulate three carriage types travelling at 300 or 360 km/h.

The Southampton Railway Testing Facility (SRTF) is capable to replicate the long-term ballast behaviour after millions of cyclic loading. It includes a single G44 concrete bearer with two 60E1 short rail sections and wooden and steel panels held at a fixed distance of 0.65 m (typical UK bearer spacing) [104]. A loading beam transfers the vertical and the lateral load to the superstructure. The testing procedures are discussed in detail in Abadi [105]. The vertical loading varies between 5 kN (unloaded condition) and 98.1 kN (loaded condition representing a 20 t axle) at 3 Hz, which has been chosen as trade-off between a reasonable testing timescale and maintenance of quasi-static conditions.

Figure 3.11 shows a comparison of the settlement equations obtained with laboratory tests (Table 3.2).

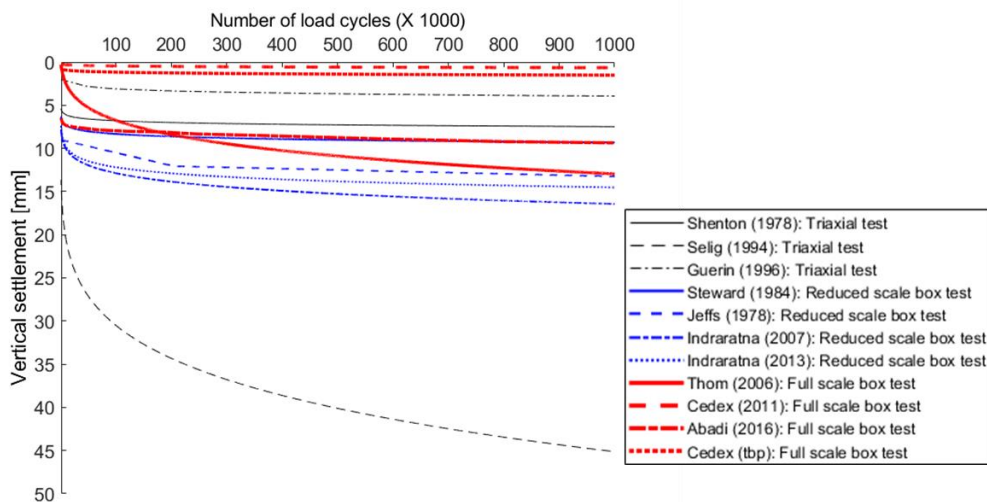


Figure 3.11: Comparison of settlement equations obtained with laboratory tests.

Table 3.2: Settlement equations obtained with laboratory tests ( $S_N$  is the vertical settlement at the cycle number  $N$ ).

Test type	Author	Empirical equation	Constants
Tri-axial test	Shenton [100]	$S_N = S_1 \cdot (1 + \text{const} \cdot \log_{10} N)$	const= 0.2
	Selig [101]	$S_N = \text{const1} \cdot N^{\text{const2}}$	const1 = 4.3; const2 = 0.17
Reduced scale ballast box test	Steward [99]	$S_N = S_1 \cdot (1 + \text{const} \cdot \ln N)$	const = 0.35 (0.63 if uncompacted)
	Jefferies [93]	$S_N = \begin{cases} \text{const1} + \text{const2} \cdot \log_{10} N + \text{const3} \cdot N, & N < 200000 \\ \text{const4} + \text{const5} \cdot N, & N \geq 200000 \end{cases}$	const1 = 90; const2 = 0.006; const3 = 0.00015; const4 = 12.5; const5 = 0.000015
	Guérin [92]	$dS_N/dN = \text{const1} \cdot d_{b,max}^{\text{const2}}$	const1 = 0.00000144; const2 = 2.51
	Indraratna [83, 94, 95]	$S_N = S_1 \cdot N^{\text{const}}$ $S_N = S_1 \cdot (1 + \text{const1} \cdot \ln N + 0.5 \cdot \text{const2} \cdot \ln N^2)$	const = 0.106 const1 = 0.43; const2 = 1.6
Full-scale ballast box test	Thom [96]	$S_N = (\log_{10} N - 2.4)^2$	
	Cedex1 [97, 98]	$S_N = \text{const1} \cdot N^{\text{const2}}$ $S_N = \text{const3} \cdot N^{\text{const4}}$	const1 = 0.07; const2 = 0.1625 const3 = 0.85; const4 = 0.18
	Abadi [84]		

The results presented in Figure 3.11 highlight how the settlement equation is strictly connected with the laboratory conditions and assumptions that have been made. It is worth noting how the equation developed at Cedex [97] gives the lowest results. This is certainly due to the fact that a bituminous mix sub-ballast layer is present to replicate the Spanish high speed line construction [106]. As noted previously, all the equations in the table can be categorised in two main groups: (1) logarithmic form, when the settlement is predicted as function of  $\log N$ , and (2) exponential form, when the settlement is predicted as function of  $N^{\text{exp}}$ .

Some discussions are presented hereafter:

- Axle load

<sup>1</sup> The first settlement equation has been derived using bituminous mix sub-ballast Sections.

*Design methodology for track systems considering the long-term ballast behaviour: application to crossings*

Shenton [100] showed through a full-scale laboratory tests that the track settlement increases linearly with axle load for the first 100 loadings. This is in line with Jeffs [93] as shown in Figure 3.12.

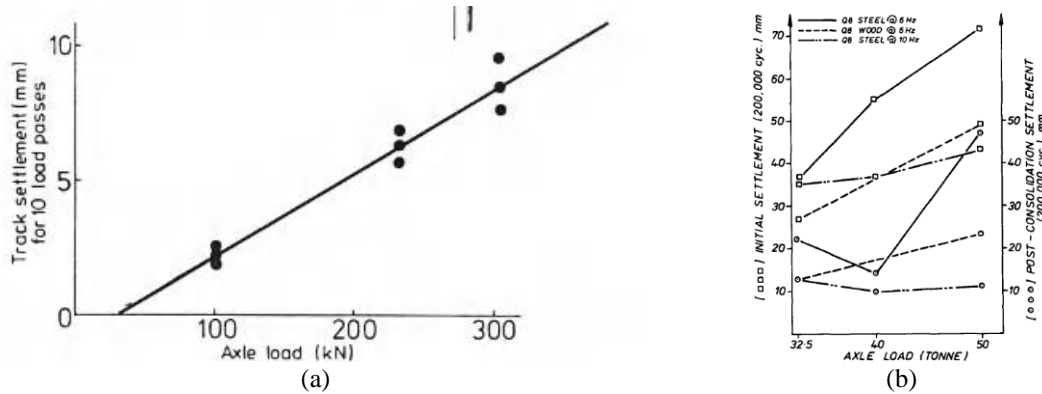


Figure 3.12: The effect of axle load according to (a) Shenton [100] and (b) Jeff [93].

Considering all the equations analysed in Figure 3.11, the relationship between vertical settlement and equivalent axle tonnage is presented in Figure 3.13 for the first phase (left plot) and the second phase (right plot). The grey dotted line represents the regression line excluding the Selig model.

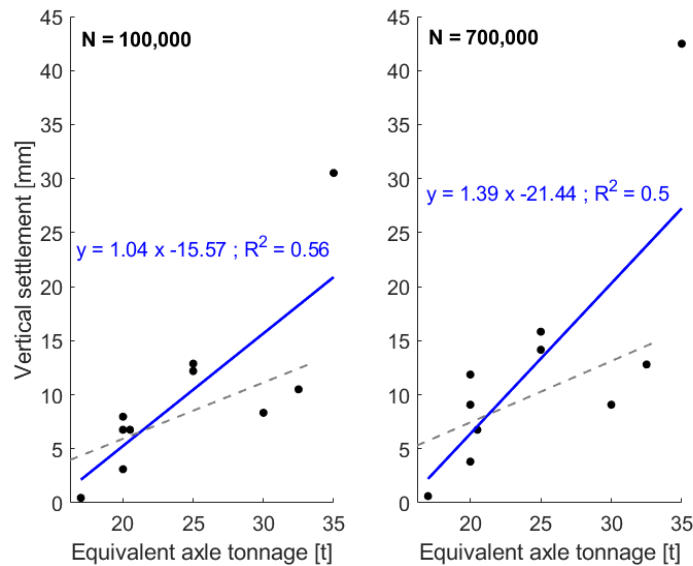


Figure 3.13: The influence of axle load on vertical settlement considering all the equations analysed in Figure 3.11.

From Figure 3.13 it is possible to conclude that there is an evident increase of settlement with increasing axle load in the case of both first and second settlement phases. The influence is more evident in the second phase (ca. 33% higher slope). Therefore, the axle load should be included in the settlement equation as a main driver.

It is necessary to highlight that the coefficient of determination  $R^2$  is relatively low in both plots shown. This can be explained with the fact that different types of test (i.e. tri-axial test, reduced scale ballast box test, full-scale ballast box test) and different procedures (i.e. loading frequency, ballast specification, material of the loading plate etc.) have been considered simultaneously.

- Loading frequency

No obvious effect of loading frequency on ballast settlement has been shown in Shenton [100] and Guérin [92], while Indraratna [107] has shown how the loading frequency deeply affects the permanent deformation (Figure 3.14).

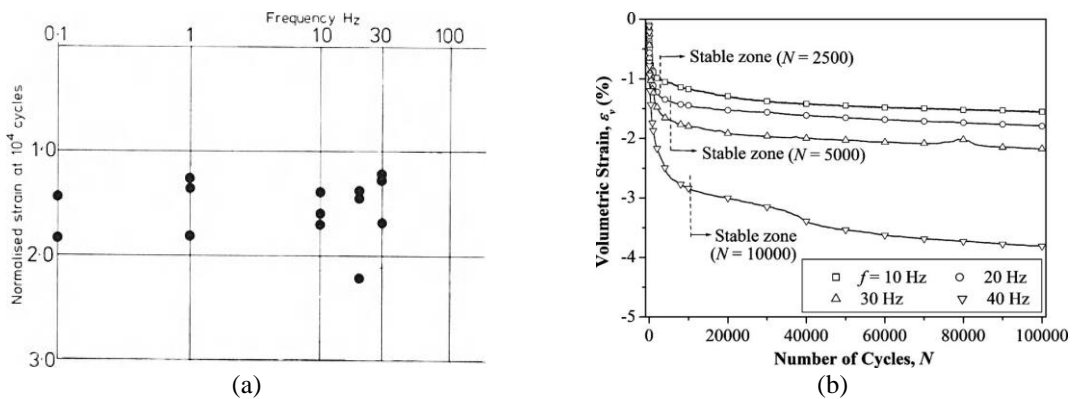


Figure 3.14: The effect of loading frequency according to (a) Shenton [100] and (b) Indraratna [107].

Considering all the equations analysed in Figure 3.11, the relationship between vertical settlement and loading frequency is presented in Figure 3.15 for the first phase (left plot) and the second phase (right plot). The dashed line represents a spline data fitting.

*Design methodology for track systems considering the long-term ballast behaviour:  
application to crossings*

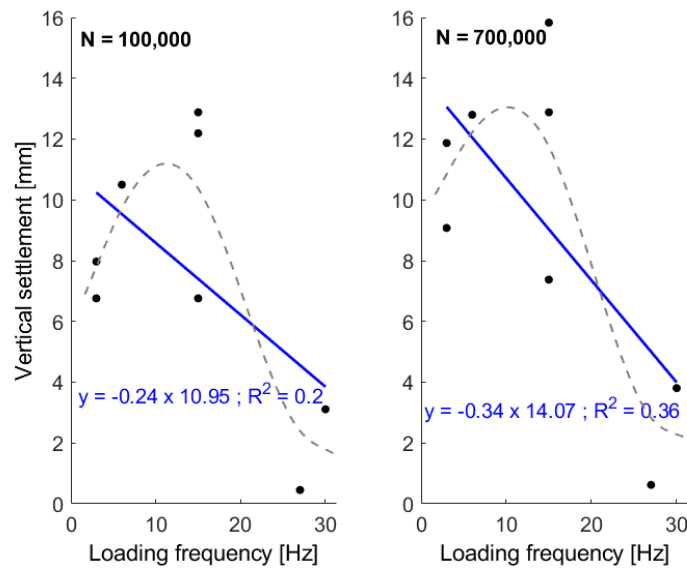


Figure 3.15: The influence of loading frequency on vertical settlement considering all the equations analysed in Figure 3.11.

There is no clear trend between ballast settlement and loading frequency as shown in Figure 3.15 in both settlement phases. It seems that there two main behaviours depending on the loading frequency. Up to 15 Hz, the vertical settlement slightly increases for increasing loading frequency, while it reduces drastically for very high loading frequencies (see experiments form Guérin [92] and Cedex [97]). This is against the results obtained by Indraratna [107] as maybe different types of test and different procedures have been considered simultaneously.

- Bearer material

Jeffs [93] shows that, *ceteribus paribus*, soft timber bearer tends to settle less than steel and concrete bearer. This can be explained by the fact that the wooden bearer offers a more conformal area of contact with the ballast stones than the hard concrete bearer under surface, thus helping spread the path loads through the granular layers and reducing pressure overall.

### 3.3.2 *In situ* testing

Partington [108] used the R&D Division track research laboratory of British Railway Research (BR) to derive the settlement equation. The track irregularity is represented by a 0.10 rad dipped joint profile, which has been dressed to avoid significant effect on track properties. Two different configurations of vehicle (high/low load) have been considered.

The test consisted in 1000 passes of the rolling load rig over the irregularity.

Four test sites have been used in Steward [99] to calculate the elastic and plastic ballast behaviour, considering both wooden and concrete bearers. Both tangent and curved sections have been considered.

Selig [101] used the FAST test track in Colorado to determine the relationship between ballast settlement and loading cycles.

By analysing measured data of average track settlement with accumulating traffic, Fröhling [109] developed an expression that, while logarithmic in form as explained in his PhD thesis, also takes account of the deviatoric stress at the sleeper-ballast interface. Note that the parameters in Table 3.3 are only valid for track stiffness between 60 and 132 kN/m as defined here by Fröhling, because the const2 product term of the equation cancels out the  $K_1$  part and the square bracket expression then becomes negative for values above 132 kN/m. Above this value, there is a reversal trend in the settlement equation that does not match any realistic physical behaviour. Different const1 and const2 parameters would need to be defined to simulate continuous settlement change for stiffness values above 132kN/m. Below 60 kN/m, however, the equation tends to converge to larger settlement values and could be applied as is with reasonable output.

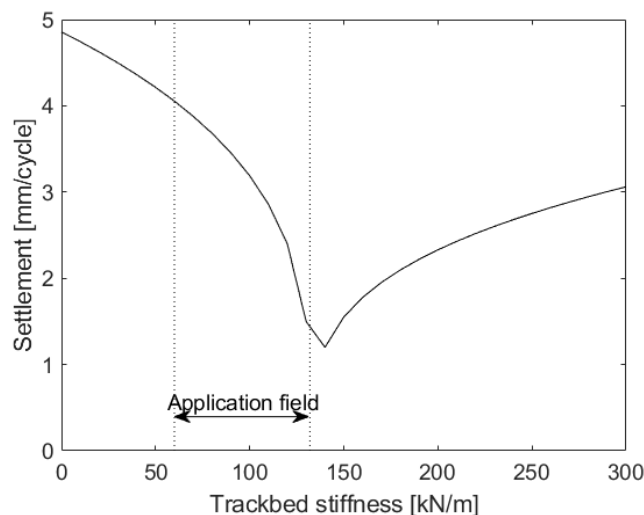


Figure 3.16: Variation of settlement predictions with trackbed stiffness using the Fröhling equation as defined ( $\ln N = 1$ ;  $P_{dyn}/P_{stat} = 1$ ) ([9])

Figure 3.17 shows a comparison of the settlement equations obtained with *in situ* tests (Table 3.3).

*Design methodology for track systems considering the long-term ballast behaviour:  
application to crossings*

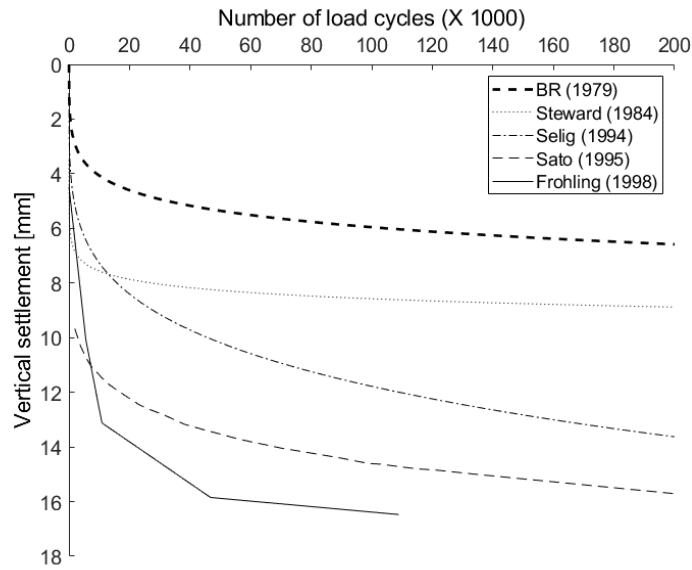


Figure 3.17: Comparison of settlement equations obtained with in situ tests.

Table 3.3: Settlement equations obtained with in situ tests ( $S_N$  is the vertical settlement at the cycle number  $N$ ).

	<b>Equation</b>	<b>Constants</b>
Partington [108]	$S_N = const1 \cdot (\log_{10} N)^{const2}$	const1= 0.29 (0.38 if high load); const2= 1.77 (1.71 if high load)
Steward [99]	$S_N = S_1 \cdot (1 + const \cdot \log_{10} N)$	const= 0.29
Selig [101]	$S_N = const1 \cdot N^{const2}$	const1= 0.0035; const2= 0.21
Fröhling [86]	$S_N = \left[ const1 + const2 \cdot \left( \frac{K_s}{const3} \right) \cdot \left( \frac{P_{dyn}}{P_{sta}} \right)^{const4} \right] \cdot \ln N$	const1= 194; const2= -1.96; const3= 1.34

Figure 3.18 shows the final comparison between the settlement equations obtained *in situ* and the settlement equations obtained with laboratory tests.

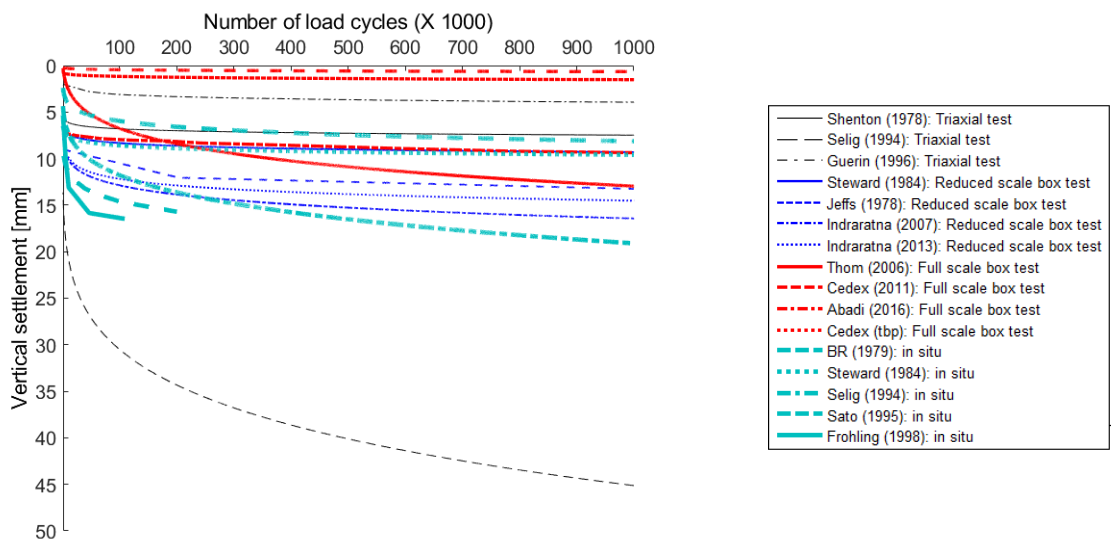


Figure 3.18: Comparison of settlement equations obtained with in situ tests and laboratory tests.

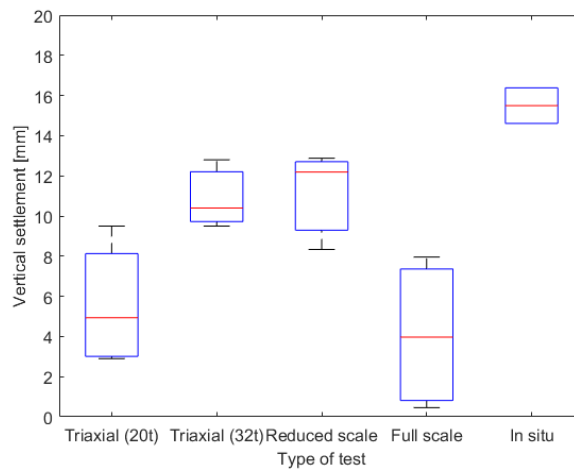


Figure 3.19: Comparison of settlement equations obtained at 100,000 cycles using the input values in Table 3.4 ([9]).

Table 3.4: Overview of the experiments considered ([9]).

Test type	Author	Equivalent axle load [t]	Average / $\Delta$ axle load [t]
Triaxial test (20 t)	Shenton [100]	20	20 / 0
	Guérin [92]	20	
	ORE [110]	20	
	Alva-Hurtado [111]	20	
Triaxial test (32 t)	Shenton [100]	32	32 / 0
	ORE [110]	32	
	Alva-Hurtado [111]	32	
Reduced scale ballast box test	Steward [99]	20	23.3 / 5
	Indraratna [112]	25	
	Indraratna [83]	25	
Full-scale ballast box test	Thom [96]	20	19 / 3
	Cedex [97]	17	
	Abadi [84]	20	
<i>In situ</i> test	Partington [108]	22	24 / 4
	Fröhling [86]	26	

From Figure 3.19 and Table 3.4 it is possible to draw the following main conclusions:

- There are large discrepancies in most of cases between the laboratory and the in-situ prediction. This suggests that the local in situ conditions, such as the actual load acting in the ballast layer and the confining pressure, play a fundamental role in the ballast degradation process and difficult to be correctly reproduced in laboratory. An example that compares the tri-axial test conditions and the full-scale test conditions is presented in Aursudkij [113], who concluded that the best agreement is obtained with 30 kPa



*Design methodology for track systems considering the long-term ballast behaviour:  
application to crossings*

confining pressure and deviatoric stress to maximum normal pressure ratio equal to 2.

- The average of the values obtained with in-situ tests are higher than all the other laboratory test results, even if the axle load observed during the measurements is not higher than the triaxial tests with 32 t.
- The average value for triaxial (20 t) and full-scale box results are similar, but the latter category presents higher dispersion of the data.
- The average value for the axle load used in reduced scale tests is similar to the in situ tests, but the average vertical settlement is about 21% lower w.r.t the in situ tests, meaning that there are other influencing factors, including the stress distribution and the excitation frequency.
- Comparing the triaxial tests, it is possible to notice a high dispersion of the data, especially in the case of 20 t, that cannot be re-conducted only to the axle load used.

Figure 3.19 highlights the fact that, even though there is a large number of settlement equations available in literature, it is very difficult to find an agreement between the test conditions under which they have been derived and therefore between the results. Another fact is that it is very difficult to translate the laboratory conditions of tri-axial tests to real track condition (i.e. definition of the confining pressure).

This reveals that moving forward it is highly important for the scientific community to agree on a common test specification and procedure to further the current understanding and enable a direct comparison of future lab and in-situ testing possible. It is also suggested that numerical vehicle-track interaction models able to replicate loading pattern in components and trackbed layers are used both to determine the loading regime required in test. Furthermore, they can be used as a mean of testing the settlement equations obtained in applications taken beyond the prescribed limits of the laboratory tests as presented next.

### **3.4 Coupling the long-term ballast behaviour with vehicle-track interaction models**

Vehicle-track interaction (VTI) may generate high variations in the wheel-rail vertical

forces, especially due to geometrical irregularities on track (e.g. welds, crossings, joints, ...) or vehicle (e.g. wheel flats, ...), leading to high deflections and stresses and, consequently, plastic deformations in the ballast and supporting layers.

From a modelling point of view, the short-term vehicle-track interaction can be coupled with the long-term track degradation using an iterative procedure based on time domain simulation (Figure 3.20). The outputs of the VTI model, including forces transmitted to the supporting structure, the ballast displacements and accelerations and the contact forces, are used to inform the ballast plastic model chosen (see below) relating them to the permanent settlement, the number of train passages and the structure characteristics. The total settlement after N cycles is then calculated as the accumulated value. If the total number of passages is reached, the program ends, otherwise the iterative routine continues until that point.

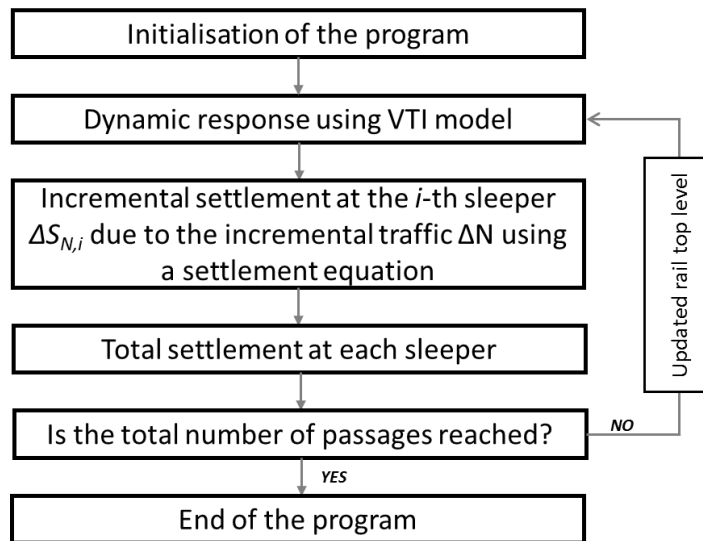


Figure 3.20: Coupling the vehicle-track interaction model with the long-term ballast behaviour ([9]).

Three models are frequently used, i.e. Guérin's, Sato's and Fröhling's models, due to the fact that they explicitly consider outputs of the dynamic model.

Looking in detail at Sato's equation, two main forms have been proposed [114]:

$$S_N = \begin{cases} a \cdot P_b^b \cdot c \cdot N & \text{3.4} \\ d \cdot (P_b - P_{th})^2 \cdot e \cdot N & \text{if } P_b > P_{th} \quad \text{3.5} \end{cases}$$

Where  $P$  is the bearer-ballast contact pressure,  $P_{th}$  the threshold sleeper-ballast contact pressure,  $N$  the number of cycles and  $a, b, c, d, e$  the model constants (Figure 3.21 and Table

*Design methodology for track systems considering the long-term ballast behaviour:  
application to crossings*

3.5). It is worth noticing that the threshold  $P_{th}$  at which the ballast plastic behaviour starts and the degradation rate  $a$  play a fundamental role in the track geometry evolution. They both depend on superstructure and material factors, such as ballast grading, ballast geometry, subgrade type and load cycle. Nevertheless, there is a lack of experimental and numerical data and thus it is difficult to set reasonable values.

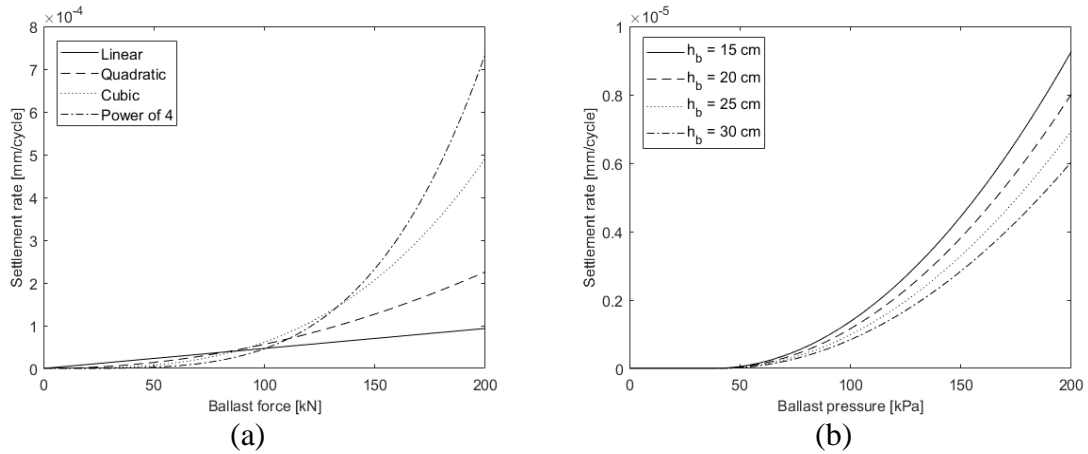


Figure 3.21: Settlement rate according to (a) Eq. 3.4 and (b) Eq. 3.5 [114].

Table 3.5: Parameters used in Sato's equation [114].

Parameter	Value	Parameter	Value	Parameter	Value
a	$1.403 \cdot 10^{-6}$	b	1	$c^2$	0.33
	$9.411 \cdot 10^{-9}$		2		0.66
	$4.382 \cdot 10^{-11}$		3		1.40
	$1.839 \cdot 10^{-13}$		4		2.50
d	$2.70 \cdot 10^{-10}$	$P_{th}(h_b = 15\text{cm})$	37.5	$e(h_b = 15\text{cm})$	1.30
		$P_{th}(h_b = 20\text{cm})$	38.6	$e(h_b = 20\text{cm})$	1.14
		$P_{th}(h_b = 25\text{cm})$	39.6	$e(h_b = 25\text{cm})$	1.00
		$P_{th}(h_b = 30\text{cm})$	40.6	$e(h_b = 30\text{cm})$	0.88

Sato has proposed also a formulation to calculate the rate of growth of irregularities in mm/100 days as [88] :

$$S = a \cdot T^\alpha \cdot V^\beta \cdot M^\gamma \cdot L^\delta \cdot P^\epsilon \quad 3.6$$

where  $a$  is a correction factor,  $T$  the tonnage (million tons/year),  $V$  the average traffic running speed (km/h),  $M$  the structure factor,  $L$  the influence factor for jointed rail or CWR (1 for CWR and 10 for jointed rail) and  $P$  the influence factor for subgrade (1 for good subgrade and 10 for bad subgrade). The values of the exponents  $\alpha$ ,  $\beta$ ,  $\gamma$ ,  $\delta$  and  $\epsilon$  obtained by Sato are 0.31, 0.98, 1.10, 0.21 and 0.26, respectively.

<sup>2</sup> Note that this parameter is added to match the figures in the reference.

The structure factor  $M$  is further defined as:

$$M = P_b \cdot \ddot{y}_s \cdot I \quad 3.7$$

where  $P_b$  is the maximum bearer pressure due to a wheel load,  $\ddot{y}_s$  the maximum ballast acceleration, also to be understood as bearer acceleration and  $I$  the impact coefficient defined as:

$$I \propto \frac{1}{\sqrt{EI \cdot k}} \quad 3.8$$

Which is inversely proportional to  $EI$  the flexural rigidity of the rail and  $k$  the equivalent support system stiffness per unit length.

As anticipated, a number of these analytical expressions can directly be substituted by VTI analysis outputs, including:

- The structure factor ( $M$ ) containing the bearer acceleration ( $\ddot{y}_s$ ) and ballast pressure ( $P_b$ ) are direct output of VTI analysis. The remaining impact factor ( $I$ ) is also directly accounted for in VTI analysis in the building of the track system, and has a direct influence on the other two quantities.
- The influence factor for joined rail or CWR ( $L$ ), attempts to capture the effect of a wide range of track quality (good quality CWR=1 and jointed rail =10), including discrete irregularities such as dipped joints or welds and their local effect on dynamic transient loads. indeed, there is a wide range of dynamic loading response to a wide range of track geometrical features falling in between these two values, and it remains up to interpretation how to set this parameter. This is especially true as dynamic load responds differently to different input wavelengths: <20 Hz for typical vehicle dynamics modal response, < ~90 Hz for the so-called P2 dynamic force [19] locally influencing trackbed condition and > ~90 Hz for dynamic forces influencing wheel-rail behaviour and track components, both responding to shorter track geometry features. Simple formulae exist to derive P2 forces acting locally on joints and crossings, or alternatively VTI models can be used to predict them with greater accuracy. However, this is an area where more investigation is necessary to

*Design methodology for track systems considering the long-term ballast behaviour:  
application to crossings*

quantify the influence factor based on track type and quality, as well as the propensity and magnitude of discrete defects.

- The influence factor for subgrade ( $P$ ) is considered as an independent parameter, but may be better of incorporated into the structure factor as it directly contributes to the overall stiffness.

Table 3.6 summarise the physical quantities considered, advantages and disadvantages of the identified settlement equations that can be coupled with VTI models.

*Table 3.6: Summary of the different settlement equation considered for use in VTI.*

	<b>Physical quantities considered</b>	<b>Advantage</b>	<b>Disadvantage</b>
Guérin	Maximum ballast displacement	Direct output from VTI models	Maximum displacement cannot be directly related to plastic deformation of ballast under varying conditions
Sato	Maximum ballast pressure Maximum bearer acceleration	Derived output from VTI models and also considering a threshold pressure	Given equation and factors cannot be directly applied to settlement as it has been derived for track quality. Only the more simplistic form using the ballast pressure [114] can be directly used for calculating settlement.
Fröhling	Dynamic wheel load w.r.t nominal	Derived output from VTI models, considering a threshold value	A number of factors are used which are difficult to calibrate for different cases analysed and track configuration, in particular the way the load is distributed from the contact level to the ballast level.

## **4 Statistical analysis of crossing failures**

In this Chapter, a summary of the statistical analysis of the most common turnout failure at rail level is presented. The full analysis can be found in Grossoni [5]. It is worth noting that in addition to the frequency of occurrence of different damage types, as considered here, it is also important to consider the impact of the different damage mechanisms in terms of the maintenance time, cost and availability (delays), but these are out of the scope of the present work.

First, the type and format of data analysed is described in Section 4.1. The classification of failure types based on Rail Defect Management System (RDMS) data codes for only the crossing panel is discussed in detail in Section 4.2. The main recommendations for future research on crossings are listed in Section 4.4.

### **4.1 Data analysed**

Seven years of GB network Rail Defect Management System (RDMS) data from 2011 to 2017 has been evaluated. Each failure included in the database has been reported detailing the location (route and site name), the rail type (i.e. left/right rail, S&C panel), the assembly type, the track category and track code, the rail profile, the steel grade, etc... A three digit code is used describe the location. The failures occurring at the switch panel are labelled with 500's codes and the failures occurring at crossing panel with 700's codes. Regarding the failures occurring at both panels, 100's codes refers to failures at rail ends, 200's codes to mid-rail damages, 400's codes to failures at welds and welding repairs, 600's codes to failures at machined rails.

Additional information is included in a comments section of the database in free-text data format. Manual analysis of these records would be time prohibitive and therefore a novel automated text analysis technique has been used to assess this information (Hughes [115]). The main purpose of this exercise was to identify correlations between the occurrence of key terms in the free text with structured and numerical data. A bottom-up search has been performed based on an ontology of terms and synonyms developed in accordance with earlier analysis (see Appendix D).

## 4.2 Classification of the failure types

The occurrence percentage of the 22 most common degradation mechanisms occurring at S&Cs according to the GB network data between 2011 and 2017 is presented in Table 4.1.

*Table 4.1: The 22 most common degradation mechanisms registered at S&Cs in the GB network from 2011 to 2017.*

Defect description	Occurrence in switch panel [%]	Occurrence in crossing panel [%]	Occurrence in both panels [%]
Switch blade damage	20%	-	-
Squat on a casting	-	13%	-
Misshapen nose or wear/damage in wheel transfer area >3mm deep	-	8%	-
Stock rail and switch blade both sidworn	7%	-	-
Lipping on crossing	-	7%	-
Lipping	-	-	5%
Flaking or Shelling of the wheel contact surface	-	5%	-
Squat	-	-	4%
Rail head deformation	-	-	4%
Lipping on reduced section rail	-	-	3%
Crossing nose wear	-	3%	-
Sidworn stock rail associated with a little-used switch blade	2%	-	-
Transverse defect from RCF	-	-	2%
Metal Breaking out in the wheel transfer area	-	2%	-
Switch blade with a sharp gauge corner profile	1%	-	-
503 - Stock rail headwear associated with a less headworn switch blade	1%	-	-
Transverse cracking of casting - crossing vee	-	1%	-
Transverse defect from RCF in a casting	-	1%	-
Flash butt weld at stainless steel insert	-	1%	-
Unstable rail	-	-	1%
Vertical transverse cracking of the foot in a casting	-	1%	-
Progressive transverse crack (tache ovale)	-	-	1%

Table 4.1 shows the weakest point of S&C is the switch blade. The number of damage failures is ca. 1/5<sup>th</sup> of all the registered failures during the seven years considered. This is expected as the switch blade is characterised by a reduced section as it needs to be moved

laterally to correctly direct the train. High dynamic forces, and thus contact stresses, are applied in a very short time frame to this structurally already weak part of the track contributing to develop damage.

The crossing panel accounts for the highest cumulative number of failures, reaching almost half of the total failures, followed by the switch panel (up to 1/3<sup>rd</sup> of the total failures).

Within the codes referring to both panels, it is difficult to distinguish within failures occurring at the switch panel or crossing panel. Thus, an additional analysis has been performed as follows. On the basis of rail profile type in the RDMS database (Table 4.2), it has been possible to reassign to the relevant category of reported failures (i.e. 79% for codes 100s, 73% for codes 200s, 69% for codes 400s and 15% for codes 600s, respectively).

Table 4.2: Division between switch and crossing panel based on rail profile type.

Switch panel	Crossing panel	Others
Adjustment switch	Casting apron	CWR
LH Lead rail	Casting check rail	Jointed
LH Stock rail	Casting leg end	Tri-metal zone
LH Switch rail	Casting nose	
RH Lead rail	Casting point rail	
RH Stock rail	Casting wing rail	
RH Switch rail	Nose in fabricated crossing	
Switch Diamond LH Switch rail	Point rail in fabricated crossing	
Switch Diamond RH Switch rail	Splice rail in fabricated crossing	
	Switch Diamond LH Wing rail	
	Switch Diamond RH Wing rail	
	Vee rail	
	Wing rail	
	Leg end	

The remaining percentage per each code category has been evaluated using the free-text analysis methodology mentioned in Section 4.1.

Eventually, the percentage S&C failure occurrence at each panel are reported in Table 4.3.



*Design methodology for track systems considering the long-term ballast behaviour:  
application to crossings*

Table 4.3: Percentage S&C failure occurrence at each panel using only the database or using database and word analysis.

	Database	Database and word analysis
Switch panel	32%	43%
Crossing panel	42%	53%
Other	26%	4%

### 4.3 Damages occurring only at crossing panel

The occurrence percentage of the most common degradation mechanisms occurring at the crossing panel according to the GB network data between 2011 and 2017 is presented in Figure 4.1.

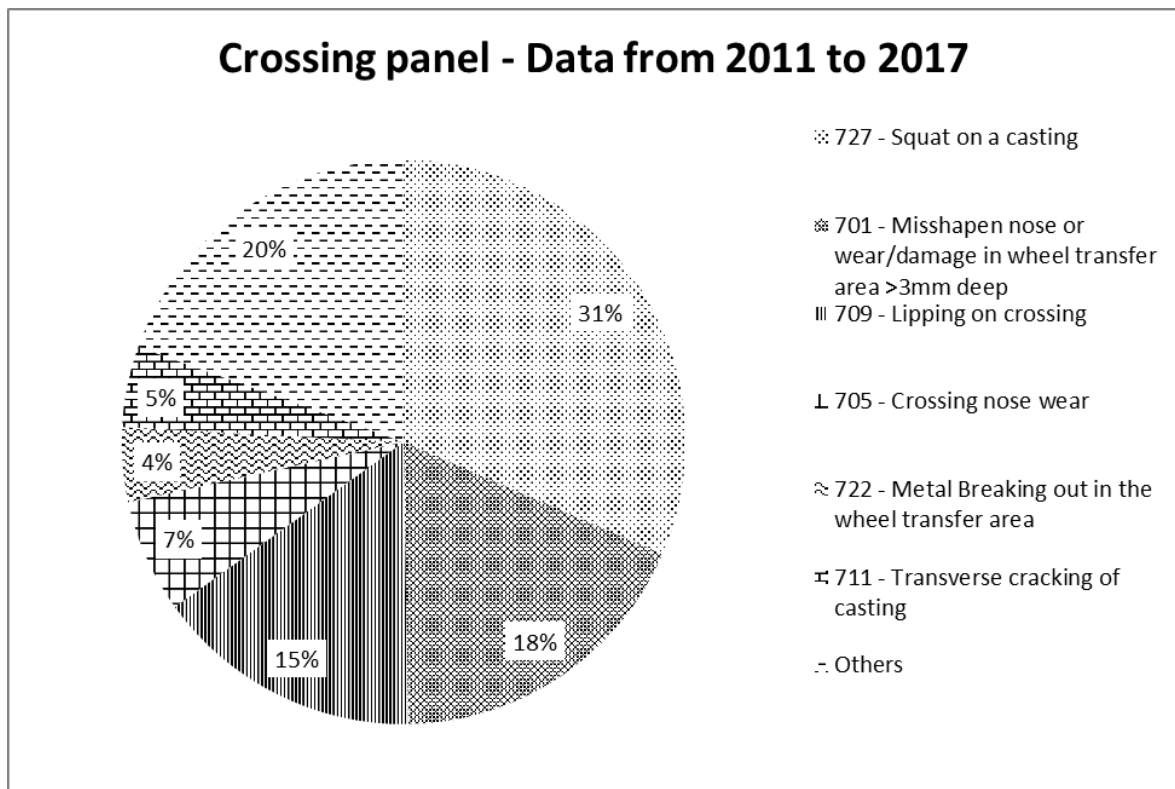


Figure 4.1: Degradation mechanisms at the crossing panel in the GB network from 2011 to 2017.

Although the database shown in Figure 4.1 suggests 19 types of failures within the crossing panel, 80% of the failures are accounted for by just six failure types.

The most common cause of failure at the crossing panel is squat on a casting, and is ca. 1/3<sup>rd</sup> of all the failures, and the second largest defect category (Figure 4.1). The data analysis and the text analysis has shown that the most common occurring location is the nose (i.e. 46% of the total occurrence), followed by the leg end (i.e. 10%) and the wing rail (i.e.

10%), while in the 34% of cases it is not possible to identify a location. Although high contact stresses resulting from wheel-crossing contact is the primary source of degradation, especially at the vertical impact area of the nose area, the severity of these stresses is amplified by non-optimal profiles, incorrect installation and insufficient maintenance. They can be further exacerbated by the presence of sub-surface flaws that are more prevalent in castings compared to rolled rails used in fabricated crossings. This is confirmed by the data analysis which shows that 41% of the squat failures occur in cast crossing, 4% in fabricated crossing, while 55% is not stated. Unfortunately, the text analysis did not add any information. Even if the material aspects are usually acknowledged as crucial, it is believed that the major contribution toward the occurrence reduction would come from a reduction in the wheel-rail impact loading optimising the contact geometry as well as the trackbed stiffness.

RCF mechanisms, such as squats and shelling, represent half of all the failure occurrences, while plastic deformation one third and wear mechanisms one quarter. Regarding the plastic deformation defects, it would be relevant to better understand the dependence on yield strength of materials, looking for instance to the metallographic assessment of the plastic flow at different key crossing sections.

The transversal cracking of casting is caused by the exceedance of total stress over the material yield threshold and usually occurs in the proximity of stress raisers, such as tri-metallic welds, near the wheel-rail impact location within the wheel transfer area or the wing rail. Its occurrence is about 5% of all the failure mechanisms (i.e. 2.6% occurring at the casting vee, 1% at the wing rail, 0.6% at the leg end and 0.4% elsewhere). Nevertheless, this failure mode represents one of the most expensive ones. Once it is cracked it needs to be immediately substituted as it is not possible to weld repair it if it is made of cast manganese or if the cracks are not superficial.

## **4.4 Recommendation**

The following recommendations for future research based on the failure analysis are proposed.

High contact stresses resulting from wheel-crossing contact is the primary source of degradation, the severity of these stresses is amplified by non-optimal profiles, incorrect

installation and insufficient maintenance. They can be further exacerbated by the presence of sub-surface flaws that are more prevalent in castings compared to rolled rails used in fabricated crossings.

The material aspects are usually acknowledged as crucial. Nevertheless, it is believed that the major contribution toward the reduction of squats occurrence (31% of all the crossing panel failures) would come from a reduction in the wheel-rail impact loading optimising the contact geometry as well as the trackbed stiffness.

Regarding the plastic deformation defects (ca. 1/3 of all the crossing panel failures), it is suggested to understand better the dependence on yield strength of materials, looking to the metallographic assessment of the plastic flow at different key crossing locations.

Even if the transversal cracking of casting, which is caused by the exceedance of total stress over the material yield threshold, has a low occurrence rate (about 5% of all the failure mechanisms), this failure mode represents one of the most expensive ones. Once it is cracked it needs to be immediately substituted as it is not possible to weld repair it if it is in cast manganese or if the cracks are not superficial.

Finally, it has been seen that there is a high proportion of failure modes that are classified with codes referring to both panels. Thus, it is difficult to distinguish between switch and crossing. Therefore, it would be beneficial to change the reporting methodology introducing, for example, illustrative examples and a tick list leading the operator to the correct classification.

#### **4.4.1 Impact of the results on the present research**

The analysis carried out has shown that the damages at the rail level can be caused and/or exacerbated by damage at the support level, especially squats and transversal cracking of the casting. The first one represents ca. 1/3<sup>rd</sup> of all the crossing panel failures and the second largest defect category for all the failures reported. The occurrence of the second one, on the contrary, is very low (i.e. 5%), however it is a very expensive failure type as the crossing needs urgent replacement. Therefore, it is clear that considering and correctly representing the degradation at the support level in a crossing panel is a key aspect during the design process and the present study goes in this direction.

## 5 Vehicle-track interaction model

This Chapter presents the vehicle-track interaction model that will be used in the optimisation process. The track model and its assumptions are presented in Section 5.1 and the vehicle model in Section 5.2. The vertical and the lateral contact models coupling the vehicle and the track are analysed in Section 5.3. Some early results in terms of wheel-rail contact geometry and forces are discussed in detail in Section 5.4. Finally, an early validation against the commercial software VI-Rail is shown in Section 5.5.

### 5.1 Modelling the track system

An example of three-dimensional track system model is shown in Figure 5.1. Note that this is just one possible configuration, as other arrangements have been considered, including presence of baseplates and ballast masses.

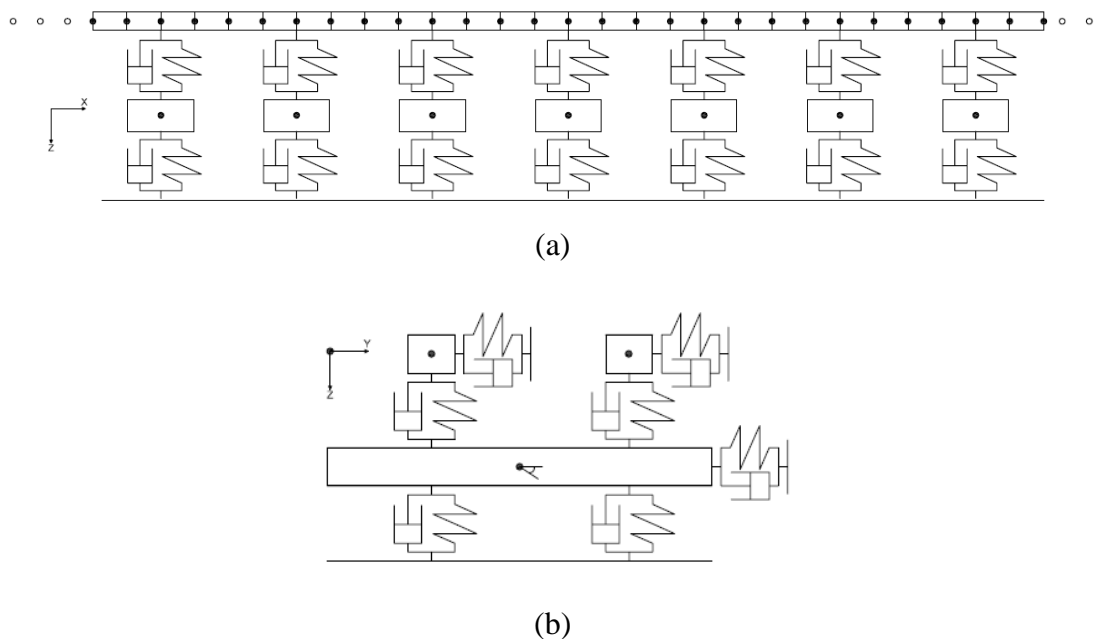


Figure 5.1: Track model in the (a)  $x-z$  plane and in the (b)  $y-z$  plane.

#### 5.1.1 Fundamental assumptions

The main assumptions are listed as following:

- i. The track is modelled as a three-dimensional discretely supported ballasted track system, including the rail-pad and the bearer trackbed resilient layers.

*Design methodology for track systems considering the long-term ballast behaviour:  
application to crossings*

This type of model is necessary when a crossing panel is considered due to the non-symmetrical geometrical properties (e.g. rail mass and inertia, geometry configuration) as well as non-symmetrical dynamic loading;

- ii. The rails are represented as three-dimensional beams with finite length. A FE model is developed approximating the displacement within an element through nodal values of displacements (i.e. vertical and lateral displacement) and rotations (i.e. rotation around the y- and z-axis). The rotation around the x-axis (i.e. torsion) has been omitted as the main focus of this work is the vertical settlement and, thus, the vertical motion of the track. Further validation of this modelling choice should be considered in the future. The Timoshenko beam theory is assumed valid for this study to capture the rail response to vertical excitation frequencies above 500 Hz [24]. In order to obtain accurate results and capture correctly the abrupt change in the geometrical properties, four beam elements are considered within each bearer-spacing. This is a trade-off between required precision (see Shih [116]) and low computational cost;
- iii. The bearers are modelled as rigid bodies;
- iv. The formation stiffness is neglected as the foundation is assumed rigid. Thus, the lower layer includes the resilience of the ballast layer considering its depth as well as its quality.

The positive axis system is shown in Figure 5.2. The vertical displacement is considered positive downward, the lateral displacement positive to the right of the direction of the travel, and the longitudinal displacement in the forward direction. The rotations are taken according to the right-hand rule.

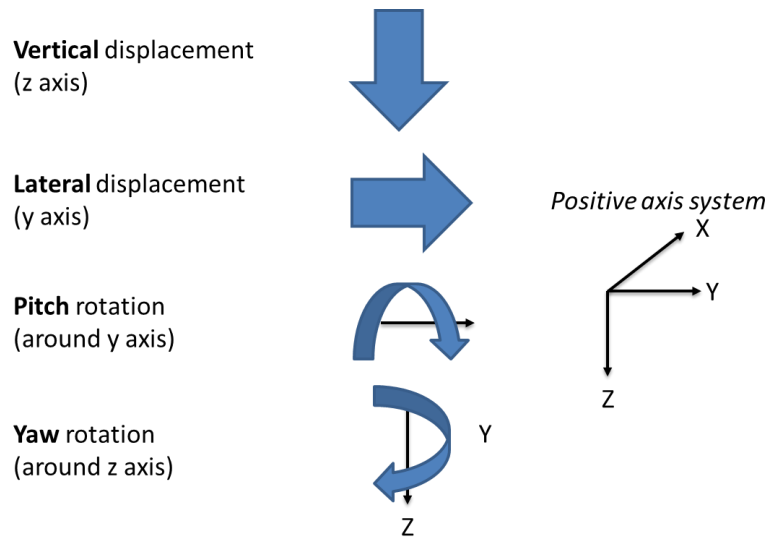


Figure 5.2: Positive axis system.

### 5.1.2 Track model

#### *FE model of rail with discrete support*

Each rail can be modelled as a periodic structure consisting of equally sized elements, connected end-to-end to form the entire structure. In order to simplify the problem, firstly only one element is considered and then the procedure is easily generalized.

The generic  $i$ -th element is shown in Figure 5.3.

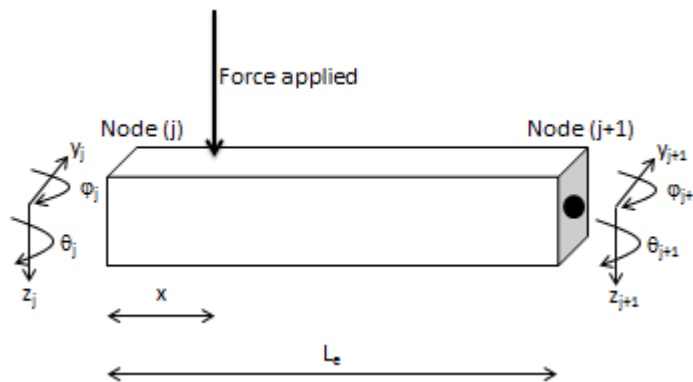


Figure 5.3: Generic beam element

Each element is modelled using two nodes  $j$  and  $j+1$  at both ends of the element and four DOFs per each node, which are vertical  $z_j$  and lateral  $y_j$  displacement and rotation around the  $z$  axis  $\theta_j$  and around the  $y$  axis  $\phi_j$ . Hence, each element has got eight DOFs:

*Design methodology for track systems considering the long-term ballast behaviour:  
application to crossings*

$$\{y_i\}^e = \begin{Bmatrix} z_j \\ y_j \\ \varphi_j \\ \theta_j \\ z_{j+1} \\ y_{j+1} \\ \varphi_{j+1} \\ \theta_{j+1} \end{Bmatrix} \quad 5.1$$

The deformation of the beam is approximated within an element using the nodal values of displacement and rotation. Thus, the rail displacement  $y_{ri}(x)$  at the generic point  $x$  can be written as follows:

$$y_{ri}(x) = [N] \cdot \{y_i\}^e \quad 5.2$$

Where:

[N] = the shape function vector:

$$[N] = [N_1 N_2 N_3 N_4]^T \quad 5.3$$

In this study, the third order Hermitian interpolation is used. The Hermitian polynomial is a  $2n+1$  degree polynomial  $p_{2n+1}(x_i)$  which is built using  $n+1$  distinct points  $x_i$  ( $i=0,1,\dots,n$ ) and satisfies the  $2n+1$  conditions:

$$\begin{aligned} p_{2n+1}(x_i) &= f(x_i) \\ p'_{2n+1}(x_i) &= f'(x_i) \end{aligned} \quad 5.4$$

Where:

$f(x_i)$  = the fitting polynomial.

In the case of beam elements, the shape vector can be expressed as (Figure 5.4):

$$\begin{aligned} N_1 &= 1 - 3\left(\frac{x}{L_e}\right)^2 + 2\left(\frac{x}{L_e}\right)^3 \\ N_2 &= L_e \cdot \left[ \left(\frac{x}{L_e}\right) - 2\left(\frac{x}{L_e}\right)^2 + \left(\frac{x}{L_e}\right)^3 \right] \\ N_3 &= \left(\frac{x}{L_e}\right)^2 \cdot \left[ 3 - 2\left(\frac{x}{L_e}\right) \right] \\ N_4 &= -L_e \cdot \left[ \left(\frac{x}{L_e}\right)^2 + L_e \cdot \left(\frac{x}{L_e}\right)^3 \right] \end{aligned} \quad 5.5$$

Where:

$(x/L_e)$  = relative longitudinal position of the generic point  $x$ ;

$L_e$  = element length [m].

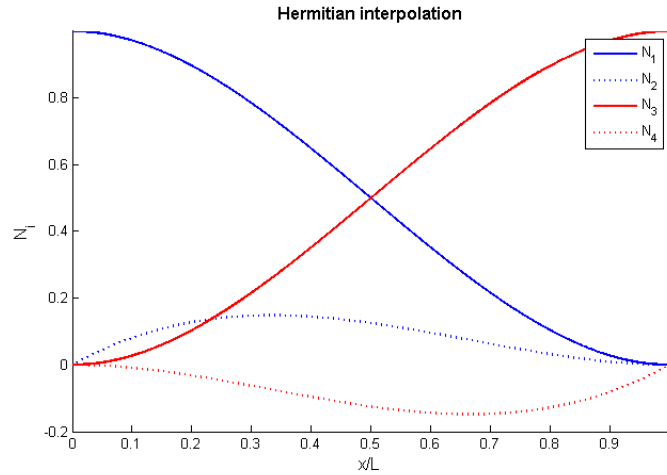


Figure 5.4: Hermitian interpolation.

Thus, it is clear that at the start node, in which  $x/L_e$  is equal to 0, the shape vector  $[N]$  becomes:

$$[N]_{x=0} = [1 \ 0 \ 0 \ 0]^T \quad 5.6$$

Whereas at the final node, in which  $x/L_e$  is equal to 1, it becomes:

$$[N]_{x=L} = [0 \ 0 \ 1 \ 0]^T \quad 5.7$$

- **Rail mass matrix**

The rail mass matrix  $[M]_{rail}$  can be divided in two main blocks, referring to the left rail and the right rail respectively:

$$[M]_{rail} = \begin{bmatrix} [M_{rail,l}] & [0] \\ [0] & [M_{rail,r}] \end{bmatrix} \quad 5.8$$

Where:

$[M_{rail,l}]$  = mass matrix for the left rail (dimension:  $4n_r \times 4n_r$ );

$[M_{rail,r}]$  = mass matrix for the right rail (dimension:  $4n_r \times 4n_r$ );

$n_r$  = number of rail nodes.

The analytical formulation of each block can be found in Wu [117].



The other blocks are equal to zero as there is no interaction between the two rails at this level.

- **Rail stiffness matrix**

The rail stiffness matrix  $[K]_{rail}$  can be divided in two main blocks, referring to the left rail and the right rail respectively:

$$[K]_{rail} = \begin{bmatrix} [K_{rail,l}] + [K_{rp,l}] & [0] \\ [0] & [K_{rail,r}] + [K_{rp,r}] \end{bmatrix} \quad 5.9$$

Where:

$[K_{rail,l}]$ ,  $[K_{rail,r}]$  = stiffness matrix for the left and right rail (dimension:  $4n_r \times 4n_r$ );

$[K_{rp,l}]$ ,  $[K_{rp,r}]$  = stiffness matrix for the left and right rail due to the rail-pad layer (dimension:  $4n_r \times 4n_r$ ).

The analytical formulation of the stiffness matrix for the left and right rail can be found in Wu [117].

Regarding the stiffness matrix for the left and right rail due to the rail-pad layer, they are expressed as:

$$[K_{rp,l}] = \begin{bmatrix} k_{r,v} & 0 & 0 & 0 & 0 & 0 & 0 \\ 0 & k_{r,l} & 0 & 0 & 0 & 0 & 0 \\ 0 & 0 & \ddots & 0 & 0 & 0 & 0 \\ 0 & 0 & 0 & k_{r,v} & 0 & 0 & 0 \\ 0 & 0 & 0 & 0 & k_{r,l} & 0 & 0 \\ 0 & 0 & 0 & 0 & 0 & 0 & 0 \\ 0 & 0 & 0 & 0 & 0 & 0 & 0 \end{bmatrix} \quad 5.10$$

Where:

$k_{r,v}$ ,  $k_{r,l}$  = vertical and lateral rail-pad stiffness [N/m].

Note that the rotational stiffness is neglected because the rail-pad has been considered as a point connection.

- **Rail damping matrix**

Similarly to the stiffness matrix, the rail damping matrix  $[C]_{rail}$  can be divided in two main blocks, referring to the left rail and the right rail respectively:

$$[C]_{rail} = \begin{bmatrix} [C_{rail,l}] + [C_{rp,l}] & [0] \\ [0] & [C_{rail,r}] + [C_{rp,r}] \end{bmatrix} \quad 5.11$$

Where:

$[C_{rail,l}]$ ,  $[C_{rail,r}]$  = damping matrix for the left and right rail (dimension:  $4n_r \times 4n_r$ );

$[C_{rp,l}]$ ,  $[C_{rp,r}]$  = damping matrix for the left and right rail due to the rail-pad layer (dimension:  $4n_r \times 4n_r$ ).

Assuming Rayleigh damping for the rail structure, the damping matrix can be calculated as:

$$[C_{rail,l}] = \alpha_{rd}[M_{rail,l}] + \beta_{rd}[K_{rail,l}] \quad 5.12$$

Where:

$\alpha_{rd}$ ,  $\beta_{rd}$  = Rayleigh damping coefficients [Ns/(kg·m)], [N/(kg·m)].

In particular, the coefficients can be determined specifying the damping ratios  $\zeta_i$  and  $\zeta_j$  for the  $i$ -th and  $j$ -th mode, respectively [118]:

$$\frac{1}{2} \begin{bmatrix} \frac{1}{\omega_i} & \omega_i \\ \frac{1}{\omega_j} & \omega_j \end{bmatrix} \begin{Bmatrix} \alpha_{rd} \\ \beta_{rd} \end{Bmatrix} = \begin{Bmatrix} \zeta_i \\ \zeta_j \end{Bmatrix} \quad 5.13$$

Regarding the damping matrix for the left and right rail due to the rail-pad layer, they are a can be expressed as:

$$[C_{rp,l}] = \begin{bmatrix} c_{r,v} & 0 & 0 & 0 & 0 & 0 & 0 \\ 0 & c_{r,l} & 0 & 0 & 0 & 0 & 0 \\ 0 & 0 & \ddots & 0 & 0 & 0 & 0 \\ 0 & 0 & 0 & c_{r,v} & 0 & 0 & 0 \\ 0 & 0 & 0 & 0 & c_{r,l} & 0 & 0 \\ 0 & 0 & 0 & 0 & 0 & 0 & 0 \\ 0 & 0 & 0 & 0 & 0 & 0 & 0 \end{bmatrix} \quad 5.14$$

Where:

$c_{r,v}$ ,  $c_{r,l}$  = vertical and lateral rail-pad damping [Ns/m].

### ***Crossing geometry***

The methodology described in the present Section has been developed by the Institute of Railway Research within the European FP7 Project Capacity4Rail [119].

*Design methodology for track systems considering the long-term ballast behaviour:  
application to crossings*

The three-dimensional geometry of the crossing is modelled using SOLIDWORKS [120]. The model is created based on an initial solid block and then all the geometrical operations are defined sequentially by adopting a similar methodology to that used in the machining process.

The 2D cross sections are imported to MATLAB and are further pre-processed to obtain the final geometry. The geometrical properties, including area and second moment of area, have been finally calculated per each cross section.

***Bearer model***

In this study, the bearers are modelled as rigid bodies with 3 DOFs: vertical  $z_s$  and lateral  $y_s$  displacement and roll rotation  $\varphi_s$ . Hence, the bearer vector can be written as follows:

$$\{y\}^s = \begin{Bmatrix} z_s \\ y_s \\ \varphi_s \end{Bmatrix} \quad 5.15$$

The equations governing the vertical, lateral and roll motions of each bearers are developed starting with the equilibrium conditions:

- Vertical direction

$$m_s \cdot \ddot{z}_s + k_{r,v} \cdot (z_s - z_j^l) + k_{r,v} \cdot (z_s - z_j^r) + 2k_{b,v} \cdot z_s + c_{r,v} \cdot (\dot{z}_s - \dot{z}_j^l) + c_{r,v} \cdot (\dot{z}_s - \dot{z}_j^r) + 2c_{b,v} \cdot \dot{z}_s = 0 \quad 5.16$$

Where:

$m_s$  = bearer mass [kg];

$\ddot{z}_s, \dot{z}_s, z_s$  = bearer vertical acceleration, velocity and displacement [m/s<sup>2</sup>], [m/s], [m];

$\dot{z}_j^l, z_j^l, \dot{z}_j^r, z_j^r$  = nodal vertical velocity and displacement for the left and right rail [m/s], [m], [m/s], [m];

$k_{r,v}$  = vertical rail-pad stiffness [N/m];

$k_{b,v}$  = vertical trackbed stiffness [N/m];

$c_{r,v}$  = vertical rail-pad damping [Ns/m];

$c_{b,v}$  = vertical support damping [Ns/m].

- Lateral direction

$$m_s \cdot \ddot{y}_s + k_{r,l} \cdot (y_s - y_j^l) + k_{r,l} \cdot (y_s - y_j^r) + 2k_{b,l} \cdot y_s + c_{r,l} \cdot (\dot{y}_s - \dot{y}_j^l) + c_{r,l} \cdot (\dot{y}_s - \dot{y}_j^r) + 2c_{b,l} \cdot \dot{y}_s = 0 \quad 5.17$$

Where:

$m_s$  = bearer mass [kg];

$\ddot{y}_s, \dot{y}_s, y_s$  = bearer lateral acceleration, velocity and displacement [m/s<sup>2</sup>], [m/s], [m];

$\dot{y}_j^l, y_j^l, \dot{y}_j^r, y_j^r$  = nodal lateral velocity and displacement for the left and right rail [m/s], [m], [m/s], [m];

$k_{r,l}$  = lateral rail-pad stiffness [N/m];

$k_{b,l}$  = lateral trackbed stiffness [N/m];

$c_{r,l}$  = lateral rail-pad damping [Ns/m];

$c_{b,l}$  = lateral trackbed damping [Ns/m].

- Roll rotation

$$I_s \cdot \ddot{\phi}_s + k_{r,v} \cdot \left( \phi_s \cdot \frac{l_g}{2} - z_j^l \right) \cdot \frac{l_g}{2} + k_{r,v} \cdot \left( \phi_s \cdot \frac{l_g}{2} - z_j^r \right) \cdot \frac{l_g}{2} + c_{r,v} \cdot \left( \dot{\phi}_s \cdot \frac{l_g}{2} - \dot{z}_j^l \right) \cdot \frac{l_g}{2} + c_{r,v} \cdot \left( \dot{\phi}_s \cdot \frac{l_g}{2} - \dot{z}_j^r \right) \cdot \frac{l_g}{2} = 0 \quad 5.18$$

Where:

$I_s$  = bearer roll inertia [kg·m];

$\ddot{\phi}_s, \dot{\phi}_s, \phi_s$  = bearer roll acceleration, velocity and rotation [rad/s<sup>2</sup>], [rad/s], [rad];

$\dot{z}_j^l, z_j^l, \dot{z}_j^r, z_j^r$  = nodal vertical velocity and displacement for the left and right rail [m/s], [m], [m/s], [m];

$l_g$  = gauge [m];

$k_{r,v}$  = vertical rail-pad stiffness [N/m];

$c_{r,v}$  = vertical rail-pad damping [Ns/m].

### **Track model**

*Design methodology for track systems considering the long-term ballast behaviour:  
application to crossings*

The mass, damping and stiffness matrices of the track system are developed consequently including the matrices of the rail and the matrices of the bearers:

- **Track mass matrix**

$$[M]_T = \begin{bmatrix} [M]_{rail} & [0] \\ [0] & [M]_{sleeper} \end{bmatrix} \quad 5.19$$

Where:

$[M]_T$  = track mass matrix;

$[M]_{rail}$  = rail mass matrix;

$[M]_{bearer}$  = bearer mass matrix.

- **Track damping matrix**

$$[C]_T = \begin{bmatrix} [C]_{rail} & [C]_{r-s} \\ [C]_{s-r} & [C]_{sleeper} \end{bmatrix} \quad 5.20$$

$[C]_T$  = track damping matrix;

$[C]_{rail}$  = rail damping matrix;

$[C]_{bearer}$  = bearer damping matrix;

$[C]_{r-s}$  = rail-bearer damping matrix.

$[C]_{s-r}$  = bearer-rail damping matrix.

- **Track stiffness matrix**

$$[K]_T = \begin{bmatrix} [K]_{rail} & [K]_{r-s} \\ [K]_{s-r} & [K]_{sleeper} \end{bmatrix} \quad 5.21$$

$[K]_T$  = track stiffness matrix;

$[K]_{rail}$  = rail stiffness matrix;

$[K]_{bearer}$  = bearer stiffness matrix;

$[K]_{r-s}$  = bearer-rail stiffness matrix.

### **5.1.3 Validation of the track model**

The main scope of this investigation is to compare the model which has been

developed in the previous Sections and the FE model of the complete turnout currently used by Li [12] at Chalmers University in Sweden.

***Description of the present track model applied to a crossing panel***

Figure 5.5 shows the model described in Section 5.1.2 and adapted to a crossing application.

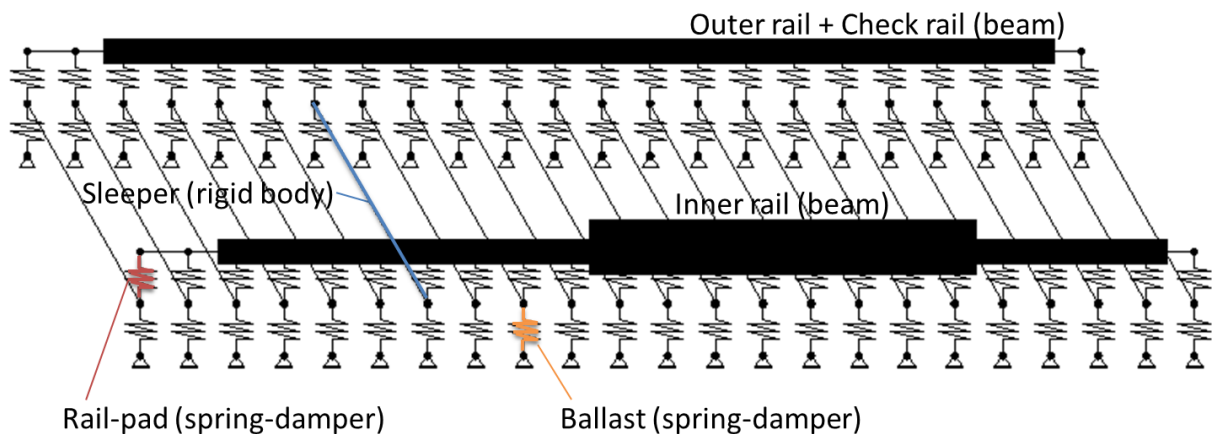


Figure 5.5: Present model (not in proportion).

The geometry considered in the current Section is a half cant CEN56 acute manganese cast centre block (CCB) crossing with a 1 in  $9^{1/4}$  crossing angle. “Half cant” refers to the flat surface of the wing rail cross section half way through its width, while “full cant” refers to 1 in 20 inclined surface across the entire rail width. A direct fixing to concrete bearers is modelled since it is common practice for CEN56 crossing type. Note that the varying bending properties of the crossing have been captured using the Cad drawings of a number of cross sections and then interpolated between the given positions.

Note that the check rail has been modelled as part of the left running rail, modifying locally the section properties.

***Description of the Chalmers track model***

A representation of the Chalmers track model is shown in Figure 5.6.

*Design methodology for track systems considering the long-term ballast behaviour:  
application to crossings*

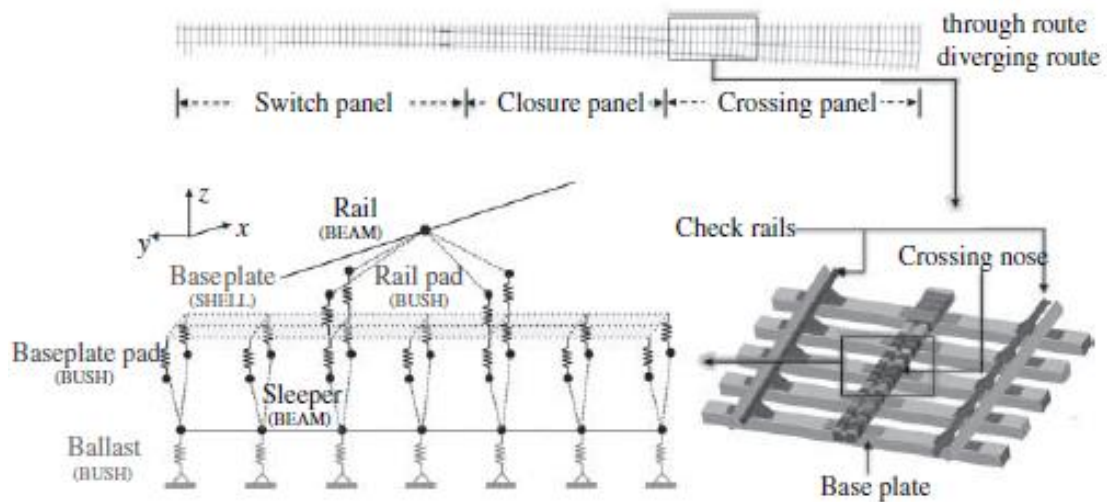


Figure 5.6: Chalmers FE model [12].

The FE model of a complete 60E1-760-1:15 turnout includes the switch panel, the closure panel and the crossing panel considering all the rails (stock rails, switch rails, closure rails, crossing nose, wing rails and check rails), rail pads, baseplates, baseplate pads and bearers laying on ballast. In particular, the rails and the bearers are modelled using beam elements and the remaining components are modelled using linear spring-dampers elements. Note that the parameter values are set in order to match the field measurements of bearer strains and wheel-rail contact forces in a turnout at Eslöv (Sweden).

The main input data used in the comparison are presented in Table 5.1.

Table 5.1: Main input parameters for the vehicle-track interaction model<sup>3</sup>

Parameter	Present model	Chalmers
Rail type	56E1	60E1
Crossing angle	1:13	1:15
Check rail type	CEN33C1	Not given
Bearer spacing	0.71 m	Not given
Rail-pad stiffness	Ref. [86]	Ref. [86]
Trackbed stiffness	150 KN/mm <sup>3</sup>	150 KN/mm <sup>3</sup>
Baseplate system	No	Yes

**Receptance at the crossing nose**

In the frequency domain, assuming stationary harmonic vibration, the equations of the vertical motion can be written as:

$$(-\omega^2[M] + i\omega[C] + [K])\hat{z}(\omega) = \hat{F}(\omega) \quad 5.22$$

Where:

$\omega$  = frequency of excitation [Hz] ( $\omega=2\pi f$ );

[M], [C], [K] = mass, damping, stiffness system matrices;

$\hat{z}(\omega)$  = amplitude of the complex-valued displacement [m];

$\hat{F}(\omega)$  = amplitude of the complex-valued input force [N].

Track receptance  $H(\omega)$  at frequency  $\omega$  is then calculated as:

$$H(\omega) = abs\left(\frac{\hat{z}(\omega)}{\hat{F}(\omega)}\right) = \frac{1}{(-\omega^2[M] + i\omega[C] + [K])} \quad 5.23$$

The results from the two models in terms of receptance of the inner rail (i.e. left side of the track) and outer rail (i.e. right side of the track) at the crossing nose are compared in Figure 5.7.

<sup>3</sup> The trackbed stiffness is converted to linear spring taking into account the actual sleeper area.



*Design methodology for track systems considering the long-term ballast behaviour:  
application to crossings*

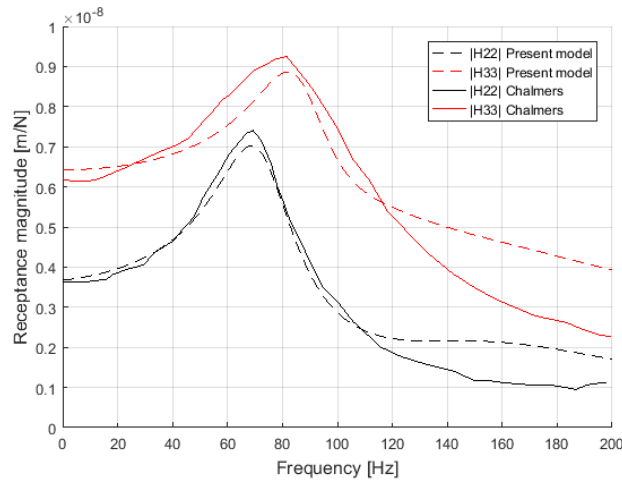


Figure 5.7: Receptance magnitude at the crossing nose for the Chalmers model and present model ( $|H_{22}|$ : direct receptance at the inner rail; ( $|H_{33}|$ : direct receptance at the outer rail).

Figure 5.7 shows a general good agreement of the results. The main differences are listed in Table 5.2.

Table 5.2: Main differences between the present model and Chalmers model.

	Present model	Chalmers	Difference [%]
Frequency at the 1 <sup>st</sup> peak – Inner rail [Hz]	70	69.35	0.9%
Frequency at the 1 <sup>st</sup> peak – Outer rail [Hz]	82.5	81.52	1.2%
Magnitude at the 1 <sup>st</sup> peak – Inner rail [ $10^{-9}$ m/N]	7.01	7.402	-5.3%
Magnitude at the 1 <sup>st</sup> peak – Outer rail [ $10^{-9}$ m/N]	8.872	9.251	-4.1%
Magnitude at 0 Hz – Inner rail [ $10^{-9}$ m/N]	3.693	3.631	1.7%
Magnitude at 0 Hz – Outer rail [ $10^{-9}$ m/N]	6.425	6.19	3.8%

The differences in terms of magnitude can be explained with the fact that the Chalmers model uses a heavier rail (60E1) than the one used in the present model (56E1). Also the use of baseplates shifts the resonance mode towards lower frequency due to an added mass and stiffness. Regarding the frequencies considered, a very good agreement has been reached.

***Static stiffness along the crossing panel***

The normalised static track stiffness has been evaluated for the complete crossing panel and the results are compared to Li [12] in Figure 5.8, where the reference shows the stiffness for the entire turnout.

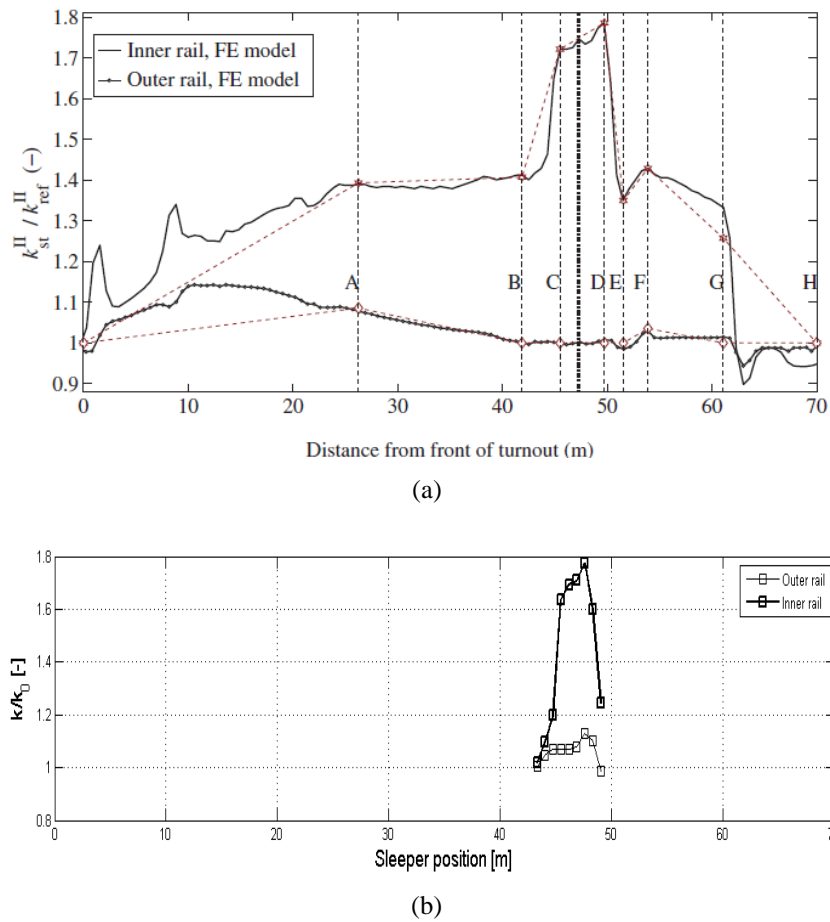


Figure 5.8: Normalised static track stiffness along through route of turnout for the (a) Chalmers model and (b) present model.

Also in this case it is possible to notice a good agreement between the two models. For example, at the crossing nose the normalised track stiffness for the inner rail is ca. 1.74 in the Chalmers model and ca. 1.7 in the present model, with a relative difference of 3%. Note that in the current model the normalisation has been done against the start of the crossing panel instead of against the switch toe position as in the Chalmers model. This is because the switch panel has not been considered in the present model. Thus, a slight vertical shift is expected.

The main difference between the two models is at the outer rail at the crossing panel, with a relative difference of ca. 6%. This discrepancy can be explained with the fact that in the present model the check rail is considered as an additional mass to the nominal profile and a different cross section is used to calculate inertial properties.

## 5.2 Modelling the vehicle

## 5.2.1 Fundamental assumptions

The fundamental assumptions are:

- A single axle with primary linear suspension stiffness and damping (lateral, vertical and yaw) is considered and the sprung mass is applied as external force;
- Vertical and lateral dynamic forces are considered in the model. The longitudinal forces (i.e. traction and braking forces) are neglected as the case of constant speed has been considered;
- The wheelset flexibility is neglected as the point of interest is the wheel-rail contact forces and the track behaviour;
- Five DOFs are considered per axle: vertical and lateral displacement, roll, pitch and yaw rotation.

## 5.2.2 Modelling the vehicle system

The vehicle-track interaction model considered in the present study is shown in Figure 5.9.

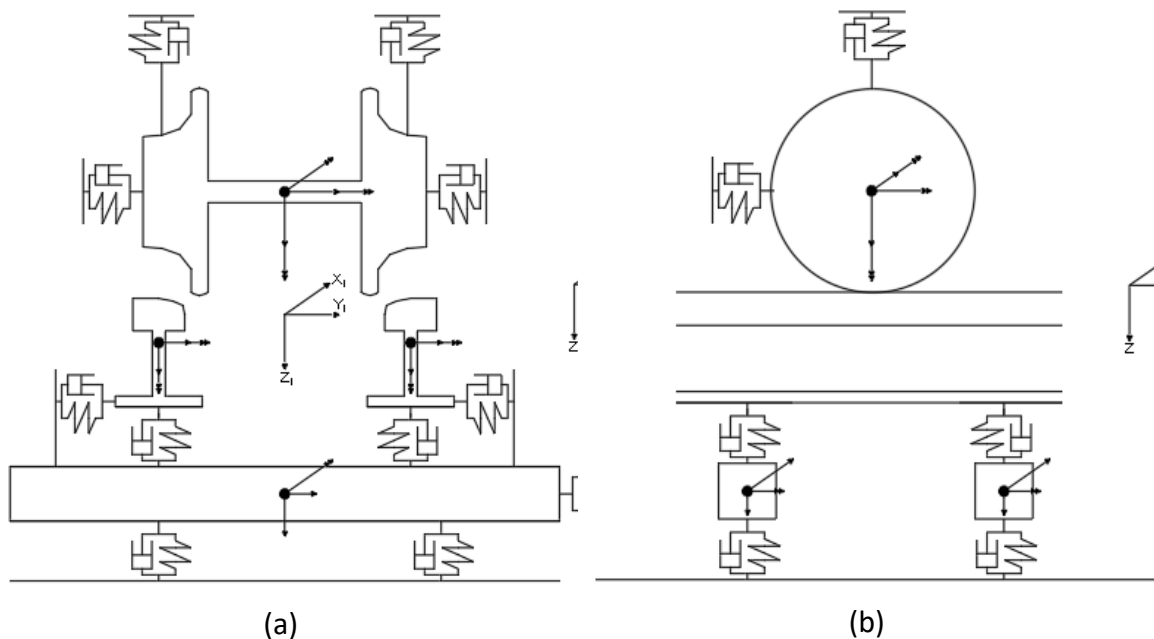


Figure 5.9: Vehicle-track interaction model considered ((a) y-z plane and (b) x-z plane).

The mass, damping and stiffness matrices of the system are:

$$[M]_v = \begin{bmatrix} M_w & 0 & 0 & 0 & 0 \\ 0 & M_w & 0 & 0 & 0 \\ 0 & 0 & J_{w,x} & 0 & 0 \\ 0 & 0 & 0 & J_{w,y} & 0 \\ 0 & 0 & 0 & 0 & J_{w,z} \end{bmatrix} \quad 5.24$$

Where:

$M_w$  = wheelset mass [kg];

$J_{w,x}, J_{w,y}, J_{w,z}$  = wheelset inertia around the x, y and z axis [kg·m].

$$[C]_v = \begin{bmatrix} 2C_{s1,z} & 0 & 0 & 0 & 0 \\ 0 & 2C_{s1,y} & 0 & 0 & 0 \\ 0 & 0 & 2C_{s1,z} \cdot d^2 & 0 & 0 \\ 0 & 0 & 0 & 0 & 0 \\ 0 & 0 & 0 & 0 & 2C_{s1,x} \cdot d^2 \end{bmatrix} \quad 5.25$$

Where:

$C_{s1,x}, C_{s1,y}, C_{s1,z}$  = damping constant of the primary suspension along the longitudinal, lateral, vertical direction [Ns/m];

$d$  = lateral span of the primary suspension system [m].

$$[K]_v = \begin{bmatrix} 2K_{s1,z} & 0 & 0 & 0 & 0 \\ 0 & 2K_{s1,y} & 0 & 0 & 0 \\ 0 & 0 & 2K_{s1,z} \cdot d^2 & 0 & 0 \\ 0 & 0 & 0 & 0 & 0 \\ 0 & 0 & 0 & 0 & 2K_{s1,x} \cdot d^2 \end{bmatrix} \quad 5.26$$

Where:

$K_{s1,x}, K_{s1,y}, K_{s1,z}$  = primary suspension stiffness along the longitudinal, lateral, vertical direction [Ns/m].

The external force vector is:

$$[F]_v = \begin{bmatrix} M_w \cdot g - F_{1,z} - F_{2,z} - N_{1,z} - N_{2,z} \\ -F_{1,y} - F_{2,y} - N_{1,y} - N_{2,y} \\ a_{w,1} \cdot (F_{1,z} + N_{1,z}) - a_{w,2} \cdot (F_{2,z} + N_{2,z}) - r_1 \cdot (F_{1,y} + N_{1,y}) - r_2 \cdot (F_{2,y} + N_{2,y}) \\ r_1 \cdot F_{1,x} + r_2 \cdot F_{2,x} + a_{w,1} \cdot \psi \cdot (F_{1,y} + N_{1,y}) + a_{w,2} \cdot \psi \cdot (F_{2,y} + N_{2,y}) + M_{1,y} + M_{2,y} \\ a_{w,1} \cdot (F_{1,x} + N_{1,x}) - a_{w,2} \cdot (F_{2,x} + N_{2,x}) + a_{w,1} \cdot \psi \cdot (F_{1,y} + N_{1,y}) - a_{w,2} \cdot \psi \cdot (F_{2,y} + N_{2,y}) + M_{1,z} + M_{2,z} \end{bmatrix} \quad 5.27$$

Where:

$M_w$  = wheelset mass [kg];

*Design methodology for track systems considering the long-term ballast behaviour:  
application to crossings*

$N_{i,x,y,z}$  = component of the normal force along the x,y,z direction for the  $i^{\text{th}}$  wheel ( $i=1,2$ ) [N];

$F_{i,x,y,z}$  = component of the creep force along the x,y,z direction for the  $i^{\text{th}}$  wheel ( $i=1,2$ ) [N];

$M_{i,y,z}$  = component of the creep moment along the y,z direction for the  $i^{\text{th}}$  wheel ( $i=1,2$ ) [Nm];

$a_{w,1}, a_{w,2}$  = distance of the left, right contact point from the wheelset centre of gravity [m];

$r_1, r_2$  = left, right rolling radius [m];

$\psi$  = wheelset yaw rotation [rad].

## **5.3 Modelling the vehicle-track interaction**

### **5.3.1 Fundamental assumptions**

The fundamental assumptions are:

- a. The contact problem is divided in two sub-problems: normal contact and tangential contact. The first is solved using non-linear Hertzian theory and the second using linear Kalker theory [60], corrected with Shen, Hedrick and Elkins theory [57];
- b. The irregularity is inherently represented by the motion of the wheel onto the crossing surface. Short wavelength corrugation of the order of 0-200 mm is neglected;
- c. For the calculation of Hertzian constant, the actual curvature of wheel and rail profiles are assumed constant in the area of contact;
- d. Material properties for standard steel are used for both wheel and rails;
- e. It is assumed that there is a single point of contact at each wheel.

The positive axis system for the vehicle sub-system is the same as that of the track sub-system (Figure 5.2).

The vehicle-track interaction model considered in the present study is shown in Figure 5.10.

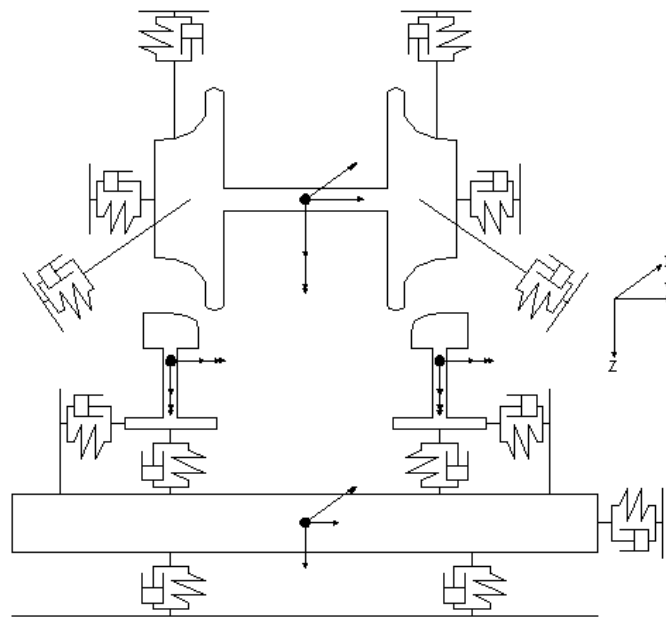


Figure 5.10: Vehicle-track interaction model considered ( $y$ - $z$  plane).

### 5.3.2 Contact model

#### *On-line approach*

Since the crossing panel is characterised by an abrupt change in geometry within few meters, it is sensible to adopt an online calculation, which consists on determining the wheel-rail contact data (e.g. example the contact point, penetration between wheel and rail, contact angle and rolling radius) at each integration time step. In this way, it is possible to avoid the interpolation between contact tables, which can easily cause remarkable errors when consecutive profiles with different width or rapidly varying contact conditions are considered.

It is necessary to highlight that in this study a two-dimensional search of the contact point is considered, neglecting the influence of wheelset yaw angle as only the through route is considered.

At each time step, the wheel and the piecewise cubically interpolated rail profiles are imported and placed in the correct position according to the respective coordinate system. The origin of the wheelset coordinate system is its centre of gravity, while the origin of the track coordinate system is the track centreline at the gauge height (i.e. 14 mm below the top of the rail) in order to bring a simplification to the calculations.

The rigid contact position is thus found searching for the minimum vertical wheel-rail

*Design methodology for track systems considering the long-term ballast behaviour:  
application to crossings*

distance. In the range of the possible contact point, both profiles are re-interpolated with a cubic spline function in order to achieve a better precision.

***Normal problem***

According to the non-linear Hertzian theory, the normal contact force can be expressed as:

$$P_z = \begin{cases} \left(\frac{\delta_{wr}}{K_H}\right)^{3/2} & \text{if } \delta_{wr} \geq 0 \\ 0 & \text{if } \delta_{wr} < 0 \end{cases} \quad 5.28$$

Where:

$\delta_{wr}$  = normal penetration between wheel and rail [m];

$K_H$  = Hertzian contact constant [(m/N)<sup>3/2</sup>].

The first equation refers to the case in which the bodies are in contact. Otherwise, when there is a jump, the contact force is set to zero.

It is worth underlining how the normal penetration is the normal distance between wheel and rail. Therefore, it may be different from the vertical distance. It is possible to express the vertical displacement of each contact point as function of the vertical wheelset displacement:

$$\delta_{wr,1} \cong \cos(\delta_1 + \varphi_w) \cdot (\Delta z_1 + \Delta R_{w,1} + \Delta z_{wr,1} - irr_1) \quad 5.29$$

$$\delta_{wr,2} \cong \cos(\delta_2 - \varphi_w) \cdot (\Delta z_2 + \Delta R_{w,2} + \Delta z_{wr,2} - irr_2) \quad 5.30$$

Where:

$\delta_1, \delta_2$  = left and right contact angle [rad];

$\varphi_w$  = wheelset roll angle [rad];

$\Delta z_1, \Delta z_2$  = left, right incremental wheel vertical position [m];

$\Delta R_{w,1}, \Delta R_{w,2}$  = left, right incremental rolling radius [m];

$\Delta z_{wr,1}, \Delta z_{wr,2}$  = left, right incremental wheel-rail vertical relative position [m];

$irr_1, irr_2$  = vertical irregularity at the left, right wheel [m].

***Tangential problem***

There are three components of creep forces: the longitudinal  $F_\xi$  and lateral  $F_\eta$  creep forces and the spin  $M_\varphi$  creep moment. They can be calculated integrating the tangential stresses in the contact area  $A_c$ :

$$F_\xi = \iint_{A_c} \tau_{x_c} dx_c dy_c \quad 5.31$$

$$F_\eta = \iint_{A_c} \tau_{y_c} dx_c dy_c \quad 5.32$$

$$M_\varphi = \iint_{A_c} (\tau_{y_c} dx_c - \tau_{x_c} dy_c) dx_c dy_c \quad 5.33$$

Assuming that the adhesion area covers the entire contact area, the three components of creep forces are calculated as following:

$$F_\xi = -f_{11}\gamma_1 \quad 5.34$$

$$F_\eta = -f_{22}\gamma_2 - f_{23}\omega_3 \quad 5.35$$

$$M_\varphi = f_{23}\gamma_2 - f_{33}\omega_3 \quad 5.36$$

Where:

$f_{11}, f_{22}, f_{23}, f_{33}$  = Kalker coefficients (Appendix C);

$\gamma_1, \gamma_2, \omega_3$  = longitudinal, lateral and spin creepages.

In particular, the creepage components can be expressed as function of the wheelset DOFs [121]:

$$\gamma_{1,i} = 1 \pm \frac{3.6a_{w,i}\dot{\psi}_w}{V} - \frac{r_i}{r_0} \pm \frac{a_{w,i}}{R} \quad i = 1,2 \quad 5.37$$

$$\gamma_{2,i} = \left( \frac{3.6\dot{\gamma}_w}{V} - \frac{r_i\psi_w}{r_0} \right) \sec(\delta_i \pm \varphi_w) \quad i = 1,2 \quad 5.38$$

$$\omega_{3,i} = \frac{\sin(\delta_i \pm \varphi_w)}{r_0} \pm \frac{3.6\dot{\psi}_w}{V} \quad i = 1,2 \quad 5.39$$

Where:

$a_{w,1}, a_{w,2}$  = distance of the left, right contact point from the wheelset centre of gravity [m];



*Design methodology for track systems considering the long-term ballast behaviour:  
application to crossings*

$\psi_w, \dot{\psi}_w$  = yaw rotation, velocity of the wheelset [rad], [rad/s];

$V$  = travelling speed [km/h];

$r_1, r_2$  = left, right rolling radius [m];

$r_0$  = nominal rolling radius [m];

$R$  = curve radius [m];

$\dot{y}_w$  = wheelset lateral velocity [m/s];

$\delta_1, \delta_2$  = left, right contact angle [rad].

Since the Coulomb's law can be violated in the case of large creepages, the correction proposed in Shen [57] is applied as follows:

$$\alpha_c = \begin{cases} \frac{\mu_a P_z}{F_R} \left[ \frac{F_R}{\mu_a P_z} - \frac{1}{3} \left( \frac{F_R}{\mu_a P_z} \right)^2 + \frac{1}{27} \left( \frac{F_R}{\mu_a P_z} \right)^3 \right] & \text{if } F_R \leq 3\mu_a P_z \\ \frac{\mu_a P_z}{F_R} & \text{if } F_R > 3\mu_a P_z \end{cases} \quad 5.40$$

Where:

$\mu_a$  = available friction coefficient;

$P_z$  = normal force [N];

$F_R$  = linear resultant creep force [N].

Finally, the creep forces are corrected:

$$F_\xi = \alpha_c F_\xi \quad 5.41$$

$$F_\eta = \alpha_c F_\eta \quad 5.42$$

$$M_\varphi = \alpha_c M_\varphi \quad 5.43$$

### 5.3.3 Numerical solution of the wheel/track interaction model

The dynamic interaction between the track system and the vehicle system is non-linear due to the geometrical effects of the contact. This is the reason why it is not possible to calculate directly the contact force between these systems.

In order to simplify the resolution of the vehicle-track coupling model, the whole structure is divided into two main sub-systems: the vehicle system and the track system.

Each sub-system is solved independently with an iterative scheme and the model is coupled through the contact force which involves also the track irregularities.

In this Section, the adopted iterative numerical calculation scheme is presented. It is worth underlining that this scheme leads to a very short computer simulation time because generally the convergence is reached after a limited number of iterations.

At each time step  $t+\Delta t$ , the following calculations at the generic  $k$ -th iteration are performed, assuming that the track displacement  $\{Y\}_t^t$ , velocity  $\{\dot{Y}\}_t^t$  and acceleration  $\{\ddot{Y}\}_t^t$  vectors and the vehicle displacement  $\{Y\}_t^v$ , velocity  $\{\dot{Y}\}_t^v$  and acceleration  $\{\ddot{Y}\}_t^v$  vectors at time step  $t$  are already known:

1. Initial computations:

- The position of the  $i$ -th contact point is calculated through the equation of linear motion with constant speed.
- The Hermitian interpolation function developed in Equation 5.5 is applied to calculate the rail displacement at the  $i$ -th contact point.
- The irregularity function is derived from the on-line contact calculation at each contact point.

2. Iterative process:

*a. First stage (calculation of the track system):*

- For the first iteration of each time step, it is assumed that the wheel and rail displacement at the  $i$ -th contact point are equal to the value of the previous time step.
- The normal contact force is calculated according to Equation 5.30.
- The tangential contact forces are then calculated according to Equation 5.43-45 in the local contact coordinate system and projected in the track coordinate system.

*Design methodology for track systems considering the long-term ballast behaviour:  
application to crossings*

- The total contact force is applied to the track system as external force and the response is calculated in terms of track displacement  $\{Y\}_{t+\Delta t}^t$ , velocity  $\{\dot{Y}\}_{t+\Delta t}^t$  and acceleration  $\{\ddot{Y}\}_{t+\Delta t}^t$  vectors through the Newmark Beta numerical integration method (Appendix D).
- The rail displacement values at each contact point are updated through the Hermitian interpolation function.

*b. Second stage (convergence):*

- The convergence of the solution is checked comparing the track displacement vector calculated at the current iteration and the track displacement vector calculated at the previous iteration within a specified tolerance. Usually, the tolerance value is assumed between  $10^{-5}$  and  $10^{-8}$ . In this model, the considered value is  $10^{-6}$ .
- If the convergence criterion is satisfied, the vectors calculated in the current iteration are equal to the vector at the current time step and it is possible to go to the next time step. Otherwise, it is necessary to continue the iteration process, which leads to the third stage.

*c. Third stage (calculation of the vehicle system):*

- The normal and tangential contact forces are updated according to the newly calculated rail displacement.
- The gravity force and the contact force are applied to the vehicle system and the response is calculated in terms of vehicle displacement  $\{Y\}_{t+\Delta t}^v$ , velocity  $\{\dot{Y}\}_{t+\Delta t}^v$  and acceleration  $\{\ddot{Y}\}_{t+\Delta t}^v$  vectors through the Newmark Beta numerical integration method.
- The wheel displacement values are updated.
- The k-th iteration is finished and the (k+1)-th iteration starts.

In order to summarize the above iterative method clearly, the flow chart of the resolution algorithm is presented in Figure 5.11.

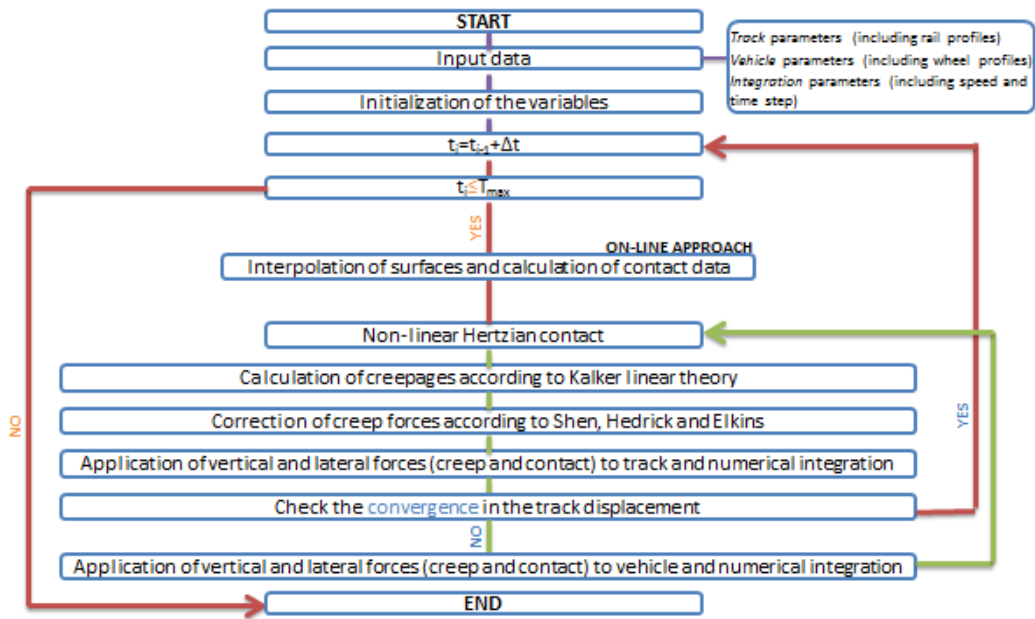


Figure 5.11: Flow chart of the resolution algorithm.

## 5.4 Simulation results

This Section presents the simulation results in terms of wheelset motion and contact geometry (Section 5.4.1) and wheel-rail contact forces (Section 5.4.2). Since the main focus is the contact algorithm, only for this purpose, the FE model developed in Section 5.1 has been replaced with a co-running track model whose characteristics do not have a physical meaning, but are chosen in order to match the frequency response of a complete layout.

In Table 5.3 the main properties of the track and the vehicle system are listed.

Table 5.3: Main parameters of the track and vehicle system.

	Parameter	Value	Units
Track	Rail type (plain line)	56E1	
	Rail type (crossing panel)	195	kg
	Bearer mass	500	kg
	Bearer roll inertia	128	kg·m
	Rail-pad vertical stiffness	150	kN/mm
	Rail-pad vertical damping	350	kNs/m
	Rail-pad lateral stiffness	400	kN/mm
	Rail-pad lateral damping	240	kNs/m
	Trackbed vertical stiffness	500	kN/mm
	Trackbed vertical damping	240	kNs/m
	Trackbed lateral stiffness	40	kN/mm
	Trackbed lateral damping	240	kNs/m
Vehicle	Wheel profile	P10 <sup>4</sup>	
	Wheelset mass	1500	kg

<sup>4</sup> This is a typical UK wheel profile.

*Design methodology for track systems considering the long-term ballast behaviour:  
application to crossings*

	Longitudinal primary suspension stiffness	1.8	kN/mm
	Lateral primary suspension stiffness	1.8	kN/mm
	Vertical primary suspension stiffness	10	kN/mm
	Static load	200	kN
	Travelling speed	80	km/h
	Initial lateral displacement	0	mm

Note that the crossing is placed on the right side and nominal 56E1 vertical rail profile is used for the left side.

### 5.4.1 Wheelset motions and contact geometry outputs

The wheelset vertical and lateral displacement and yaw rotation are presented in Figure 5.12.

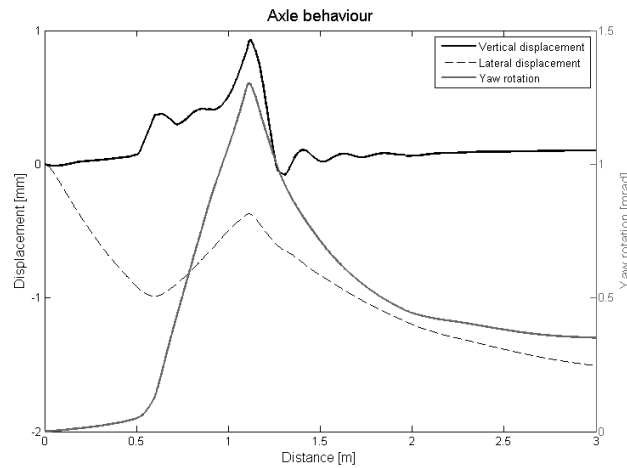


Figure 5.12: Wheelset outputs: vertical displacement (black line), lateral displacement (black dashed line) and yaw rotation (grey line).

The vertical displacement of the wheelset (Figure 5.12 black line) shows how the axle follows the vertical dip due to the crossing panel geometry. Note that positive vertical displacements occur when the wheelset is going downwards. After the wheel load transfer lowest point, which occurs at ca. 1.1 m, the axle tends to stabilise to a constant vertical position.

Regarding the lateral and yaw motions (Figure 5.12 black dashed and grey lines), the axle starts centrally aligned. Firstly, the right wheel moves onto the wing rail and this pushes the axle to the left (0 to 0.55 m) due to the change in the rolling radius difference (Figure 5.13) and, thus, creepage components. Then the wing rail moves away and the right wheel rolls onto a reduced radius, the axle then yaws towards the right (crossing) and the lateral displacement is reversed (0.55 to 1.1 m). After the load transfer location, the contact on the

right wheel suddenly moves towards the flange root and rolling radius is now larger than on the left. The axles yaw displacement returns towards being aligned and the axle lateral displacement is reversed to follow its original deviation to the left. When it reaches the end of the panel, the wheelset does not self-align. This can be explained with the fact that the transverse profile of the crossing is not the same as on the left side, as in shown in Figure 5.14. Therefore, the contact geometry characteristics are different, leading to non-centred steady-state position.

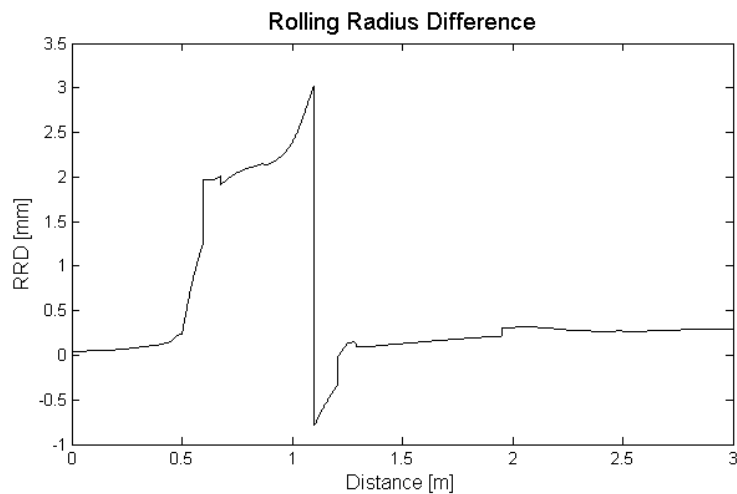


Figure 5.13: Rolling radius difference along the crossing panel.

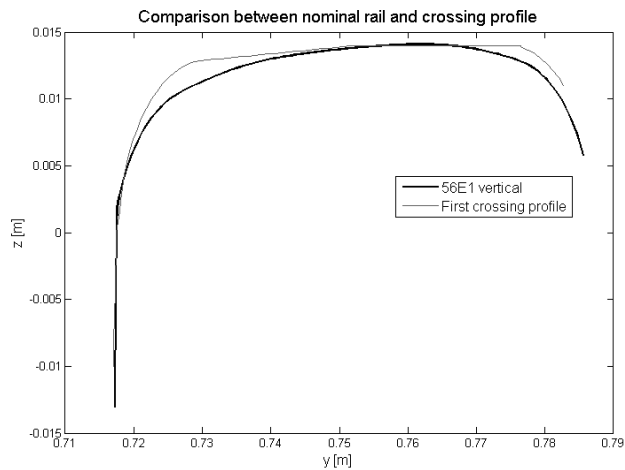
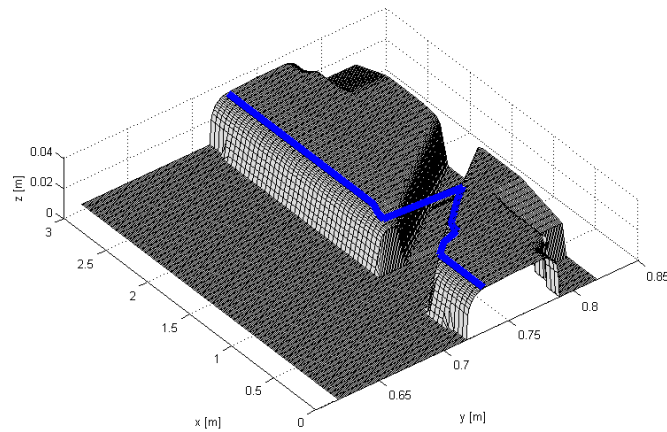


Figure 5.14: Comparison between nominal rail (black line) and initial crossing profile (grey line).

The three-dimensional contact point trajectory of the wheel negotiating the crossing panel is shown in Figure 5.15.

*Design methodology for track systems considering the long-term ballast behaviour:  
application to crossings*



*Figure 5.15: Three-dimensional wheel trajectory on the crossing surface.*

From Figure 5.15 it is possible to notice how the wheel follows the wing rail geometry edge until it jumps onto the crossing nose. The point at which there is the change in the contact point depends on various factors, such as:

- *Crossing geometry*: wing rail inclination, flange way, crossing topping, crossing nose geometry, tolerances;
- *Track geometry*: gauge, check rail distance, cross level;
- *Vehicle characteristics*: primary suspension stiffness values, in particular the longitudinal component, influencing leading and trailing axle attitudes (lateral offset and yaw angle of attack).

## **5.4.2 Wheel-rail contact forces**

Figure 5.16 presents the dynamic wheel-rail contact forces at the left and the right wheels as well as the vertical irregularity seen by the right wheel.

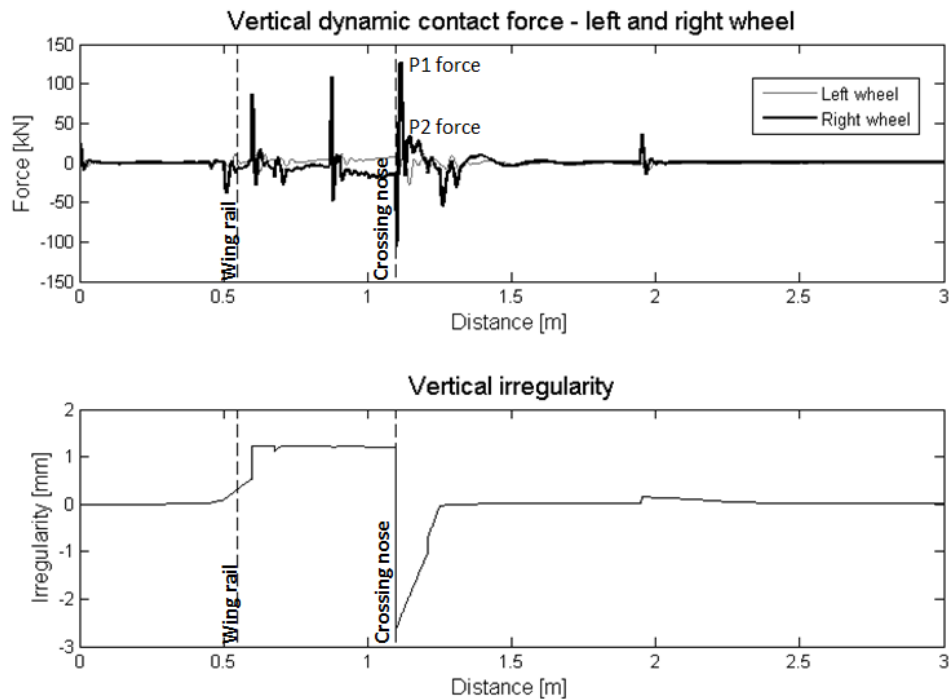


Figure 5.16: Dynamic contact forces at left (grey line) and right (black line) wheel compared with vertical irregularity seen by the right wheel.

The right wheel firstly unloads up to circa one third of the nominal static load while passing on the diverging wing rail, that is between 0.5 and 1.1 metre from the starting point. As soon as the contact point jumps from the wing rail to the crossing nose, there is an impact leading to a first peak in the contact force (P1 force) and then a second one (P2 force), lower in magnitude and longer in duration than the first one. On the contrary, the left side is characterised by a progressive loading, corresponding to the unloading of the right wheel, and then is also affected by the impact at the crossing nose.

Unfiltered and filtered contact forces below 280 Hz are shown in Figure 5.17.



*Design methodology for track systems considering the long-term ballast behaviour: application to crossings*

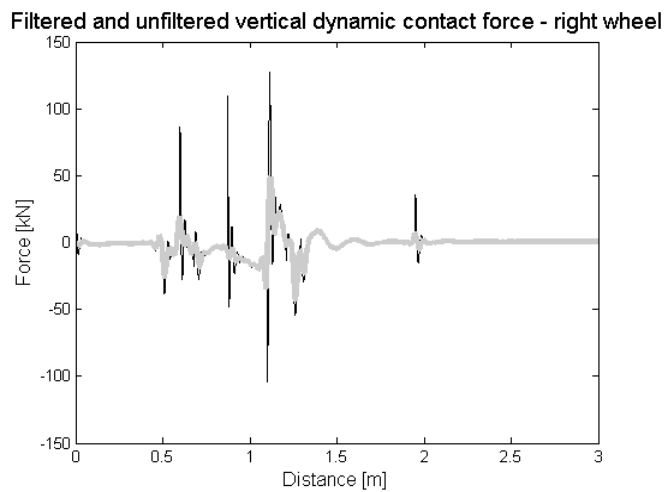


Figure 5.17: Unfiltered (black) and filtered (grey) dynamic contact force at right wheel.

A cut-off frequency of 280 Hz has been used as it is equal to 1.5 times the first resonance frequency (i.e. first track mode) of the equivalent track model, which is mainly linked with the support characteristics. In this way, it is possible to detect the force levels that actually causes the track deterioration.

The characteristics wheel-rail vibration modes represented in the current dynamic models are described as (Figure 5.18):

- *First mode*: rail coupled with wheel bouncing in phase with bearer mass and ballast;
- *Second mode*: rail bouncing in phase with wheel against bearer mass;
- *Third mode*: wheel moving out-of-phase against the rail.

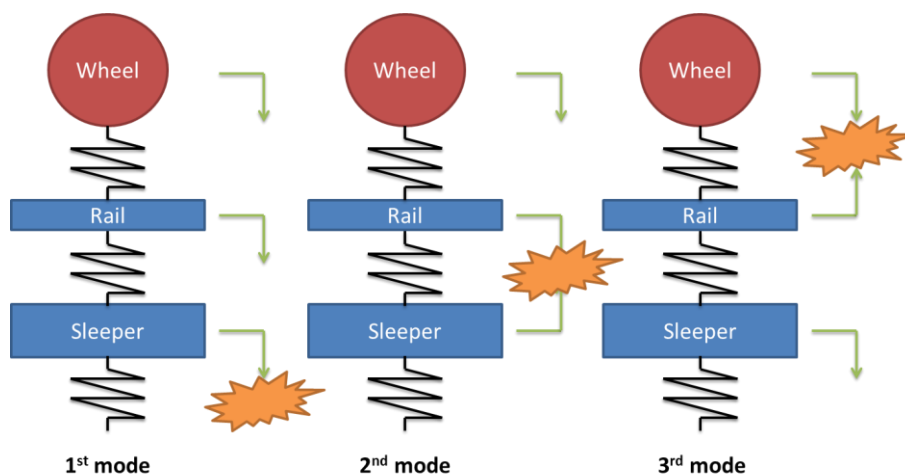


Figure 5.18: Typical wheel-rail vibration modes.

The degradation mechanisms corresponding to each mode are as follows:

- *First mode*: it is usually known as P2 force (main part). As the mode frequency and ballast natural frequency matches, the energy flows to the ballast layer, leading to settlement and localised defects such as voided bearers;
- *Second mode*: it is usually known as P2 force (contribution). The damage is concentrated at the superstructure level, leading to component degradation and failure;
- *Third mode*: it is usually known as P1 force. The energy is transferred to the contact, leading to high contact stresses and therefore plastic flow, surface and sub-surface initiated defect and abrasive wear.

Applying the Fast Fourier Transform (FFT) to the dynamic contact force (Figure 5.19), it is possible to see how the first impact force is within the typical frequency range of the P1 peak force (400-600 Hz [29]), while the following peak within the frequency range of the P2 peak force (40-200 Hz [29]).

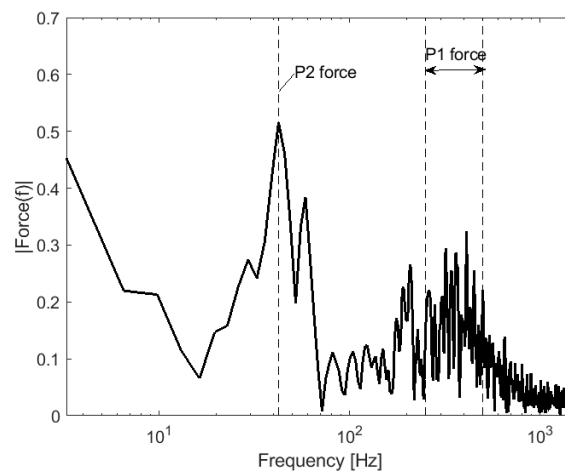
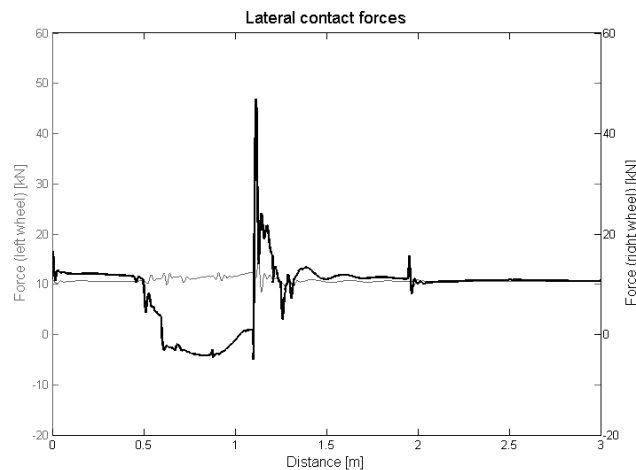


Figure 5.19: FFT of the vertical dynamic force at the right wheel.

Lateral contact forces are presented in Figure 5.20.

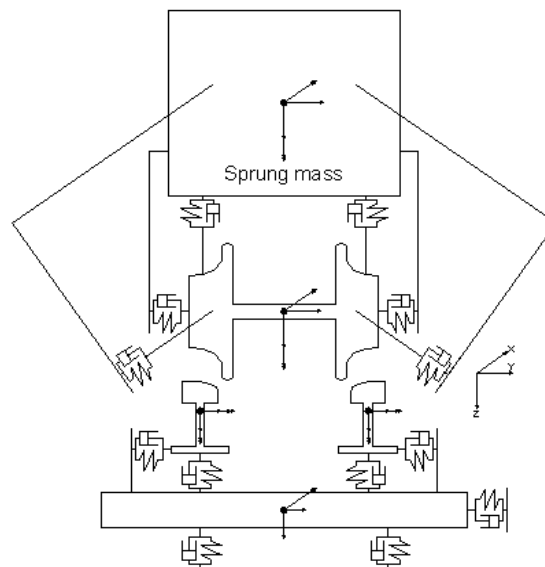
*Design methodology for track systems considering the long-term ballast behaviour: application to crossings*



*Figure 5.20: Lateral wheel-rail contact forces at the left (grey line) and right wheel (black line).*

The trend of the lateral forces at both left and right wheels is following the same as that of vertical force (Figure 5.16).

For the sake of completeness, the results of vertical and lateral forces in the time and frequency domain obtained with the model in Figure 5.10 are compared with the same quantities obtained from the model in Figure 5.21, which includes the bogie and the car-body sprung masses.



*Figure 5.21: Vehicle-track interaction model including sprung masses.*

The comparison in terms of vertical contact forces in the time domain is shown in Figure 5.22 , in the frequency domain in Figure 5.23 and the comparison in terms of lateral contact forces in Figure 5.24. Note that the grey line refers to the model with only the unsprung mass (Figure 5.10) and the black line to the model with unsprung and sprung

masses (Figure 5.21).

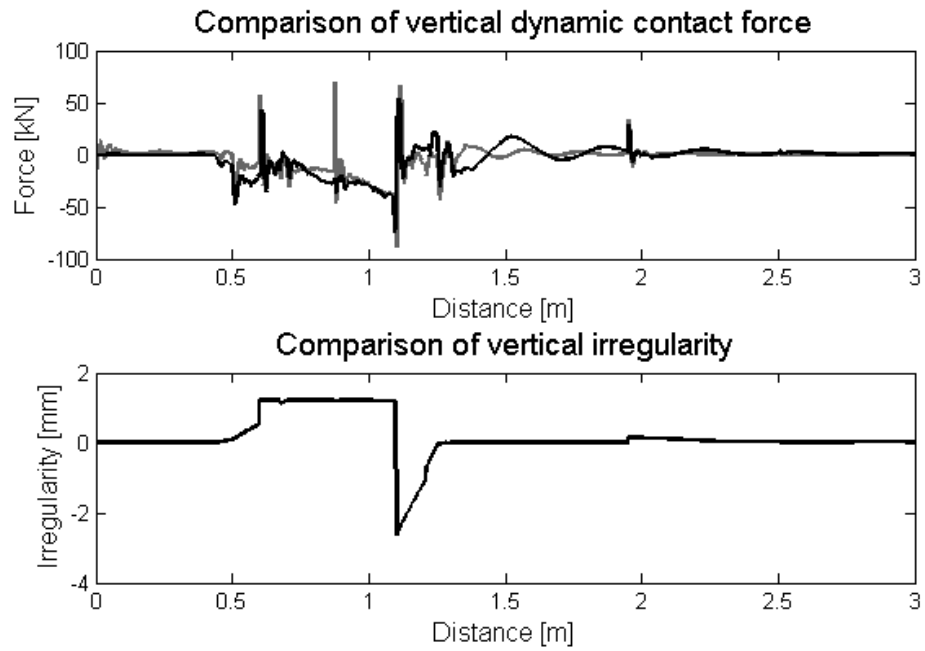


Figure 5.22: Dynamic vertical contact force at the right wheel considering only the unsprung mass (grey line) and considering unsprung and sprung masses (black line).

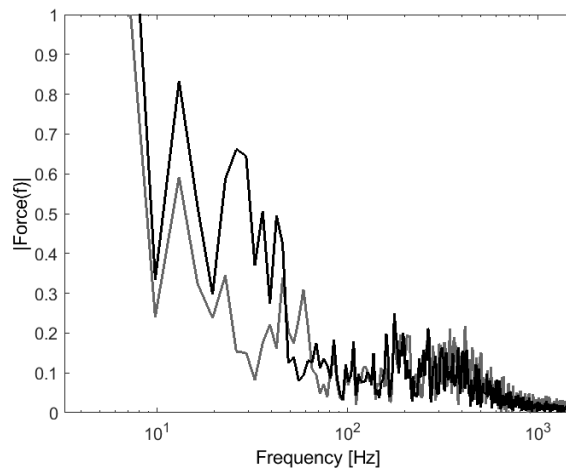


Figure 5.23: FFT of the vertical dynamic force at the right wheel considering only the unsprung mass (grey line) and considering unsprung and sprung masses (black line).

*Design methodology for track systems considering the long-term ballast behaviour:  
application to crossings*

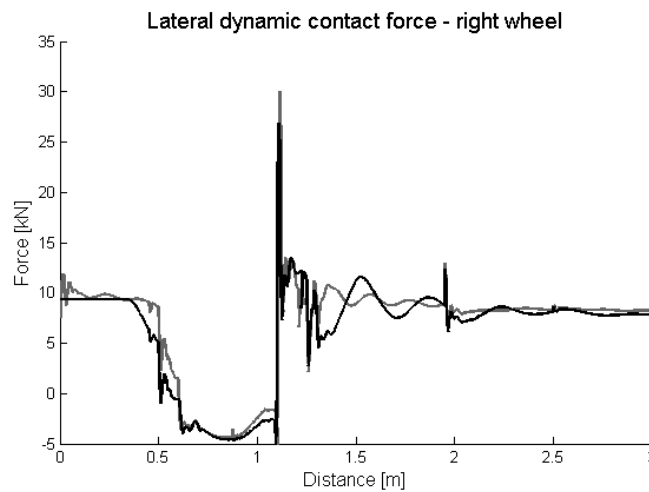


Figure 5.24: Lateral contact force at the right wheel considering only the unsprung mass (grey line) and considering unsprung and sprung masses (black line).

As expected, the effect of considering the sprung masses is to add to the contact forces a low frequency content corresponding to the sprung mass bouncing on top of the unsprung mass. The typical range is between 5 and 15 Hz, as shown in Figure 5.23.

## 5.5 Initial validation of the contact algorithm

In order to validate the model developed in the previous Sections, a comparison of the main outputs has been carried out against the same outputs calculated using the commercial software VI-Rail [122].

In both models, a single wheelset is considered without connections to the ground. The mass is set equal to 1500 kg, the roll and yaw inertia equal to  $810 \text{ kg}\cdot\text{m}^2$  and the pitch inertia equal to  $112 \text{ kg}\cdot\text{m}^2$ .

Regarding the superstructure, it consists on a co-running track model, including two rails and a bearer, as shown in Figure 5.25. In particular, the bearer roll stiffness is introduced due to the presence of a single vertical connection with the ground at the centre of the bearer mass.

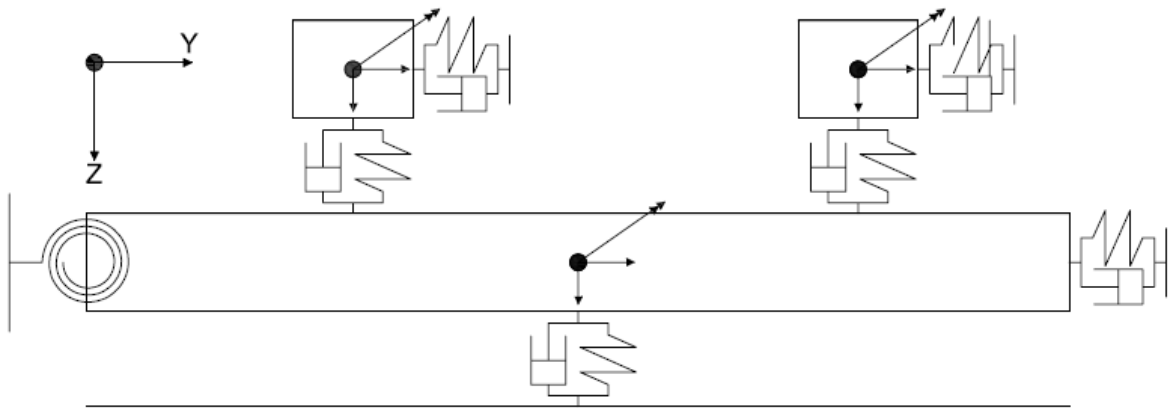


Figure 5.25: Track model in VI-Rail.

The parameters for the above track model are adjusted in order to match the one from the model developed in Matlab and summarised in Table 5.4.

Table 5.4: Main parameters of the co-running track model.

Parameter	Value	Units
Rail mass	195	kg
Bearer mass	1200	kg
Rail-pad vertical stiffness	530	kN/mm
Rail-pad lateral stiffness	430	kN/mm
Rail-pad vertical damping	350	kNs/m
Rail-pad lateral damping	240	kNs/m
Trackbed vertical stiffness	390	kN/mm
Trackbed lateral stiffness	37	kN/mm
Trackbed vertical damping	480	kNs/m
Trackbed lateral damping	480	kNs/m
Trackbed roll stiffness	10	kN/mm
Trackbed roll damping	10	kNs/m

The main differences between the contact algorithms considered are presented in Table 5.5.

Table 5.5: Main differences between the contact algorithms considered.

	VI-Rail	Matlab1
Number of contact points	Up to 10	1
Normal contact	Non-Hertzian	Hertzian
Tangential contact	Non-linear Kalker	Linear Kalker with saturation (Shen&Hendrick theory)

### 5.5.1 Contact geometry

The rolling radius difference is presented in Figure 5.26, the wheel-rail lateral contact position in Figure 5.27 and the wheel vertical trajectory in Figure 5.28.

*Design methodology for track systems considering the long-term ballast behaviour:  
application to crossings*

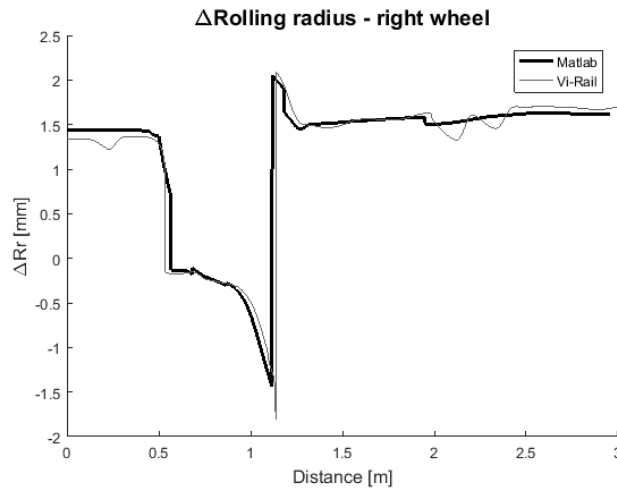


Figure 5.26: Comparison between the present model and VI-Rail in terms of rolling radius difference along the crossing panel.

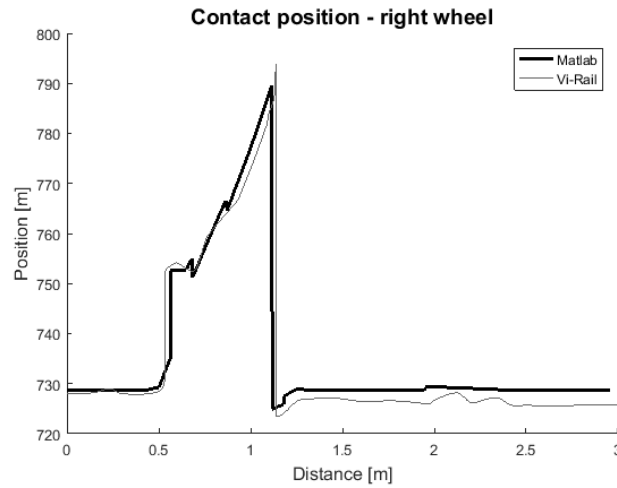


Figure 5.27: Comparison between the present model and VI-Rail in terms of wheel-rail lateral contact position along the crossing panel.

In both cases presented, the match is definitely satisfying (Figure 5.26 and Figure 5.27). The maximum difference at the crossing nose location is less than 4%. This slight difference can be explained with the different contact algorithm utilized in the present study and in VI-Rail (i.e. Hertzian single point of contact and non-Hertzian multiple point of contact).

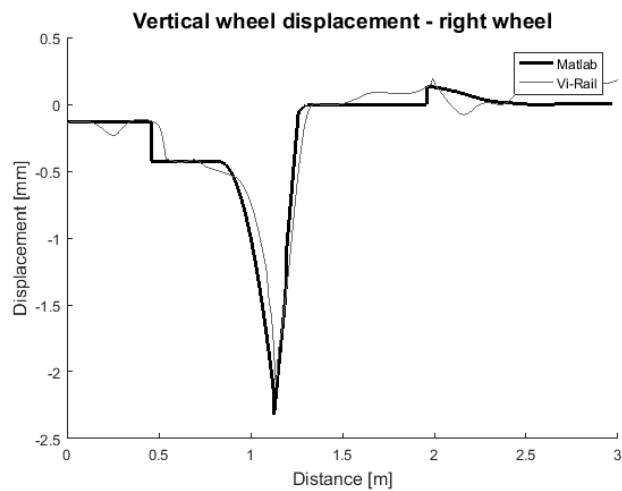


Figure 5.28: Comparison between the present model and VI-Rail in terms of wheel vertical trajectory along the crossing panel.

Also in the case of wheel vertical trajectory, the match is definitely satisfying with a maximum difference of 2.5% at the crossing nose.

### 5.5.2 Contact indices

Figure 5.29 shows the vertical component of the wheel-rail contact forces and Figure 5.30 the lateral component.

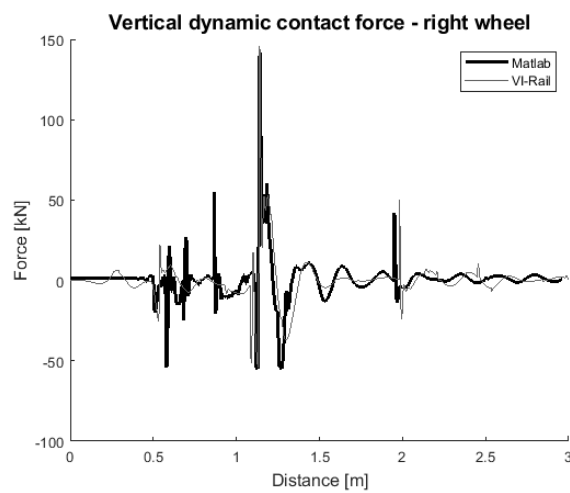
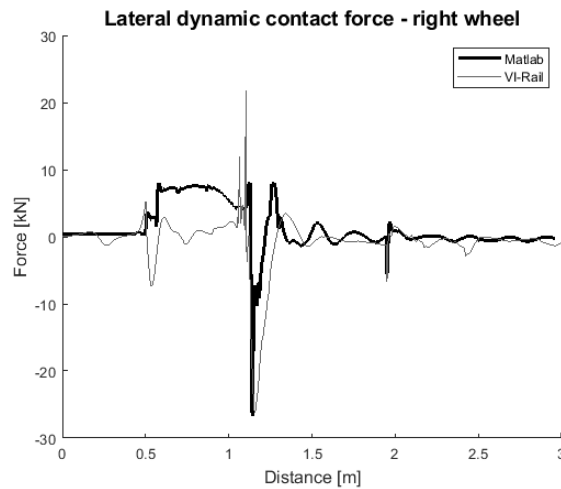


Figure 5.29: Comparison between the present model and VI-Rail in terms of vertical wheel-rail contact force along the crossing panel.



*Design methodology for track systems considering the long-term ballast behaviour:  
application to crossings*



*Figure 5.30: Comparison between the present model and VI-Rail in terms of lateral wheel-rail contact force along the crossing panel.*

Also in this case, there is a very good agreement between the curves in Figure 5.29. Both peak forces P1 and P2 are well captured by the Matlab model. The maximum difference between the P1 forces is about 0.5% and between the P2 circa 2.1%.

It is worth noticing that, as in the previous plots, there is a difference located at about 0.6 m from the front. The Matlab results show a peak which is not in the VI-Rail results. It can be interpreted taking in account the slight difference in the contact point at that location (Figure 5.27) which leads to slightly different rolling radius difference in the two cases and, therefore, slightly different creepages.

Similar conclusions can be drawn for Figure 5.30, although the differences are slightly larger than for the vertical forces due to the accumulation of variation of both normal and tangential contact approaches.

## **6 Validation of the dynamic model with experimental data**

This Chapter discusses the validation of the developed dynamic vehicle-track interaction model. Details are also shown in Grossoni [7]. The validation is carried out against experimental data of bearer displacements at a crossing panel fitted with Under Sleeper Pad (USP) that has been collected using vertical geophones.

In Section 6.1 the description of the main site characteristics and the field data is presented, including the geophone measurements and the Track Recording Coach (TRC) data. In Section 6.2 the behaviour of long bearer in time and frequency domain is analysed and justifications for the modelling approach adopted hereafter are given. Section 6.3 the methodology adopted to tune the model trackbed stiffness against the experimental data is detailed. In Section 6.4 the comparison of numerical results with site data in terms of bearer vertical displacement is discussed. Finally, Section 6.5 discusses the influence of track flexibility on the dynamic behaviour predicted along the crossing.

### **6.1 Site data**

#### **6.1.1 Site description**

The experimental data originates from a double crossover site in UK. The site has been monitored on repeated occasions by the University of Southampton (UoS), a partner in the EPSRC project Track to the Future who is gratefully acknowledged for the data provided, to which the author has contributed to.

The monitoring mainly consists on capturing bearer vertical and lateral movements using geophones, accelerometers and MEMS sensors. Geophones used here are ground motion transducers usually adopted by geophysicists and seismologists to observe the ground movements. They are made of a spring suspended mass, which starts moving only when the exciting velocity frequencies are smaller than the resonance system frequency. The mass movement depends on magnets or coils, whose response is proportional to the exciting velocity. Note that the resonance frequency is the key aspect of this equipment and strictly depends on the type of measured signal.

*Design methodology for track systems considering the long-term ballast behaviour: application to crossings*

The geophones were applied directly at selected bearers at the top of bearer on cess and 6ft side some distance away from bearer edge, as explained in Le Pen [123] and in Figure 6.1. Hereafter, the nomenclature “cess side” will refer to the external side of the track and “6ft side” to the internal side, in line with the glossary used by UK track operators.

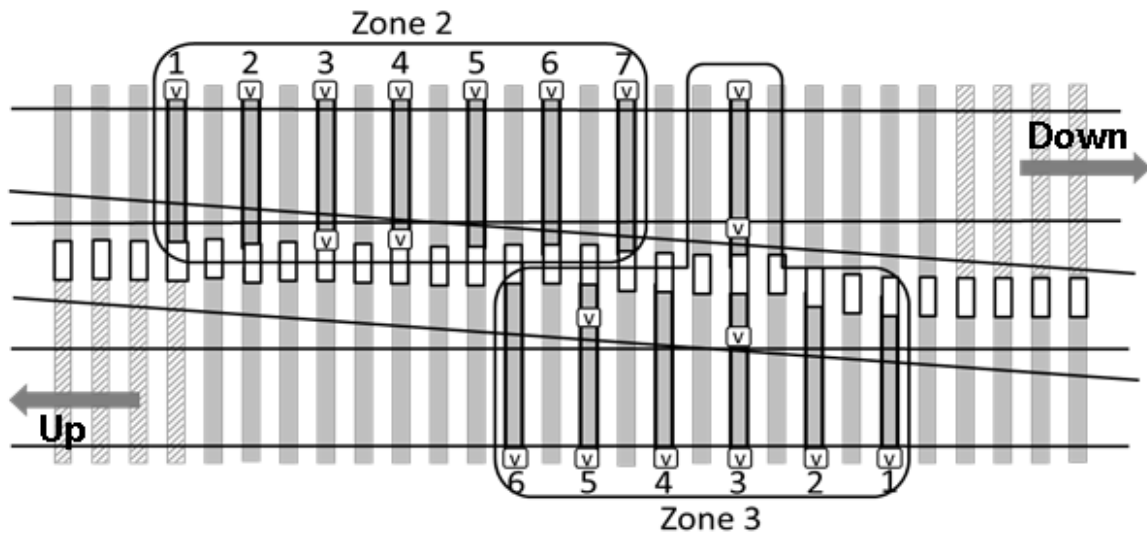


Figure 6.1: Site plan. The bearers monitored are marked with “v” (Le Pen [123]).

In this study, Zone 2 of the Down line (i.e. right-hand crossing with a 1:13 angle) has been used for the comparison and calibration of the model. The rail type is 56E1 on type 001E concrete bearer spaced 0.71 m. Long bearers are present on site and they are linked together with a steel plate and bolts. After the site complete renewal in 2012, the crossing panel has been equipped with Under Sleeper Pads (USPs), whose static bedding modulus is  $0.15 \text{ N/mm}^3$ .

Several records have been performed and the typical train composition is a pulling Class 91 locomotive, nine Mark IV coaches and a tractor locomotive. A recorded passage on the crossing panel at 33 m/s (ca. 119 km/h) is used hereafter.

### **6.1.2 Field data: measurements with geophones**

The geophones used are able to record the bearer velocity in the range between 1 to 250 Hz. This range is enough to capture the main system dynamics due to the train passage and the P2 impact force occurring at the crossing nose. Figure 6.2 shows the Power Spectral Density of the raw velocity measurements up to 250 Hz.

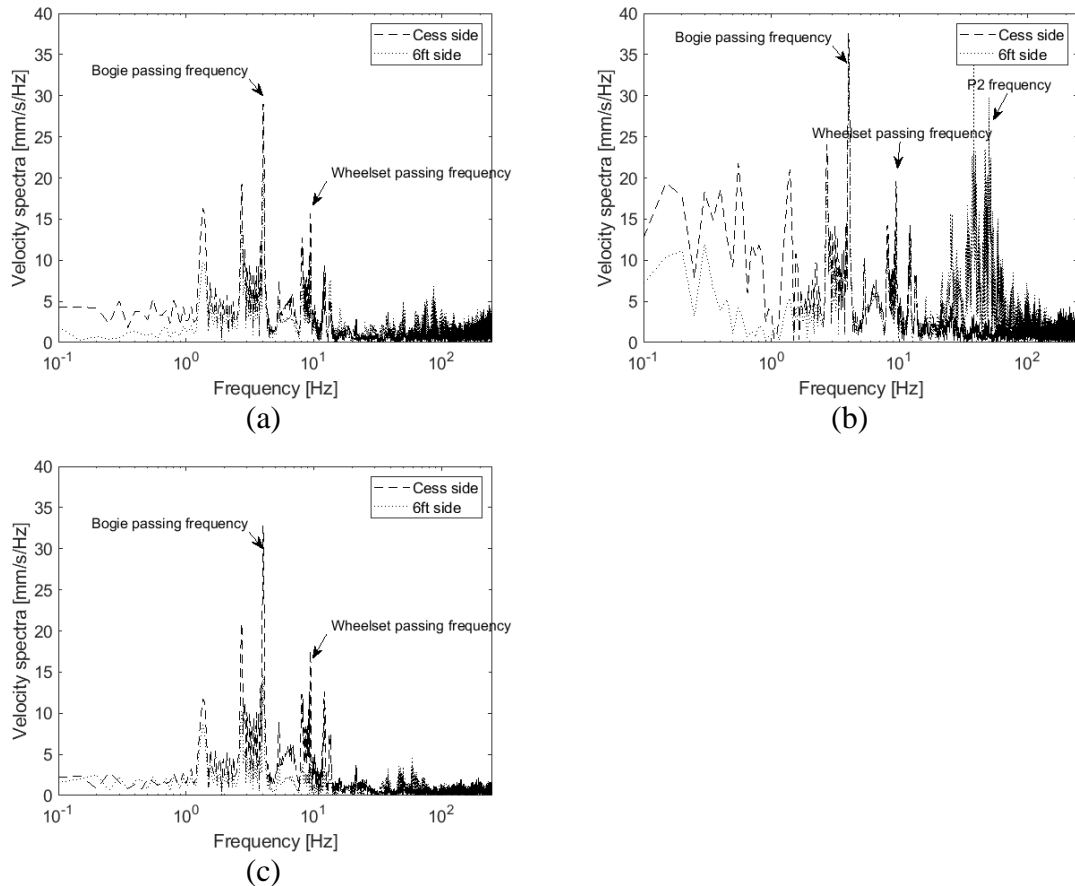


Figure 6.2: Geophones measurements up to 250 Hz at bearer (a) 3, (b) 4 and (c) 6 for cess and 6ft side.

The wheelset spacing for a Class 91 train is 3.35 m and the bogie spacing 10.50 m. Since the travelling speed is equal to 33 m/s, the corresponding theoretical vibration frequencies are 9.85 Hz and 3.14 Hz, respectively. These values are found consistent with the ones in the graphs in Figure 6.2 (i.e. 9.40 Hz and 4.00 Hz).

The theoretical frequency range for the P2 impact force (see Section 5.4.2) is coherent with the experimental spectrum which shows peaks in the range between 38 Hz and 60 Hz at bearer 4 under the 6ft rail closest to the wheel load transfer onto the crossing nose.

### 6.1.3 Field data: TRC data

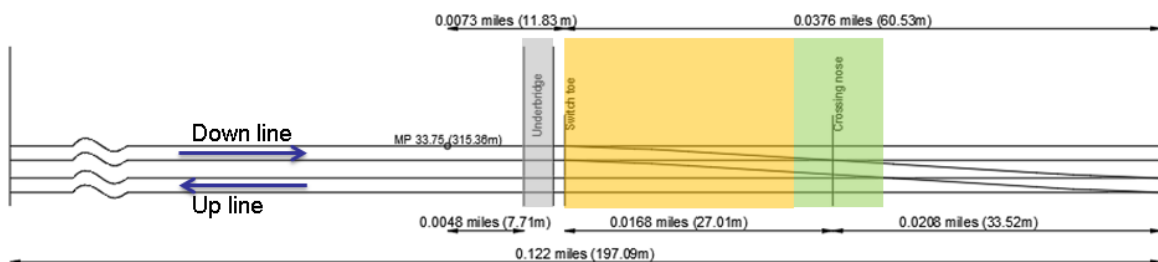
The Track Recording Coach (TRC) is an instrumented vehicle that periodically runs along the whole network to acquire and process the main track characteristics, including alignment, gauge and rail top level, for maintenance purposes.

Data of the monitored site covering the period between June 2014 and March 2016 have been aligned and analysed. Note that only the latest set has been included in the

*Design methodology for track systems considering the long-term ballast behaviour: application to crossings*

dynamic analysis since it is closest in time to the geophone measurements. Also it is important to highlight that the TRC data is valid for plain line track, while for the crossing panel its validity is questionable. Nevertheless, this is the only data available for this site.

The main dimensions and features around the turnout, such as the presence of an underbridge, switch toe and crossing nose, are shown in Figure 6.3. All the following figures (i.e. Figure 6.4, Figure 6.5 and Figure 6.6) refer to the distance between the start of the underbridge and the crossing panel on the down line.



*Figure 6.3: Main dimensions of the analysed site.*

Note that the TRC axes system used in the following graphs is according to the British standard RT/CE/C/038 [124].

***Top level***

Figure 6.4 shows the top level measurements and the rate of growth for left and right rail. Note that the latter has been calculated as the difference between two consecutive curves and averaged by the elapsed time.

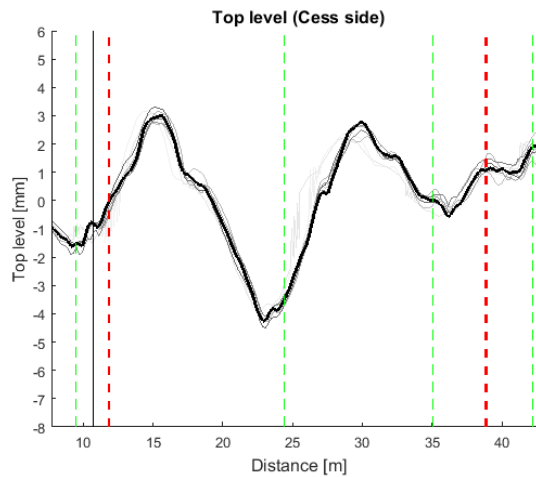
Looking at Figure 6.4(a), it is possible to notice that the turnout area on the cress side is characterised by cyclic patterns whose wavelength corresponds to the typical vehicle dynamics dynamic response. There are three clearly detectable cycles, whose wavelengths are 14.9 m, 13.2 m and 16.7 m, respectively, corresponding to frequencies between 2 and 3.4 Hz at the travelling speeds registered (i.e. 51 m/s on the switch panel and 33 m/s on the crossing panel). These frequencies are within the range of the bogie (5-6 Hz) and car-body (1-2 Hz) bouncing frequencies.

On the other hand, the 6ft rail top level is undoubtedly influenced by the change in mass and stiffness properties at the crossing panel area, as shown by the peak at ca. 43 m (Figure 6.4(b)) corresponding to the wing rail/crossing nose wheel transfer area. It is interesting noticing how the left cress rail follows locally a similar trend with lesser

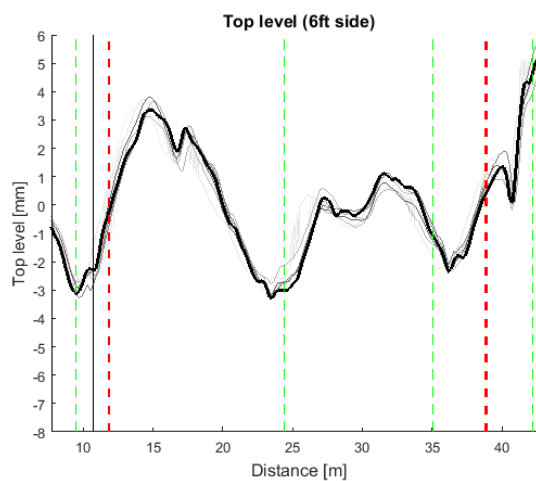
amplitude.

Also, the underbridge at ca. 10 m causes a local variation in stiffness, which is expected to cause a high point in the signal. Nevertheless, the data shows a low point at each rail, which can be explained with the presence of deformed rail potentially due to the presence of a welded joint.

Regarding the top level rate of growth within the turnout, the peaks occur on the right 6ft side, as expected, at the switch-stock rail assembly area, at the weld in the closure panel, at the crossing nose and at the start and end of the long bearer area. It is worth highlighting how the highest value growth rate for left and right side is located at bearers just after the crossing nose.

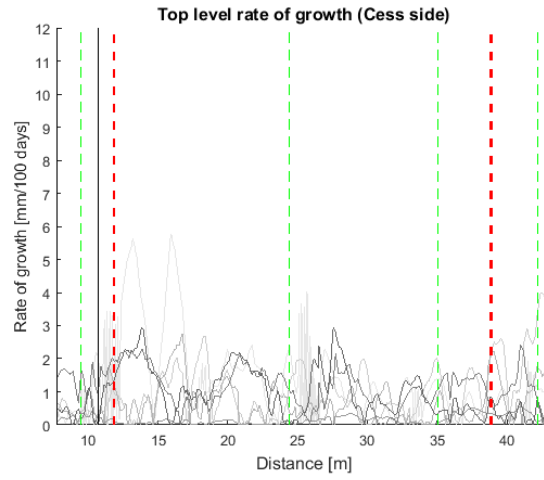


(a)

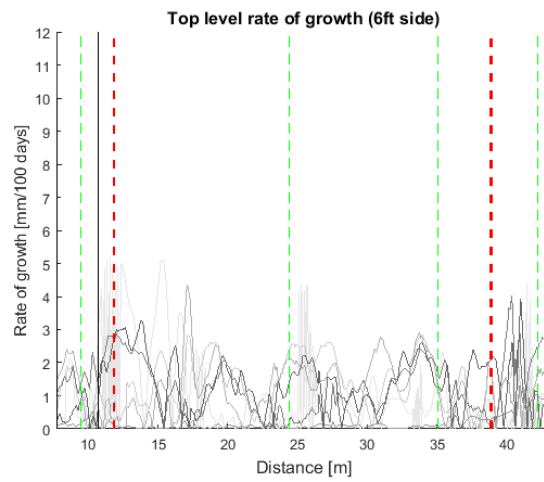


(b)

*Design methodology for track systems considering the long-term ballast behaviour:  
application to crossings*



(c)

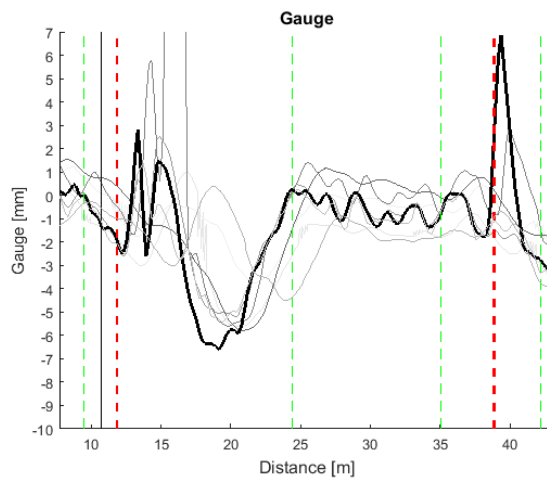


(d)

Figure 6.4: (a, b) Top level measurements and (c, d) top level rate of growth in mm/100 days for cess and 6ft sides, respectively (--- Welded joint; — Underbridge; --- Switch toe/crossing nose).

**Gauge**

Figure 6.5 shows the gauge measurements and its rate of growth.



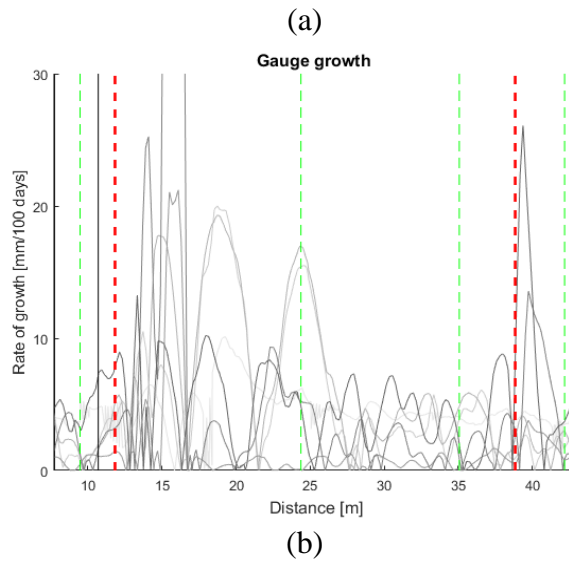
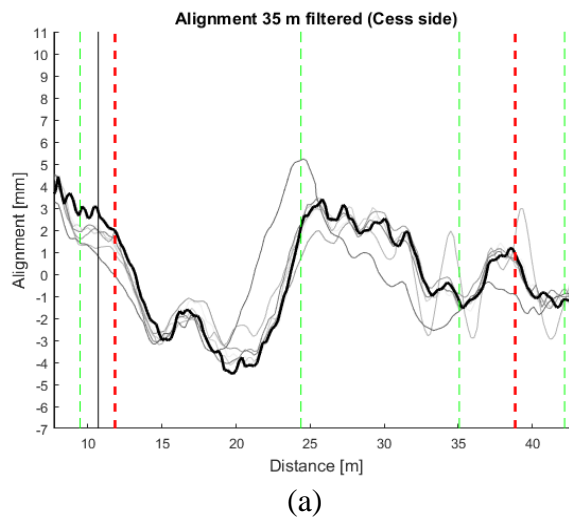


Figure 6.5: (a) Gauge measurement and (b) gauge rate of growth in mm/100 days (--- Welded joint; --- Insulated joint; — Underbridge; - - - Switch toe/crossing nose; - · - · First/last long bearer).

The measurements of gauge reveal very small changes in the gauge, in the range  $\pm 3$  mm. The exceptions of very high peaks are revealed at the switch-stock rails assembly and load transfer area due to remarkable lateral shift in rail and contact position on the 6ft side (i.e. right rail) and therefore noticeable apparent local increase in gauge measurement.

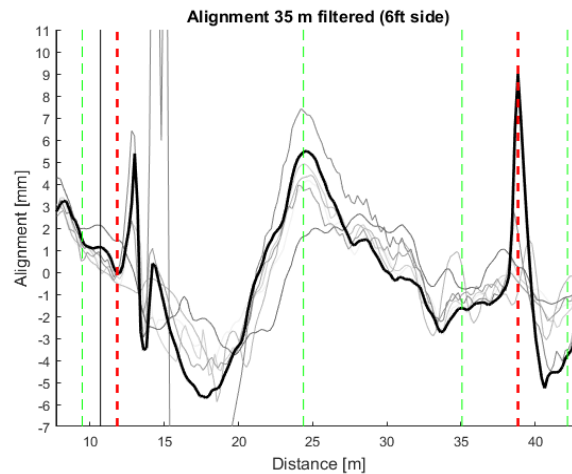
### Alignment

Figure 6.6 shows the alignment measurements filtered between 1 and 35 m wavelength for cess and 6ft sides.





*Design methodology for track systems considering the long-term ballast behaviour:  
application to crossings*



(b)

Figure 6.6: Alignment measurements filtered at 35 m for (a) cress and (b) 6ft side (--- Welded joint; - - - Insulated joint; — Underbridge; - - - Switch toe/crossing nose; - · - · First/last long bearer).

As expected from Figure 6.5, the alignment measurements show large and sharp peaks. This is a limitation of the measurement method when rail shape changes rapidly (i.e. at the crossing nose, where there is a sudden jump of wheel-rail lateral contact position, as shown in Figure 5.15, or at the switch-stock rail load transfer area).

## 6.2 Considerations for long bearer modelling in the crossing panel

Long bearers are a key element in a crossing panel as they ensure the correct rail position in both through and diverging trajectories. Due to manufacture and transportation limitations, usually they are built in two parts and then assembled together through a mechanical connection. These can vary from country to country and a detailed review of connection types is presented in the European project In2Track [125]. From a modelling point of view, their potential high variability and non-linear stiffness behaviour representation can be challenging especially in a vehicle-track interaction context.

A FE model of long bearers has been developed and the results in terms of displacements for various load and trackbed conditions are presented in Section 6.2.1. Section 6.2.2 focuses the attention to the influence of trackbed stiffness transversal stiffness on the dynamic system behaviour. In Section 6.2.3 a study in the frequency domain is carried out to choose the most suitable bearer model to be integrated in the vehicle-track interaction analysis.

### 6.2.1 Long bearer FE model

Under load the long bearers might be subject to non-negligible bending compared to shorter plain line bearers. In order to understand better the influence of bearer flexibility, a two-dimensional vertical FE model of a single bearer has been developed using the Timoshenko beam theory and distributed trackbed support using localised springs at each node. This approach is able to capture the static bearer shape under symmetrical or asymmetrical loads with different configurations of non-linear trackbed stiffness also allowing lifting.

The main bearer characteristics that will be considered in the present study are reported in Table 6.1.

Table 6.1: Bearer input values.

Parameter	Value	Unit	Considerations
Bearer material	Concrete		
Young's modulus	43	GPa	Thompson [126]
Shear modulus	18.7	GPa	Thompson [126]
Poisson's ratio	0.15	-	Thompson [126]
Density	2500	kg/m <sup>3</sup>	Thompson [126]
Shear coefficient	0.84	-	
Length	5.99	m	Monitored site, 2.75 m and 3.24 m
Width	0.295	m	In2Rail [127]
Height	0.165	m	In2Rail [127]
Second moment of area	$1.104 \cdot 10^{-4}$	m <sup>4</sup>	In2Rail [127]
Connection	Neglected		
Rail spacing gauge	1.5	m	See Figure 6.7
Loading points	0.625/2.125	m	See Figure 6.7
Trackbed modulus	50	kN/mm/m	In2Rail [127]

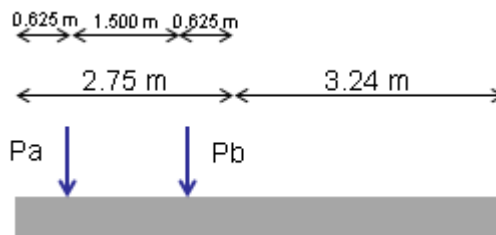


Figure 6.7: Bearer loading point configuration.

Four types of loading configurations will be analysed as follows (refer to Figure 6.7 for notation):

- Passenger train: a typical regional passenger train has a 12 t axle load. Assuming that half of the load transfers on the bearer, both Pa and Pb are equal to 29 kN;

*Design methodology for track systems considering the long-term ballast behaviour: application to crossings*

- Freight train: the maximum allowable axle load in the European infrastructure is 22.5 t. Assuming that half of the load transfers on the bearer, both  $P_a$  and  $P_b$  are equal to 55 kN;
- Symmetrical impact loading: high impact loading can occur at the crossing nose location, up to 3-4 times the static wheel load. Assuming that half of the load transfers on the bearer and a dynamic factor equal to 3 for a passenger vehicle, both  $P_a$  and  $P_b$  are equal to 88 kN;
- Asymmetrical loading: the crossing panel is characterised by an asymmetrical loading between cess and 6ft rail. In the case of a passenger train, assuming a dynamic factor equal to 1.1 and 2.2 respectively,  $P_a$  is equal to 32 kN and  $P_b$  64 kN.

Regarding the trackbed stiffness, each bearer is assumed to be divided into 5 sections ( $K_1$  to  $K_5$ ) as shown in Figure 6.8 corresponding each to three main stiffness regions (i.e. under the rail seats, at the external part of rail seats, between the rails) for the loaded and the unloaded part of the bearer. The total trackbed stiffness is then calculated as the product of each coefficient  $K_i$  at the  $i$ -th region and the trackbed modulus reported in Table 6.1.

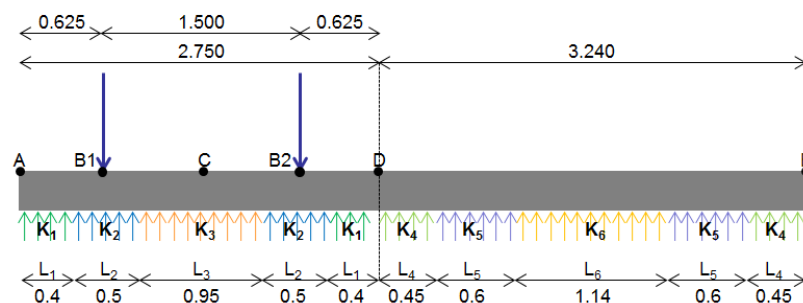


Figure 6.8: Stiffness distribution arrangements along the bearer.

Three main cases will be analysed (Table 6.2):

- Constant trackbed
- Variable trackbed 1: this case replicates the “centre-binding effect” seen during laboratory experiments after 3 million cycles [128] where the ballast tends to migrate towards the bearer center stiffening this region and leading to bending cracks
- Variable trackbed 2: this case replicates the facts that the highest number of bearer-ballast contacts points is concentrated under the rail seats while a low

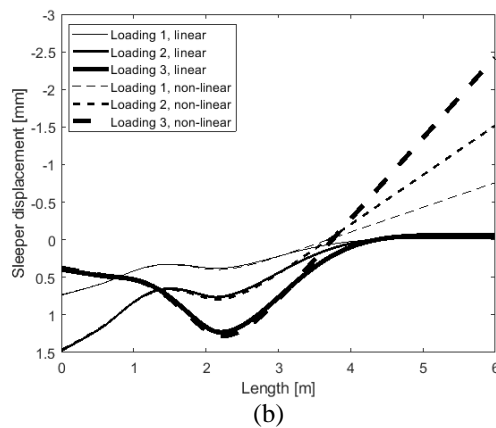
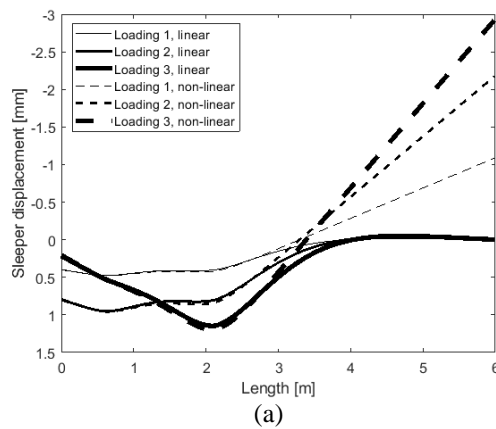
concentration is shown below the bearer centre.

The total number of cases is thus 12.

Table 6.2: Cases analysed in terms of loading configuration and trackbed stiffness type.

Case	Loading configuration	Pa	Pb	Trackbed stiffness type
1	Passenger train	29	29	Constant
2	Passenger train	29	29	Variable 1
3	Passenger train	29	29	Variable 2
4	Freight train	55	Constant	
5	Freight train	55	55	Variable 1
6	Freight train	55	55	Variable 2
7	Symmetrical impact loading	88	88	Constant
8	Symmetrical impact loading	88	88	Variable 1
9	Symmetrical impact loading	88	88	Variable 2
10	Asymmetrical impact loading	32	64	Constant
11	Asymmetrical impact loading	32	64	Variable 1
12	Asymmetrical impact loading	32	64	Variable 2

Same cases are then analysed for the non-linear trackbed stiffness, i.e. considering the bearer uplifting. Figure 6.9 shows some examples of bearer displacement for different types of trackbed configuration and applied load.



*Design methodology for track systems considering the long-term ballast behaviour: application to crossings*

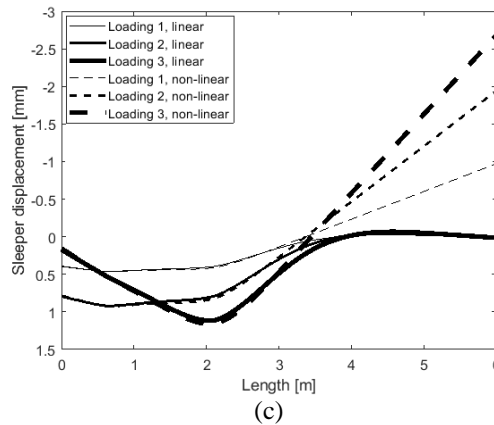


Figure 6.9: Bearer displacement for different type of loading and different type of trackbed ((a): constant; (b): variable 1; (c): variable 2).

Figure 6.9 shows the importance of correctly modelling the trackbed transversal stiffness distribution. For instance, considering a constant distribution leads to relevant differences in displacements w.r.t. the “variable 1” support type, especially at the cess end (up to an average of 45%) as well as under the cess rail seat (up to up to an average of 16%). On the contrary, similar results are found in case of the “variable 2” support type in comparison with constant one. This means that when the support is in a good state (i.e. new construction or after maintenance cycle) the flexural behaviour of the bearer tends to be uniform across its length, while in a degraded state the behaviour may tend to be extreme rising tensional stresses and may lead to potential fractures in the concrete structure.

## 6.2.2 Influence of trackbed stiffness transversal distribution on the vehicle-track dynamics

In the previous Section, it has been seen that the type of trackbed and the impact loading considered both have a very strong influence on the displacement results obtained. This means that it is crucial to use the correct assumptions for both. In order to assess this aspect in the dynamic context, a three-dimensional vehicle-track interaction model in plain line has been built following the same approach as in Section 5 and considering two independent wheelsets running over 15 flexible sleepers. The main input parameters are listed in Table 6.3. Three rail irregularity types are considered, i.e. perfectly smooth track, dip joint of 1 mm over 1 metre and track irregularities according to class 6 in the AAR regulations.

Table 6.3: Main input values for the plain line model.

Parameter	Value	Units
Rail type	56E1	
Bearer type	G44 concrete monobloc	
No. of bearer elements	6	-
Bearer spacing	0.65	m
Trackbed stiffness	89	kN/mm/bearer end
Vehicle type	Freight	
Axle load	24	t
Wheelset spacing	2.50	m
Speed	80	km/h

Figure 6.10 shows the results of the cases considered in terms of bearer displacement for the cases of trackbed distribution and top level irregularities defined.

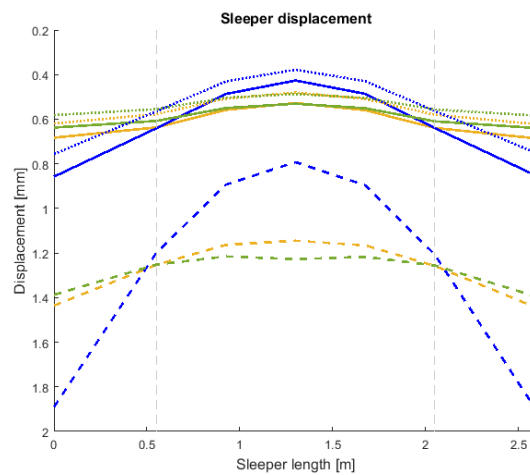


Figure 6.10: Bearer displacement at the middle of the track for various trackbed distributions and different impact types. Continuous lines refer to perfect track, dashed lines to dip joint case and dotted lines to top level irregularities. Yellow lines refer to constant distribution, blue to “variable 1” type and green to “variable 2” type. The vertical dashed lines refer to both loads transversal position.

As expected, Figure 6.10 confirms that the trackbed conditions play a fundamental role in the system behaviour for all the top irregularity cases considered. Looking in more detail, Table 6.4 summarises the displacements at key locations for the irregularity types and trackbed distributions considered. Also the percentage differences of the variable trackbed cases w.r.t. the constant trackbed case are reported.

*Design methodology for track systems considering the long-term ballast behaviour:  
application to crossings*

*Table 6.4: Summary of displacements and percentage differences at key locations for the irregularity types and trackbed distributions considered. All displacement values are in mm.*

<b>Irregularity type</b>	<b>Position</b>	<b>Constant</b>	<b>Variable 1</b>		<b>Variable 2</b>	
Perfect track	Bearer end	0.683	0.858	26%	0.638	-7%
	Bearer centre	0.528	0.427	-19%	0.530	1%
	Under loading point	0.637	0.641	1%	0.608	-5%
Dip joint	Bearer end	1.436	1.891	32%	1.388	-3%
	Bearer centre	1.145	0.793	-31%	1.228	7%
	Under loading point	1.253	1.200	-4%	1.252	0%
Top level irregularities	Bearer end	0.619	0.756	22%	0.582	-6%
	Bearer centre	0.481	0.378	-21%	0.487	1%
	Under loading point	0.578	0.565	-2%	0.555	-4%

From Table 6.4 it can be noticed that the highest differences w.r.t. the case of constant trackbed occur when the “variable 1” type is considered, especially at the bearer end and the bearer centre. The differences calculated under the loading point are negligible in all the cases considered, ranging between -5% to 1%.

It is possible to conclude that the effect of support variation is relevant especially when the outer displacements are used, for example looking at the behaviour of different bearer connections. Nevertheless, the settlement routines that are usually implemented in conjunction with vehicle-track models (see Section 3.4) account for displacements and/or other physical quantities calculated under the rail seats as the result is an average value along the bearer area. In that case, then, the differences between models are negligible and can be interchangeably used. Section 8.2 will discuss these comparisons in detail.

### **6.2.3 Frequency analysis of the long bearer behaviour and modelling selection**

It has been seen in the crossing area (see Section 5.4) that the frequency content of the contact force P2 component, that is transmitted to the lower part of the track, is up to 100-120 Hz. Using the Nyquist theorem for sampling analog signals, the frequency of interest results to be up to 500 Hz (i.e. five time the required frequency). Using the input parameters listed in Table 6.1 and a bearer length of 2.75 m (i.e. bearer length under the crossing nose along the down line through route), a modal analysis has been performed to find out the bearer mode shapes and the natural frequencies. The results are shown in Figure 6.11.

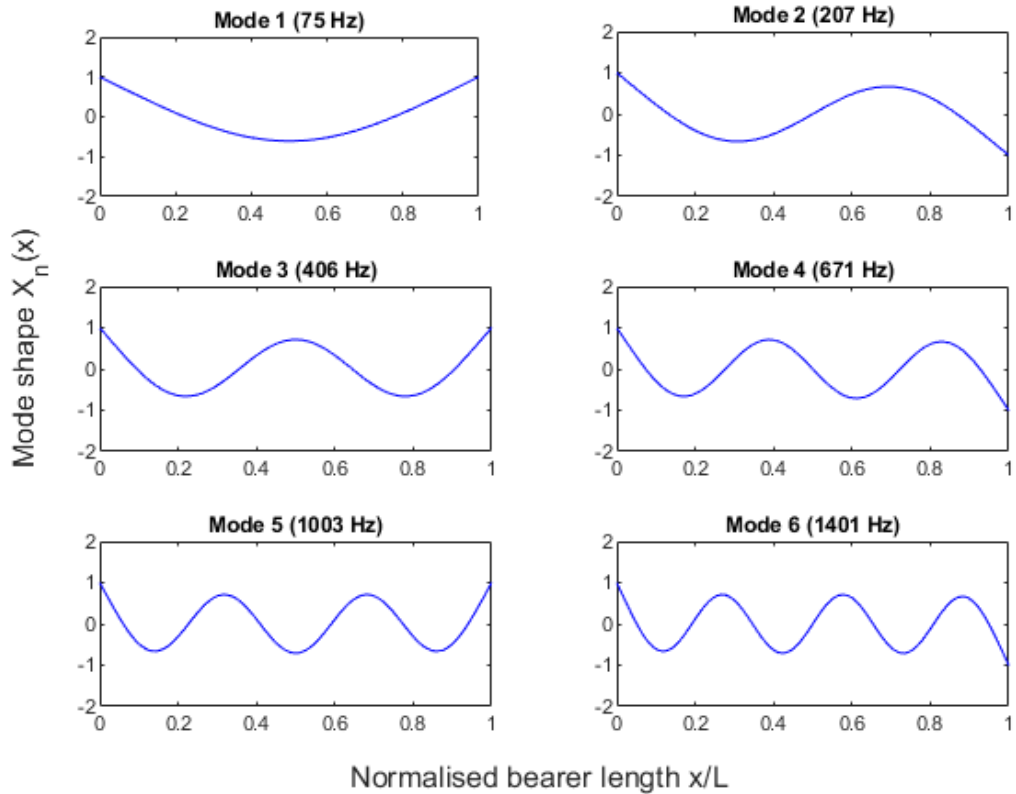


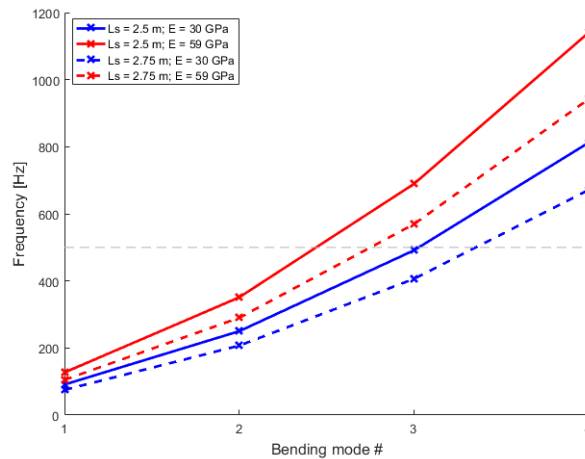
Figure 6.11: Modal analysis for the bearer under the crossing nose.

In order to appropriately capture the P2, it is necessary to consider at least three modes and thus four elements.

Note that both the length and the material Young's modulus influence the bending modes, as shown in Figure 6.12. For example, looking at the first one (Table 6.5) it is possible to conclude that increasing the bearer length for a given Young's modulus lowers the modal frequencies, whereas increasing the Young's modulus for a given bearer length increases the modal frequencies.



*Design methodology for track systems considering the long-term ballast behaviour:  
application to crossings*



*Figure 6.12: Influence of the bearer length and the material Young’s modulus on the bending modes considered.*

*Table 6.5: Natural frequency for the first bending mode considering different lengths and material Young’s moduli.*

Length [m]	Young’s modulus [GPa]	I bending mode frequency [Hz]
2.50	30	91
2.75	30	75
2.50	59	127
2.75	59	105

As stated in the modelling assumptions, only the through route is considered in the present study. An equivalent bearer model is thus needed to correctly capture the frequency response of the full bearer. Three model approaches (i.e. fully flexible bearer as developed in Section 6.2.1, semi-flexible flexible considering four elements in line with the modal analysis and rigid bearer) are compared considering the case of passenger vehicle and “variable 2” trackbed type (see Section 6.2.1 for details). The adjacent track is accounted for using an equivalent vertical stiffness, which is equal to the sum of the stiffness values under the cess and the 6ft side of the adjacent track<sup>5</sup>, and rotational stiffness, which is equal to product of the stiffness at each support side in the adjacent track and the distance of each support end to the connection joint (Figure 6.13).

<sup>5</sup> These are assumed equal to the respective ends in the considered track.

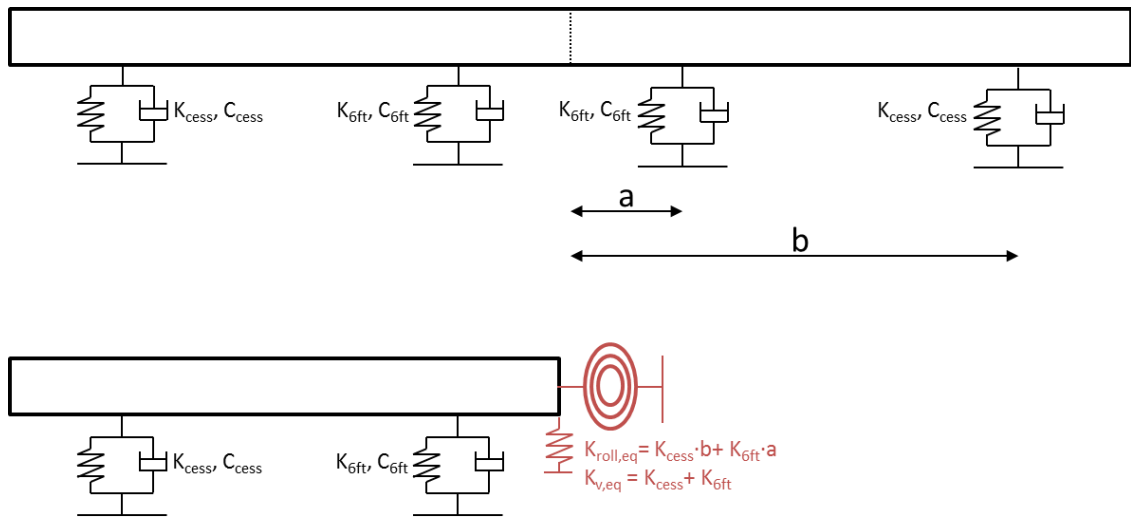


Figure 6.13: Equivalent vertical and roll stiffness to account for the adjacent track.

Figure 6.14 and Table 6.6 show the comparison between the three bearer models in terms of bearer displacement.

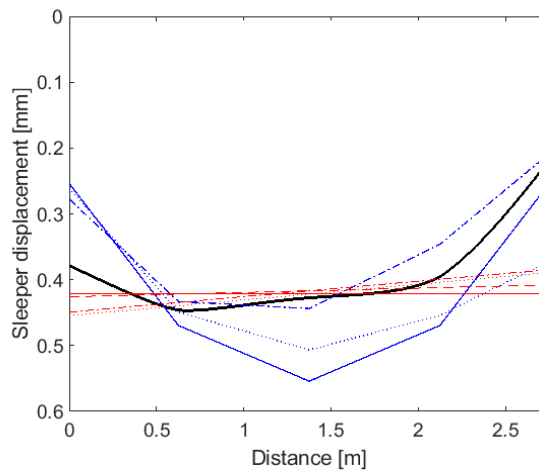


Figure 6.14: Comparison between fully flexible (black), semi-flexible (blue) and rigid (red) bearer models in terms of displacement. The continuous lines refers to case of no additional stiffness, the dashed lines to case of vertical stiffness addition, the dotted lines to case of roll stiffness addition and the dashed-dotted lines to case of vertical and roll stiffness addition.

*Design methodology for track systems considering the long-term ballast behaviour:  
application to crossings*

Table 6.6: Summary of displacements from the bearer models considered and differences w.r.t. fully flexible model. All displacement values are in mm.

Bearer model type		Under cess side load		Under 6 ft side load		Under 6ft end	
Fully flexible		0.45		0.42		0.22	
Semi-flexible	No additional stiffness	0.47	5%	0.51	22%	0.25	16%
	Additional vertical stiffness	0.47	5%	0.51	22%	0.25	16%
	Additional roll stiffness	0.45	1%	0.48	14%	0.37	70%
	Additional vertical and roll stiffness	0.43	-3%	0.39	-6%	0.21	-5%
Rigid	No additional stiffness	0.42	-5%	0.42	0%	0.42	93%
	Additional vertical stiffness	0.42	-5%	0.41	-1%	0.41	87%
	Additional roll stiffness	0.44	-1%	0.41	-2%	0.39	78%
	Additional vertical and roll stiffness	0.43	-3%	0.41	-3%	0.38	76%

Since the ballast settlement under the rail seats is the focus of the thesis and it is generally linked with the force/displacement, the displacement values of each simplified model (i.e. semi-rigid and rigid model) at these location are compared to the displacement values of the full FE model minimising the differences. From Figure 6.14 and Table 6.6 it is possible to conclude that when the semi-flexible model is used, the model with both vertical and roll additional stiffness should be considered. On the other hand, when the rigid model is used the roll additional is sufficient to replicate the displacement under both loading points.

### 6.3 Tuning the trackbed stiffness along the crossing panel

It has been recognised that there generally exist a longitudinal variation of track stiffness on railway track (see for example the study by Grossoni et al. [8] for plain lines). Additional variations such as ballast voids can appear mostly in the vicinity of short-wave irregularities (e.g. crossing panel or welds), at which the high dynamic impact forces may lead to ballast migration and/or ballast breaking and thus localised decrease of the total trackbed stiffness.

Above all the site uncertainties, the longitudinal variation in trackbed stiffness along the turnout is one of the biggest. To ease the numerical model validation process, an optimisation routine is proposed in order to calibrate the model.

The methodology is presented in Section 6.3.1, the initial estimation of trackbed stiffness distribution along the crossing panel in Section 6.3.2 and, finally, the results in Section 6.3.3.

### 6.3.1 Methodology

The methodology flow chart is reported in Figure 6.15.

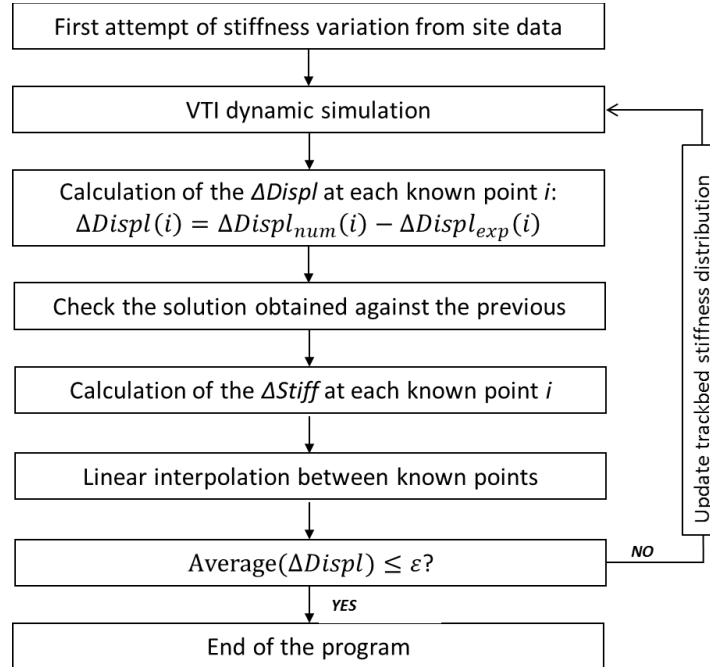


Figure 6.15: Methodology flow chart.

At the first step, the stiffness variation is calculated on the basis of the site data considering the differences of displacement of each bearer w.r.t. a reference one (for details see Section 6.3.2). After calculating the numerical displacement solution for the given configuration, the percentage difference between numerical and experimental data at each known point is computed for both the cess and the 6ft rail. Assuming linear relationship between applied force and displacement, the same percentage variation is applied to the trackbed stiffness after checking that the current solution is on average better than the previous one. A linear interpolation is applied between known points in order to get the stiffness at each simulated bearer, which is then used as input in the next iteration. The process is stopped when the average of the percentage difference at the cess and the 6ft rail is less than 7%. This value has been chosen as a sensible trade-off between accuracy and computational time.

Note that, since no information is given on the 6ft bearer end, the same variation between second and third bearer as that calculated for the cess end is assumed.

### 6.3.2 Initial estimation of support stiffness distribution

*Design methodology for track systems considering the long-term ballast behaviour:  
application to crossings*

In order to avoid the transient effect in the geophone measurements occurring when the first coaches pass, the deflection under the trailing bogie of the middle passenger carriage and next leading bogie has been used. In addition to that, the cess end has been considered in order to avoid the dynamics induced by the impact on the 6ft rail in the area of the crossing.

Considering bearer 6 as a reference bearer, it is possible to calculate the variation of stiffness  $\Delta K_b$  along the crossing in relation with this reference bearer starting from the variation of bearer displacement  $\Delta z/\Delta z(6)$ . Note that the assumed value for bearer 6 trackbed stiffness is the results of the combined reference trackbed stiffness ( $K_0$ ) 40 kN/mm/bearer end (taken from Li [129]) in series with the USP stiffness of 53.5 kN/mm/bearer end.

The results are reported in Table 6.7. The values are then used as initial estimation in the iteration calculation pictured in Figure 6.15.

*Table 6.7: Initial estimation for the variation of total trackbed stiffness (all stiffness per bearer end).*

<b>Bearer</b>	<b><math>\Delta z</math> [m]</b>	<b><math>\Delta z/\Delta z(6)</math> [%]</b>	<b><math>\Delta K_b</math> [%]</b>	<b><math>K_b</math> [kN/mm]</b>
1	1.525	126%	-26%	16.9
2	1.232	102%	-2%	22.5
3	1.287	106%	-6%	21.4
4	1.756	145%	-45%	12.6
5	2.128	176%	-76%	5.5
6	1.210	100%	0%	22.9
7	1.819	150%	-50%	11.4

### **6.3.3 Tuned trackbed stiffness distribution along the crossing panel**

The results in terms of percentage displacement difference between measurements and numerical simulations as well as the total trackbed stiffness are reported in Table 6.8 and Figure 6.16. The reduction of the objective function is shown in Figure 6.17.

Table 6.8: Variation of total tracked stiffness after the tuning (all stiffness per bearer end).

Bearer	Cess end		6ft end	
	$\Delta$ Displ [%]	$K_b$ [kN/mm]	$\Delta$ Displ [%]	$K_b$ [kN/mm]
2	3.2	23.1	-	28.1
3	5.8	21.1	3.4	28.1
4	1.3	18.2	4.2	13.8
5	1.2	20.4	-	6.4
6	10.3	44.8	1.5	26.6
7	1.1	9.8	-	16.6

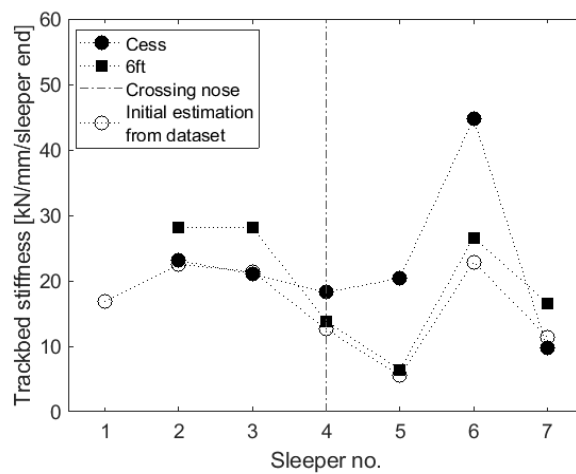


Figure 6.16: Variation of total tracked stiffness after the tuning.

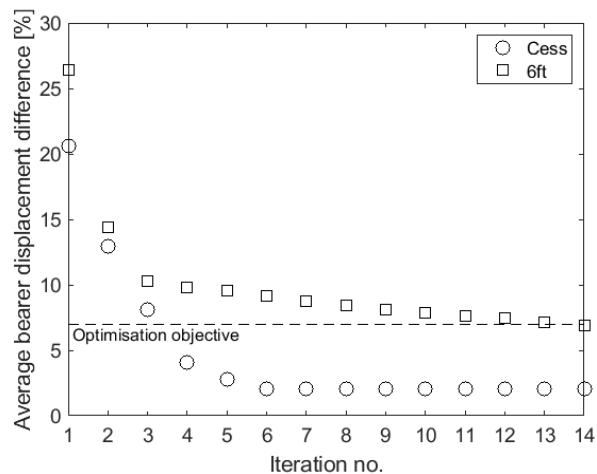


Figure 6.17: Objective function evolution with number of iterations (○: cess end; □: 6ft end).

Figure 6.16 shows that the dynamics influence the tracked stiffness. For example, at bearer 6 low displacement is registered, which can be explained with the high rigidity of the structure due to the long bearer, the localised rigidity from the casting and the rebound load after load transfer. On the contrary, at bearer 7 high displacement is registered and a possible

explanation is linked with dynamic loading at the leg end associated with transition to plain line rail.

From Figure 6.17 it can be deduced that the solution may vary depending on the threshold imposed, however a reasonable conversion is observed after six or seven iterations, particularly for the cess bearer end.

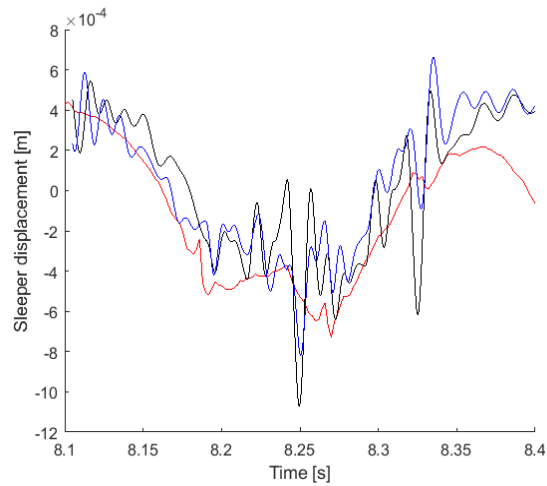
## 6.4 Bearer displacement validation along the crossing panel

The vehicle-track interaction model developed in Section 5 has been used for the following comparisons with experimental data considering (a) two independent wheelsets with external forces simulating the total axle load and (b) two wheelsets linked with a bogie and half car-body. The main inputs of the track and the vehicle systems are reported in Table 6.9.

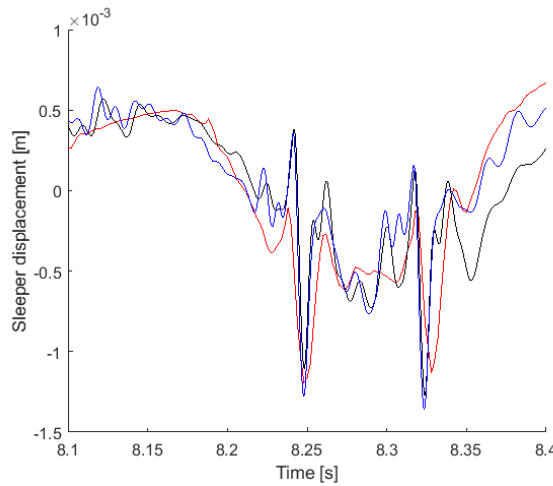
*Table 6.9: Main parameters of the track and vehicle system.*

	Parameter	Value	Units
Track	Rail type (plain line)	56E1	
	Bearer type	001E concrete	
	Rail-pad vertical stiffness	70	kN/mm
	Rail-pad loss factor	0.3	-
	Rail-pad lateral stiffness	60	kN/mm
	Trackbed vertical stiffness	As in Table 6.8	
	Trackbed loss factor	1.0	-
	Trackbed lateral stiffness	40	kN/mm
	Trackbed lateral damping	25% of the values in Table 6.8	
Vehicle	Vehicle type	Mark IV coach	
	Car-body mass	34300	kg
	Bogie mass	2469	kg
	Unsprung mass	1850	kg
	Primary vertical suspension stiffness	1.035	kN/mm
	Secondary vertical suspension stiffness	0.484	kN/mm
	Static axle load	110	kN
	Travelling speed	33	m/s
	Initial lateral displacement	0	mm

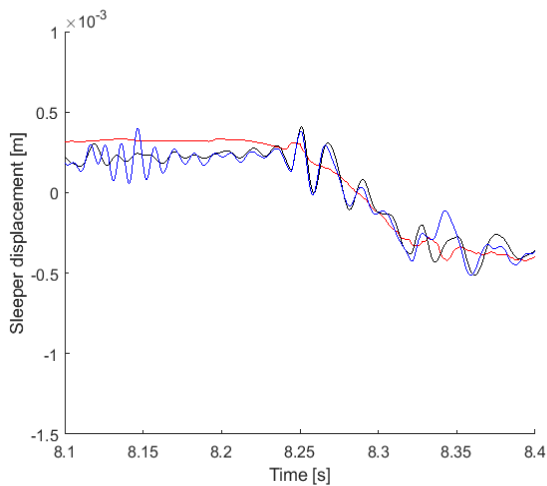
The comparison between experimental data and numerical results in terms of bearer displacement time history of the 6ft side at location 3, 4 and 6 in the time domain are shown in Figure 6.18.



(a)



(b)



(c)

Figure 6.18: Bearer displacement of the 6ft end at location (a) 3, (b) 4 and (c) 6 (red line: experimental data; black line: numerical results with un-linked unsprung masses; blue line: numerical results with complete vehicle). The displacement data has been collected by the Infrastructure Group team at University of Southampton, which is greatly acknowledged.

All the plots in Figure 6.18 show a very good agreement between the experimental



*Design methodology for track systems considering the long-term ballast behaviour: application to crossings*

data and the numerical results from both models considered in the low frequency range. In the higher frequency range, it is not possible to comment as the measured signal is low pass filtered and does not show any of the higher frequencies shown from both models.

The comparison for the first axle in terms of total bearer displacement at the cess and 6ft end is presented in Figure 6.19.

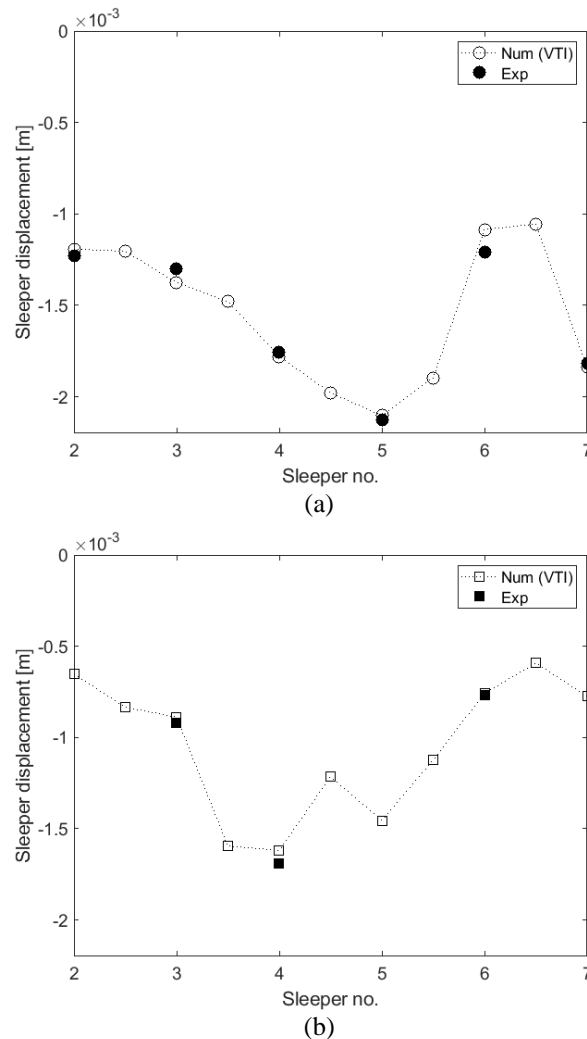


Figure 6.19: Comparison between numerical and experimental results in terms of bearer vertical displacement at (a) cess side and (b) 6ft side at first axle.

Figure 6.19 shows a very good agreement between numerical results and experimental data, with an average difference below 8%.

Looking at the measured data, it would be expected that the trackbed stiffness at the 6ft side would be stiffer than the cess side at the crossing nose location. Nevertheless, the increased bending stiffness of the whole track system (i.e. increased bending stiffness at the rail level and presence of long bearer) counter-balances this phenomenon and a lower

trackbed stiffness is calculated instead. Also, loss of trackbed support at the 6ft side around the crossing nose can be explained with the impact force, especially the P2 force component which is recognised to be influencing the trackbed degradation.

## 6.5 The influence of bearer flexibility

In this Section, the influence of bearer flexibility on the model results is discussed in detail. An additional set of results have been produced substituting the rigid bearer model with the flexible model using four elements in total (see Section 6.2.3 and Figure 6.20), i.e. two within the track gauge and two external. Note that the length of the external elements at the 6ft side varies along the track while the length of the internal elements and the external elements at the cess side is kept constant and equal to 0.75 m and 0.625 m, respectively.

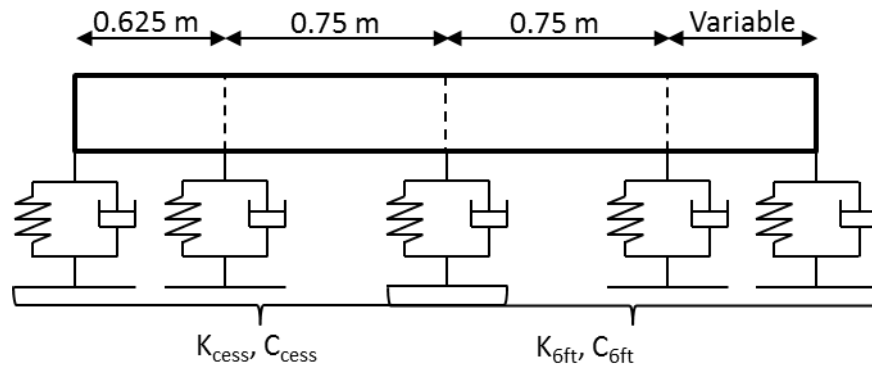


Figure 6.20: Semi-rigid bearer model.

Regarding the distribution of stiffness along the bearer length, the following assumptions have been made. Five springs are considered. To calculate the stiffness of each, the equivalent ones in the rigid model for the cess side and 6ft side are divided by 2.5. A non-constant distribution equal to “Variable 1” distribution (i.e. “centre-bound” case as explained in Section 6.2.1) is then assumed to reflect the results from the FE work carried in the project Track2Future by Alizadeh Otorabad [130], showing that the best approximation of the experimental results is obtained.

The trackbed stiffness has been tuned again following the same methodology proposed in Section 6.3.1. The comparison of rigid and flexible bearer model in terms of trackbed stiffness distribution and in terms of bearer displacement at cess side and 6ft side are shown in Figure 6.21 and Figure 6.22, respectively.

*Design methodology for track systems considering the long-term ballast behaviour:  
application to crossings*

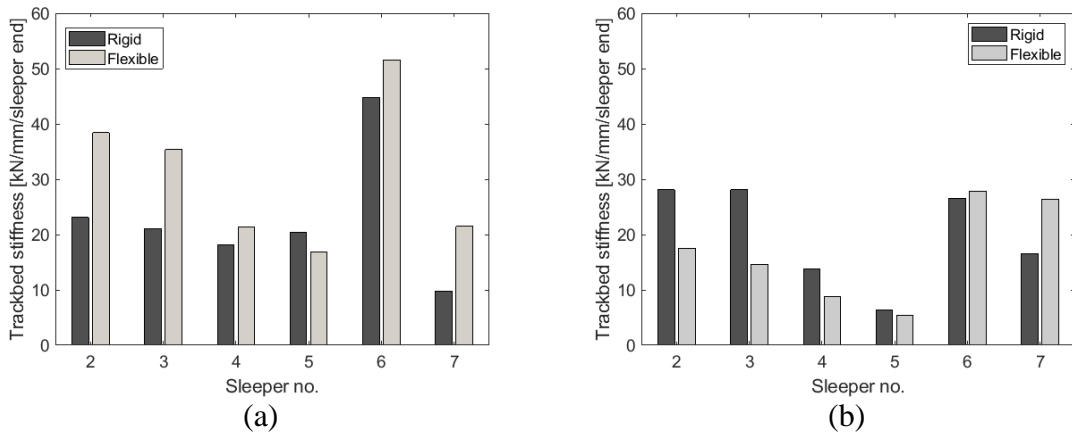


Figure 6.21: Comparison of rigid and flexible bearer model in terms of trackbed stiffness distribution at the (a) cess and (b) 6ft side.

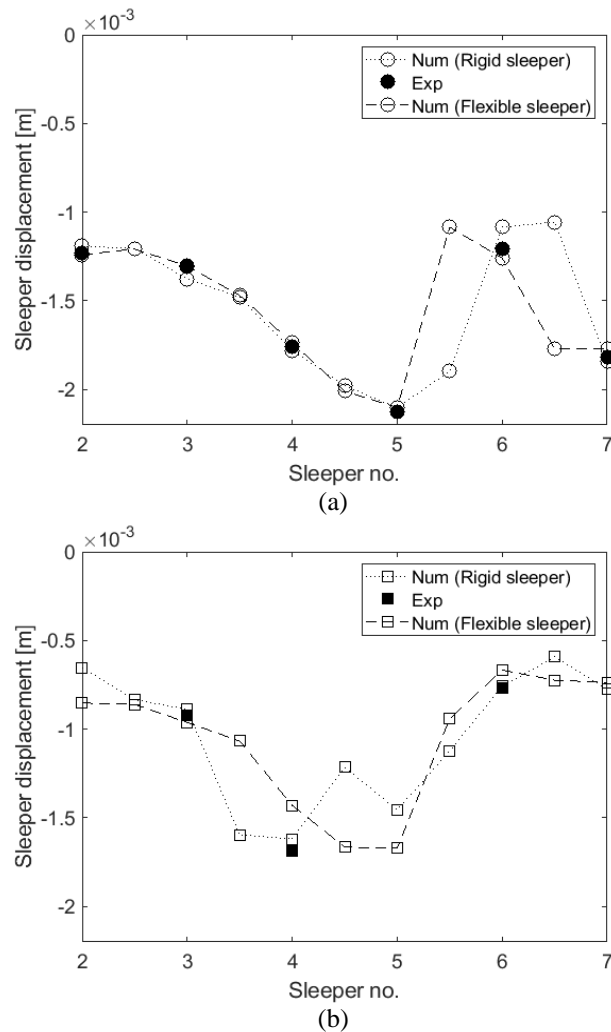


Figure 6.22: Comparison between numerical results with rigid bearer model and flexible bearer model and experimental results in terms of bearer vertical displacement at (a) cess side and (b) 6ft side at first axle.

Figure 6.22 shows that a change in equivalent trackbed stiffness for both cess side and 6ft side is needed in order to better match the experimental results available. Generally

speaking, stiffer trackbed is required for the cess side and slightly softer for the 6ft side. This can be explained with the fact that in the flexible bearer model an equivalent vertical stiffness is considered at the 6ft end of each bearer in addition to the equivalent rotation (see Figure 6.13 and Section 6.2).

The three-dimensional distribution of bearer displacement along the crossing panel is shown in Figure 6.23 and the three-dimensional distribution of maximum ballast forces in Figure 6.24.

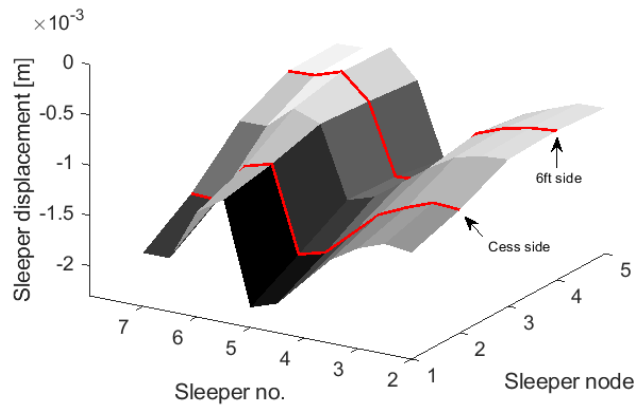


Figure 6.23: 3D map of bearer displacement along the crossing panel considering the flexible model. The rail positions are marked in red. The cess side is at node 2 and 6ft side at node 4.

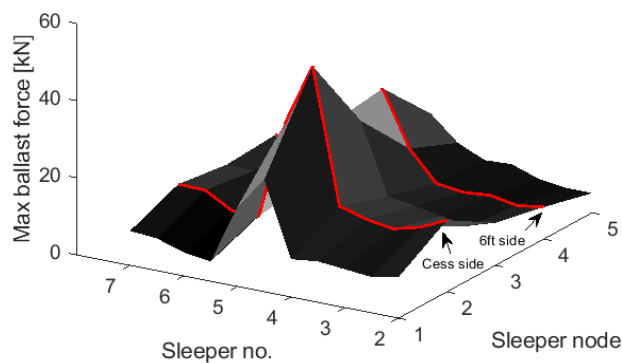


Figure 6.24: 3D map of maximum ballast force along the crossing panel considering the flexible model. The rail positions are marked in red. The cess side is at node 2 and 6ft side at node 4.

Figure 6.24 shows that the highest value of the maximum ballast force distribution occurs at the bearer under the crossing nose at the cess side due to the long bearer roll motion. The additional force at the cess side is a result of the low stiffness at the 6ft side making the outer rail heaving to support more passing load, in line with the finding of Li [12]. It can be

anticipated that this behaviour will change over time as the cess will degrade and loose support.

## **6.6 Summary**

In this Chapter, the validation of the vehicle-track interaction model against site measurements has been presented, including modelling considerations for the long bearer.

The chosen site is a double crossover equipped with USPs that has been monitored using geophones, accelerometers and MEMS sensors by University of Southampton. The crossing of the first turnout in the Down line (i.e. right-hand crossing with a 1:13 angle) has been used for the comparison and calibration of the model. TRC data has then been processed. For the rail top level irregularity, the turnout area on the cess side shows cyclic patterns whose wavelength corresponds to the typical vehicle dynamics dynamic response. In addition, the 6ft rail top level is undoubtedly influenced by the change in mass and stiffness properties at the crossing panel area, while the cess rail follows locally a similar trend with lesser amplitude. Regarding the top level rate of growth, the peaks occur on the 6ft side, as expected, at the switch-stock rail assembly area, at the weld in the closure panel, at the crossing nose and at the start and end of the long bearer areas. It is worth highlighting how the highest growth rate value for left and right side is located at bearers just after the crossing nose.

It is acknowledged that the long bearers are a key element in a crossing panel and their flexural behaviour plays an important role in the system response. Therefore, a study has been carried out to justify the modelling approach used hereafter. First, a two-dimensional vertical FE model of a single bearer has been developed using the Timoshenko beam theory and distributed trackbed support in order to capture the static bearer shape under symmetrical or asymmetrical loads with different trackbed configurations. The FE model is then compared to two other approaches (i.e. semi-flexible flexible considering four elements in line with the modal analysis and rigid bearer) that can easily be integrated in the numerical vehicle-track interaction routine. Since only the through route is considered in this research work, an equivalent shorter bearer is examined and the adjacent track is accounted for using an equivalent vertical stiffness and a rotational stiffness. The results show that when the semi-flexible model is used the model with both vertical and roll additional stiffness should be considered in order to best match the displacements under the rail seats of the full FE

model. On the other hand, when the rigid model is used, the roll additional stiffness is sufficient to replicate the displacement under both loading points.

It has been seen that above all the site uncertainties, the longitudinal variation in trackbed stiffness along the turnout is one of the biggest. To ease the numerical model validation process, an optimisation routine is proposed in order to close the gap between the numerical and experimental data. The results using the rigid bearer model show that stiffer trackbed is evaluated for the cress side and slightly softer for the 6ft side.

In a second stage, the semi-rigid bearer model is incorporated in the dynamic routine. The results in terms of optimised trackbed distribution are compared with the ones using the rigid model. Generally speaking, stiffer trackbed is predicted for the cress side and slightly softer for the 6ft side. This can be explained with the different modelling assumptions in terms of equivalent stiffness (i.e. only rotational for the rigid model and rotational and vertical for the semi-rigid). Also, distribution of ballast forces is plotted along the crossing panel the increase force under the 6ft is also significant compared to the rest of the panel and more significantly under the cress side due to the long bearer roll motion. The additional force at the cress side is a result of the low stiffness at the 6ft side making the outer rail heaving to support more passing load, in line with the finding of Li [12]. It can be anticipated that this behaviour will change over time as the cress will degrade and loose support.

## **7 Modelling the ballast long-term behaviour**

As explained previously in the literature review section (Section 3.3), there is a very wide range of equations available that aim to capture the ballast long-term behaviour. The settlement equations are principally driven by axle load and number of axle pass. However, few of them consider the actual track dynamics under the passage of a moving load using physical quantities such as sleeper displacement (see Guérin's equation), ballast forces (see Sato's equation), load amplification factor and trackbed stiffness (see Fröhling's equation). The general trend of these quantities, though, can vary with different applied loads and when the trackbed stiffness varies and, thus, the trend of the settlement prediction can be very different.

This Chapter discusses the influence of the loading and trackbed characteristics on the main physical quantities at the sleeper and ballast level using a simplified track FE model for plain line under a quasi-static excitation (Section 7.1) and a moving sinusoidal excitation (Section 7.2). The first approach is developed to capture mainly the loading frequencies typically used during laboratory tests (i.e. 1-15 Hz), while the second approach is used to capture higher loading frequencies that are typical of VTI. In Section 7.3 the main conclusions are discussed in relation to the equations that are commonly coupled with VTI modelling highlighting the strengths and the weaknesses of each. A new settlement approach is then proposed to overcome the main issues raised.

### **7.1 Application of an external quasi-static load**

A vertical two-dimensional ballasted track model with 20 sleepers has been developed in Matlab (see Figure 7.1) in order to assess the influence of load characteristics and trackbed stiffness on the main physical quantities involved in the track degradation process. The outputs investigated are sleeper displacement, velocity and acceleration and force, energy (i.e. product between the force and the displacement) and power (i.e. product between the force and the velocity) at the sleeper-ballast interface.

The vehicle load is applied as an external sinusoidal force with (1) a given amplitude reproducing different axle loads and relative dynamic amplifications and (2) a given

frequency reproducing different travelling speed. This is designed to replicate the set-up of ballast settlement laboratory tests. Also, the trackbed stiffness is assumed to be constant along the track.

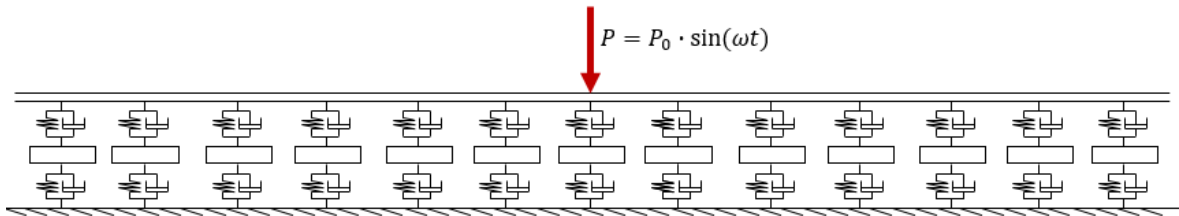


Figure 7.1: Vertical two-dimensional ballasted track model with sinusoidal force input.

The main inputs and the parametric variation considered are listed in Table 7.1 and Table 7.2, respectively.

Table 7.1: Main inputs for the track model.

Parameter	Value
Rail profile	60 E1
Rail-pad stiffness	140 kN/mm
Rail-pad loss factor	0.2
Trackbed stiffness (reference)	80 kN/mm/bearer end
Trackbed loss factor	0.5
Bearer type	G44 concrete bearer
Bearer spacing	0.65 m
Load amplitude (reference)	100 kN
Load frequency (reference)	3 Hz

Table 7.2: Parametric study on the track model.

Parameter	Value
Trackbed stiffness (kN/mm/bearer end)	20 to 150 with a step of 10
Load amplitude (kN)	40 to 360 <sup>6</sup> with a step of 20
Load frequency (Hz)	1 to 15 <sup>7</sup> with a step of 1

Figure 7.2 shows the variation of bearer displacement, velocity and acceleration varying load amplitude and frequency.

<sup>6</sup> These values correspond to axle loads between 12 t and 24 t with a dynamic loading and unloading of 50%.

<sup>7</sup> Considering an axle spacing of 3.0 m, the corresponding vehicle speeds are between 10 and 162 km/h. These frequencies are typical of laboratory tests.



*Design methodology for track systems considering the long-term ballast behaviour:  
application to crossings*

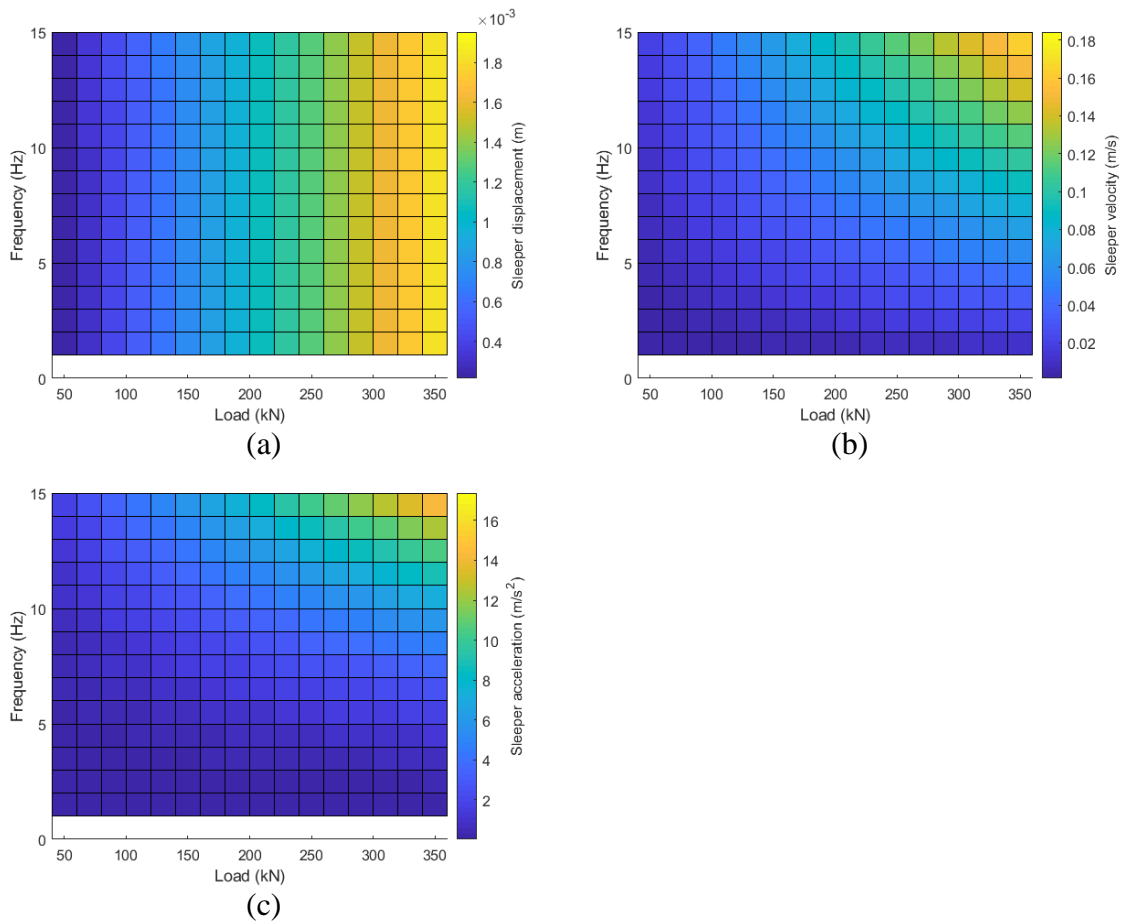


Figure 7.2: Variation of (a) bearer displacement, (b) velocity and (c) accelerations for different load and frequency considered.

While the bearer displacement (Figure 7.2(a)) is mainly influenced by the load, both load frequency and amplitude influence the velocity and the acceleration (Figure 7.2(b) and Figure 7.2(c)). This means that, for a given wheel load, a faster train causes higher velocity and accelerations of the sleeper over the ballast than a slower one. It is commonly recognised that high sleeper accelerations lead to ballast migration at the sleeper-ballast interface as well as stone breaking with a consequent re-arrangement of the particles, leading to a local acceleration of degradation process. Therefore, it is expected that faster trains cause higher settlement than slower one, for a given wheel load.

Figure 7.3 shows the variation of ballast force, ballast energy and power varying load amplitude and frequency.

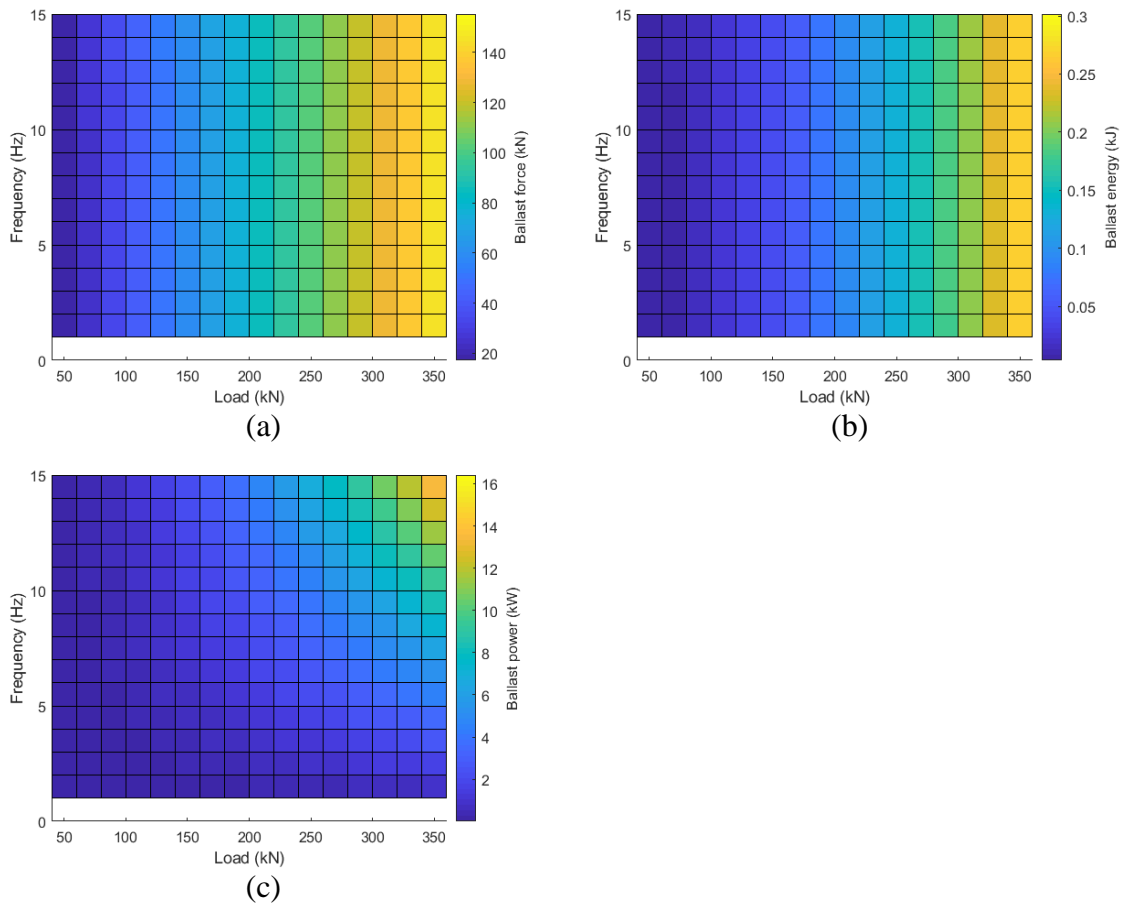


Figure 7.3: Variation of (a) ballast forces, (b) ballast energy and (c) ballast power for different load and frequency considered.

From Figure 7.3(a) and Figure 7.3(b) it is possible to notice that both the force and energy transmitted to the ballast increase with increasing load amplitude only, while the frequency effect is negligible. However, the ballast power is as much influenced by the load frequency as by the load amplitude (see the velocity trend in Figure 7.2(b)).

To summarise, all the physical quantities presented show an increase with increasing load, as expected. However, a few (i.e. sleeper velocity and acceleration and ballast power) also vary with the loading frequency and, thus, with the travelling speed when the moving load is considered (see following Section where the effects of the travelling load are discussed).

Figure 7.4 shows the variation of bearer displacement, velocity and acceleration varying trackbed stiffness for three load values.

*Design methodology for track systems considering the long-term ballast behaviour:  
application to crossings*

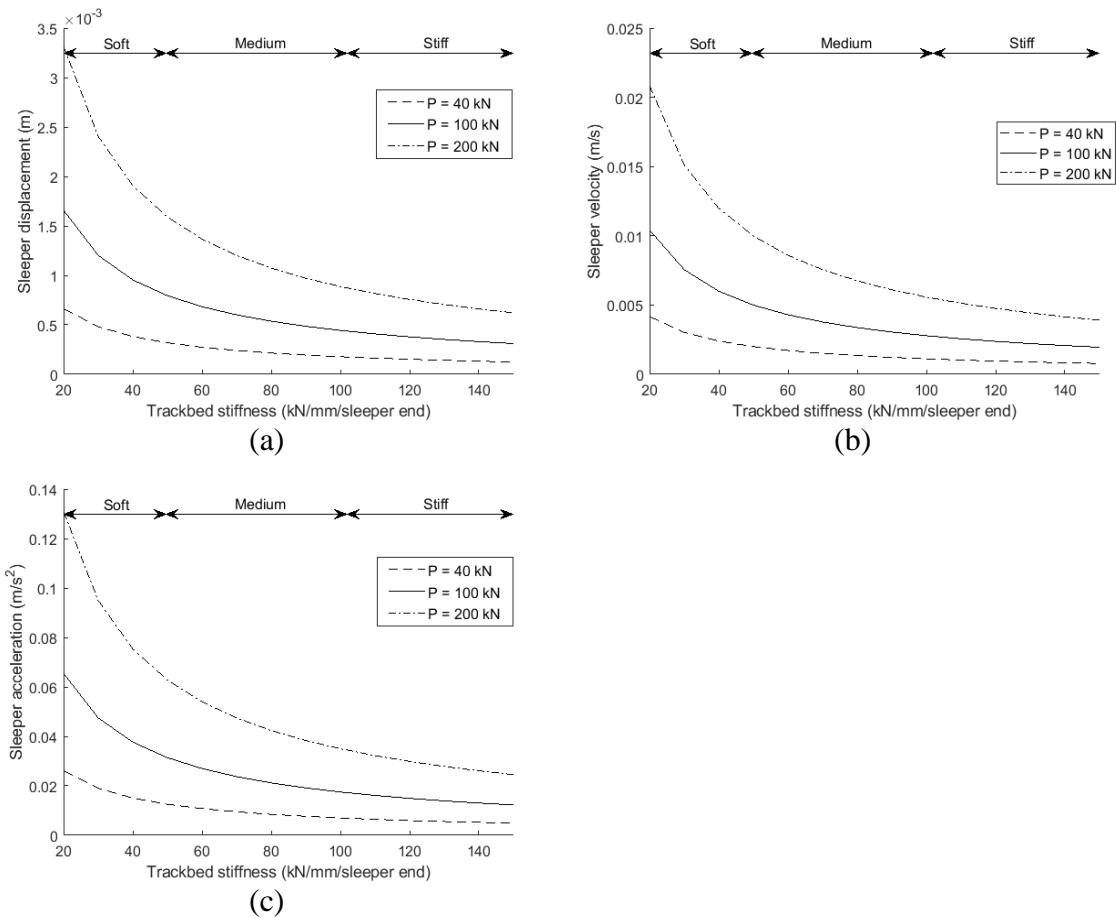


Figure 7.4: Variation of (a) bearer displacement, (b) velocity and (c) accelerations for different trackbed stiffness values and three loads considered.

All the quantities considered are exponentially decaying function of increasing trackbed stiffness. The highest responses are concentrated in the region of soft trackbed (i.e. 20-50 kN/mm), while for medium/stiff trackbed (i.e. higher than 60 kN/mm) the response converges to lower values. This means that the variation of sleeper quantities in stiff trackbeds is much lower than the case of soft trackbeds. Thus, even in the case of longitudinally variable trackbed stiffness, the relative variations of the physical quantities are limited leading to expected lower differential settlement (see Nielsen [131])

Figure 7.5 shows the variation of ballast force, ballast energy and power varying trackbed stiffness for three load values.

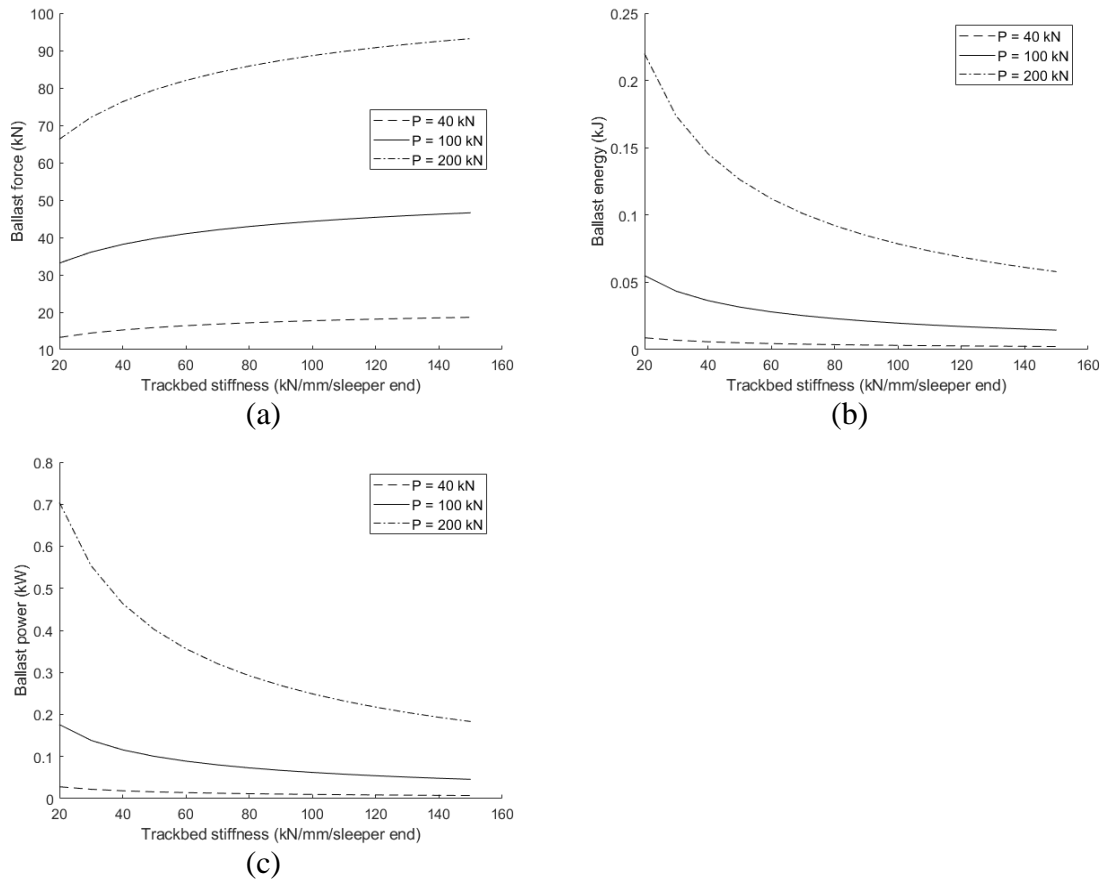
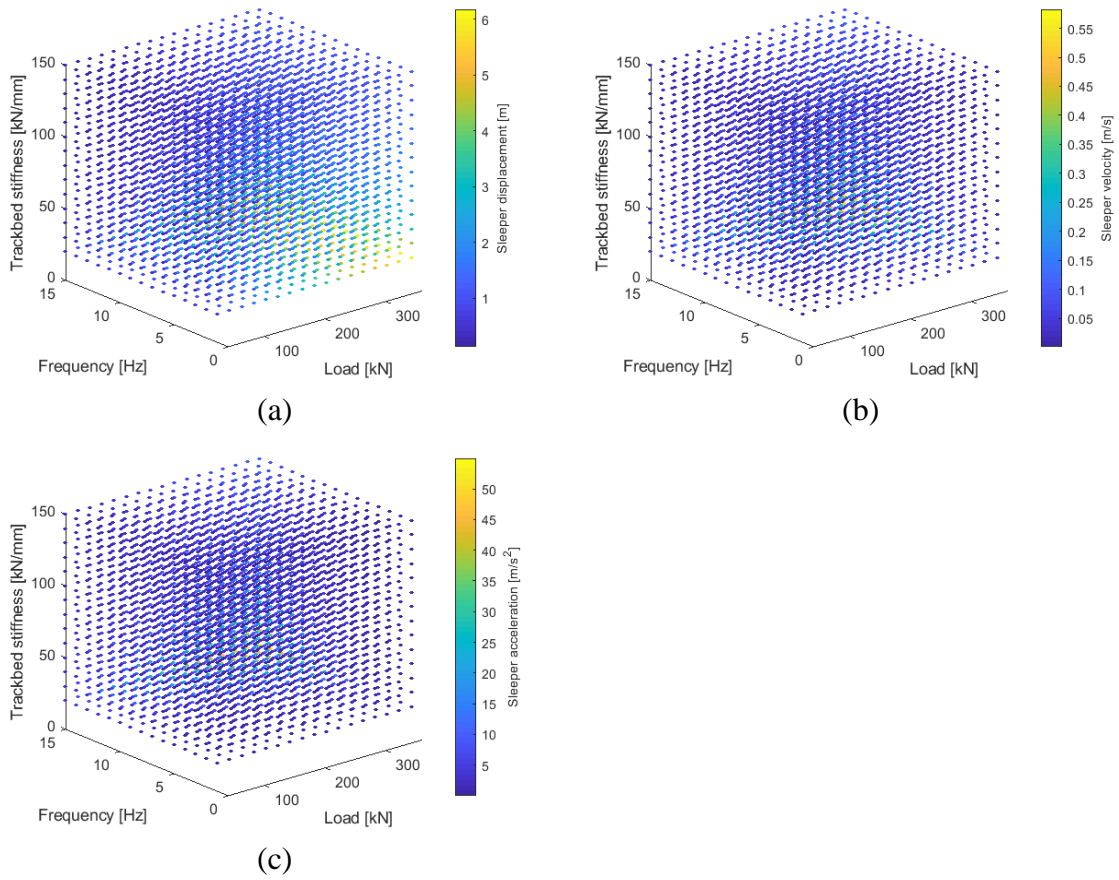


Figure 7.5: Variation of (a) ballast forces, (b) ballast energy and (c) ballast power for different trackbed stiffness values and three loads considered.

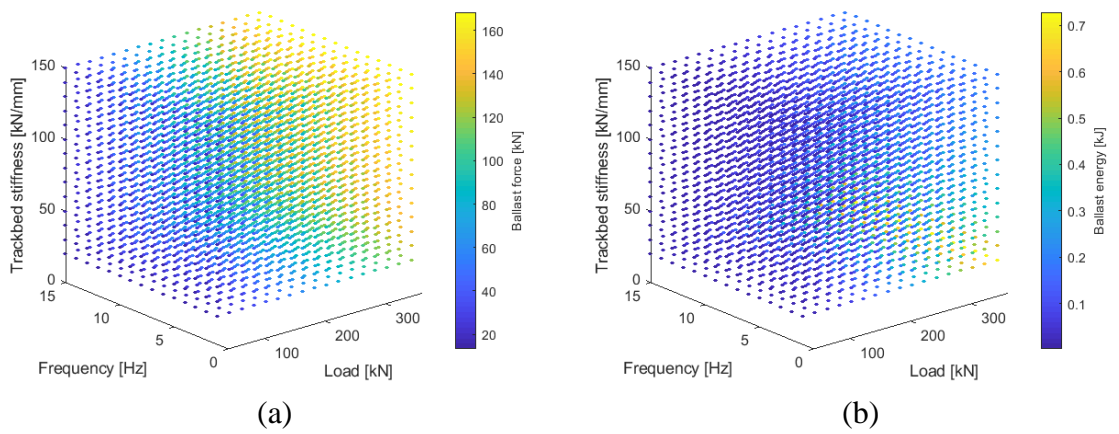
As expected, soft trackbed experiences a lower force level than a stiff one, but the energy content is higher. Thus, increasing trackbed stiffness there is a slight increase in ballast force associated with a significant decrease in ballast energy and power. This implies that soft trackbeds are characterised by higher energy transmitted to the ground than stiff trackbed and therefore expected higher ballast settlement. Using an analytical formulation of a vehicle-track interaction model in frequency domain, Sadri [132] has arrived to similar conclusions assuming that the only contribution to the ballast degradation is given by the viscous forces used to represent energy dissipation in most of linear track models.

Three-dimensional maps of sleeper and ballast quantities have been plotted in order to simultaneously consider the effect of load characteristics, frequency of loading and trackbed stiffness. The colour of markers indicates the relative magnitude of the quantity. They are shown in Figure 7.6 and Figure 7.7, respectively.

*Design methodology for track systems considering the long-term ballast behaviour: application to crossings*



*Figure 7.6: Three-dimensional variation of (a) bearer displacement, (b) bearer velocity and (c) bearer acceleration considering load characteristics and trackbed stiffness.*



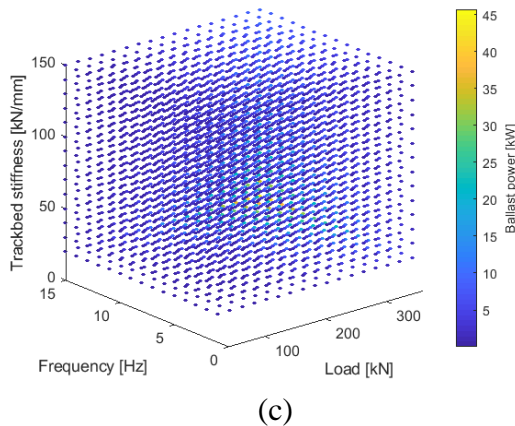


Figure 7.7: Three-dimensional variation of (a) ballast forces, (b) ballast energy and (c) ballast power considering load characteristics and trackbed stiffness.

From Figure 7.6(a), it is possible to notice that in the case of sleeper displacement the trackbed stiffness is the major influencing factor for a given load considered, while the frequency is reasonably negligible. On the contrary, in the case of velocity and acceleration the loading frequency is as critical as the trackbed stiffness (Figure 7.6(b,c)). This means that the settlement models that take into account sleeper velocity and/or acceleration are able to capture not only the effect of trackbed stiffness but also the effect of travelling speed.

As a direct consequence of this, Figure 7.7 shows that out of the other quantities the ballast power is the only one that is influenced by both the loading frequency and the trackbed stiffness.

Table 7.3 summaries the main findings.

Table 7.3: Summary of the findings from the parametric study. ↑: increase with the parameter consider; ↓: decrease with the parameter consider; -: no influence. The intensity is marked with the number of arrows from 1 (low influence) to 3 (high influence).

		Load amplitude	Load frequency	Trackbed stiffness
Bearer	Displacement	↑↑↑	-	↓↓↓
	Velocity	↑↑	↑↑	↓↓
	Acceleration	↑↑	↑↑↑	↓↓
Ballast	Force	↑↑↑	-	↑↑
	Energy	↑↑↑	-	↓↓↓
	Power	↑↑	↑↑↑	↓↓↓

The simultaneous variation of the three parameters considered shows that in the case of sleeper displacement, the trackbed stiffness is the major influencing factor for a given load considered, while the frequency is reasonably negligible. On the contrary, in the case of velocity and acceleration the loading frequency is as critical as the trackbed stiffness. This means that a settlement model that would take into account sleeper velocity and/or acceleration would be able to capture not only the effect of track bed stiffness but also the

effect of travelling speed. If that is the case then the ballast power is the only quantity among those considered that captures both the loading frequency and the trackbed stiffness and it might be considered as a suitable proxy for settlement calculations.

## 7.2 Application of an external moving load

Further investigations have been carried out to include the additional loading variation in mid-frequencies range, up to 1000 Hz, in order to capture not only the effects of the vehicle passing load equivalent frequencies (as covered in the previous Sections), but also the effect of the track dynamics, including wheel-ballast resonance (in the range 40-70 Hz), rail-sleeper resonance (in the range 40-200 Hz), sleeper passage resonance (in the range 100-200 Hz) and rail-railpad resonance (in the range 150-600 Hz) [133].

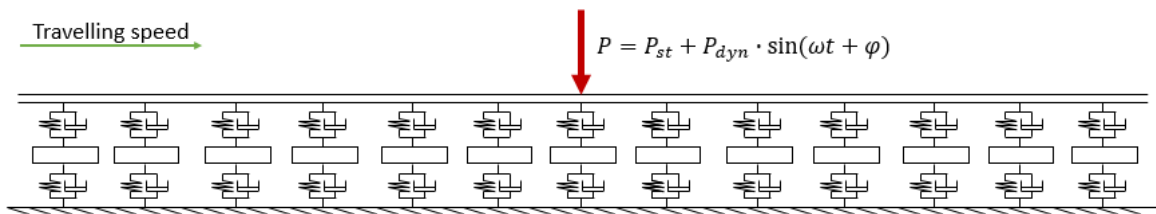


Figure 7.8: Vertical two-dimensional ballasted track model with travelling sinusoidal force input.

The set of parameters used are reported in Table 7.4. Note that the applied load has been divided in two parts, i.e. the quasi-static part of the moving load  $P_{st}$  and the added dynamic component part  $P_{dyn}$ , assumed to be 50% of the quasi-static load. The dynamic component is represented by a sine-wave with a  $\phi$  phase to reach a maximum on top of the monitored middle sleeper. This is especially important when low frequencies are considered, to avoid a lag between peak load and measured track response.

Table 7.4: Parametric study on the track model with travelling load.

Parameter	Value
Trackbed stiffness (kN/mm/bearer end)	20 to 150 with a step of 10
Wheel load (kN)	40 to 210 <sup>8</sup> with a step of 20
Dynamic load frequency (Hz)	1/3/5/10/40/50/60/70/80/90/100/110/120/130/140 200/250/300/400/500/700/800/900/1000
Travelling speed (km/h)	40 to 310 with a step of 30

Three-dimensional maps of sleeper (Figure 7.9) and ballast quantities (Figure 7.10)

<sup>8</sup> To match the range used in the static analysis (Section 7.1.1).

have been plotted for a travelling speed equal to 100 km/h, in order to simultaneously consider the effect of load characteristics (i.e. magnitude and frequency) and trackbed stiffness.

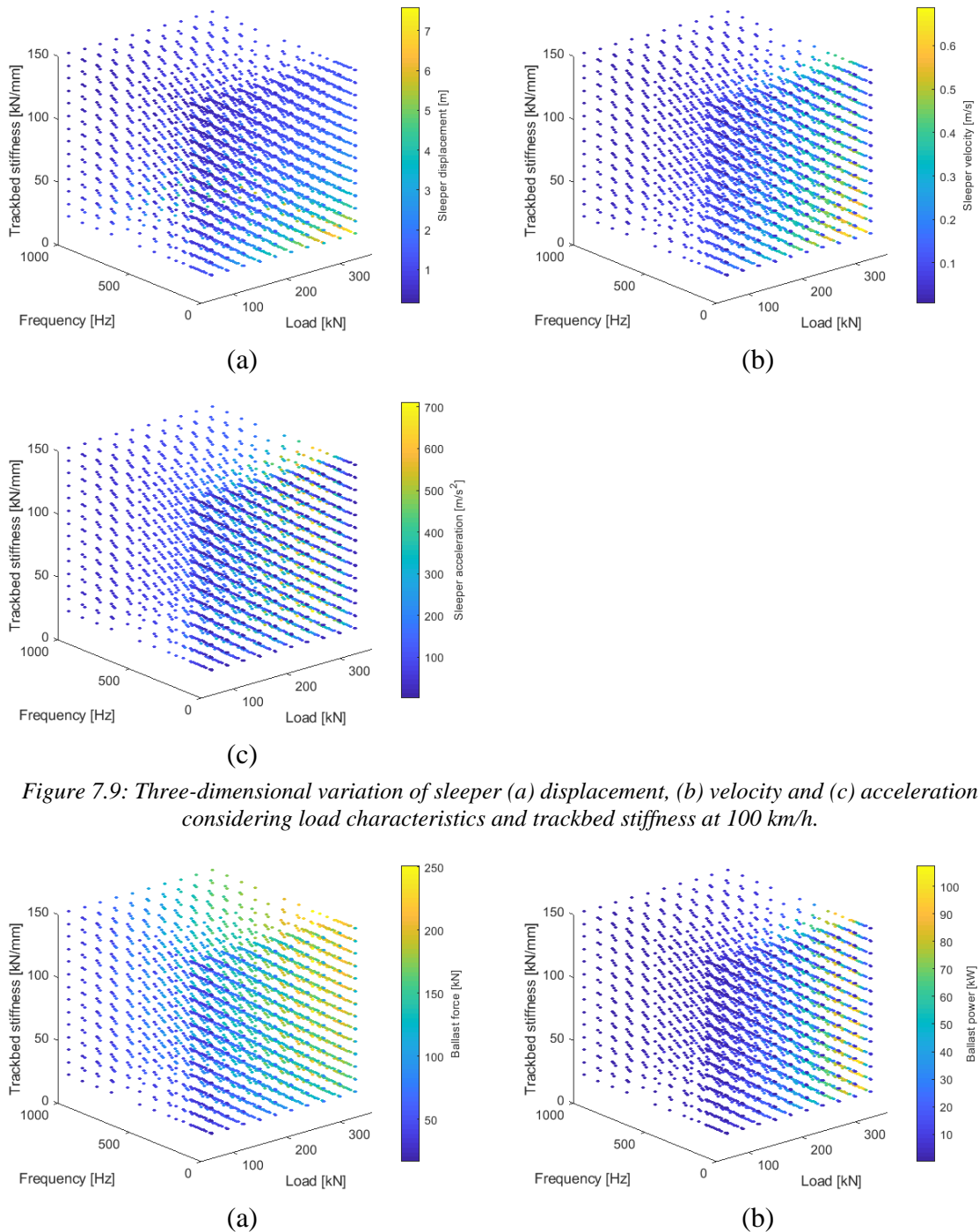


Figure 7.9: Three-dimensional variation of sleeper (a) displacement, (b) velocity and (c) acceleration considering load characteristics and trackbed stiffness at 100 km/h.



*Design methodology for track systems considering the long-term ballast behaviour:  
application to crossings*

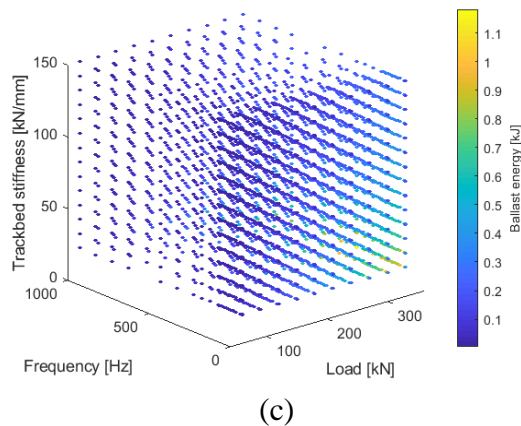


Figure 7.10: Three-dimensional variation of ballast (a) force, (b) energy and (c) power considering load characteristics and trackbed stiffness at 100 km/h.

Regarding the influence of trackbed stiffness and load amplitude, all the above figures show similar trends to the case of applied static load (see Table 7.3 for details), as expected.

In order to understand the influence of loading frequency, further analyses have been performed. Figure 7.11 shows the influence of this parameter on sleeper displacement, velocity and acceleration considering three trackbed stiffness values, a given static load (i.e. 100 kN) and a given travelling speed (i.e. 100 km/h).

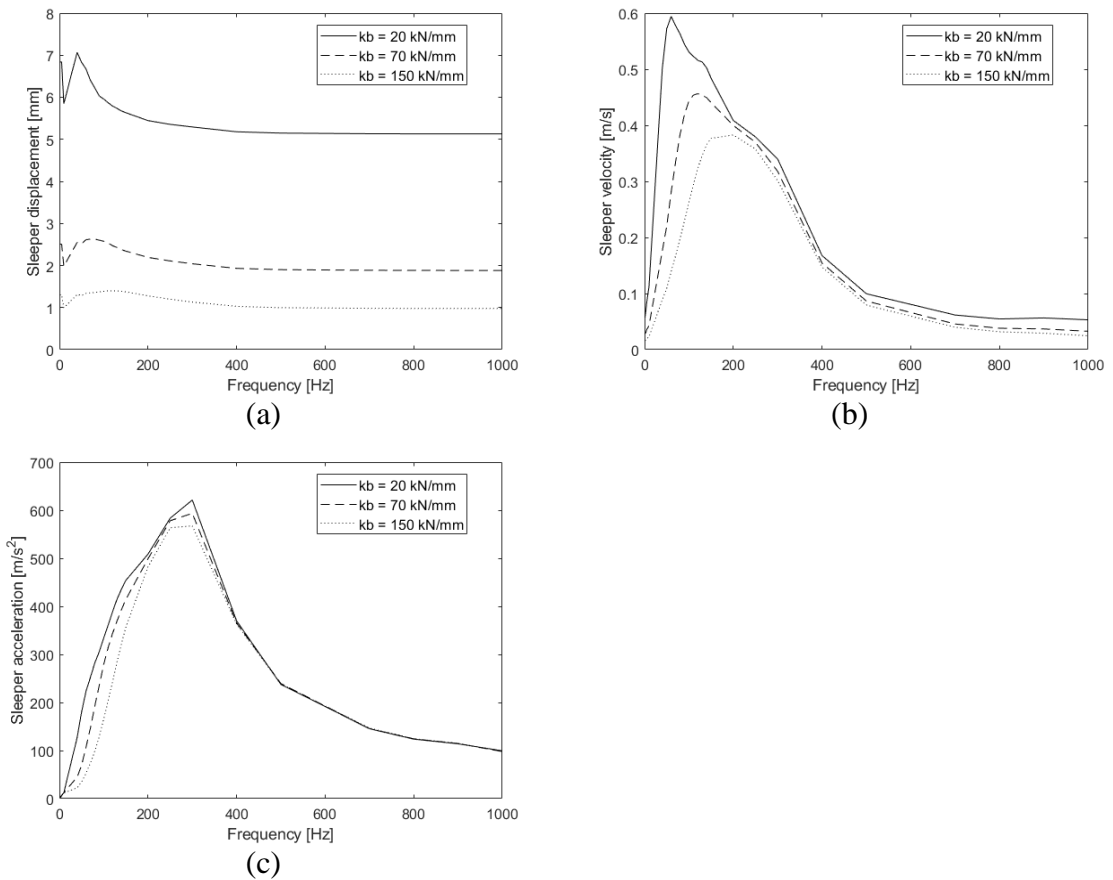


Figure 7.11: The influence of loading frequency on sleeper (a) displacement, (b) velocity and (c) acceleration for three different trackbed stiffness. The static load considered is 100 kN and the travelling speed is 100 km/h.

From Figure 7.11 it is possible to conclude that the loading frequency is affecting all the sleeper physical quantities considered. For instance, the maximum value of sleeper displacement and sleeper velocity occurs at roughly the first resonance peak of the track considered (see the mobility plot in Figure 7.12 showing the first and second resonance peaks), which represents the natural frequency of the coupled rail-sleeper mass bouncing in phase against the ballast spring stiffness. This is mainly dominated by the sleeper and the trackbed characteristics. On the other hand, the maximum value of the sleeper acceleration occurs at the second resonance peak, which represents the natural frequency of the sleeper mass bouncing out of phase with the rail mass [134]. This is mainly dominated by the rail-pad characteristics. The detected frequencies appear to be approximately invariant with increasing travelling speed considered as it is a function of mass and stiffness of the track-unsprung mass system. Combining these findings with the ones from the previous Section, it is possible to conclude that the sleeper velocity seems to be the quantity that can capture not only the vehicle characteristics in the range of low frequencies (i.e. up to 10-15 Hz) but

*Design methodology for track systems considering the long-term ballast behaviour: application to crossings*

also the trackbed characteristics in the range of medium frequencies (i.e. 50-200 Hz).

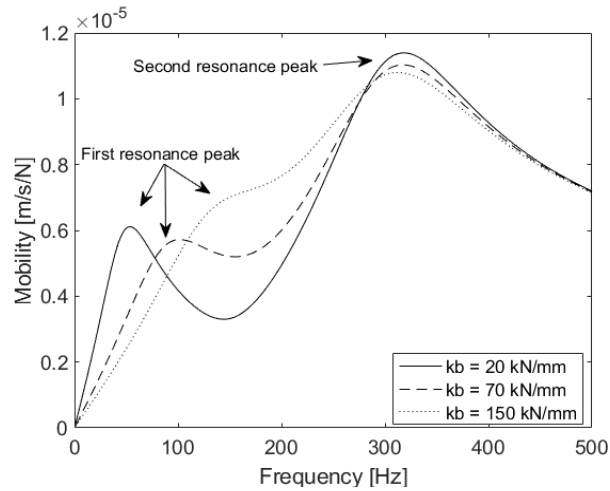


Figure 7.12: Mobility curve for three selected trackbed stiffness values.

Figure 7.13 shows the influence of loading frequency on ballast force, energy and power considering three trackbed stiffness values, a given static load (i.e. 100 kN) and a given travelling speed (i.e. 100 km/h).

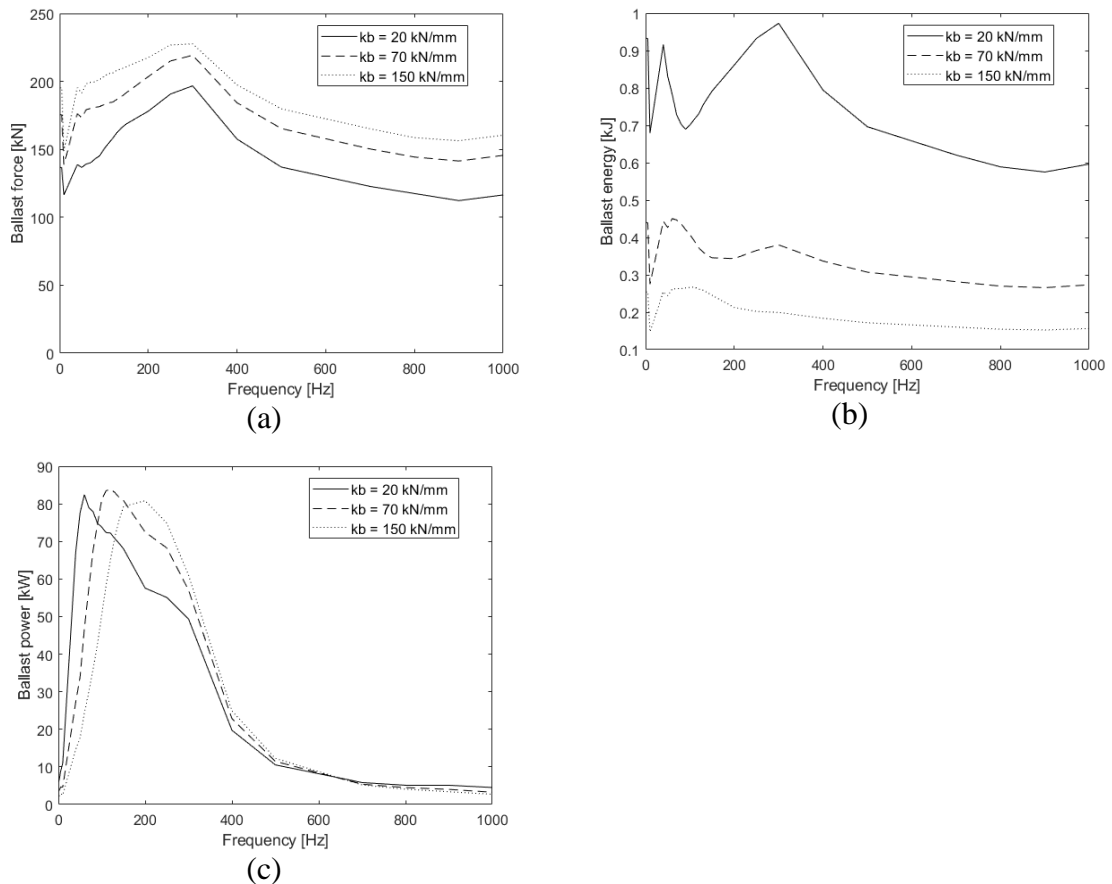


Figure 7.13: The influence of loading frequency on ballast force, energy and power for three different trackbed stiffness. The static load considered is 100 kN and the travelling speed is 100 km/h.

As in the case of sleeper quantities, the loading frequency plays an important role on the ballast quantities (Figure 7.13). For instance, the maximum value of the ballast force seems to be dominated by the second resonance peak of the track considered (Figure 7.12), the ballast energy by both the first and the second resonance peak and the ballast power by the first resonance peak and second peak to a lesser degree. These frequencies appear to be approximately invariant with increasing travelling speed considered. Combining these findings with the ones from the previous Section, the ballast energy seems to be the quantity that can capture mainly the whole track characteristics in the range of medium frequencies (i.e. 50-500 Hz), while the ballast power is the quantity for the vehicle characteristics and the trackbed characteristics.

To conclude, it has been seen that the current settlement equations account for either quasi-static forces or peak deflections. The VTI model or a moving load model, though, produces higher frequency dynamic loads that may have an influence on settlement and reveal more details into the triggering mechanisms for track deterioration. The results show that the ballast forces increase mainly around certain frequencies corresponding to the second track mode while the sleeper displacements increase around frequencies corresponding to the first track mode. In terms of settlement prediction using the numerical coupling with a VTI tool, this means that using an equation based on ballast forces (for example, a Sato's type equation) will fundamentally give different results than using an equation based on sleeper displacements (for example, a Guérin's type equation).

All these effects depend on many factors, including trackbed stiffness, track and vehicle characteristics and track irregularities and local defects. On the other hand, if settlement is related to the energy transmitted to the sub-structure, there will be a tendency for it to increase at frequencies corresponding to the first and second track mode. It is worth pointing out that the energy transmitted to the sub-structure is the sum of (1) a part that can be considered as elastically recoverable, mainly linked with the spring stiffness, and (2) a part that can be considered as dissipated and thus associated with the material degradation, mainly linked in terms of VTI model with the dashpot damping and the acceleration levels. Nevertheless, it is quite difficult to capture the system damping characteristics, especially using a linear model. Thus, this aspect is left as further work.

A summary of the main dominating frequencies for the sleeper and ballast quantities

is presented in Table 7.5.

*Table 7.5: Summary of the main dominating frequencies for the sleeper and ballast quantities.*

Parameter	Dominating frequency	
Sleeper	Deflection	First track mode
	Velocity	First track mode
	Acceleration	Second track mode
Ballast	Force	Second track mode
	Energy	First and second track mode
	Power	First track mode

### **7.3 Variation of ballast settlement predictions**

This Section contains the main novelty of the present research work. It explores in detail the consequences of the different behaviour shown by the main physical quantities varying load characteristics and trackbed stiffness (see Sections 7.1 and 7.2) on the settlement predictions according to the Guérin's, Sato's and Fröhling's equations. The strengths and weaknesses of each approach are pointed out. A new formulation is then proposed in order to overcome the main issues highlighted.

In Figure 7.14 the variation of settlement rate predictions according to the Guérin's, Sato's and Fröhling's equation varying the applied load amplitude and the trackbed stiffness is presented. The static load model is used in this case. Note that the Sato's equation used is in the form of [135]:

$$S_N = 4.365 \cdot P_b^{5.276} \cdot N \quad 7.1$$

Where  $P_b$  is the maximum bearer-ballast contact force in kN and  $N$  the number of cycles considered. Also note that the coefficients used in the Fröhling's equation are only valid for trackbed stiffness between 60 and 130 kN/mm and thus outside this range it is not possible to make predictions unless changing them.

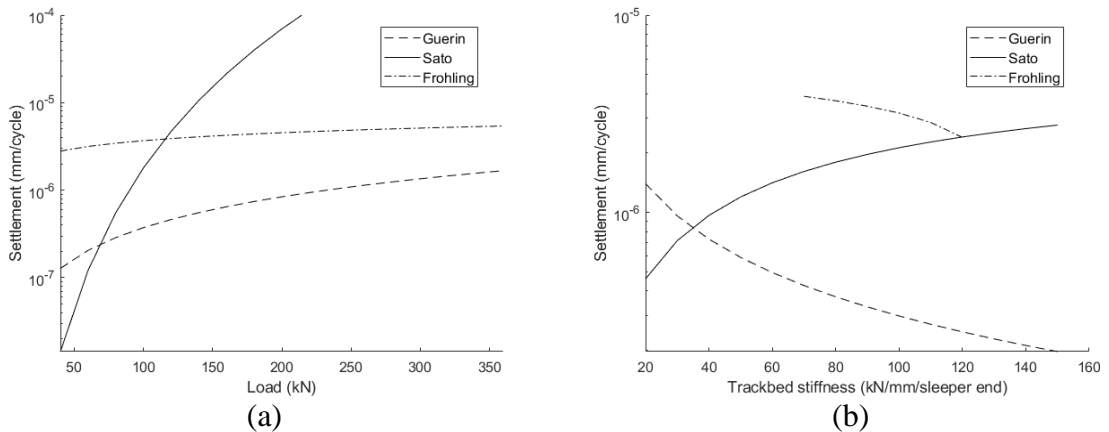


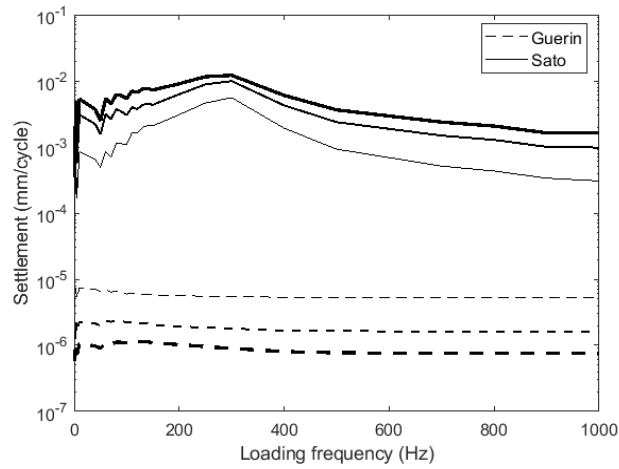
Figure 7.14: Variation of settlement rate predictions according to the Guérin's, Sato's and Fröhling's equation varying (a) the load amplitude and (b) trackbed stiffness.

Firstly, Figure 7.14 shows clearly the large discrepancy between the settlement rate predictions considering the Guérin's, Sato's and Fröhling's equations, not only in terms of actual values but also in terms of trend. For instance, the settlement rate according to the Guérin's and the Fröhling's equations slightly increases with increasing load and decreases non-linearly with increasing trackbed stiffness (i.e. stiffer supports will settle less than softer ones – this is in line with the series of track measurements shown by Nielsen [131]), while the settlement rate according to the Sato's model shows the opposite tendency (i.e. stiffer supports will settle more than softer ones). This can be explained with the opposite behaviours revealed by the main physical quantities involved, i.e. displacement for the Guérin's equation, the ballast force for the Sato's equation and variation in load and stiffness for the Fröhling's equation (see the summary in Table 7.3).

In addition, from Figure 7.14 it is possible to conclude that for wheel loads lower than 120 kN, the Sato's results are between the Fröhling's (upper limit) and the Guérin's (lower limit) ones. For higher loads, instead, the Sato's results are diverging from the other predictions. Also, only for very soft trackbeds (i.e. stiffness lower than 30 kN/mm), Sato's equation predicts lower settlement rate than Guérin's, while Fröhling's seems to converge to the Sato's results for medium/stiff trackbeds (i.e. stiffness between 110 and 130 kN/mm).

In Figure 7.15 the variation of settlement rate predictions according to the Guérin's and Sato's equations for increasing loading frequency and three different trackbed stiffness is shown using the travelling load model. The static load considered is 100 kN and the travelling speed is 100 km/h.

*Design methodology for track systems considering the long-term ballast behaviour:  
application to crossings*



*Figure 7.15: Variation of settlement rate predictions according to the Guérin's and Sato's equations for increasing loading frequency and three different trackbed stiffness (20, 70, 150 kN/mm for increasing line thickness). The static load considered is 100 kN and the travelling speed is 100 km/h.*

Once again, Figure 7.15 shows that increasing the trackbed stiffness leads to an increase in the Sato's predictions and a decrease in the Guérin's ones. In addition to that, the Sato's prediction is mainly dominated by the second resonance peak of the track considered and thus the rail-pad characteristics, as its main driver is the ballast force (see previous Section main results). On the other hand, the Guérin's prediction is mainly dominated by the first resonance peak of the track considered and thus the trackbed characteristics.

Ideally, the settlement equation used should account for all the main track resonance modes as well as the vehicle characteristics. Considering all the results previously shown, a possible solution can be written as follows:

$$S_N = A_{1s} \cdot N \cdot E_{b,max}^{A_{2s}} \quad 7.2$$

Where N the number of cycles considered,  $E_{b,max}$  the maximum energy in the ballast layer and  $A_{1s}$ ,  $A_{2s}$  the regression coefficients. These have been tuned in order to result in a settlement rate value between the Guérin's and the Sato's prediction, being  $A_{1s}$  equal to 0.001 and  $A_{2s}$  equal to 2.5.

The comparison of the settlement rate predictions variation with load, trackbed stiffness and loading frequency is shown in Figure 7.16.

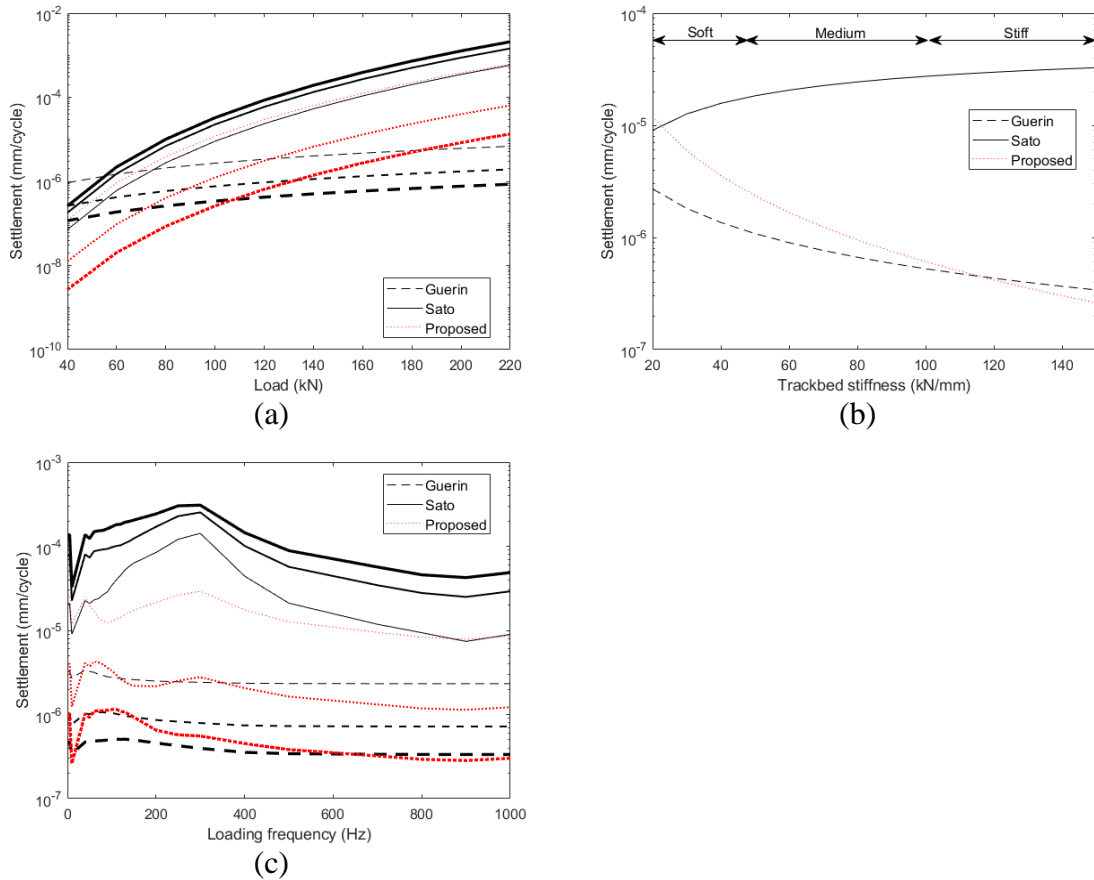


Figure 7.16: Variation of settlement rate predictions according to the Guérin's, Sato's and proposed equations for increasing (a) load, (b) trackbed stiffness and (c) loading frequency (scenarios considered: three trackbed stiffness values, i.e. 20, 70, 150 kN/mm represented by increasing line thickness, static load equal to 100 kN and travelling speed 100 km/h).

From Figure 7.16 it is possible to deduce the main characteristics of the proposed approach:

- An increase in external load leads to an increase in predicted settlement rate of logarithmic nature;
- An increase in trackbed stiffness leads to a rapid decrease in predicted settlement rate, especially in the region of soft (i.e. 20-50 kN/mm) and medium (50-100 kN/mm) supports. This implies that more energy is required to settle stiff track than soft track, as from experience on track;
- Dynamic loads at certain frequencies corresponding to the first and the second track mode lead to an increase in the predicted settlement rate.

All these attributes are in line with the long-term ballast behaviour seen in track.



## **7.4 Summary**

In this chapter, the fundamental physical quantities involved in driving ballast settlement, including sleeper displacement, velocity and acceleration and ballast force, energy and power, have been analysed in detail in response to variations in trackbed stiffness, axle load and loading frequency. A simplified vertical track FE model under a quasi-static and a travelling sinusoidal force has been used for this purpose.

The results from the quasi-static load model with the simultaneous variation of the three parameters considered show that considering sleeper displacement, the trackbed stiffness is the major influencing factor for a given load considered, while the frequency is reasonably negligible. On the contrary, in case of velocity and acceleration the loading frequency is as critical as the trackbed stiffness.

The results from the travelling load model show that the influence of the loading frequencies are strictly linked with the main track mode resonance frequencies. For instance, the sleeper displacement and velocity and the ballast power peaks occur around the first modal frequency, while the sleeper acceleration and the ballast force around the second modal frequency. The ballast energy is the only quantity that reflects both track modal frequencies as well as lower values linked with the vehicle characteristics. It has been noted that the total energy transmitted to the sub-structure is the sum of a recoverable part and a dissipated part that is associated with the material degradation. Nevertheless, it is quite difficult to capture the system damping characteristics, especially in case of a linear model. Thus, this aspect is left as further work (see Section 9.2 for more details on how to develop further the methodology).

Using the previous results from the quasi-static load model, the predictions of settlement rate according to Guérin's, Sato's and Fröhling's equations are compared varying the load and the trackbed stiffness. The results show clearly the large discrepancy between the predictions, not only in terms of actual values but also in terms of trend. For instance, the settlement rate according to the Guérin's and the Fröhling's equations slightly increases with increasing load and decreases non-linearly with increasing trackbed stiffness (i.e. stiffer supports will settle less than softer ones), while the settlement rate according to the Sato's model shows the opposite tendency (i.e. stiffer supports will settle more than softer ones). This can be explained with the opposite behaviours revealed by the physical quantities

involved, i.e. displacement for the Guérin's equation, the ballast force for the Sato's equation and variation in load and stiffness for the Fröhling's equation. Therefore, none of these results are entirely satisfactory and the need of a more comprehensive equation that can capture the trends seen on track as well as physical quantities that can be easily recorded *in situ* is highlighted.

Using the main conclusions from the travelling load model, a new settlement equation is proposed based on the maximum energy transmitted to the ballast layer, which in essence combines both deflection and forces quantities, both independent physical attributes of the reviewed settlement equations.

## **8 Predicting the rate of degradation at the study site**

The analysis carried out in Chapter 4 showed that the most common failure type at the crossing panel is the squats, which are mainly caused by an increase in contact stresses as well as trackbed degradation. The findings of the previous Chapter are used in the following Section to highlight how the proposed methodology can predict these aspects.

Section 8.1 details the interpretation of track recorded geometry data together with the back-calculated trackbed stiffness and the predicted wheel-rail contact forces. The comparison between recorded data and numerical predictions is shown in Section 8.2. Discussions about the importance of the sleeper flexibility are presented in Section 8.3 and discussions about the impact of correctly model the longitudinal variation of trackbed stiffness in Section 8.4. Finally, the main findings of this chapter are summarised in Section 8.5.

### **8.1 Interpretation of track recorded geometry data**

Figure 8.1 shows the rate of growth of the track top level that has been calculated as the difference between the data from March 2016 and the data from April 2016 (i.e. the period closest to the bearer displacement measurement campaign presented in Section 6.1) and normalised by 100 days. The back-calculated stiffness and stiffness gradient (see Section 6.2 for details) as well as the predicted wheel-rail contact forces are presented in the same figure. Note that the displacement measurements were taken at every other bearer.

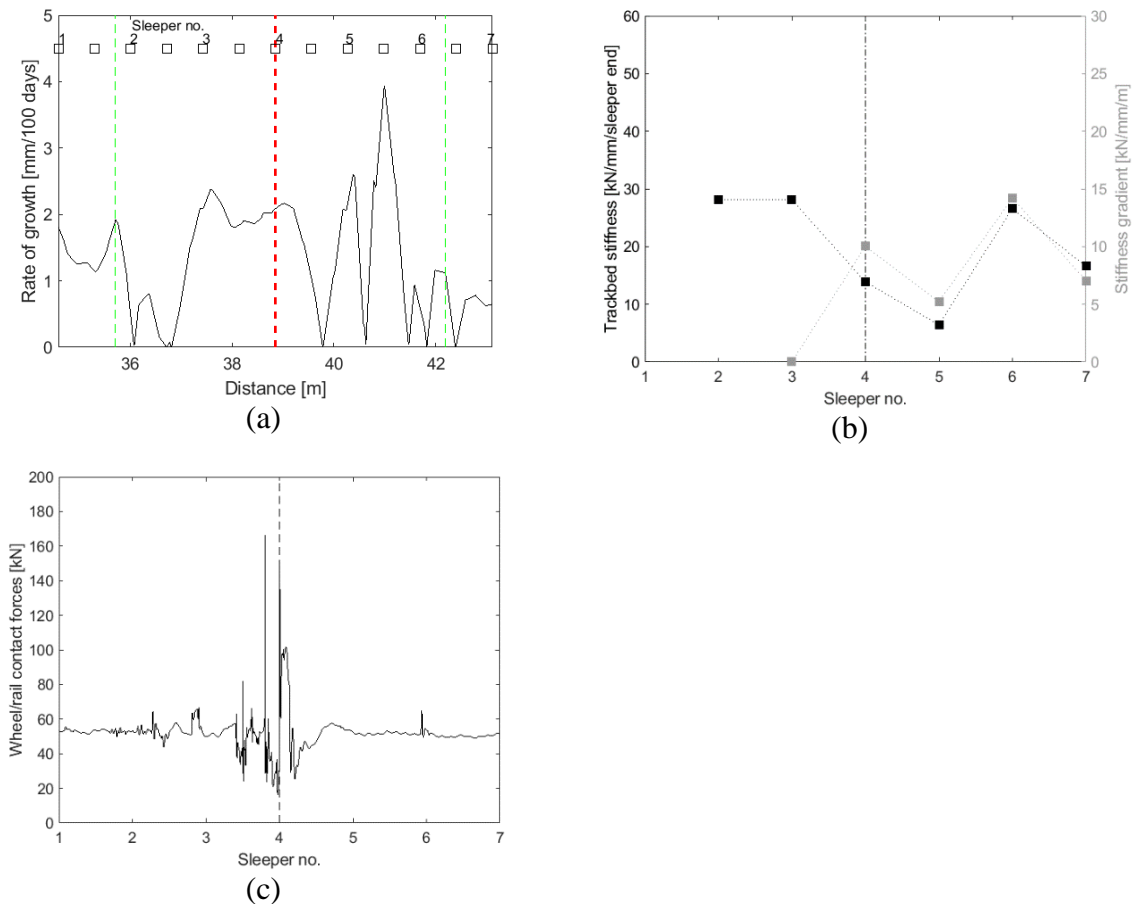


Figure 8.1: (a) Rate of growth of the track top level; (b) back-calculated trackedbed stiffness and stiffness absolute gradient; (c) predicted wheel-rail contact forces at the 6ft side. The crossing nose is marked with a vertical dashed line and the locations of leg ends with a green line.

From Figure 8.1(b), it is possible to isolate four main areas where deterioration occurs:

- between bearer 1 and bearer 2: this area is characterised by the weld at the leg end. It is well known how the change of rail section from standard to wing rail shape in conjunction with the weld profile (see for example Grossoni [136]) can trigger dynamic excitation at the wheel-rail contact level;
- between bearer 3 and bearer 4: this area is located just before the wheel transfer between wing rail and crossing nose, where a general load reduction before the load transfer area occurs in addition to a relative high trackedbed stiffness gradient;
- between bearer 5 and bearer 6: this is where the highest degradation occurs, corresponding to the highest displacement at the cess side and the lowest stiffness at the 6ft side as well as dynamic forces being transmitted to the lower

ground;

- between bearer 6 and bearer 7: this area is characterised by high longitudinal stiffness variation as well as dynamic loading happening at the leg end.

## **8.2 Comparison between numerical model and TRC data**

The available traffic data has been analysed for March 2014, i.e. the nearest month to the measurement period, and it has been assumed to be unchanged in the following two years. Almost 90% of the whole traffic operating on the site is passenger traffic. Thus, for simplicity of analysis, all the simulated trains have been given the same characteristics as the Mark IV coach (see Section 6 for the reference parameters).

The Class 91 locomotive is characterised by 32% higher axle load than the Mark IV coach, but the unsprung mass, which is considered the main driver of track settlement among the vehicle parameters, is comparable. Moreover, in a typical train configuration running in the site considered there are about 10 times more wheelsets of the Mark IV coach types. Therefore, only the contribution of the Mark IV coach has been considered hereafter

This Section is divided in two main stages. The first one shows the prediction of ballast settlement rates at the selected site using the Sato's and the Guérin's equations, pointing out the areas that are characterised by the highest differences with the TRC data. In the second part, the proposed settlement equation is improved and a good agreement with the site data is reached showing the validity of the tool.

In the first stage, Figure 8.2 shows the comparison between TRC data and numerical prediction using the Sato's and the Guérin's equation in terms of settlement growth per 100 days. The rigid bearer model is considered.

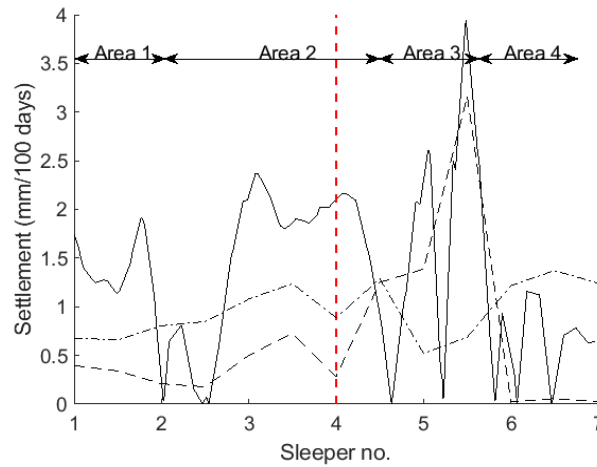


Figure 8.2: Comparison between TRC data (continuous line) and numerical predictions using the Sato's equation (dashed line) and Guérin's equation (dashed-dotted line) in terms of settlement rate. The crossing nose position is marked with the dashed red line.

From Figure 8.2, it is possible to conclude that the general trend of settlement growth is captured by the numerical model using both the Sato's and the Guérin's equations. It is therefore possible to use either of these within a reasonably fast methodology to compare different design approaches and assess them not only considering the dynamic impact but also the long-term ballast behaviour, as shown in Chapter 7.

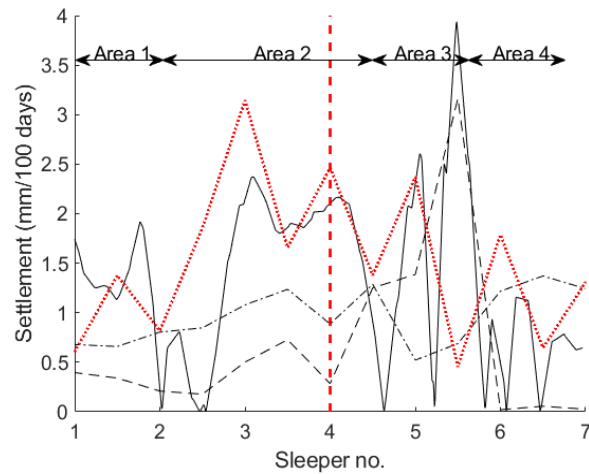
Some differences are, though, present. For instance, the Guérin's equation seems to be more suitable for representing area 1, area 2 and area 4 characterised by averagely constant rate, while the Sato's equation appears to be more suitable for area 3 which is characterised by high transient ballast force linked to the P2 impact force.

In a second stage, the equation proposed in Section 7.3 has been slightly changed to take into account the dynamic amplification happening at the ballast level as follows:

$$S_N = A_{1s} \cdot N \cdot E_{b,max}^{A_{2s}} \cdot \left( \frac{F_{b,max}}{F_{b,stat}} \right)^{A_{3s}} \quad 8.1$$

Where  $N$  is the number of cycles,  $E_{b,max}$  the maximum ballast energy,  $F_{b,max}$  the maximum ballast force and  $F_{b,stat}$  the ballast force under the static wheel load. The regression coefficients  $A_{1s}$ ,  $A_{2s}$  and  $A_{3s}$  have then calibrated in order to achieve the best fit of the predicted settlement with the TRC data (i.e.  $1.935 \cdot 10^{-5}$ , 1.5 and 5, respectively). The results comparing the TRC data and the numerical predictions in terms of settlement rate are presented in Figure 8.3.

*Design methodology for track systems considering the long-term ballast behaviour:  
application to crossings*



*Figure 8.3: Comparison between TRC data (continuous line) and numerical predictions using the Sato's equation (dashed line), Guérin's equation (dashed-dotted line) and the proposed equation (dotted red line) in terms of settlement rate. The crossing nose is marked with the dashed red line.*

From Figure 8.3 it is possible to reasonably conclude that the proposed equation is able to capture the settlement rate trend of the TRC data not only in the area around the crossing nose (Area 2) matching adequately the peak values, but also in Area 3 where the collected data show a local peak. The main difference appears to be in Area 4, where the predictions suggest an increase in local degradation rate. This can be explained with the fact that locally there is a low trackbed stiffness and thus a high settlement prediction.

### **8.3 The influence of sleeper flexibility**

Figure 8.4 shows the comparison between TRC data and numerical prediction using the rigid bearer model and the flexible bearer model in terms of settlement growth per 100 days. The Guérin's equation is considered as it is the one showing the best match with measurement data within the equations available in literature.

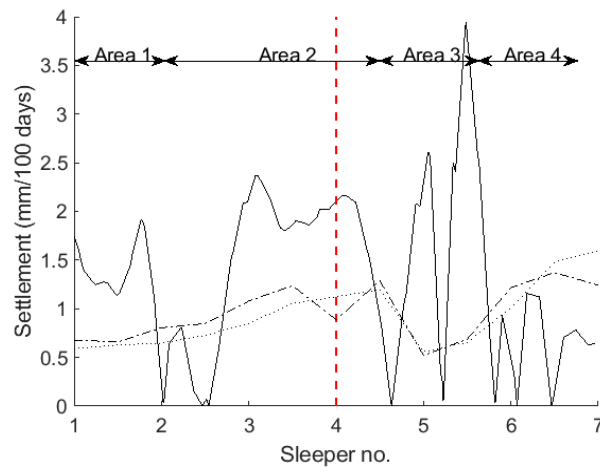


Figure 8.4: Comparison between TRC data (continuous line) and numerical predictions using the rigid bearer model (dashed-dotted line) and the flexible bearer model (dotted line) in terms of settlement growth. The crossing nose is marked with the dashed red line.

The differences between rigid and flexible bearer model are rather negligible when the settlement rate of growth is considered, as presented in Figure 8.4. Nevertheless, the advantage of the latter model is that it can give information not only on the longitudinal variation of settlement but also on the transversal one, helping assessing the bearer stiffness over time as well as its possible susceptibility to crack due to developed bending stresses.

## 8.4 The influence of trackbed conditions

From the experimental measurements presented in Chapter 6, it has been seen that the variability of the trackbed stiffness plays a fundamental role in defining the whole system behaviour not only in the longitudinal but also in the transversal direction. Nevertheless, in the literature this aspect is commonly neglected and a constant value is considered along the whole crossing panel. The main aim of this Section is to quantify the impact of this assumption in the short- and long-term system behaviour prediction.

### 8.4.1 Dynamic results of two wheelset passages

Figure 8.5, Figure 8.6 and Figure 8.7 show the comparisons between the case with constant trackbed stiffness and with variable trackbed stiffness in terms of bearer displacement and contact forces along the crossing panel.



*Design methodology for track systems considering the long-term ballast behaviour:  
application to crossings*

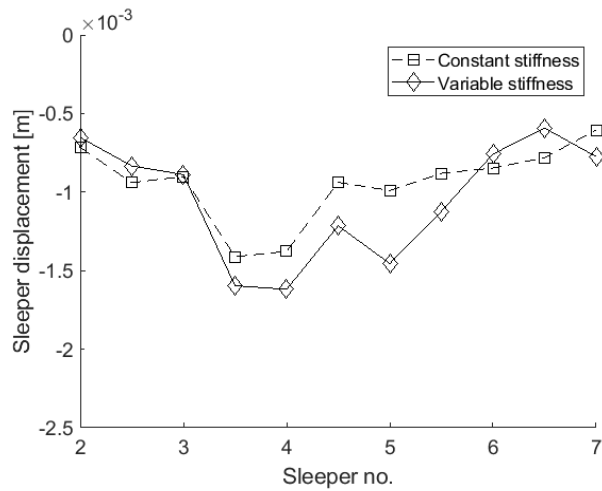


Figure 8.5: Comparison between the case with and without considering variable trackbed stiffness in terms of bearer displacement at the 6ft side.

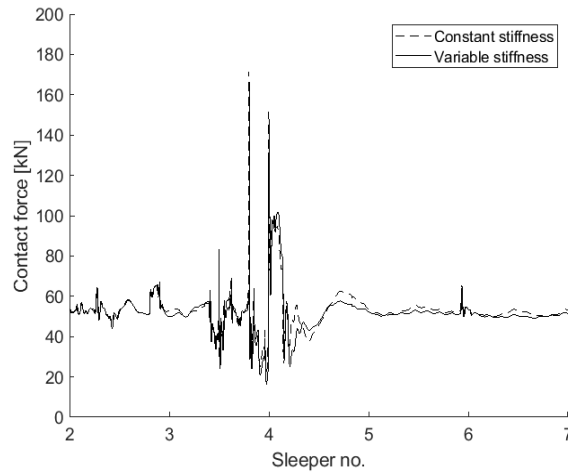


Figure 8.6: Comparison between the case with and without considering variable trackbed stiffness in terms of contact forces at 6ft side.

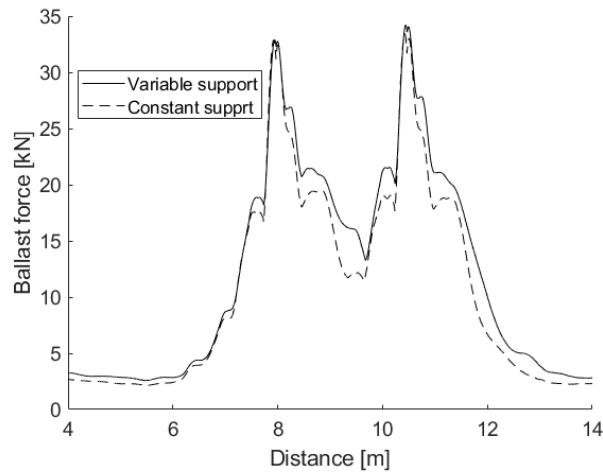


Figure 8.7: Comparison between the case with and without considering variable trackbed stiffness in terms of ballast forces at 6ft side of bearer 4.

Table 8.1: Summary of contact forces and bearer displacements for the cases analysed.

		Baseline scenario (constant stiffness)	Variable stiffness	
			Value	Δ w.r.t. baseline
Contact forces [kN]	P1 force	151.3	147.6	-2%
	P2 force	97.2	101.8	5%
	Standard Deviation (2 to 7)	7.7	8.2	6%
Ballast forces [kN]	Force under bearer 4	34	33.2	-2%
6ft side bearer displacements [m]	Maximum at bearer 4	0.00138	0.00162	17%
	Maximum at bearer 5	0.00099	0.00146	47%
	Maximum at bearer 6	0.00085	0.00076	-11%
	Maximum at bearer 7	0.00061	0.00077	26%
	Standard Deviation (2 to 7)	0.00025	0.00038	52%

Considering the actual variation in stiffness (see Figure 8.5, Figure 8.6 and Figure 8.7) leads to slightly different response in terms of predicted wheel-rail contact forces especially in the areas where local support deficiency is not accounted for (e.g. 5% increase in the P2 force and 6% decrease in the signal standard deviation). Regarding the bearer displacement, differences between considering and not considering the variable stiffness distribution range between -11 and +47%. The signal standard deviation difference is very high, reaching 52%. These discrepancies can contribute to important under- or over-prediction of long-term behaviour of the track.

### 8.4.2 Settlement rate analysis

Figure 8.8 shows the comparison of the case considering and not considering the longitudinal variation of trackbed stiffness in terms of settlement growth rate along the crossing panel.

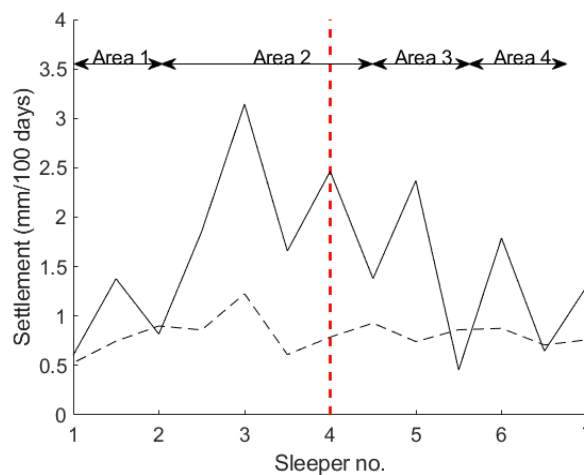


Figure 8.8: Comparison of the case considering (continuous line) and not considering (dashed line) the

*Design methodology for track systems considering the long-term ballast behaviour:  
application to crossings*

*longitudinal variation of trackbed stiffness in terms of settlement growth rate along the crossing panel. The crossing nose is marked with the vertical line.*

As expected from the previous Section, not considering the variation in trackbed stiffness leads to significant errors in long-term predictions, namely a decrease in the mean value of -47% and in the standard deviation of -79% w.r.t. the case of considering the variation. Therefore, it is crucial to include this aspect in the modelling used to predict the long-term behaviour of the track.

## **8.5 Summary**

This chapter summarises the application of the findings from the previous chapter to the assessment of settlement rate for the selected study site.

The TRC rail top level data is used to calculate the rate of settlement growth at the crossing panel. The main areas of the graph are highlighted in combination with the back-calculated trackbed stiffness and the predicted wheel-rail forces.

The rate of degradation is predicted using the Sato's and the Guérin's equations and compared with measurement. The general trend of settlement growth is captured by the proposed numerical model. Some differences are, though, present and cannot be captured by the settlement equations considered.

The new equation is then slightly modified to include a dynamic ballast force factor. The results show a reasonably good agreement between TRC data and numerical predictions, revealing the strength and advantages of the proposed methodology and proposed equation. Therefore, this tool can be used as a methodology to compare different designs proposed and assess them not only considering the dynamic impact but also the long-term ballast behaviour.

Finally, the differences in the prediction considering constant and variable trackbed stiffness are quantified in the short- and long-term system behaviour. The results consistently show important differences between the two cases, up to 47% in case of vertical bearer displacement and 79% in case of standard deviation of the rate of settlement growth. It is thus clear how these discrepancies can contribute to important under- or over-prediction of long-term behaviour of the track.

## 9 Conclusions, discussion and further work

Switches and Crossings (S&Cs) have been proven to be the central part of the railway infrastructure and, at the same time, are subjected to the highest failure rates. One of the main root causes identified is the non-uniform track degradation over time that leads to further failures in the whole system. The main aim of this research was to propose a methodology that is able to assess a range of design options from the understanding of transient loading and a long-term point of view.

In Section 9.1 the summary of the main achievements of this work and the conclusions are presented, and in Section 9.2 the recommendations for further work are listed.

### 9.1 Summary of achievements and conclusions

A detailed review of the current methodologies to model the dynamic behaviour of the vehicle and track coupled system with a specific focus on the S&Cs was given in Chapter 3. Additionally, the large variety of ballast settlement models present in the literature has been identified, highlighting the fact that the long-term predictions are intrinsically linked to the methodology adopted to develop the equation (i.e. from laboratory test, from *in situ* tests or from theoretical models) as well as to the condition considered. Three equations, i.e. Sato's, Guérin's and Fröhling's, were then studied in detail in relation to the coupling of the dynamic track behaviour with the long-term ballast evolution, as these are models directly use the dynamic outputs as input in the long-term predictions. Nevertheless, all three present disadvantages. The first equation is based on the ballast pressure and shows increasing settlement for increasing trackbed stiffness, which is against what it is usually experienced on track (i.e. stiffer supports lead to less settlement than softer supports). The maximum displacement that is at the base of the second equation cannot be directly related to plastic deformation of ballast under varying conditions. In the case of the third equation, a number of factors are used which are difficult to calibrate for different cases and track configurations, in particular the way the load is distributed from the contact level to the ballast level. Therefore, the necessity of proposing a new settlement equation to be used in the vehicle-track interaction context is highly recommended.

*Design methodology for track systems considering the long-term ballast behaviour:  
application to crossings*

The statistical analysis of a large failure database from the UK railway network was presented in Chapter 4 focussing on the types of failures occurring at the crossing panel. It has been seen that even if the occurrence of the transversal cracking of casting is very low (about 5%), it represents a very expensive failure mode requiring the complete replacement of the casting and is very much a priority for infrastructure managers in the UK. It has been identified that this failure mode is directly linked with the non-homogenous longitudinal support conditions and thus the ballast differential settlement, providing a major motivation to support the whole work carried out.

As one of the major achievements of the current work, the development of a three-dimensional vehicle-track interaction model at the crossing panel was introduced in Chapter 5, including the detailed three-dimensional FE model of the rail and its characteristic longitudinal variability. In this way, it is possible to overcome the limitations of commercial software available in terms of track flexibility. Furthermore, the model can be easily adapted to other track forms, including plain line and switch panel. In order to validate the wheel-rail contact routine, an early validation against the commercial software VI-Rail is proposed and a good match of the main dynamic outputs has been achieved even if the contact algorithm is quite simplified (i.e. only one point of contact considered per each wheel and Hertzian contact model for the normal dynamics).

The successful model validation against bearer vertical displacement measured at a UK site equipped with Under Sleeper Pads is presented in Chapter 6. Tuning the trackbed stiffness along the crossing panel it is possible to achieve a very good match between experimental data and predicted numerical values, with an average difference lower than 7%, increasing the confidence in the model developed. The measured data shows that the 6ft side is stiffer than the cess side at the crossing nose location. The major learning point is that the actual behaviour of the whole system is counter-intuitive, as the increased bending stiffness of the whole track system (i.e. increased bending stiffness at the rail level and presence of long bearer) counter-balances this phenomenon and a lower trackbed stiffness is calculated instead. In addition to that, the loss of trackbed support seen at the 6ft side around the crossing nose can be explained with the impact force, especially the P2 force component which is recognised to be influencing the trackbed degradation.

One of the key achievements of this research is the detailed discussion presented in

Chapter 7 about the basic mechanisms involved in the long-term ballast behaviour and the implications considering a range of settlement equations that are available in literature. A simplified two-dimensional track FE model is proposed for plain line under a quasi-static excitation and a moving sinusoidal excitation. The results from the quasi-static load model show that considering sleeper displacement, the trackbed stiffness is the major influencing factor for a given load considered, while in case of velocity and acceleration the loading frequency is as critical as the trackbed stiffness. The results from the travelling load model show that the influence of the loading frequencies are strictly linked with the main track mode resonance frequencies. The ballast energy is the only quantity that reflects both track modal frequencies as well as lower values linked with the vehicle characteristics. Using the previous results from the quasi-static load model, the predictions of settlement rate according to Guérin's, Sato's and Fröhling's equations are compared and the results show clearly the large discrepancy between the predictions, not only in terms of actual values but also in terms of trend. For instance, the settlement rate according to the Guérin's and the Fröhling's equations slightly increases with increasing load and decreases non-linearly with increasing trackbed stiffness (i.e. stiffer supports will settle less than softer ones), while the settlement rate according to the Sato's model shows the opposite tendency (i.e. stiffer supports will settle more than softer ones). None of these results are entirely satisfactory and the need of a more comprehensive equation that can capture the trends seen on track as well as physical quantities that can be easily recorded *in situ* is highlighted. Using the main conclusions from the travelling load model, a new settlement equation is proposed based on the maximum energy transmitted to the ballast layer, which in essence combines both deflection and forces quantities, both independent physical attributes of the reviewed settlement equations.

Finally, in Chapter 8 the calibration of the proposed settlement equation was performed against the settlement rate at the same site used in Chapter 6 and a good overall trend is achieved, increasing the strength of the proposed methodology. The assessment of longitudinal variation of trackbed stiffness below the crossing panel is then proposed. It has been shown that it is necessary to include this in the numerical model in order to correctly capture the long-term ballast behaviour.

To conclude, the three-dimensional VTI model proposed in this thesis offers a valuable and independent instrument to give insight into the whole system dynamic behaviour taking into account not only the non-linearities at the wheel-rail contact level but also the

longitudinal and transversal variability of the track super-structure characteristics. The main application presented is in the crossing panel, but it can be conveniently used in other contexts that require a high level of accuracy, such as the switch panel or transition zones. In addition to that, it has been demonstrated how the tool, including the long-term ballast behaviour is flexible and can be used to quantitatively help the key decision-makers in the assessment of various track design aspects.

## **9.2 Further work**

Further work is listed as follows:

- Additional validation of the VTI model can be achieved using available on-track acceleration data not only at the bearer level but also at the rail level. The measurements should be taken not only at crossing panel but also in plain line, over transition zones and at switch panel. In this way, it is possible to capture the super-structure behaviour induced by different types of excitations, i.e. no excitations, excitations due to change in trackbed stiffness, excitations due to change in wheel-rail contact surface and excitation due to the combination of the above.
- The proposed equation for the long-term ballast behaviour is based on the total energy transmitted to the ballast. It has been pointed out that only the dissipated part is the one associated with the material degradation. Nevertheless, it is quite difficult to capture the system damping characteristics, especially using a linear model. Thus, it is suggested to further develop the dynamic model to correctly capture the damping behaviour and the dissipated energy transmitted to the ballast. Also, the proposed equation has been derived theoretically and tuned against one set of data available for a given UK site. Further validations should be carried out against laboratory tests in order to capture the overall behaviour under controlled conditions and for low loading frequencies. In addition, further measurement sites should be considered in order to assess the influence of higher loading frequency.
- Additional applications of the tool developed include the assessment of the following aspects:

- Modification of the resilient track layers, such as rail-pads, baseplate pads and potential USPs;
- Change of the crossing structural design on the long-term system degradation;
- Variation of the crossing layout due to a change in bearer spacing, which leads to a change in the whole system stiffness distribution;
- Modification of sleeper design and sleeper material design.



## 10 References

1. Lichtberger, B., *Track Compendium - Formation, Permanent way, Maintenance, Economics*. 2005, Hamburg: Eurailpress.
2. Johansson, A., Palsson, B., Ekh, M., Nielsen, J.C.O., Ander, M.K.A., Brouzoulis, J., and Kassa, E., *Simulation of wheel-rail contact and damage in switches and crossings*. *Wear*, 2011. **271**(1-2): p. 472-481.
3. Kassa, E., Andersson, C., and Nielsen, J.C.O., *Simulation of dynamic interaction between train and railway turnout*. *Vehicle System Dynamics*, 2006. **44**(3): p. 247-258.
4. Garrud, C., *Swiss S&C Life Extension Method – SLS*. 2015, PWI Technical Seminar.
5. Grossoni, I., Hughes, P., Bezin, Y., Bevan, A., and Jaiswal, J., *Observed failures at railway turnouts: failure analysis, possible causes and links to current and future research*. *Engineering Failure Analysis*, 2020.
6. Grossoni, I., Bezin, Y., and Neves, S., *Optimisation of support stiffness at railway crossings*. *Vehicle System Dynamics*, 2018. **56**(7): p. 1072-1096.
7. Grossoni, I., Le Pen, L.M., Jorge, P.F.M., Bezin, Y., Watson, G., Kostovasilis, D., and Powrie, W., *The role of support stiffness in switches and crossings: comparison of vehicle-track interaction models against field measurements*. *Proceedings of the Institution of Mechanical Engineers, Part F: Journal of Rail and Rapid Transit*, 2019.
8. Grossoni, I., Andrade, A., Bezin, Y., and Neves, S., *The role of track stiffness and its spatial variability on long-term track quality deterioration*. *Proceedings of the Institution of Mechanical Engineers, Part F: Journal of Rail and Rapid Transit*, 2019. **233**(1): p. 16-32.
9. Grossoni, I., Powrie, W., Zervos, A., Bezin, Y., and Le Pen, L.M., *Modelling railway ballasted track settlement in vehicle-track interaction analysis*. *Transportation Geotechnics*, 2020.
10. (CRTB) Tycoon Industrial Development Co. *Symmetrical Turnout*. [cited 2014 10/10]; Available from: <http://www.crby.com/ChannelTempletPage.aspx?CID=ef7344eb-2781-4295-8d1f-1a351aff29d6>.
11. European Committee For Standardization, *EN 13232-1 Railway applications - Track - Switches and crossings for Vignole rails - Part 1: Definitions*. 2013: Brussel.
12. Li, X., Nielsen, J.C.O., and Palsson, B.A., *Simulation of track settlement in railway turnouts*. *Vehicle System Dynamics*, 2014. **52**: p. 421-439.
13. European Committee For Standardization, *Railway applications - Track - Switches and crossings for Vignole rails - Part 6: Fixed common and obtuse crossings* 2014: Brussel.

14. Cope, G.H., ed. *British Railway Track - Design, Construction and, Maintenance*. VI Edition ed. 1993, The Permanent Way Institution.
15. Caught (Up) in Traffic. *Monthly Archive: October 2011*. [cited 2014 11-10]; Available from: <https://dOctrine.com/2011/10/page/2/>.
16. Port Kersey Railway. *Crossings on the Port Kersey*. [cited 2014 11-10]; Available from: <http://www.port-kersey.com/?p=76>.
17. TranslationDirectory.com. *Rail Glossary*. [cited 2014 11-10]; Available from: <http://www.translationdirectory.com/glossaries/glossary256.php>.
18. Network Rail, *RT/CE/S/012 Cast austenitic manganese steel crossings*. 2002: London.
19. Jenkins, H.H., Stephenson, J.E., Clayton, G.A., Morland, G.W., and Lyon, D., *The effect of track and vehicle parameters on wheel-rail vertical dynamic forces*. *Railway Engineering Journal*, 1974. **3**(1): p. 2-17.
20. Jonsson, J., Khouy, I.A., Lundberg, J., Rantatalo, M., and Nissen, A., *Measurement of vertical geometry variations in railway turnouts exposed to different operating conditions*. *Proceedings of the Institution of Mechanical Engineers, Part F: Journal of Rail and Rapid Transit*, 2016. **230**(2): p. 486-501.
21. Dahlberg, T., *Some railroad settlement models—a critical review*. *Proceedings of the Institution of Mechanical Engineers, Part F: Journal of Rail and Rapid Transit*, 2001. **215**(4): p. 289-300.
22. Suiker, A.S.J. and de Borst, R., *A numerical model for the cyclic deterioration of railway tracks*. *International Journal for Numerical Methods in Engineering*, 2003. **57**(4): p. 441-470.
23. Iwnicki, S., ed. *Handbook of Railway Vehicle Dynamics*. 2006, CRC Press: Boca Raton.
24. Grassie, S.L., Gregory, R.W., and Johnson, K.L., *The dynamic response of railway track to high frequency vertical excitation*. *Journal of Mechanical Engineering Science*, 1982. **24**(2): p. 103-111.
25. Knothe, K. and Grassie, S.L., *Modelling of railway track and vehicle/track interaction at high frequencies*. *Vehicle System Dynamics*, 1993. **22**(3-4): p. 209-262.
26. Timoshenko, S. and Langer, F.B., *Stresses in the rail*. *Journal of applied Mechanics*, 1932. **AMP-54-26**: p. 277-302.
27. Jezequel, L., *Response of periodic systems to a moving load*. *Journal of Applied Mechanics*, 1981. **48**(3): p. 613-618.
28. Chebli, H., Othman, R., and Clouteau, D., *Response of periodic structures due to moving loads*. *Comptes Rendus Mécanique*, 2006. **334**: p. 347-352.
29. Jenkins, H.H., Stephenson, J.E., Clayton, G.A., Morland, G.W., and Lyon, D., *The effect of track and vehicle parameters on wheel/rail vertical dynamic forces*. *Railway Engineering Journal*, 1974. **3**(1): p. 2-16.
30. Grossoni, I., Iwnicki, S., Bezin, Y., and Gong, C., *Dynamics of a vehicle-track*

*Design methodology for track systems considering the long-term ballast behaviour:  
application to crossings*

- coupling system at a rail joint*. Proceedings of the Institution of Mechanical Engineers, Part F: Journal of Rail and Rapid Transit, 2015. **229**(4): p. 354-364.
31. Grassie, S.L. and Cox, S.J., *The dynamic response of railway track with flexible sleepers to high frequency vertical excitation*. Proceedings of the Institution of Mechanical Engineers, Part D: Journal of Automobile Engineering, 1984. **198**(2): p. 117-124.
  32. Wu, T.X. and Thompson, D.J., *Theoretical investigation of wheel/rail non-linear interaction due to roughness excitation*. Vehicle System Dynamics, 2000. **34**(4): p. 261-282.
  33. Ripke, B. and Knothe, K., *Die unendlich lange Schiene auf diskreten Schwellen bei harmonischer Einzellasterregung*. Fortschritt-Berichte VDI, 1991. **155**(11).
  34. Bezin, Y., *An integrated flexible track system model for railway vehicle dynamics*, in *Department of Engineering & Technology*. 2008, Manchester Metropolitan University: Manchester.
  35. Zhai, W. and Cai, Z., *Dynamic interaction between a lumped mass vehicle and a discretely supported continuous rail track*. Computers & structures, 1997. **63**(5): p. 987-997.
  36. Lei, X. and Noda, N.A., *Analyses of dynamic response of vehicle and track coupling system with random irregularity of track vertical profile*. Journal of Sound and Vibration, 2002. **258**(1): p. 147-165.
  37. Lu, F., Kennedy, D., Williams, F.W., and Lin, J.H., *Symplectic analysis of vertical random vibration for coupled vehicle track systems*. Journal of Sound and Vibration, 2008. **317**(1-2): p. 236-249.
  38. Zhai, W., Wang, K., and Cai, C., *Fundamentals of vehicle-track coupled dynamics*. Vehicle System Dynamics, 2009. **47**(11): p. 1349-1376.
  39. Network Rail, *RT/CE/S/052 Rail and baseplate pads*. 2002: London.
  40. Network Rail, *NR/L2/TRK/2049 Track design handbook*. 2010: London.
  41. European Committee for Standardization, *EN 13146 Railway applications - Track - Test methods for fastening systems - Part 9: Determination of stiffness*. 2009: Brussels.
  42. European Committee for Standardization, *EN 13481 Railway applications - Track - Performance requirements for fastening systems - Part 2: Fastening systems for concrete sleepers*. 2012: Brussels.
  43. European Committee for Standardization, *EN 13481 Railway applications - Track - Performance requirements for fastening systems - Part 3: Fastening systems for wood sleepers*. 2012: Brussels.
  44. European Committee for Standardization, *EN 13481 Railway applications - Track - Performance requirements for fastening systems - Part 4: Fastening systems for steel sleepers*. 2012: Brussels.
  45. European Committee for Standardization, *EN 13481 Railway applications - Track - Performance requirements for fastening systems - Part 5: Fastening systems for slab track with rail on the surface or rail embedded in a channel*. 2012: Brussels.

46. Chen, G. and Zhai, W., *A new wheel/rail spatially dynamic coupling model and its verification*. *Vehicle System Dynamics*, 2004. **41**(4): p. 301-323.
47. Shen, G., Ayasse, J.B., Collette, H., and Pratt, I., *A design method for wheel profiles according to the rolling radius difference function*. *Proceedings of the Institution of Mechanical Engineers, Part F: Journal of Rail and Rapid Transit*, 2011. **225**(5): p. 457-462.
48. Johnson, K.L., *Contact mechanics*. 1985, Cambridge: Cambridge University Press.
49. Yan, W. and Fisher, F.D., *Applicability of the Hertz contact theory to wheel/rail contact problems*. *Archive of Applied Mechanics*, 2000. **70**(4): p. 255-268.
50. Enblom, R. and Berg, M., *Impact of non-elliptic contact modelling in wheel wear simulation*. *Wear*, 2008. **265**(9-10): p. 1532-1541.
51. Wiest, M., Kassa, E., Daves, W., Nielsen, J.C.O., and Ossberger, H., *Assessment of methods for calculating contact pressure in wheel-rail/switch contact*. *Wear*, 2008. **265**(9-10): p. 1439-1445.
52. Telliskivi, T. and Olofsson, U., *Contact mechanics analysis of measured wheel/rail profiles using the finite element method*. *Proceedings of the Institution of Mechanical Engineers, Part F: Journal of Rail and Rapid Transit*, 2001. **215**(2): p. 65-72.
53. Piotrowski, J. and Chollet, H., *Wheel-rail contact models for vehicle system dynamics including multi-point contact*. *Vehicle System Dynamics*, 2005. **43**(6-7): p. 455-484.
54. Pascal, J.P. and Sauvage, G., *The available methods to calculate the wheel/rail forces in non Hertzian contact patches and rail damaging*. *Vehicle System Dynamics*, 1993. **22**(3-4): p. 263-275.
55. Piotrowski, J. and Kik, W., *A simplified model of wheel/rail contact mechanics for non-Hertzian problems and its application in rail vehicle dynamic simulations*. *Vehicle System Dynamics*, 2008. **46**(1-2): p. 27-49.
56. Kalker, J.J., *Survey of wheel/rail rolling contact theory*. *Vehicle System Dynamics*, 1979. **8**(4): p. 317-358.
57. Shen, Z.Y., Hedrick, J.K., and Elkins, J.A., *A comparison of alternative creep force models for rail vehicle dynamic analysis*. *Vehicle System Dynamics*, 1983. **12**(1-3): p. 79-83.
58. Vermeulen, P.J. and Johnson, K.L., *Contact of nonspherical elastic bodies transmitting tangential forces*. *Journal of Applied Mechanics*, 1964. **31**(2): p. 338-341.
59. CMCC, V. *Contact - Vollebregt & Kalker's rolling and sliding contact model*. 2014 [cited 2015 14/03/2015]; Available from: [www.kalkersoftware.org](http://www.kalkersoftware.org).
60. Kalker, J.J., *Wheel/rail rolling contact theory*. *Wear*, 1991. **144**(1-2): p. 243-261.
61. Shackleton, P. and Iwnicki, S., *Comparison of wheel-rail contact codes for railway vehicle simulation: an introduction to the Manchester Contact Benchmark and initial results*. *Vehicle System Dynamics*, 2008. **46**(1-2): p. 129-149.

*Design methodology for track systems considering the long-term ballast behaviour: application to crossings*

62. British Railways Board, *GM/TT0088: Permissible track forces for railway vehicles*. 1993, Group Standards Railway Technical Centre: Derby.
63. Kabo, E., Nielsen, J.C.O., and Ekberg, A., *Prediction of dynamic train-track interaction and subsequent material deterioration in the presence of insulated rail joints*. *Vehicle System Dynamics*, 2006. **44**: p. 718-729.
64. UIC, *UIC518: Testing and approval of railway vehicles from the point of view of their dynamic behaviour - Safety - Track fatigue - Ride quality*. 2005.
65. SKF, *Railway Technical Handbook: A Handbook for the Industrial Designer and Operator. Axleboxes, wheelset bearings, sensors, condition monitoring, subsystems and services*. Vol. 1. 2011: SKF. 212.
66. NewRail. *SPECTRUM - Solutions and Processes to Enhance the Competitiveness of Transport by Rail in Unexploited markets*. [cited 2015 30/05/2015]; Available from: <http://www.spectrumrail.info/>.
67. Eickhoff, B.M., Evans, J.R., and Minnis, J., *A review of modelling methods for railway vehicle suspension components*. *Vehicle System Dynamics*, 1995. **24**(6-7): p. 469-496.
68. Bruni, S., Vinolas, J., Berg, M., Polach, O., and Stichel, S., *Modelling of suspension components in a rail vehicle dynamics context*. *Vehicle System Dynamics*, 2011. **49**(7): p. 1021-1072.
69. Lagos, R.F., Alonso, A., Vinolas, J., and Pérez, X., *Rail vehicle passing through a turnout: analysis of different turnout designs and wheel profiles*. *Proceedings of the Institution of Mechanical Engineers, Part F: Journal of Rail and Rapid Transit*, 2012. **226**(6): p. 587-602.
70. Sun, Y.Q., Cole, C., and McClanachan, M., *The calculation of wheel impact force due to the interaction between vehicle and a turnout*. *Proceedings of the Institution of Mechanical Engineers, Part F: Journal of Rail and Rapid Transit*, 2010. **224**(5): p. 391-403.
71. Pålsson, B.A., *Optimisation of railway crossing geometry considering a representative set of wheel profiles*. *Vehicle System Dynamics*, 2015. **53**(2): p. 274-301.
72. Alfi, S. and Bruni, S., *Mathematical modelling of train–turnout interaction*. *Vehicle System Dynamics*, 2009. **47**(5): p. 551-574.
73. Bruni, S., Anastasopoulos, I., Alfi, S., Van Leuven, A., and Gazetas, G., *Effects of train impacts on urban turnouts: Modelling and validation through measurements*. *Journal of Sound and Vibration*, 2009. **324**(3–5): p. 666-689.
74. Coleman, I., *The development of modelling tools for railway switches and crossings*. 2014, Imperial College: London.
75. Kassa, E. and Nielsen, J.C., *Dynamic interaction between train and railway turnout: full-scale field test and validation of simulation models*. *Vehicle System Dynamics*, 2008. **46**: p. 521-534.
76. Ren, Z., Sun, S., and Xie, G., *A method to determine the two-point contact zone and transfer of wheel–rail forces in a turnout*. *Vehicle System Dynamics*, 2010. **48**(10):

- p. 1115-1133.
77. Burgelman, N., Li, Z., and Dollevoet, R., *A new rolling contact method applied to conformal contact and the train–turnout interaction*. *Wear*, 2014. **321**: p. 94-105.
  78. Sebes, M., Ayasse, J.B., Chollet, H., Pouligny, P., and Pirat, B., *Application of a semi-Hertzian method to the simulation of vehicles in high-speed switches*. *Vehicle System Dynamics*, 2006. **44**: p. 341-348.
  79. khouy, I.A., Larsson-Kråik, P.-O., Nissen, A., Lundberg, J., and Kumar, U., *Geometrical degradation of railway turnouts: A case study from a Swedish heavy haul railroad*. *Proceedings of the Institution of Mechanical Engineers, Part F: Journal of Rail and Rapid Transit*, 2014. **228**(6): p. 611-619.
  80. Kennedy, J., Woodward, P.K., Medero, G., and Banimahd, M., *Reducing railway track settlement using three-dimensional polyurethane polymer reinforcement of the ballast*. *Construction and Building Materials*, 2013. **44**: p. 615-625.
  81. Nielsen, J.C. and Li, X., *Railway track geometry degradation due to differential settlement of ballast/subgrade–Numerical prediction by an iterative procedure*. *Journal of Sound and Vibration*, 2018. **412**: p. 441-456.
  82. Li, X., Ekh, M., and Nielsen, J.C., *Three - dimensional modelling of differential railway track settlement using a cycle domain constitutive model*. *International Journal for Numerical Analytical Methods in Geomechanics*, 2016. **40**(12): p. 1758-1770.
  83. Indraratna, B. and Nimbalkar, S., *Stress-strain degradation response of railway ballast stabilized with geosynthetics*. *Journal of geotechnical and geoenvironmental engineering*, 2013. **139**(5): p. 684-700.
  84. Abadi, T., Le Pen, L., Zervos, A., and Powrie, W., *A Review and Evaluation of Ballast Settlement Models using Results from the Southampton Railway Testing Facility (SRTF)*. *Procedia Engineering*, 2016. **143**: p. 999-1006.
  85. Mauer, L., *An interactive track-train dynamic model for calculation of track error growth*. *Vehicle System Dynamics*, 1995. **24**: p. 209-221.
  86. Frohling, R.D., *Low frequency dynamic vehicle-track interaction: modelling and simulation*. *Vehicle System Dynamics*, 1998. **29**(1): p. 30-46.
  87. Iwnicki, S., Grassie, S., and Kik, W., *Track settlement prediction using computer simulation tools*. *Vehicle System Dynamics*, 2000. **33**: p. 37-46.
  88. Sato, Y., *Japanese studies on deterioration of ballasted track*. *Vehicle System Dynamics*, 1995. **24**: p. 197-208.
  89. Demharter, K., *Setzungsverhalten des Gleisrostes unter vertikaler Lasteinwirkung. Mitteilungen des Prüfamtes für Bau von Landverkehrswegen der Technischen Universität München*. 1982.
  90. Nguyen Gia, K., Goicolea Ruigómez, J.M., and Gabaldón Castillo, F., *Dynamic effect of high speed railway traffic loads on the ballast track settlement*, in *Congresso de Métodos Numéricos em Engenharia*. 2011, APMTAC: Coimbra.
  91. Ferreira, P. and López-Pita, A., *Numerical modeling of high-speed train/track*

*Design methodology for track systems considering the long-term ballast behaviour: application to crossings*

- system to assess track vibrations and settlement prediction. *Journal of Transportation Engineering*, 2012. **139**(3): p. 330-337.
92. Guerin, N., *Approche experimentale et numerique du comportement du ballast des voies ferrees*, in *Structures et materiaux*. 1996, Ecole nationale des ponts et chaussées: Paris.
  93. Jeffs, T. and Marich, S. *Ballast characteristics in the laboratory*. in *Conference on Railway Engineering 1987: Preprints of Papers*. 1987. Institution of Engineers, Australia.
  94. Indraratna, B. and Salim, W., *Deformation and degradation mechanics of recycled ballast stabilised with geosynthetics*. *Soils and Foundations*, 2003. **43**(4): p. 35-46.
  95. Indraratna, B., Ngo, N.T., and Rujikiatkamjorn, C., *Deformation of coal fouled ballast stabilized with geogrid under cyclic load*. *Journal of Geotechnical and Geoenvironmental Engineering*, 2012. **139**(8): p. 1275-1289.
  96. Thom, N. and Oakley, J. *Predicting differential settlement in a railway trackbed*. in *Proceedings of Railway foundations conference: Railfound*. 2006.
  97. Cuellar, V., Navarro, F., Andreau, M.A., Camara, J.L., Gonzalez, F., Rodriguez, M., Nunes, A., Gonzale, P., Diaz, R., Navarro, J., and Rodriguez, R., *Short and long term behaviour of high speed lines as determined in 1:1 scale laboratory tests*, in *9<sup>th</sup> World Congress on Railway Research*. 2011: Lille.
  98. Estaire, J. and Vincente, F., *CEDEX Track Box as an experimental tool to test railway tracks at 1:1 scale*, in *Proceedings of the 19th International Conference on Soil Mechanics and Geotechnical Engineering*. 2017: Seoul.
  99. Stewart, H.E. and Selif, E., *Correlation of concrete tie track performance in revenue service and at the facility for accelerated service testing-Volume ii: Predictions and evaluations of track settlement*. 1984.
  100. Shenton, M. *Deformation of railway ballast under repeated loading conditions*. in *Symposium on Railroad Track Mechanics, RRIS 01 130826, Publication 7602*. 1975.
  101. Selig, E.T. and Waters, J.M., *Track geotechnology and substructure management*. 1994, London: Thomas Telford.
  102. Brown, S., Brodrick, B., Thom, N., and McDowell, G., *The Nottingham railway test facility, UK*. *Proceedings of the Institution of Civil Engineers-Transport*, 2007. **160**(2): p. 59-65.
  103. Thom, N.H., *Rail trafficking testing*, in *Jubilee Symposium on Polymer Geogrid Reinforcement*. 2006.
  104. Le Pen, L. and Powrie, W., *Contribution of base, crib, and shoulder ballast to the lateral sliding resistance of railway track: a geotechnical perspective*. *Proceedings of the Institution of Mechanical Engineers, Part F: Journal of Rail and Rapid Transit*, 2011. **225**(2): p. 113-128.
  105. Abadi, T., Le Pen, L., Zervos, A., and Powrie, W., *Measuring the area and number of ballast particle contacts at sleeper/ballast and ballast/subgrade interfaces*. *The International Journal of Railway Technology*, 2015. **4**(2): p. 45-72.

106. Teixeira, P., López-Pita, A., Casas, C., Bachiller, A., and Robuste, F., *Improvements in high-speed ballasted track design: Benefits of bituminous subballast layers*. Transportation Research Record, 2006(1943): p. 43-49.
107. Indraratna, B., Thakur, P.K., and Vinod, J.S., *Experimental and numerical study of railway ballast behavior under cyclic loading*. International Journal of Geomechanics, 2009. **10**(4): p. 136-144.
108. Partington, W., *TM-TS-097: Track deterioration study - Results of the track laboratory experiments*. 1979, British Railway Research: Derby.
109. Frohling, R.D., Scheffel, H., and Ebersohn, W., *The vertical dynamic response of a rail vehicle caused by track stiffness variations along the track*. Vehicle System Dynamics, 1996. **25**: p. 13.
110. ORE, *Question D 71 Stresses in the Rails, the Ballast and in the Formation Resulting from Traffic Loads*. 1970, Uthecht.
111. Alva-Hurtado, J.E. and Selig, E.T., *Permanent strain behavior of railroad ballast, in 10th International Conference on Soil Mechanics and Foundation Engineering*. 1981: Stockholm (Sweden).
112. Indraratna, B., Shahin, M.A., and Salim, W., *Stabilisation of granular media and formation soil using geosynthetics with special reference to railway engineering*. Ground Improvement, 2007. **11**(1): p. 27-43.
113. Aursudkij, B., *A laboratory study of railway ballast behaviour under traffic loading and tamping maintenance*. 2007, University of Nottingham: Nottingham.
114. Sato, Y. *Optimization of track maintenance work on ballasted track*. in *Proceedings of the world congress on railway research (WCRR '97)*. 1997. Florence.
115. Hughes, P., Figueres-Esteban, M., El Rashidy, R., Van Gulijk, C., and Slovack, R., *A computer learning approach to obtain safety information from multi-lingual accident reports*, in *Safety and Reliability – Safe Societies in a Changing World: Proceedings of ESREL 2018*. 2018, CRC Press / Balkema: Trondheim, Norway. p. 3107-3114.
116. Shih, J.-Y., Kostovasilis, D., Bezin, Y., and Thompson, D.J., *Modelling options for ballast track dynamics*, in *24th international congress on sound and vibration*. 2017: London.
117. Wu, J.-S., *Analytical and numerical methods for vibration analyses*. 2013: John Wiley & Sons.
118. Zakeri, J.A., Xia, H., and Fan, J.J., *Dynamic response of train-track system to single rail irregularity*. Latin American Journal of Solids and Structures, 2009. **6**(2): p. 89-104.
119. CAPACITY4RAIL, *D1.3.2: Innovative concepts and designs for resilient S&Cs*. 2016.
120. SOLIDWORKS, *Release 2015*, D. Systèmes, Editor.
121. AEA Technology, *VAMPIRE User Guide*.



*Design methodology for track systems considering the long-term ballast behaviour: application to crossings*

122. VI-Grade Engineering software and solutions. *VI-Rail 18.0 manual users*. 2017.
123. Le Pen, L., Watson, G., Hudson, A., and Powrie, W., *Behaviour of under sleeper pads at switches and crossings–Field measurements*. Proceedings of the Institution of Mechanical Engineers, Part F: Journal of Rail and Rapid Transit, 2017. **232**(4): p. 1049-1063.
124. British Railways Board, *RT/CE/C/038: Track recording handbook*. 1996: London.
125. In2Track, *Deliverable D2.1: Identifying and understanding the core S&C issues*. 2018.
126. Thompson, D., *Railway noise and vibration: mechanisms, modelling and means of control*. 2008: Elsevier.
127. In2Rail, *Deliverable D3.3: Evaluation of optimised track systems*. 2017.
128. Abadi, T., Le Pen, L., Zervos, A., and Powrie, W., *Improving the performance of railway tracks through ballast interventions*. Proceedings of the Institution of Mechanical Engineers, Part F: Journal of Rail and Rapid Transit, 2016. **232**(2): p. 337-355.
129. Li, H. and McDowell, G.R., *Discrete element modelling of under sleeper pads using a box test*. Granular Matter, 2018. **20**(2): p. 26.
130. Alizadeh Otorabad, H., *Finite Element Analysis of a crossing - presentation for T2F workshop (16-17/7/2019)*. 2019.
131. Nielsen, J.C., Berggren, E.G., Hammar, A., Jansson, F., and Bolmsvik, R., *Degradation of railway track geometry – Correlation between track stiffness gradient and differential settlement*. Proceedings of the Institution of Mechanical Engineers, Part F: Journal of Rail and Rapid Transit, 2020. **234**(1): p. 108-119.
132. Sadri, M., Lu, T., and Steenbergen, M., *Railway track degradation: The contribution of a spatially variant support stiffness-Local variation*. Journal of Sound and Vibration, 2019. **455**: p. 203-220.
133. Connolly, D.P., Kouroussis, G., Laghrouche, O., Ho, C., and Forde, M., *Benchmarking railway vibrations – Track, vehicle, ground and building effects*. Construction and Building Materials, 2015. **92**: p. 64-81.
134. Bezin, Y., *An integrated flexible track system model for railway vehicle dynamics*. 2008, Manchester Metropolitan University: Manchester.
135. Wang, H. and Markine, V., *Modelling of the long-term behaviour of transition zones: Prediction of track settlement*. Engineering Structures, 2018. **156**: p. 294-304.
136. Grossoni, I., Shackleton, P., Bezin, Y., and Jaiswal, J., *Longitudinal rail weld geometry control and assessment criteria*. Engineering Failure Analysis, 2017. **80**: p. 352-367.
137. McEwen, I.J. and Harvey, R.F., *Interpretation of wheel/rail wear numbers*. 1986, British Rail Research: Derby UK.
138. Lewis, R., Braghin, F., Ward, A., Bruni, S., Dwyer-Jones, R., Bel Knani, K., and Bologna, P., *Integrating dynamics and wear modelling to predict railway wheel*

- profile evolution in 6th International Conference on Contact Mechanics and Wear of Rail/Wheel Systems* A. Ekberg, E. Kabo, and J.W. Ringsberg, Editors. 2003, CHARMEC: Gothenburg.
139. Bevan, A., Molyneux-Berry, P., Mills, S., Rhodes, A., and Ling, D., *Optimisation of wheelset maintenance using whole-system cost modelling*. Proceedings of the Institution of Mechanical Engineers, Part F: Journal of Rail and Rapid Transit, 2013. **227**(6): p. 594-608.
  140. Burstow, M.C., *Proposed new WLRM damage function for alternative rail materials*. 2009, Network Rail.
  141. Archard, J.F., *Contact and rubbing of flat surfaces*. Journal of Applied Physics, 1953. **24**: p. 981-987.
  142. Dirks, B. and Enblom, R., *Prediction model for wheel profile wear and rolling contact fatigue*. Wear, 2011. **271**(1-2): p. 210-217.
  143. Enblom, R. and Berg, M., *Simulation of railway wheel profile development due to wear—influence of disc braking and contact environment*. Wear, 2005. **258**(7-8): p. 1055-1063.
  144. Johansson, A. and Andersson, C., *Out-of-round railway wheels - a study of wheel polygonalization through simulation of three-dimensional wheel-rail interaction and wear*. Vehicle System Dynamics, 2005. **43**(8): p. 539-560.
  145. Donzella, G., Mazzù, A., and Petrogalli, C., *Competition between wear and rolling contact fatigue at the wheel-rail interface: some experimental evidence on rail steel*. Proceedings of the Institution of Mechanical Engineers, Part F: Journal of Rail and Rapid Transit, 2009. **223**(1): p. 31-44.
  146. Tunna, J., Sinclair, J., and Perez, J., *A review of wheel wear and rolling contact fatigue*. Proceedings of the Institution of Mechanical Engineers, Part F: Journal of Rail and Rapid Transit, 2007. **221**(2): p. 271-290.
  147. Burstow, M.C., *Whole Life Rail Model application and development of RSSB - Continued development of an RCF damage parameter*. 2004, Rail Safety and Standards Board.
  148. INNOTRACK, *DI.3.3: Final report on Root Causes of Problem Conditions and Priorities for Innovation 2009*.
  149. Ekberg, A., Kabo, E., and Andersson, H., *An engineering model for prediction of rolling contact fatigue of railway wheels*. Fatigue & Fracture of Engineering Materials & Structures, 2002. **25**(10): p. 899-910.
  150. Dang Van, K. and Maitournam, M.H., *Rolling contact in railways: modelling, simulation and damage prediction*. Fatigue & Fracture of Engineering Materials & Structures, 2003. **26**(10): p. 939-948.
  151. Cai, W., Wen, Z., Jin, X., and Zhai, W., *Dynamic stress analysis of rail joint with height difference defect using finite element method*. Engineering Failure Analysis, 2007. **14**(8): p. 1488-1499.
  152. Dukkipati, R.V. and Dong, R., *The dynamic effects of conventional freight car running over a dipped-joint*. Vehicle System Dynamics, 1999. **31**(2): p. 95-111.

*Design methodology for track systems considering the long-term ballast behaviour: application to crossings*

153. Duncheva, G.V. and Maximov, J.T., *A new approach to enhancement of fatigue life of rail-end-bolt holes*. Engineering Failure Analysis, 2013. **29**: p. 167-179.
154. Mohammadzadeh, S., Sharavi, M., and Keshavarzian, H., *Reliability analysis of fatigue crack initiation of railhead in bolted rail joint*. Engineering Failure Analysis, 2013. **29**: p. 132-148.
155. Gustavson, R. and Gylltoft, K., *Influence of cracked sleepers on the global track response: coupling of a linear track model and nonlinear finite element analyses*. Proceedings of the Institution of Mechanical Engineers, Part F: Journal of Rail and Rapid Transit, 2002. **216**(1): p. 41-51.
156. Thun, H., Utsi, S., and Elfgrén, L., *Load carrying capacity of cracked concrete railway sleepers*. Structural Concrete, 2008. **9**(3): p. 153-161.
157. Bari, S. and Hassan, T., *Anatomy of coupled constitutive models for ratcheting simulation*. International Journal of Plasticity, 2000. **16**(3-4): p. 381-409.
158. Dettmer, W. and Reese, S., *On the theoretical and numerical modelling of Armstrong–Frederick kinematic hardening in the finite strain regime*. Computer Methods in Applied Mechanics and Engineering, 2004. **193**(1-2): p. 87-116.
159. Johansson, G., Ekh, M., and Runesson, K., *Computational modeling of inelastic large ratcheting strains*. International Journal of Plasticity, 2005. **21**(5): p. 955-980.
160. Johansson, G., Ahlström, J., and Ekh, M., *Parameter identification and modeling of large ratcheting strains in carbon steel*. Computers and Structures, 2006. **84**(15-16): p. 1002-1011.
161. Kassa, E. and Johansson, G., *Simulation of train–turnout interaction and plastic deformation of rail profiles*. Vehicle System Dynamics, 2006. **44**: p. 349-360.
162. Nicklisch, D., Kassa, E., Nielsen, J.C.O., Ekh, M., and Iwnicki, S., *Geometry and stiffness optimization for switches and crossings, and simulation of material degradation*. Proceedings of the Institution of Mechanical Engineers, Part F: Journal of Rail and Rapid Transit, 2010. **224**(4): p. 279-292.
163. Pletz, M., Daves, W., and Ossberger, H., *A wheel set/crossing model regarding impact, sliding and deformation—Explicit finite element approach*. Wear, 2012. **294**: p. 446-456.
164. Wen, Z., Xiao, G., Xiao, X., Jin, X., and Zhu, M., *Dynamic vehicle–track interaction and plastic deformation of rail at rail welds*. Engineering Failure Analysis, 2009. **16**(4): p. 1221-1237.
165. Dukkupati, R.V., *MATLAB. An introduction with applications*. 2010, New Delhi: New Age International (P) Ltd. 680.
166. Thompson, R.S.G., *Development of non-linear numerical models appropriate for the analysis of JACK-UP units*. 1996, Jesus College: Oxford.

# Appendix A DEGRADATION MODES AT THE RAIL LEVEL<sup>9</sup>

## A.1 Wear

Wear models can be generally divided in two main categories:

### 1 Energy transfer models

The material loss is a function of the energy dissipated in the contact patch. An example is the methods based on the  $T\gamma$  (T-gamma) function, which is defined as:

$$T\gamma = T_1\gamma_1 + T_2\gamma_2 + T_3\omega_3 \quad 10.1$$

Where:

$T_1, T_2, T_3$  = longitudinal, lateral and spin component of creep force [N], [N], [Nm];

$\gamma_1, \gamma_2, \omega_3$  = longitudinal, lateral and spin component of creepages [-], [-],[rad/m].

There are several studies about the  $T\gamma$  function, for example [137, 138]. More recently, it has been applied to develop a wheelset management tool supporting the optimization of the maintenance and renewal processes [139]. Change of material type and application to S&C might in practice necessitate a modified damaged function. This has been done applying the methodology described in Burstow [140] considering cast manganese.

### 2 Sliding models

The material loss depends on combinations of sliding distance, normal force, and material hardness.

An example is the Archard's law [141], which calculates the lost volume due to the wear as:

$$W = \frac{k_w}{H} \cdot P_z \cdot s \quad 10.2$$

Where:

$W$  = volume of material lost due to wear [m<sup>3</sup>];

$k_w$  = wear coefficient [m<sup>2</sup>/N];

$H$  = material hardness [Pa];

---

<sup>9</sup> The main reference is [5].

*Design methodology for track systems considering the long-term ballast behaviour:  
application to crossings*

$P_z$  = normal force applied [N];

$s$  = sliding distance [m].

The wear coefficient depends on several aspects, such as the governing wear regime, the steel properties, the sliding speed and the environmental conditions.

In several studies this formula has been applied due to the relative easiness, for example in [2, 142-144]. In Johnsson [2], the wear damage has been included in a wider routine to calculate the evolution of the switch profile due to the cumulative effects of wear and plastic deformation.

Some further considerations about the interactions between the wear and the fatigue phenomena are reported in the following Section.

## A.2 Fatigue (RCF)

Two main approaches are possible to define as follows:

- Energy transfer models

The  $T\gamma$  function (Eq. 10.1) is also used to predict the RCF growth. In reality wear and RCF are competitive phenomena, as the wear tends to limit the propagation of cracks due to cyclic contact stresses by removing material from contact surface [145, 146]. Recently, a model including these two damage mechanisms has been developed by calculating accumulated damage on strips across the head of the rail and comparing the totals with RCF damage observed in practice [147]. Taking in account the R260 steel grade, here are four main areas in which the graph is divided (Figure 10.1):

- $T\gamma < 15 \text{ N}$ : there is no surface damage on the rail;
- $T\gamma = 15 \div 65 \text{ N}$ : the RCF increases linearly with  $T\gamma$ ;
- $T\gamma = 65 \div 175 \text{ N}$ : both RCF and wear appear on the rail surface;
- $T\gamma > 175 \text{ N}$ : there is only wear since the wear rate exceeds the rate of propagation of RCF.

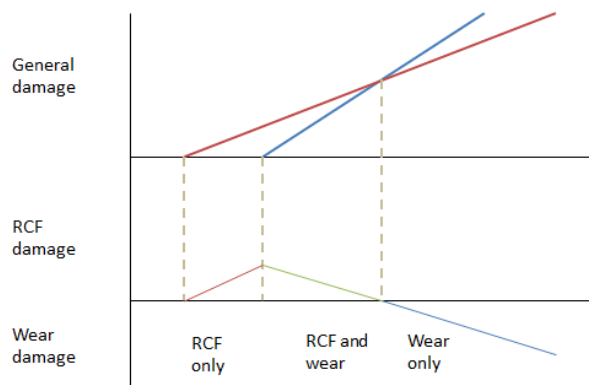


Figure 10.1: WLRM Damage Index algorithm, showing separate RCF and Wear functions as well as the composite form [147].

In the INNOTRACK final report [148] the authors regard this method as more accurate and useful

than the shakedown map due to the unambiguous numeric output which is directly relatable to fatigue life. Note that this model has been validated against specific conditions (traffic, rail types and material hardness) from comprehensive studies in the UK.

- Shakedown map

In Ekberg [149] a fast predictive method using shakedown maps is presented. In particular, surface and subsurface-initiated fatigue mechanisms are considered through two indices:

- *Surface fatigue index*

$$FI_{surf} = \mu - \frac{1}{\nu} - \mu - \frac{2\pi abk_y}{3P_z} \quad 10.3$$

Where:

$\nu$  = normalized vertical load;

$a, b$  = semiaxes of the Hertzian contact patch [m];

$k_y$  = yield stress in pure shear [Pa];

$P_z$  = vertical load [N];

$\mu$  = utilized friction coefficient, defined as:

$$\mu = \frac{\sqrt{F_x^2 + F_y^2}}{P_z} \quad 10.4$$

Where:

$F_x, F_y$  =

The surface fatigue occurs if the index is not lower than 0. Figure 10.2 shows the geometrical meaning of the index in the shakedown map. Point X indicates the actual stress conditions: if it is in the left part of the plasticity curve (bold continuous curve), there can be elastic state, elastic or plastic shakedown. On the contrary, if it is on the right side, ratcheting may occur. Therefore, the  $FI_{surf}$  represents the horizontal distance from the plasticity surface.

Design methodology for track systems considering the long-term ballast behaviour:  
application to crossings

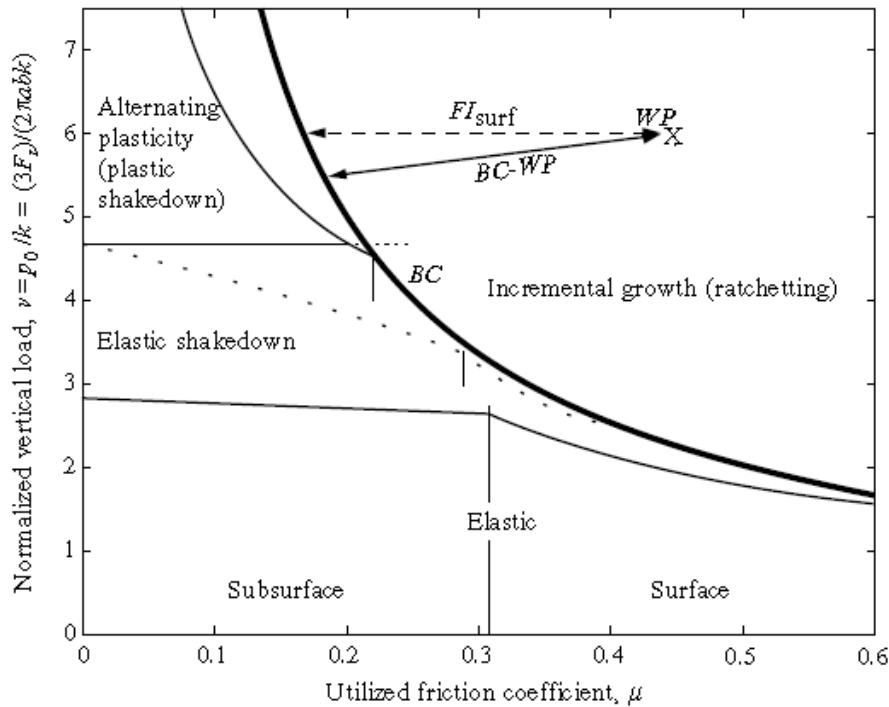


Figure 10.2: Shakedown map showing the  $FI_{surf}$  index [149].

The yield stress in pure shear is calculated as following. The yield stress  $S$  for non-martensitic materials is estimated through a liner relationship depending on the Vickers hardness  $HV$ . The yield stress in pure shear  $S_{ps}$  is then equal to the yield stress divided by the square root of three. Since it is known that the steel grade 350HT has yield stress in pure shear equal to 430 MPa, it is possible to calculate a rectified yield stress in pure shear for any material. Table 10.1 shows the calculation for a manganese crossing during the service life.

Table 10.1: Yield stress in pure shear for manganese crossing during the service life.

HB	HV	S [MPa]	$S_{ps}$ [MPa]	R	$k_y$ [MPa]
220	232	528	305	0.71	213
250	263	612	353	0.82	246
280	295	695	401	0.93	280
310	326	779	450	1.05	314
340	358	863	498	1.16	347
370	390	946	546	1.27	381
400	421	1030	595	1.38	415
430	453	1113	643	1.49	448
460	484	1197	691	1.61	482
490	516	1281	739	1.72	516
520	548	1364	788	1.83	549
550	579	1448	836	1.94	583

- Subsurface fatigue index

$$FI_{sub} = \frac{P_z}{4\pi ab} (1 + \mu^2) + a_{DV} \sigma_{h,res} \quad 10.5$$

Where:

$a_{DV}$  = material parameter;

$\sigma_{h,res}$  = residual hydrostatic stress.

This is an approximation of the Dang Van equivalent stress [150], according to which the fatigue damage occurs when the equivalent material stress exceeds the equivalent fatigue limit, usually assumed to be equal to the fatigue in pure shear.

In the formula, the first term represents the approximation of the maximum Dang Van equivalent stress in the case of pure rolling with a correction to take into account the slight increase due to lateral loads. The second term, on the contrary, represents the influence of residual stress on the hydrostatic part.

It has been proven how accurate this formulation is, comparing the results with the exact Dang Van formulation: the differences are always not greater than 8%.

### A.3 Fatigue (component fatigue)

The fatigue of the track components is particular dangerous as it may leads to derailments and, consequently, to accidents. In the following, two main parts of the track are considered: rail joints and bearers.

- **Rail joints**

The joints represent a discontinuity in the system. Thus, all the components are subjected to very high impact loads, as investigated in several studies (for example [29, 30, 151, 152]).

In Duncheva [153], particular attention is paid to the zones around the bolt holes, since they natural stress risers and, then, potentially very dangerous. The fatigue life of a holed component subjected to cyclic load can be increased by generating compressive normal stresses around the holes and thus significantly reducing the maximum values of the operating tensile stresses at the critical points of the components. In this way, it is possible to impede the formation of mode I cracks (Grossoni [5]). The Authors propose a coldworking of the holes, based on split sleeve cold expansion (CE) method. The essence of this approach is generating a field of residual compressive stresses around the hole, pulling a tool with a diameter greater than the diameter of the preliminary drilled hole. The beneficial effect is in enhancement of fatigue life by 3–10 times and significant savings from reduced



supervision of railways, current maintenance and rail replacement costs. In this paper, the beneficial effects are also demonstrated with a complete FE model, comparing the case with and without CE process.

In Mohammadzadeh [154], a statistical approach is adopted to provide a comprehensive probability model of fatigue crack initiation prediction in railhead of joint area. After calculating the peak forces as proposed in Jenkins [29], a quasi-static analysis is performed with the FE software ABAQUS including the rail mechanical properties. Afterward, applying an appropriate fatigue crack initiation model, the fatigue life estimate for each wheel passing. Damage parameter is calculated for each train passing by linear Miner's law. Finally, reliability analysis is carried out by providing an appropriate limit state function. According to sensitive analysis and Monte Carlo simulations with Latin hypercube sampling, it is found that the axle load and yield stress have the most effect and Poisson's ratio have the least effect on output results.

- **Cracked bearers**

In this study only concrete bearers are considered as they are the most common type in the main lines. Failure in the bearers may be a critical issue in the railway track system, as it greatly reduces their lifetime and thus increases maintenance needs and costs. Nevertheless, it has been shown how cracks in bearers have minor effects on the dynamic response of the entire track [155].

In Thun [156], four types of tests (i.e. bending capacity of the mid-Section, bending capacity of the rail Section, horizontal load carrying capacity of the fasteners and control of the concrete properties of the tested bearers) have been performed in order to assess the load carrying capacities of non-cracked and cracked bearers. The results show that small cracks do not influence the horizontal load carrying capacity. When the cracking becomes severe, the capacity is reduced that much to reach the level of the applied load. Also, the weather conditions play an important role in increase the crack deterioration.

## **A.4 Plastic deformations**

Plastic deformation and ratcheting phenomena have been extensively studied, but most of the developed theories are still very specific. In Bari [157] the authors critically compare five constitutive models to predict ratcheting responses, that are the Prager, Armstrong-Frederick, Chaboche, Ohno-Wang and Guionnet models. Kinematic hardening rule and backstress direction on multiaxial ratcheting simulation are found to be strongly influent. In particular, it is commonly accepted that the

Armstrong-Frederick model is appropriate to simulate the hardening behaviour of metals for small strains [158]. Nevertheless, in railway applications it is very unlikely to have this situation. Therefore, it is necessary to consider large strains under cyclic loading, as in Johansson [159, 160], where a multi-axial ratcheting model has been proposed using multiple Armstrong-Frederick and Burlet-Cailletaud formulations. That has been applied in many studies (e.g. in [2, 161, 162]) involving S&C and their components, as this is the main target of the model ([159, 160]).

Instead of calculating the actual evolution of the rail profile, which may be highly costly, some authors, for example in [163, 164], refer to overall quantities, such as the accumulated equivalent plastic strain (PEEQ) and the equivalent Von Mises stresses, both available in commercial FE packages, as an indication of the plastic damage in the railway system.

Plastic deformations cause change in the rail cross Section and therefore the distribution of contact stresses. Those changes are somehow captured within the wear model presented previously, especially the sliding models which quantify the material loss. As the approach of the present study is to reasonably simplify the reality, this aspect will be incorporated in the wear part.

## Appendix B HERTZ CONTACT THEORY<sup>10</sup>

### B.1 Geometry of surfaces in contact

Given two generic bodies (Figure A.10.3) and following the assumptions listed in Section 5.3.1, the two contact surfaces are expressed as a second order polynomial as follows:

$$\begin{aligned} z_1 &= A_1x_1^2 + B_1y_1^2 + C_1x_1y_1 \\ z_2 &= A_2x_2^2 + B_2y_2^2 + C_2x_2y_2 \end{aligned} \quad \text{A.6}$$

Where:

$x_1, y_1, x_2, y_2$  = directions of the principal curvatures of the  $i$ -th body;

$A_1, B_1, C_1, A_2, B_2, C_2$  = coefficients depending on the  $i$ -th body geometry.

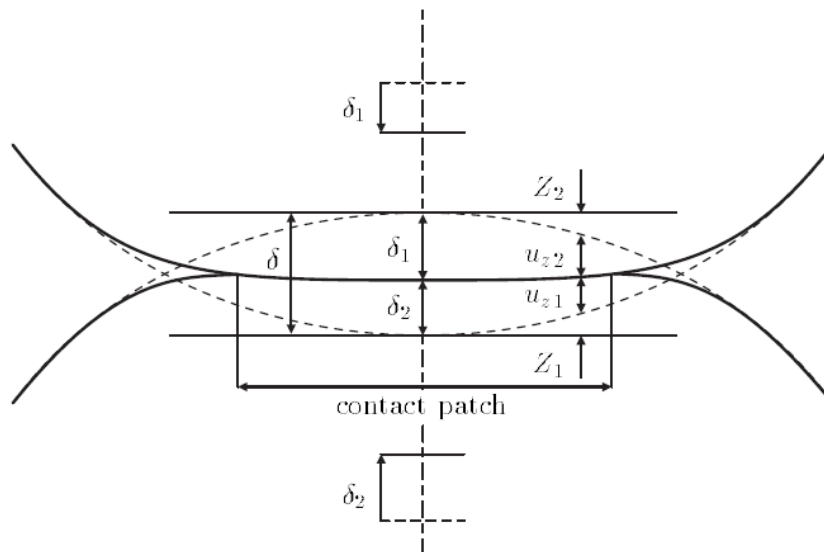


Figure A.10.3 – The normal deformation of elastic bodies in contact.

The gap between the two bodies is:

$$h = z_1 - z_2 = Ax^2 + By^2 + Cxy \quad \text{A.7}$$

Where:

$x, y$  = directions that form an angle  $\alpha$  and  $\beta$  respectively with body 1 and body 2 (Figure A.1).

<sup>10</sup> The main reference is [48]

Considering the principal radii of curvature of each body  $R_{i,x}$  and  $R_{i,y}$  ( $i=1,2$ ) and neglecting the mixed term, it is possible to express the coefficients A and B as:

$$A + B = \frac{1}{2} \left( \frac{1}{R_{1,x}} + \frac{1}{R_{2,x}} + \frac{1}{R_{1,y}} + \frac{1}{R_{2,y}} \right)$$

$$B - A = \frac{1}{2} \sqrt{\left( \frac{1}{R_{1,x}} - \frac{1}{R_{1,y}} \right)^2 + \left( \frac{1}{R_{2,x}} - \frac{1}{R_{2,y}} \right)^2 + 2 \left( \frac{1}{R_{1,x}} - \frac{1}{R_{1,y}} \right) \left( \frac{1}{R_{2,x}} - \frac{1}{R_{2,y}} \right) \cos \psi}$$

A.8

Where:

$\psi$  = angle between the principal directions of the bodies considered (Figure A.10.4) [rad].

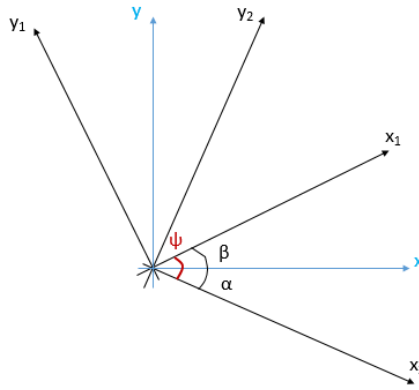


Figure A.10.4 – Angles between the principal directions of contacting bodies.

In the case of contact between wheel and rail, the rail curvature along the longitudinal direction can be neglected ( $\kappa_{r,x} \approx 0$ ). Also, the wheel curvature along the longitudinal direction can be calculated taking in account the total contact angle:

$$\kappa_{w,y} = \frac{1}{R_{w,y}} = \frac{\cos(\delta - \phi_w)}{R_w}$$

A.9

Where:

$\delta$  = contact angle [rad];

$\phi_w$  = wheelset roll angle [rad];

$R_w$  = wheel rolling radius [m].

## B.2 Normal contact pressure

If the assumptions of Hertz theory are satisfied, the contact area is elliptical and is described by

*Design methodology for track systems considering the long-term ballast behaviour:  
application to crossings*

the semi-axes a and b along the longitudinal and lateral direction respectively. The pressure at the contact point can be expressed as following:

$$\sigma(x_c, y_c) = \frac{3P_z}{2\pi ab} \sqrt{1 - \left(\frac{x_c}{a}\right)^2 - \left(\frac{y_c}{b}\right)^2} \quad \text{A.10}$$

Where:

$x_c, y_c$  = coordinate of point of contact;

$P_z$  = normal force applied at the contact interface [N];

a, b = semi-axis of the contact patch ellipse [m].

In particular, the semi-axes a and b can be calculated as:

$$a = m \sqrt[3]{\frac{3}{2} P_z \frac{1 - \nu_c^2}{E_c} \frac{1}{A + B}} \quad \text{A.11}$$

$$b = n \sqrt[3]{\frac{3}{2} P_z \frac{1 - \nu_c^2}{E_c} \frac{1}{A + B}}$$

Where:

m, n = coefficients as function of the parameter  $\theta$ ;

$\nu_c$  = Poisson's coefficient of the contacting bodies;

$E_c$  = Young's modulus of the contacting bodies [Pa].

In particular, the parameter  $\theta$  is defined as:

$$\theta = \cos^{-1} \left( \frac{B - A}{A + B} \right) \quad \text{A.12}$$

## Appendix C COEFFICIENTS FOR THE TANGENTIAL CONTACT PROBLEM

The coefficients in Equations B.1-B.4 are expressed in function of the geometrical characteristics of the contact patch:

$$f_{11} = E_{wr} ab C_{11} \quad \text{B.1}$$

$$f_{22} = E_{wr} ab C_{22} \quad \text{B.2}$$

$$f_{23} = E_{wr} (ab)^{3/2} C_{23} \quad \text{B.3}$$

$$f_{33} = E_{wr} (ab)^2 C_{33} \quad \text{B.4}$$

Where:

$E_{wr}$  = Young's modulus of the wheel-rail contact [Pa];

a, b = semi-axes of the contact ellipse [m];

$C_{11}$ ,  $C_{22}$ ,  $C_{23}$ ,  $C_{33}$  = Kalker creepage coefficients (Table D.1).

Table B.1 – Kalker coefficients.

a/b;v	$C_{11}$			$C_{22}$			$C_{23}$			$C_{33}$		
	0	0.25	0.5	0	0.25	0.5	0	0.25	0.5	0	0.25	0.5
0	$\pi^2/(4(1-\nu))$			$\pi^2/4$			$\Lambda$			$\pi^2/(16(1-\nu)(a/b))$		
0.1	2.51	3.31	4.85	2.51	2.52	2.53	0.33	0.47	0.73	6.42	8.28	11.7
0.2	2.59	3.37	4.81	2.59	2.63	2.66	0.48	0.6	0.81	3.46	4.27	5.66
0.3	2.68	3.44	4.8	2.68	2.75	2.81	0.61	0.72	0.89	2.49	2.96	3.72
0.4	2.78	3.53	4.82	2.78	2.88	2.98	0.72	0.82	0.98	2.02	2.32	2.77
0.5	2.88	3.62	4.83	2.88	3.01	3.14	0.83	0.93	1.07	1.74	1.93	2.22
0.6	2.98	3.72	4.91	2.98	3.14	3.31	0.93	1.03	1.18	1.56	1.68	1.86
0.7	3.09	3.81	4.97	3.09	3.28	3.48	1.03	1.14	1.29	1.43	1.5	1.6
0.8	3.19	3.91	5.05	3.19	3.41	3.65	1.13	1.15	1.4	1.34	1.37	1.42
0.9	3.29	4.01	5.12	3.29	3.54	3.82	1.23	1.36	1.51	1.27	1.27	1.27

In Table B.1:

$$\Lambda = \frac{\pi\sqrt{a/b}}{3(1-\nu)} \left[ 1 + \nu \left( \frac{1}{2} \ln \left( \frac{16}{(a/b)^2} \right) + \ln 4 - 5 \right) \right] \quad \text{B.5}$$

# Appendix D NEWMARK BETA INTEGRATION METHOD<sup>11</sup>

Firstly presented in 1959 by Nathan M. Newmark for use in structural dynamics, particularly for the solution of structural dynamics problems, this method has been modified and improved by many researchers during the time. The most important aspects are the possibility of the unconditional stability and the second order accuracy.

## D.1 Deriving the expressions

The acceleration is assumed to vary linearly between two succeeding instants of time. Moreover, it is possible to modify the value of two constants in order to indicate how much the acceleration enters into the velocity and the displacement equations at the end of interval  $\Delta t$ .

Instead of consider directly the Taylor's series both for displacement  $\{X_{t+\Delta t}\}$  and velocity  $\{\dot{X}_{t+\Delta t}\}$  vectors at the time  $t+\Delta t$ , Newmark expressed them as:

$$\{X_{t+\Delta t}\} = \{X_t\} + \Delta t \cdot \{\dot{X}_t\} + \frac{\Delta t^2}{2} \{\ddot{X}_t\} + \beta \cdot \Delta t^3 \cdot \{\ddot{X}_{t+\Delta t}\} \quad \text{C.1}$$

$$\{\dot{X}_{t+\Delta t}\} = \{\dot{X}_t\} + \Delta t \cdot \{\ddot{X}_t\} + \alpha \cdot \Delta t^2 \cdot \{\ddot{X}_{t+\Delta t}\} \quad \text{C.2}$$

Where:

$\alpha, \beta$  = model parameters.

Assuming the acceleration linear with the time step, the jolt  $\{\ddot{X}_{t+\Delta t}\}$  at the time  $t+\Delta t$  can be written as following:

$$\{\ddot{X}_{t+\Delta t}\} = \frac{\{\ddot{X}_{t+\Delta t}\} - \{\ddot{X}_t\}}{\Delta t} \quad \text{C.3}$$

Substituting the Equation E.3 into E.1 and E.2, it can be easily found in the standard form:

$$\{X_{t+\Delta t}\} = \{X_t\} + \Delta t \cdot \{\dot{X}_t\} + (1 - 2\beta) \cdot \frac{\Delta t^2}{2} \{\ddot{X}_t\} + \beta \cdot \Delta t^3 \cdot \{\ddot{X}_{t+\Delta t}\} \quad \text{C.4}$$

$$\{\dot{X}_{t+\Delta t}\} = \{\dot{X}_t\} + (1 - \alpha) \cdot \Delta t \cdot \{\ddot{X}_t\} + \alpha \cdot \Delta t^2 \cdot \{\ddot{X}_{t+\Delta t}\} \quad \text{C.5}$$

---

<sup>11</sup> The main reference is [165]

Substituting the equations found previously into the general dynamic equation of the motion, the Newmark equations can be obtained with the following relation:

$$[\bar{K}]\{X_{t+\Delta t}\} = \{\bar{F}_{t+\Delta t}\} \quad \text{C.6}$$

Where:

$[\bar{K}]$  = effective stiffness matrix [N/m];

$\{\bar{F}_{t+\Delta t}\}$  = effective force vector at the time  $t+\Delta t$  [N].

In Table C.1, the algorithm based on Newmark Beta method is reported.

Table C.1 - Algorithm based on Newmark Beta method.

<b>Initial computations:</b>
<ol style="list-style-type: none"> <li>1. Form stiffness [K], mass [M] and damping [C] matrices;</li> <li>2. Calculate the displacement <math>\{X_0\}</math> vector, velocity <math>\{\dot{X}_0\}</math> vector and force <math>\{F_0\}</math> vector at the time <math>t=0</math> (initializing);</li> <li>3. Calculate the acceleration <math>\{\ddot{X}_0\}</math> vector at the time <math>t=0</math> as:  <math display="block">\{\ddot{X}_0\} = -[M]^{-1}[K]\{X_0\} - [M]^{-1}[C]\{\dot{X}_0\} + [M]^{-1}\{F_0\};</math> </li> <li>4. Select time step <math>\Delta t</math> and model parameters <math>\alpha</math> and <math>\beta</math>;</li> <li>5. Calculate the integration constants: <math>a_0 = \frac{1}{\alpha \cdot \Delta t^2}</math>; <math>a_1 = \frac{\beta}{\alpha \cdot \Delta t}</math>; <math>a_2 = \frac{1}{\alpha \cdot \Delta t}</math>; <math>a_3 = \frac{1}{2\alpha} - 1</math>; <math>a_4 = \frac{\beta}{\alpha} - 1</math>; <math>a_5 = \frac{\Delta t}{2}(\frac{\beta}{\alpha} - 2)</math>; <math>a_6 = \Delta t(1 - \beta)</math>; <math>a_7 = \beta \cdot \Delta t</math>;</li> <li>6. Form the effective stiffness matrix: <math>[\bar{K}] = [K] + \frac{1}{\alpha \cdot \Delta t^2} \cdot [M] + \frac{\beta}{\alpha \cdot \Delta t} \cdot [C]</math>;</li> <li>7. Triangularize the effective stiffness matrix: <math>[\bar{K}] = [L][D][L]^T</math>.</li> </ol>
<b>For each time step:</b>
<ol style="list-style-type: none"> <li>1. Calculate effective force vector at time <math>(t+\Delta t)</math>: <math>\{\bar{F}_{t+\Delta t}\} = \{F_{t+\Delta t}\} + [M] \cdot (a_0 \cdot \{X_t\} + a_2 \cdot \{\dot{X}_t\} + a_3 \cdot \{\ddot{X}_t\}) + [C] \cdot (a_1 \cdot \{X_t\} + a_4 \cdot \{\dot{X}_t\} + a_5 \cdot \{\ddot{X}_t\})</math>;</li> <li>1. Solve for displacements at time <math>(t+\Delta t)</math>: <math>[\bar{K}]\{X_{t+\Delta t}\} = \{\bar{F}_{t+\Delta t}\}</math>;</li> <li>2. Calculate the velocity vector <math>\{\dot{X}_{t+\Delta t}\}</math> and the acceleration vector <math>\{\ddot{X}_{t+\Delta t}\}</math> at the time <math>(t+\Delta t)</math>:  <math display="block">\{\ddot{X}_{t+\Delta t}\} = a_0 \cdot (\{X_{t+\Delta t}\} - \{X_t\}) - a_2 \cdot \{\dot{X}_t\} - a_3 \cdot \{\ddot{X}_t\}</math> <math display="block">\{\dot{X}_{t+\Delta t}\} = \{\dot{X}_t\} + a_6 \cdot \{\ddot{X}_t\} + a_7 \cdot \{\ddot{X}_{t+\Delta t}\}.</math> </li> </ol>

## D.2 Model parameters

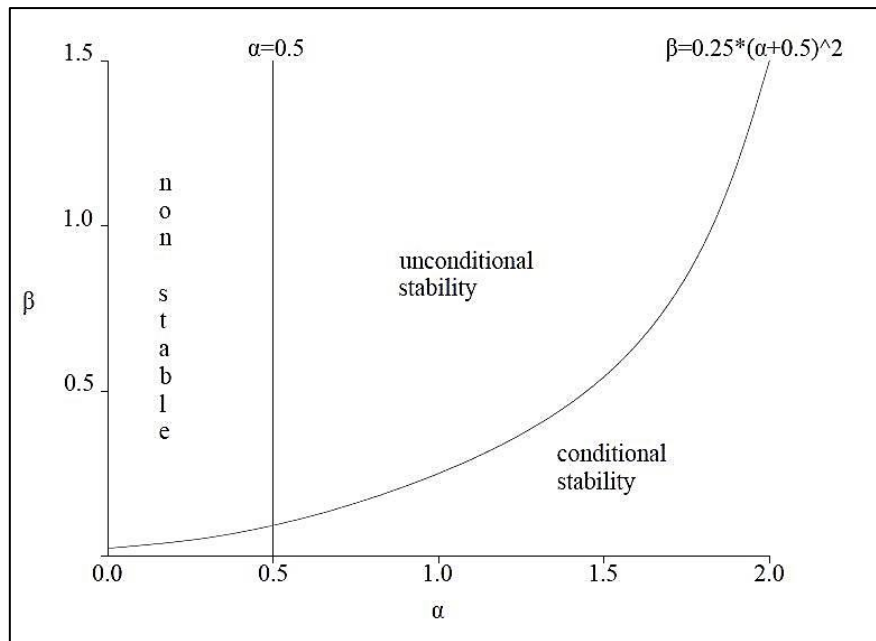
As said previously, in this model the value of two model parameters  $\alpha$  and  $\beta$  are varied in order



*Design methodology for track systems considering the long-term ballast behaviour:  
application to crossings*

to indicate how much the acceleration enters into the velocity and the displacement equations at the end of interval  $\Delta t$  which depends on the optimum accuracy, stability and dissipative characteristics that would be reached [166].

It is required that the parameter  $\alpha$  is not lower than 0.5 and the parameter  $\beta$  not lower than  $\frac{1}{4} \cdot (\alpha + \frac{1}{2})^2$  in order to have an unconditional stability. The possible cases varying the parameters are presented in Figure E.1.



*Figure C.1 - Stability of Newmark Beta integration methods.*

It can appear that there are a large number of cases specifying different integration parameters. Few of them are the most commonly used and are reported in Table C.2.

*Table C.2 - Main cases of Newmark Beta model parameters with corresponding type of acceleration and stability.*

	$\alpha$	$\beta$	Type of acceleration	Type of stability
1	1/6	1/2	Linear	Conditional stability
2	1/2	0	Constant	Conditional stability
3	1/2	1/8	Constant with two values (changing in the mid-point)	Conditional stability
4	1/2	1/4	Constant (trapezoidal rule)	Unconditional stability

It is worth noticing that in the fourth case the largest truncation errors are introduced in the frequency of response compared with other ones.

Finally, for values of parameter  $\beta$  different from 0.5, it occurs a false damping proportional to  $\beta - 0.5$ :

- if  $\beta$  equals *zero*, there will be a *negative* damping, which creates a self-excited vibration due to only the integration method;
- if  $\beta$  is *greater than 0.5*, there will be a *positive* damping, which creates a damping effect even without real damping in the problem.